

**FINITE ELEMENT ANALYSIS OF CYCLIC BEHAVIOR OF
STEEL SHEAR LINKS OF DIFFERENT GEOMETRY**

ISHFAQ AZIZ

MASTER OF SCIENCE IN CIVIL ENGINEERING (STRUCTURAL)



**DEPARTMENT OF CIVIL ENGINEERING
BANGLADESH UNIVERSITY OF ENGINEERING AND TECHNOLOGY
DHAKA**

NOVEMBER 2020

**FINITE ELEMENT ANALYSIS OF CYCLIC BEHAVIOR OF
STEEL SHEAR LINKS OF DIFFERENT GEOMETRY**

by

ISHFAQ AZIZ

Student ID No.: 1017042326 P

A thesis submitted to Department of Civil Engineering,
Bangladesh University of Engineering and Technology, Dhaka
in partial fulfillment of the requirements for the degree of

**MASTER OF SCIENCE IN CIVIL ENGINEERING
(STRUCTURAL)**

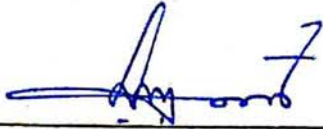


**DEPARTMENT OF CIVIL ENGINEERING
BANGLADESH UNIVERSITY OF ENGINEERING AND TECHNOLOGY
DHAKA**

NOVEMBER 2020

The thesis titled "Finite Element Analysis of Cyclic Behavior of Steel Shear Links of Different Geometry" submitted by Ishfaq Aziz, Roll No.: 1017042326 P, Session: October 2017 has been accepted as satisfactory in partial fulfillment of the requirement for the degree of Master of Science in Civil Engineering (Structural) on November 29, 2020.

BOARD OF EXAMINERS



Dr. Khan Mahmud Amanat
Professor,
Department of Civil Engineering,
BUET, Dhaka-1000.

Chairman
(Supervisor)



Dr. Md. Delwar Hossain
Professor and Head,
Department of Civil Engineering,
BUET, Dhaka-1000.

Member
(Ex-Officio)



Dr. Tahsin Reza Hossain
Professor,
Department of Civil Engineering,
BUET, Dhaka-1000.

Member



Dr. Mahbuba Begum
Professor,
Department of Civil Engineering,
BUET, Dhaka-1000.

Member



Lt Col Md Jahidul Islam, PhD
Associate Professor,
Department of Civil Engineering,
MIST, Mirpur Cantonment, Dhaka-1216.

Member
(External)

DECLARATION

It is hereby declared that, except for the contents where specific references have been made to the work of others, the research work presented in this thesis has been carried out by the author under the supervision of Dr. Khan Mahmud Amanat, Professor, Department of Civil Engineering, BUET. This thesis or any part of it has not been submitted elsewhere for the award of any degree or diploma.



Ishfaq Aziz

Student ID: 1017042326 P

Date: 29.11.2020

ACKNOWLEDGEMENT

All praises to Allah the most beneficial and merciful. By the grace and proper guidance of Almighty Allah, I have been able to complete the thesis as a requirement for the degree of Master of Science in Civil Engineering (Structural) after a journey of nearly three years.

I am grateful to all my family members for their unconditional support, love, and blessing. My parents are the one who comes next to the Almighty. Though words can never be enough to express my gratefulness to them, I just want to say that I am greatly indebted to them for bringing me up with love and encouragement to this stage and for everything they did for me. I would also like to thank my wife for all the inspiration and support throughout the research work. I am indebted to her for all the tireless motivation and support. I would also like to thank my sister for all her supports throughout the whole journey. For all these people the journey of my entire academic career till today has been so easy and comfortable.

I would like to express my utmost gratitude to my supervisor, Dr. Khan Mahmud Amanat, Professor, Department of Civil Engineering, Bangladesh University of Engineering and Technology (BUET), for his earnest supervision, prudent guidance, inclusive and important comments, along with timely and efficient discussion sessions. It was my honor and pleasure to work under his constant guidance. His impeccable focus on perfection has always galvanized me to strive for better outcomes. His expertise and valuable knowledge sharing throughout the research work have provided immense assistance to me. I shall always be indebted to him for not only the support in this research but for many other academic advice he rendered to me. I would also like to express gratitude to my friend and colleague Mohammad Irfan Hossain for his support in this research.

Next, I am thankful to all the honorable board members for their valuable time. My sincere gratitude to the teachers of Department of Civil Engineering, BUET for sharing their knowledge and experience and thus enlightening me.

Finally, I would like to thank all my friends and well-wishers for all their encouraging words and constant support.

Dedicated

to

My Parents

ABSTRACT

In seismic resilient structural systems like coupled shear wall systems and eccentrically braced frames, a small beam like segment known as the shear link is used as a replaceable structural fuse which dissipates seismic energy primarily by shear deformation. However, the feasibility of interchangeability between the different types of links is yet to be established. Different aspects of links, e.g., stocky short links without stiffeners which are not available in the existing codes need further research. The present study focuses on the numerical investigation of cyclic behavior of shear link to address some of these issues.

Several three-dimensional finite element models of shear links have been developed considering both geometric and material nonlinearity. The developed models were validated against experimental studies on shear links conducted in the past. With the validated models, studies have been carried on shear links with I-shaped sections and box-type sections. Applicability of existing equations for capacities of shear links having solid webs has been investigated. For shear strength reduction of short links with compact webs, perforated links (links having circular openings in web) have been investigated. Two different patterns of perforations for perforated links were studied and it was found that links with diagonal pattern of perforation can perform better than those with rectangular pattern. The effect of perforation density in link web has been investigated and it was found that dense perforations in link webs result in earlier web buckling during cyclic loading. Certain web compactness limit has also been suggested to avoid web buckling of links with even extremely dense perforations. Comparative study on energy dissipation and hysteresis efficiency of different types of links was done. Equal amount of energy was found to be dissipated by two links of the same shear capacity when the shear capacities are based on the suggested equations. However, the hysteresis efficiencies of I-shaped links are found to be higher than those of box-shaped links at rotations less than 0.09 radian. Refined equations for predicting plastic shear capacities of perforated links have been proposed and are validated against finite element analysis results. These equations for perforated shear links can be used in design for achieving cyclic response equivalent to that of a commonly used solid I-link of the same shear capacity.

TABLE OF CONTENTS

DECLARATION	i
ACKNOWLEDGEMENT	ii
ABSTRACT	iv
LIST OF FIGURES	ix
LIST OF TABLES	xvii
LIST OF ABBREVIATIONS	xix
LIST OF SYMBOLS	xx
CHAPTER 1: INTRODUCTION	1
1.1 General	1
1.2 Background and Research Significance	2
1.3 Objective of the Present Study	3
1.4 Methodology of the Study	4
1.5 Organization of the Thesis	4
CHAPTER 2: LITERATURE REVIEW	6
2.1 Introduction	6
2.2 Seismic Load Resisting Systems	6
2.3 Concept of Shear Link in Structural Systems	8
2.4 Design Philosophy of Structural Systems with Shear Links	11
2.5 Existing Design Guidelines for Shear Links	12
2.5.1 Shear and Moment Capacity of Solid Link	15
2.5.2 Classification of Links	15
2.5.3 Dimensioning of Links	16
2.5.4 Overstrength Factor	17
2.5.5 Link Rotation Angle	17

2.5.6	Intermediate Web Stiffeners	18
2.6	Review of State-of-the-Art Research on Shear Link and its Diversified Use	19
2.6.1	Loading Protocol, Overstrength and Inelastic Rotation	19
2.6.2	Material Variation in Shear Links	22
2.6.3	Shear Link in Coupled Shear Wall Systems	23
2.6.4	Shear Link in Moment Resisting Frames	24
2.7	Evaluation of Stiffener Requirements in Shear Links with Compact Web	26
2.8	Strength Reduction of Short Links	28
2.9	Energy Dissipation	32
2.9.1	Total Energy	32
2.9.2	Hysteresis Efficiency	32
2.10	Remarks	33
CHAPTER 3: METHODOLOGY FOR FINITE ELEMENT MODELING		35
3.1	Introduction	35
3.2	ANSYS - FEM Package for the Present Study	35
3.3	Modeling of Shear Links	35
3.3.1	Modeling Parameters	36
3.3.2	Element Modeling	36
3.3.3	Material Modeling	37
3.3.4	Generation of the Model Geometry	42
3.3.5	Meshing	46
3.3.6	Boundary Conditions	47
3.3.7	Loading	49
3.4	Typical FE Models Developed	49

3.5	Remarks	53
CHAPTER 4: NUMERICAL MODEL VALIDATION		54
4.1	Introduction	54
4.2	Simulation of Experimental Research on Replaceable Q345GJ Shear Links	54
4.2.1	FE Modeling Parameters and Loading History	54
4.2.2	Verification Results	57
4.3	Simulation of Experimental Study on Intermediate Web Stiffener Spacing of Shear Links	63
4.3.1	FE Modeling Parameters and Loading History	65
4.3.2	Verification Results	67
4.4	Simulation of Ductility and Energy Dissipation Behavior of Perforated Shear Link	69
4.4.1	FE Modeling Parameters and Loading History	73
4.4.2	Verification Results	74
4.5	Simulation of Cyclic Loading Behavior of Shear Links Constructed of ASTM A992 Steel	78
4.5.1	FE Modeling Parameters and Loading History	80
4.5.2	Verification Results	80
4.6	Remarks	83
CHAPTER 5: NUMERICAL STUDY AND DISCUSSIONS		84
5.1	Introduction	84
5.2	Effect of Length Ratio on Cyclic Behavior of Links	85
5.3	Solid I-Shaped and Solid Box-Shaped/Tubular Links	88
5.4	Perforated Links	93
5.4.1	Pattern of Perforation	94

5.4.2	Performance of Links with Different Perforations Patterns	95
5.5	Solid I-Shaped and Perforated I-Shaped Link	100
5.5.1	Equations of Shear Capacity for Interchangeability	100
5.5.2	Equivalent Cyclic Response of Perforated I-Link	105
5.6	Solid I-Link and Perforated Box/Tubular Link	111
5.6.1	Equations of Shear Capacity for Interchangeability	111
5.6.2	Equivalent Cyclic Response of Perforated Box-Link	113
5.7	Energy Dissipation	117
5.7.1	Total Energy	117
5.7.2	Hysteresis Efficiency	119
5.8	Effect of Perforation Size and Density	121
5.8.1	Geometric Parameters of the Developed Models	121
5.8.2	Hysteretic Responses	125
5.8.3	Investigation of Web Compactness Limit to Avoid Buckling of Densely Perforated Links	131
5.9	Remarks	133
	CHAPTER 6: CONCLUSIONS	135
6.1	General	135
6.2	Outcomes of the Study	136
6.3	Design Recommendations for Perforated Links	137
6.4	Scopes for Future Investigation and Recommendations	137
	REFERENCES	139

LIST OF FIGURES

Figure 2.1: Protected zone of moment resisting frame	7
Figure 2.2: Protected zone of concentrically braced frame	7
Figure 2.3: Protected zone of eccentrically braced frame	8
Figure 2.4: Typical configurations of Eccentrically Braced Frame	9
Figure 2.5: Eccentrically Braced Frame construction	9
Figure 2.6: Configuration for proposed replaceable I-link by Bozkurt et al. (2018)	10
Figure 2.7: Moment and shear force diagram of shear links in EBF subjected to lateral load	10
Figure 2.8: Replaceable shear links in coupled shear wall systems	11
Figure 2.9: Expected deformed configurations of Special Concentrically Braced Frame and Eccentrically Braced Frame	11
Figure 2.10: Yield Mechanism of Eccentrically Braced Frame	12
Figure 2.11: I-shaped shear link showing forces and dimensional parameters	13
Figure 2.12: Schematic view and deformed shape of a box-link	14
Figure 2.13: Classification of links	16
Figure 2.14: Rotation of the shear link	17
Figure 2.15: Cyclic response of unstiffened and stiffened W18×40 links, $h/t_w = 53.62$, $e = 28$ in.	18
Figure 2.16: Loading protocols used by Okazaki and Engelhardt (2007)	20
Figure 2.17: AISC loading protocol for cyclic testing of links up to 0.15 radian	21
Figure 2.18: Link overstrength factors reported in different experimental studies	22
Figure 2.19: Inelastic link rotation capacities reported in different experimental studies	22

Figure 2.20: Schematic view and test setup of replaceable coupling beam with shear link	24
Figure 2.21: Replaceable shear links in moment resisting frames	25
Figure 2.22: (a) Schematic view of link in moment resisting frames (b) Slit shear link (c) Perforated shear link	25
Figure 2.23: Damage of specimens: (a) web buckling (Specimen L13); (b) stiffener-to-flange weld fracture (Specimen L22); (c) web fracture (Specimen L12); (d) flange-to-end plate weld fracture (Specimen Q12) (Ji et al. 2016)	26
Figure 2.24: Hysteresis results of specimens of Volynkin et al. (2019) for evaluation of the necessity of web stiffeners	28
Figure 2.25: Slit dampers with elliptic holes used by Shahri and Mousavi (2018) in beam-column connection	29
Figure 2.26: Fuses with slits and butterfly shaped openings	29
Figure 2.27: Slit damper in beam-to-column connection	29
Figure 2.28: Special perforated steel plate shear walls	30
Figure 2.29: Numerical models of perforated (Perf) and slit (SL) shear links for strength reduction showing damage indices	31
Figure 2.30: Perforated link specimens of Tong et al. (2018), (a) Specimen L-C-1, (b) Specimen L-C-2	32
Figure 2.31: Hysteresis Efficiency	33
Figure 3.1: SOLID185 homogeneous structural solid geometry	36
Figure 3.2: Stress vs. plastic strain for Voce hardening	38
Figure 3.3: Illustration of the combined strain hardening model (a) Isotropic strain hardening model; (b) Kinematic strain hardening model; (c) Combined hardening model	40
Figure 3.4: Volume formation of the endplate	43

Figure 3.5: Volume formation of the flanges and web of I-shaped link (without stiffeners)	43
Figure 3.6: Volume of the whole assembly of I-link without stiffeners	44
Figure 3.7: Volume formation of intermediate web stiffeners within the I-link	44
Figure 3.8: Volume of the whole assembly of I-link with stiffeners	45
Figure 3.9: Isometric view of the link model after meshing (without stiffeners)	45
Figure 3.10: Isometric view of the link model after meshing (with stiffeners)	46
Figure 3.11: Boundary conditions of the link showing restraints at one end and coupling at the other end (where the load is to be applied)	47
Figure 3.12: Link rotation and applied displacement at link end	48
Figure 3.13: Link with web stiffeners on one side only (specimen 4A-RLP of Okazaki and Engelhardt, 2006)	50
Figure 3.14: Link with web stiffeners (specimen AL-BU-N2 of Volynkin et al. 2018)	51
Figure 3.15: Link with perforation in web for reduction of shear strength (Specimen L-C-2 of Tong et al. 2018)	52
Figure 4.1: Experimental setup of Liu et al. (2017)	55
Figure 4.2: Geometric details of shear link (Liu et al. 2017)	55
Figure 4.3: Loading history for specimens RSL-3, RSL-4, RSL-7, RSL-9 and RSL-10 of Liu et al. (2017) (time/s indicates the cycle number)	57
Figure 4.4: Comparison between FEM and experimental results of the specimen RSL-3	58
Figure 4.5: Comparison between FEM and experimental results of the specimen RSL-4	59
Figure 4.6: Comparison between FEM and experimental results of the specimen RSL-7	60

Figure 4.7: Comparison between FEM and experimental results of the specimen RSL-9	61
Figure 4.8: Comparison between FEM and experimental results of the specimen RSL-10	62
Figure 4.9: Deformed shape and von Mises stress of RSL-3 at 40mm shear displacement	63
Figure 4.10: Deformed shape of RSL-4	63
Figure 4.11: Test setup of eccentrically braced frame of Volynkin et al. (2018)	64
Figure 4.12: X-sectional dimensions of link specimen AL-BU-N2 of Volynkin et al. (2018)	64
Figure 4.13: FE model of specimen AL-BU-N2	66
Figure 4.14: FE model of specimen AL-BU-B2	66
Figure 4.15: Comparison between FEM and experimental results of link AL-BU-B2	67
Figure 4.16: Comparison between FEM and experimental results of link AL-BU-N2	68
Figure 4.17: Deformed shape of specimen AL-BU-B2 (Volynkin et al. 2018)	68
Figure 4.18: von Mises stress (MPa) and deformed shape of specimen AL-BU-B2 (FEM)	69
Figure 4.19: Experimental setup of Tong et al. (2018) (a) Schematic illustration (b) Photo	70
Figure 4.20: Dimensions of the cast steel link specimens tested by Tong et al. 2018 (perforations are not shown in this figure)	71
Figure 4.21: Web perforation pattern of perforated link specimens of Tong et al. (2018)	71
Figure 4.22: FE model of specimen L-C-1	72
Figure 4.23: FE model of specimen L-C-2	72

Figure 4.24: Isometric view of the FE model of specimen L-C-2	73
Figure 4.25: Loading history for specimens L-C-1 and L-C-2 (Tong et al. 2018)	74
Figure 4.26: Comparison between FEM and experimental results of specimen L-C-1	75
Figure 4.27: Comparison between FEM and experimental results of specimen L-C-2	75
Figure 4.28: Deformed shape after failure of L-C-1 (at -0.07 radian rotation) (Tong et al. 2018)	76
Figure 4.29: Plastic strain intensity and deformed shape of L-C-1 (Present study by FEM)	76
Figure 4.30: Deformed shape after failure of L-C-2 (at 0.11 radian rotation) (Tong et al. 2018)	77
Figure 4.31: Plastic strain intensity and deformed shape of L-C-2 (Present study by FEM)	77
Figure 4.32: Test setup of Okazaki and Engelhardt (2006)	78
Figure 4.33: Details of the link specimens (Okazaki and Engelhardt, 2006)	78
Figure 4.34: Numerical model of specimen 4A and 4A-RLP	79
Figure 4.35: Comparison between FEM and experimental results of specimen 4A	81
Figure 4.36: Comparison between FEM and experimental results of specimen 4A-RLP	81
Figure 4.37: Deformed shape showing web fracture of specimen 4A-RLP (Okazaki and Engelhardt, 2006)	82
Figure 4.38: von Mises stress (MPa) and deformed shape of specimen 4A-RLP at 0.1-radian rotation (present study by FEM)	82
Figure 4.39: Equivalent plastic strain and deformed shape of specimen 4A-RLP (present study by FEM)	83

Figure 4.40: Damage index of specimen 4A-RLP from the numerical study of Kalehbasti and Dolatshahi (2018)	83
Figure 5.1: Numerical model of link specimen ILR4	85
Figure 5.2: Deformed shape and von Mises stress (MPa) of link specimen ILR4	86
Figure 5.3: Monotonic behavior of links with same shear capacity but different length ratios	87
Figure 5.4: Shear-rotation hysteresis of link ILR1 and ILR4	87
Figure 5.5: Schematic view of box-shaped link with loading and geometric details	88
Figure 5.6: Numerical model of solid box-shaped/tubular link: B3	89
Figure 5.7: Numerical model of solid I-shaped link: I3	89
Figure 5.8: Responses of links based on V_{p2}	90
Figure 5.9: Monotonic response of I-link and box-link based on different shear capacity equations	91
Figure 5.10: Monotonic response of I-link and box-link based on different shear capacity equations	91
Figure 5.11: Responses of links I1 and B1 based on V_{p1}	92
Figure 5.12: Responses of links I2 and B2 based on V_{p1}	92
Figure 5.13: Perforated links with rectangular and diagonal pattern of perforations	94
Figure 5.14: Numerical model of E5-rect	96
Figure 5.15: Numerical model of E5-diag	96
Figure 5.16: Hysteretic response of links with rectangular and diagonal perforations	97
Figure 5.17: Plastic strain energy density of link with rectangular perforations	98
Figure 5.18: Plastic strain energy density of link with diagonal perforations	98
Figure 5.19: von Mises stress (MPa) of link with rectangular perforations	99

Figure 5.20: von Mises stress (MPa) of link with diagonal perforations	99
Figure 5.21: Developed model of a perforated I-shaped link: Iperfa	101
Figure 5.22: Monotonic results of solid and perforated I-link (using Equation 5-1)	103
Figure 5.23: Response of perforated link using reduction factor of $1-0.6 \times D/S$	103
Figure 5.24: Response of perforated link using reduction factor of $1-0.68 \times D/S$	104
Figure 5.25: Response of perforated link using reduction factor of $1-0.64 \times D/S$	104
Figure 5.26: Hysteretic results of solid and perforated I-link: Pair 1	106
Figure 5.27: Hysteretic results of solid and perforated I-link: Pair 2	107
Figure 5.28: Hysteretic results of solid and perforated I-link: Pair 3	107
Figure 5.29: Hysteretic results of solid and perforated I-link: Pair 4	108
Figure 5.30: Hysteretic results of solid and perforated I-link: Pair 5	108
Figure 5.31: Hysteretic results of solid and perforated I-link: Pair 6	109
Figure 5.32: Hysteretic results of solid and perforated I-link: Pair 7	109
Figure 5.33: Deformed shape and von Mises stress (MPa) of link I-14 at 0.13 radian	110
Figure 5.34: Deformed shape and von Mises stress (MPa) of link Iperf-14 at 0.13 radian	110
Figure 5.35: Developed model of perforated box-shaped/tubular link	111
Figure 5.36: Superimposed plot of I-shaped and perforated tubular link using the equation of special perforated steel plate shear walls	112
Figure 5.37: Hysteretic results of solid I-link and perforated box-link: Pair 1	114
Figure 5.38: Hysteretic results of solid I-link and perforated box-link: Pair 2	114
Figure 5.39: Hysteretic results of solid I-link and perforated box-link: Pair 3	115
Figure 5.40: Hysteretic results of solid I-link and perforated box-link: Pair 4	115
Figure 5.41: Hysteretic results of solid I-link and perforated box-link: Pair 5	116

Figure 5.42: Hysteretic results of solid I-link and perforated box-link: Pair 6	116
Figure 5.43: Hysteretic results of solid I-link and perforated box-link: Pair 7	117
Figure 5.44: Energy dissipation of I-links and perforated I-links listed in Table 5-8	118
Figure 5.45: Energy dissipation of I-link and perforated box-links listed in Table 5-9	118
Figure 5.46: Comparison of hysteresis efficiency of I shaped and perforated box-shaped link with same yield capacity	120
Figure 5.47: Comparison of hysteresis efficiency of I shaped and box-shaped link with same yield capacity	121
Figure 5.48: Perforated I-link sample-E3	122
Figure 5.49: Perforated I-link sample-E5	123
Figure 5.50: Perforated I-link sample-E7	123
Figure 5.51: Perforated I-link sample-E9	124
Figure 5.52: Perforated I-link sample-E11	124
Figure 5.53: Hysteretic response of E3, E5, E7, E9 and E11 ($t_w = 8.1$ mm, $h/t_w = 23.46$)	125
Figure 5.54: Hysteretic plots of links with five different perforation densities (E3, E5, E7, E9 and, E11) for $h/t_w = 23.46$	126
Figure 5.55: Deformed shape and von Mises stress (MPa) of link E3 and E11 ($h/t_w=19$) at -0.11 radian rotation	128
Figure 5.56: Deformed shape and von Mises stress (MPa) of link E3 and E11 ($h/t_w=19$) at -0.13 radian rotation	129
Figure 5.57: Deformed shape and von Mises stress (MPa) of link E3 and E11 ($h/t_w=19$) at -0.15 radian rotation	130
Figure 5.58: Ratio of peak shear forces to plastic shear capacities of E11 samples at different rotations showing shear force drop due to buckling	132

LIST OF TABLES

Table 2-1: Standard loading protocol for link testing as per AISC 341-16	20
Table 2-2: Specimen details of Volynkin et al. (2019) for evaluation of necessity of web stiffeners	27
Table 3-1: Material data table for Chaboche nonlinear kinematic hardening model	41
Table 3-2: Material data table for nonlinear isotropic hardening model using Voce law	41
Table 3-3: Command lines in ANSYS for providing nonlinear hardening parameters	42
Table 4-1: Details of the modeled link specimens of Liu et al. (2017)	56
Table 4-2: Material parameters for verification of study of Liu et al. (2017)	56
Table 4-3: Parameters of modeled specimens of Volynkin et al. (2018)	65
Table 4-4: Material parameters for verification of study of Volynkin et al. (2018)	65
Table 4-5: Specimen details of perforated links of Tong et al. (2018)	71
Table 4-6: Material parameters for verification of study of Tong et al. (2018)	73
Table 4-7: Parametric details of specimen 4A and 4A-RLP (Okazaki and Engelhardt, 2006)	79
Table 4-8: Material parameters for verification of study of Okazaki and Engelhardt (2006)	80
Table 5-1: Material parameters for parametric studies	84
Table 5-2: Parameters of link of same capacity but different length ratio	86
Table 5-3: Equations of shear capacities of I-links and box-links	88
Table 5-4: Shear capacities of I-links and box-shaped links	90
Table 5-5: Parameters of link specimen with diagonal and rectangular pattern of perforations	95

Table 5-6: Details of perforated I-link specimens	101
Table 5-7: Trial reduction factors for different perforated link specimens	102
Table 5-8: Parameters of solid I-links and perforated I-links	105
Table 5-9: Parameters of I-links and perforated box-links	113
Table 5-10: Parameters of hysteresis efficiency of perforated box-link and I-link	119
Table 5-11: Parameters of hysteresis efficiency of solid box and I-link	120
Table 5-12: Parameters of the five perforated links with different perforation density	122
Table 5-13: Shear drop due to buckling for different densities of web perforations ($h/t_w = 23.46$)	127
Table 5-14: Shear drop due to buckling for different densities of web perforations ($h/t_w = 19$)	127
Table 5-15: E11 links with different values of web compactness (h/t_w)	131

LIST OF ABBREVIATIONS

AISC	:	American Institute of Steel Construction
ANSYS	:	Analysis System
CBF	:	Concentrically Braced Frame
CSW	:	Coupled Shear Wall
EBF	:	Eccentrically Braced Frame
FE	:	Finite Element
FEA	:	Finite Element Analysis
FEM	:	Finite Element Method
MRF	:	Moment Resisting Frame
SL	:	Shear Link
SPSPSW	:	Special Perforated Steel Plate Shear Walls
SPSW		Steel Plate Shear Wall
PSL	:	Perforated Shear Link
SSL	:	Slit Shear Link
SCBF	:	Special Concentrically Braced Frames
CCSW	:	Coupled Concrete Shear Walls
LCF	:	Linked Column Framed

LIST OF SYMBOLS

b_f	: Flange width of link
b	: Exponential saturation parameter of isotropic hardening
C_i	: Hardening modulus of i^{th} Chaboche kinematic model
d	: Total link depth
D	: Hole diameter of perforated links
e	: Length of the link
E	: Young's modulus
E_{hyst}	: Area of hysteresis loop at a definite rotation of a link
E_{max}	: Maximum area of hysteresis at definite rotation of a link
F_y	: Yield strength of steel
$F_{y(flange)}$: Yield strength of flange steel
$F_{y(web)}$: Yield strength of web steel
h	: Height of the link web
M_p	: Plastic Moment capacity
R	: Yield stress
R_∞	: Exponential coefficient of isotropic hardening
S	: Diagonal center to center spacing between perforation holes of perforated links
S_{clear}	: Clear diagonal spacing between perforation holes of perforated links
t_{EP}	: Thickness of endplates of link
t_f	: Flange thickness of link

t_{st}	:	Stiffener thickness
t_w	:	Web thickness of link
V_{max}	:	Maximum shear strength
V_p	:	Plastic shear capacity
x_L	:	Displacement applied at one end of a shear link
Z	:	Plastic section modulus
α	:	Backstress
γ	:	Shear displacement angle / Link rotation angle
γ_P	:	Inelastic rotation of link
γ_i	:	Decreasing rate of hardening modulus of i^{th} Chaboche kinematic model
ε_{pl}	:	Accumulated plastic strain
θ	:	Temperature
ν	:	Poisson's ratio
Ω	:	Overstrength factor
R_o	:	Linear coefficient of isotropic hardening
σ_o	:	Initial yield stress
λ_{hd}	:	Limiting width to thickness ratio for highly ductile members

CHAPTER 1

INTRODUCTION

1.1 GENERAL

Since the late 1970s, earthquake engineering research has clearly demonstrated that special care must be taken to ensure ductile structural behavior. Inherent material ductility does not seem to be enough in seismic design of steel structures. As an evidence of this, numerous steel structures were seen to suffer significant damages during the Northridge (Los Angeles) earthquake of January 17, 1994 and the Kobe (Japan) earthquake that occurred, coincidentally, exactly one year later (January 17, 1995). Both earthquakes occurred in highly developed urban areas confirmed previous research findings that material ductility alone is not a guarantee of ductile structural behavior when steel components and connections can fail in a brittle manner (e.g. Bruneau et al. 1996; Tremblay et al. 1995, 1996). So, there are many situations in which an explicit approach to the design of ductile steel structures is necessary and appropriate design strategies should be adopted to allow for stable and reliable hysteretic energy-dissipation mechanisms.

Responding to the above-mentioned demand, seismic control systems have become subject matter of growing interest. These systems refer to modern techniques in Earthquake Resistant Design that prevent or divert a major portion of earthquake energy from entering into the main structural components of the system. There are generally three types of seismic control systems viz. (i) Passive seismic control (ii) Active seismic control and (iii) Hybrid seismic control. Active control systems are those structures equipped with real-time processing sensors and force delivery devices which require an external source of power to generate structural control forces. Passive seismic control does not require any additional energy source to operate and are activated by cyclic input motion only like earthquake, wind etc. Hybrid seismic control apply both of these techniques.

Passive control systems, also known as passive energy dissipation systems, have been considered an effective and inexpensive way to mitigate earthquake risks to structures.

With designated energy dissipative devices installed in a structure, a large portion of the input energy supplied by wind and/or earthquake can be dissipated; and thus, the damage to the parent structure is minimized. It must be noted that, repair of buildings suffering damage from seismic events has been found to be costly in terms of both money and time. For minimum disruption in the life and business of urban society, prompt economic recovery of buildings is also a clear need. Thus, the use of easily replaceable components or passive energy dissipating devices in the structure is expected to provide a resilient structure and at the same time aid in time saving and economic recovery in post disaster period.

Several passive energy dissipating devices have been seen to be investigated in different earthquake resilient structural systems like shear links in Eccentrically Braced Frame EBF's, shear dampers in beam-column connections etc. This study focuses on the study of cyclic behavior of shear links which can be used as a replaceable energy dissipating device in various structural systems like the Coupled Shear Wall systems, Eccentrically Braced Frames, Moment Resisting Frames etc.

1.2 BACKGROUND AND RESEARCH SIGNIFICANCE

The inception of the concept of shear links occurred from the invention of Eccentrically Braced Frames (EBF) (Fujimoto et al. 1972, Tanabashi et al. 1974), which consisted of a small beam like segment called the 'Shear Link'. Being subjected to cyclic loading shear links dissipate energy primarily by shear deformation. These shear links absorb energy by undergoing large plastic deformation and keep the other members of the primary structural system free of damage.

Shear links of different lengths and geometry were studied by previous researchers (Okazaki and Engelhardt, 2006, Okazaki et al. 2005, Liu et al. 2018 etc.). Meanwhile, codes were also developed for providing guidelines regarding the design of the links (AISC 341-16). Due to the effectiveness of the shear link as an energy dissipating replaceable structural fuse, numerous studies were further performed on it as a part of different earthquake resilient structural systems like the coupled shear wall system (Ji et al. 2017), special moment resisting frames (Nikoukalam and Dolatshahi, 2015, Shen et al. 2011) etc. However, recent studies on some links reveal that, certain aspects of

the existing codes need some modification and some other need further investigation (Azad and Topkaya, 2017). Very short compact links without stiffeners which are found to be promising in sustaining high inelastic shear deformation (Volynkin et al. 2018) have high shear and overstrength values (Duscika et al. 2010), provisions for which are not stated in the existing codes. Though these links can sustain high inelastic deformation, high ultimate shear strengths of these links put more demand on peripheral structural component attached to it in the whole system. As a solution to this, different types of openings can be made in the webs of these links to reduce their shear strengths. Thus, different types of perforations in link web can be used to control ultimate shear strength and decouple strength and inelastic rotation capacity, a phenomenon which still lacks adequate study.

Moreover, despite having adequate research on different geometries of links the feasibility of interchangeability between these links is yet to be established. Guidelines for interchangeability between different types of links are necessary since shear links are used as replaceable components and link of one type may be required to be replaced by a link of another type in post damage period.

So, investigation on different geometries of the links including different types of perforations in the link web and feasibility of interchangeability between the different types of shear links with respect to energy dissipation, strength and ductility (inelastic rotation) is necessary. This study focuses on the cyclic behavior of different types of shear links including links with perforations in the webs for reduction of shear strength and also on interchangeability between the links of different geometry which involves links with both solid and perforated webs. Since conducting experiments on steel tend to be costly, different types of shear links will be investigated by finite element analysis and further parametric studies to have a clear understanding of their relative performance under cyclic loading.

1.3 OBJECTIVE OF THE PRESENT STUDY

The main objectives of the present study are as follows

- (i) To investigate the behavior of solid steel shear links of different geometry under cyclic loading.

- (ii) To analyze the cyclic behavior of links with perforations/openings in the web.
- (iii) To compare the performances of links of different geometry both with and without perforations in the web.
- (iv) To investigate the feasibility of obtaining equivalent behavior by different types of links for establishing the interchangeability between them.

1.4 METHODOLOGY OF THE STUDY

Finite element models of steel shear link would be developed first. The developed models would be validated against the results of experimental studies of past researchers to establish the reliability of the finite element analysis scheme. Then, shear links of different geometry (box-shaped link, I-shaped link etc.) would be analyzed numerically to investigate their response under cyclic loading. Introduction of circular perforations in link webs would be studied for shear strength reduction. The pattern and density of perforations in perforated links would also be comparatively examined. Further, attempts would be made to establish interchangeability between the different types of links studied for which design equations would be proposed. Hysteretic response, energy dissipation, and other related factors of different links would also be studied and compared.

1.5 ORGANIZATION OF THE THESIS

The thesis organizes the whole research work which includes the existing research needs in this area of study, parametric studies done by Finite Element Analysis, findings of the study and scopes of further study. The whole work is presented in six different chapters which are as follows.

Chapter 1 introduces the overall subject matter and the idea of the present study.

Chapter 2 presents the literature review of the topic where, existing research about the shear link as an energy dissipating device is depicted. The eclectic potential of the link in different seismic resilient structural systems are also presented in this chapter.

Chapter 3 contains the methodology of Finite Element Analysis used in the present study. This chapter contains the description of element modeling, material modeling, generation of model geometry, meshing, boundary conditions and cyclic load application. Some typical FE models developed in this research have also been shown at the end of this chapter.

Chapter 4 portrays the verification of the models developed in Chapter 3 with reference to past experimental and numerical studies carried out by previous researchers.

Chapter 5 presents all the parametric studies done with the verified finite element models. In addition to the solid links, links with perforated webs for shear strength reduction were studied and presented in this chapter. As a part of investigating the interchangeability between different links, refined design equations for predicting plastic shear strengths of different shear links were developed and presented in this chapter. It also presents the studies related to energy dissipation and web compactness of solid and perforated links.

Chapter 6 is the concluding chapter that summarizes the entire research work as well as indicates probable study area for further research in this field of study.

CHAPTER 2

LITERATURE REVIEW

2.1 INTRODUCTION

To improve the seismic behavior of structures, structural systems capable of dissipating seismic energies were started to be proposed in the final third of the twentieth century. These structural systems contain energy dissipating devices. Energy dissipating devices (e.g. shear links, dampers, structural fuses, etc.) are primarily designed to undergo inelastic deformation and dissipate seismic energy when subjected to earthquake and similar cyclic loading. One major invention in the field of energy dissipating structural systems was the proposal of a system called the Eccentrically Braced Frame (Fujimoto et al. 1972, Tanabashi et al. 1974). In an EBF, a small beam like segment which is called the ‘Shear Link’ acts as the key energy-dissipating element. The capacity of energy dissipation of these shear links further makes these links potential structural members of many earthquake-resilient structures. For these reasons, eclectic studies about the shear link and its cyclic behavior became an important subject matter of study in recent years.

2.2 SEISMIC LOAD RESISTING SYSTEMS

The different seismic load resisting systems used in steel buildings includes Moment Resisting Frame, Concentrically Braced Frame, Eccentrically Braced Frame, Coupled Shear Wall system etc. Each of these systems consists of protected zones in which seismic energy will be dissipated by means of cyclic behavior. Some examples of the protected zones are illustrated in Figure 2.1 to Figure 2.3. Protected zones shall comply with the following (Engelhardt 2007)

- i. No welded shear studs are permitted
- ii. No decking attachments that penetrate the beam flange are permitted, but decking arc spot welds are permitted
- iii. No welded, bolted, screwed, or shot-in attachments for edge angles, exterior facades, partitions, duct work, piping, etc. are permitted

- iv. Discontinuities from fabrication or erection operations (such as tack welds, erection aids, etc.) shall be repaired

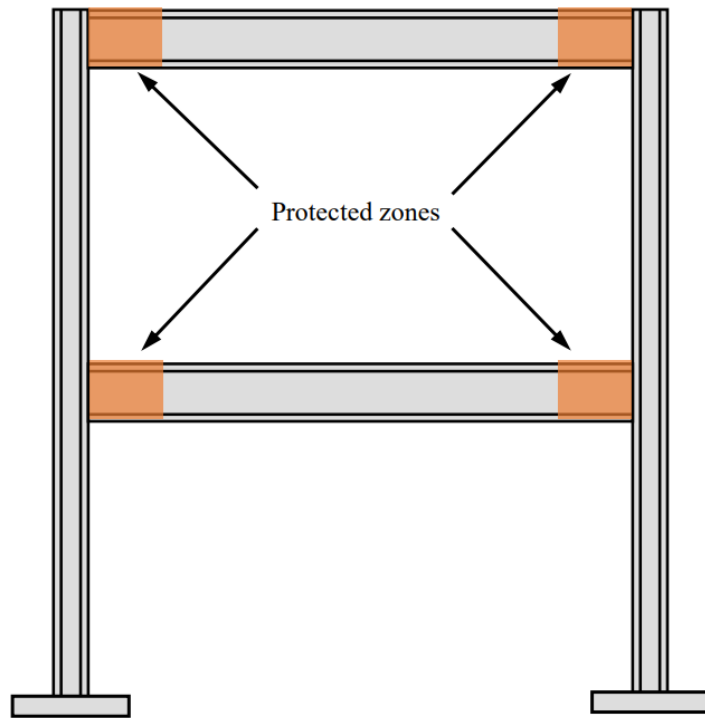


Figure 2.1: Protected zone of moment resisting frame (Engelhardt 2007)

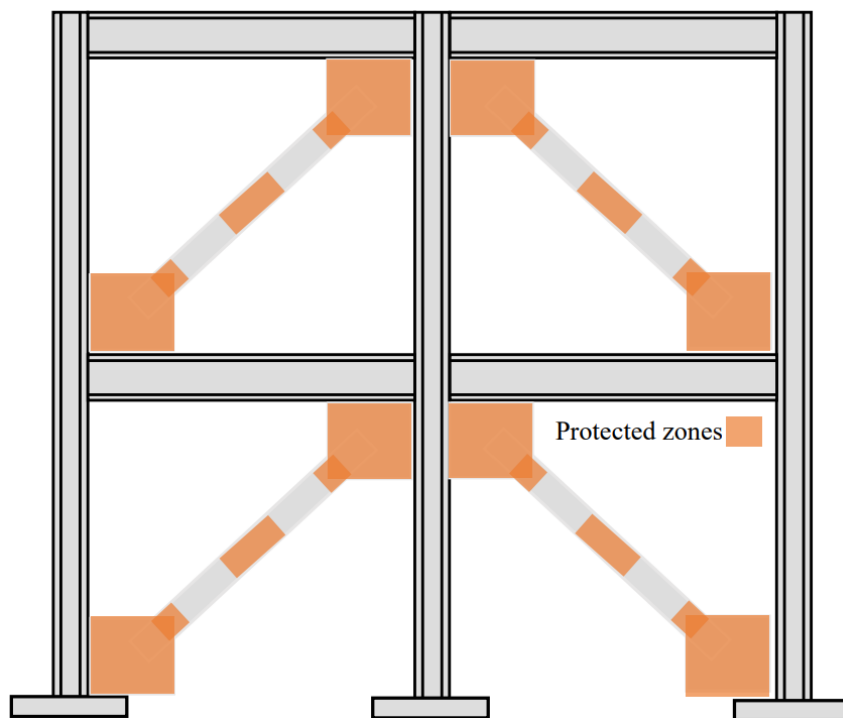


Figure 2.2: Protected zone of concentrically braced frame (Engelhardt 2007)

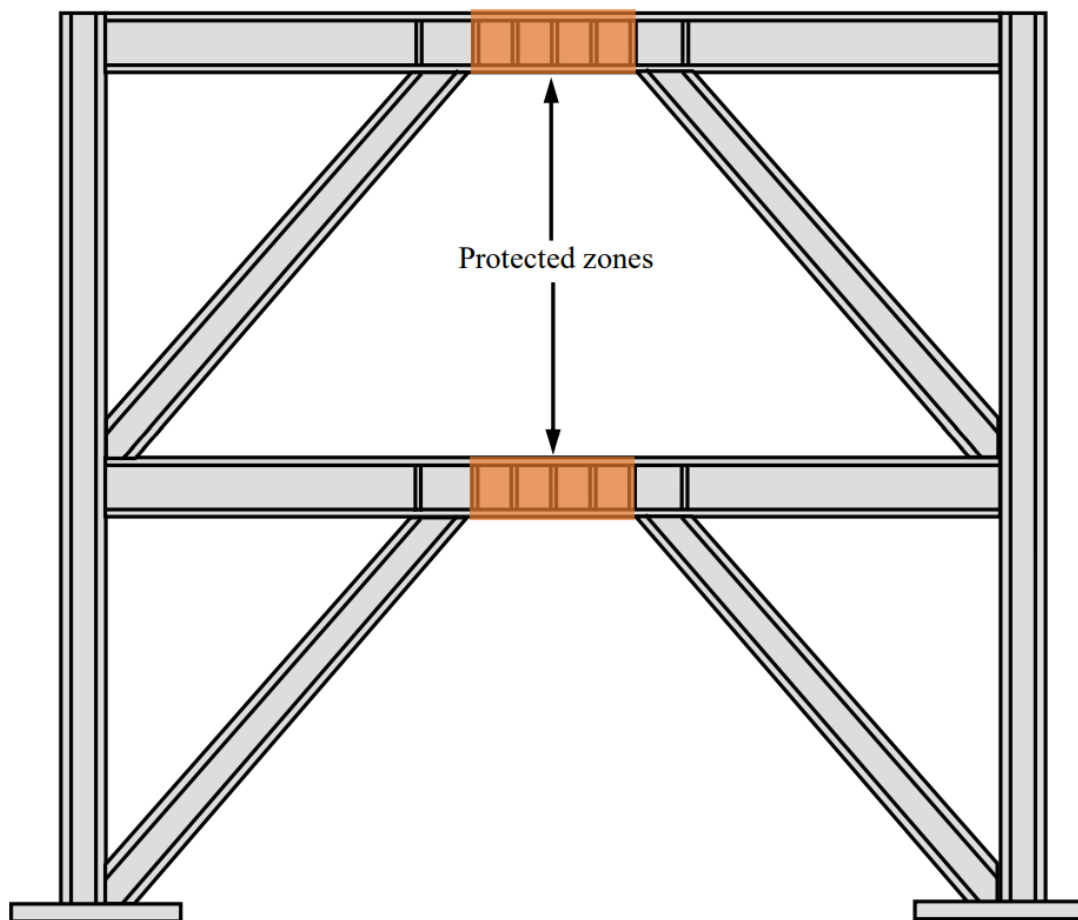


Figure 2.3: Protected zone of eccentrically braced frame (Engelhardt 2007)

2.3 CONCEPT OF SHEAR LINK IN STRUCTURAL SYSTEMS

Eccentrically Braced Frame was first proposed by in Japan (Fujimoto et al. 1972, Tanabashi et al. 1974) which combines the advantages of both high elastic stiffness and high ductility. Consequently, greater energy dissipation is attained by the system. Seismic energy is dissipated in this system by small beam like segments known as the ‘links’. Few typical configurations of EBF system are shown in Figure 2.4 where, length of a link is designated as ‘ e ’. A shear link can be placed both vertically and horizontally. Figure 2.4(a) shows EBF with interior link and Figure 2.4(b) shows EBF with exterior link both of which are also depicted in EBF construction images of Figure 2.5. Shear links have also been proposed and studied as a replaceable component in Coupled Shear Wall systems (Ji et al. 2017), a schematic view of which is shown in Figure 2.8.

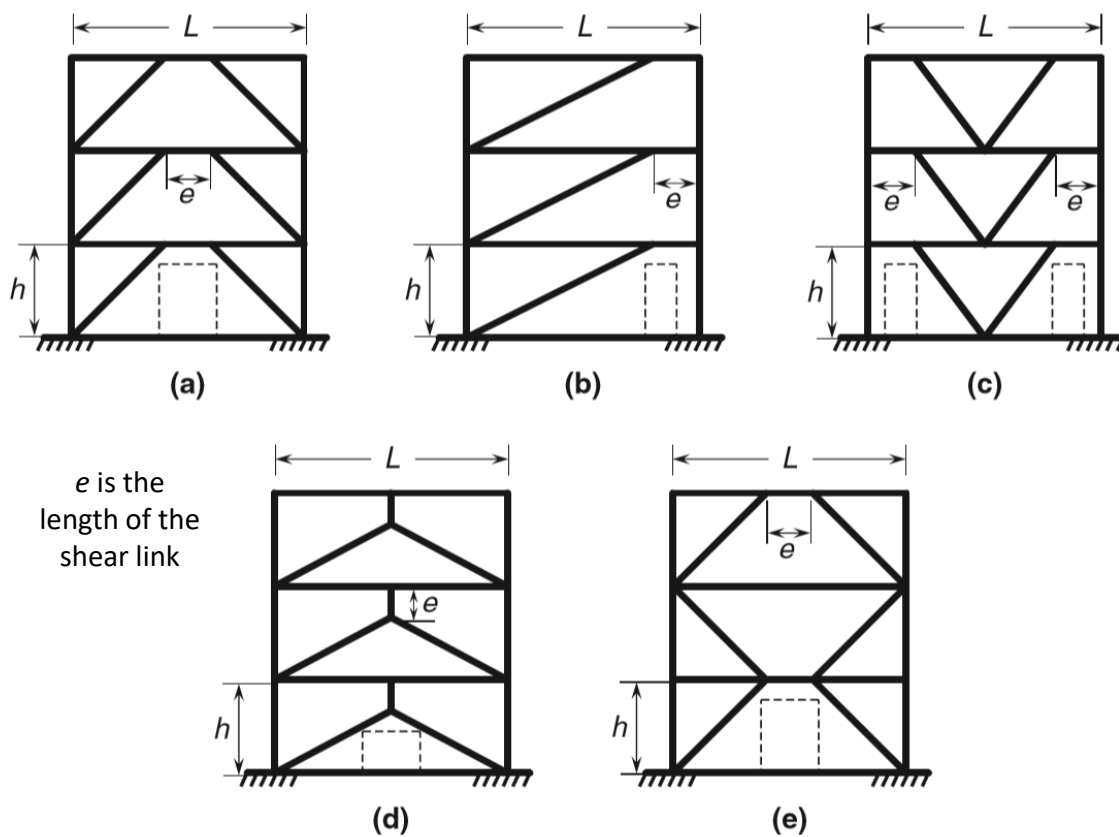


Figure 2.4: Typical configurations of Eccentrically Braced Frame (Bruneau, et al. 1998.)

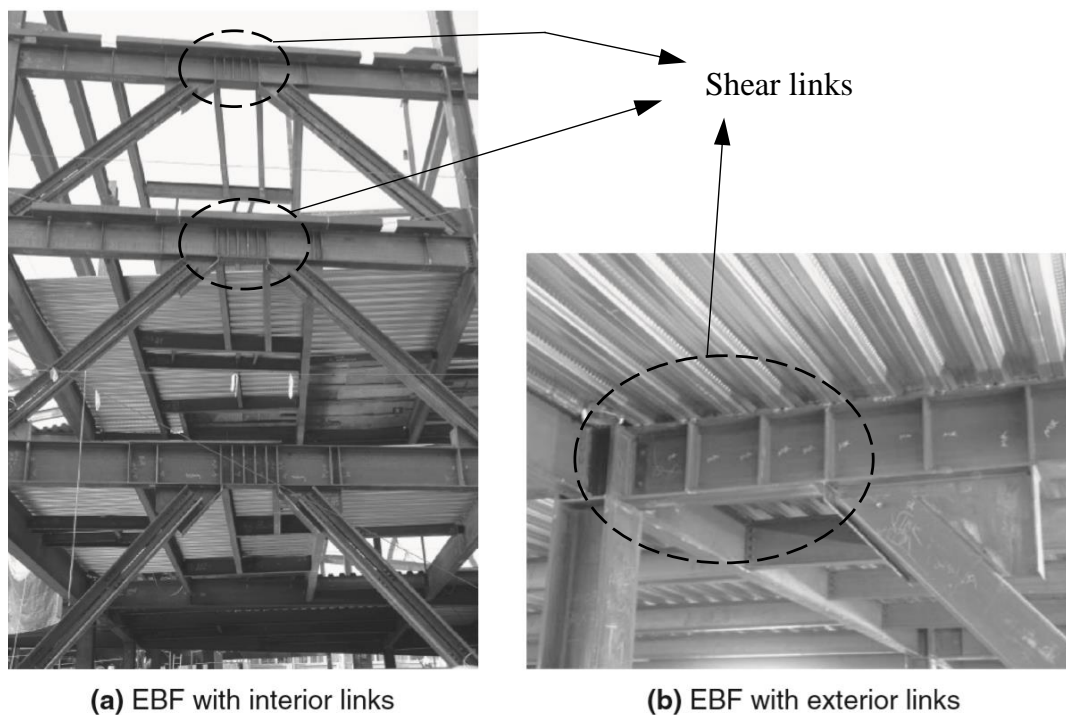


Figure 2.5: Eccentrically Braced Frame construction (Bruneau, et al. 1998.)

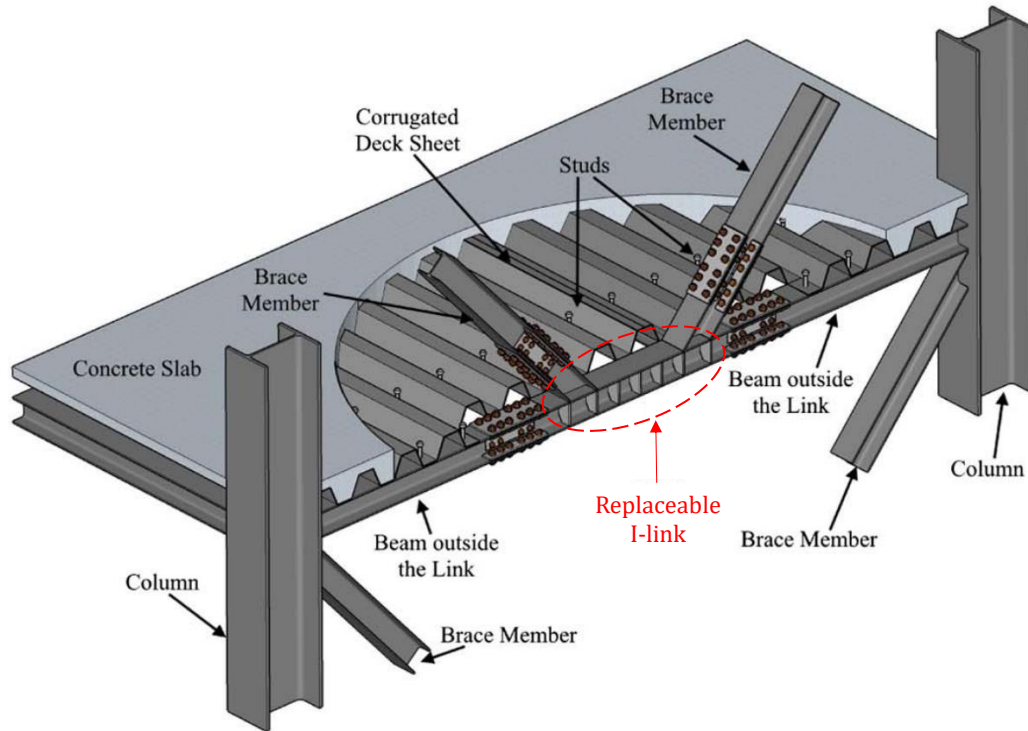


Figure 2.6: Configuration for proposed replaceable I-link by Bozkurt et al. (2018)

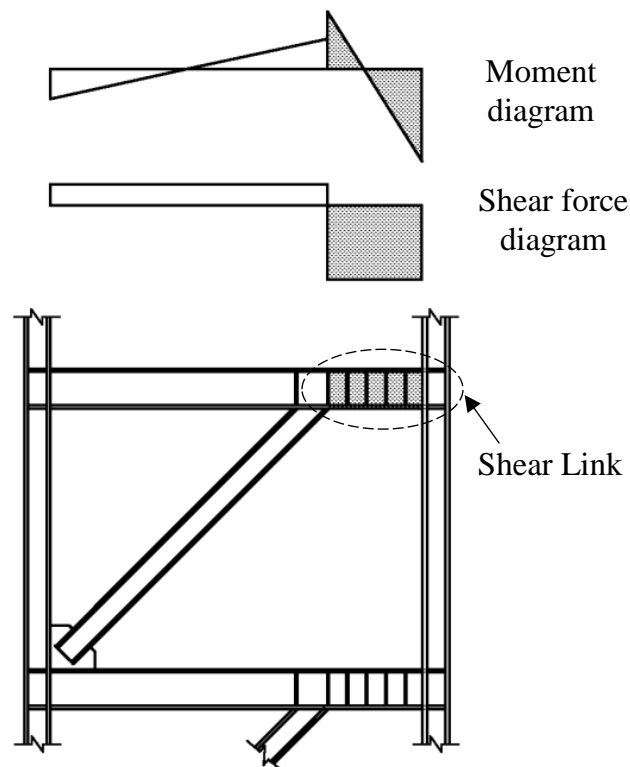


Figure 2.7: Moment and shear force diagram of shear links in EBF subjected to lateral load (Okazaki et al. 2006)

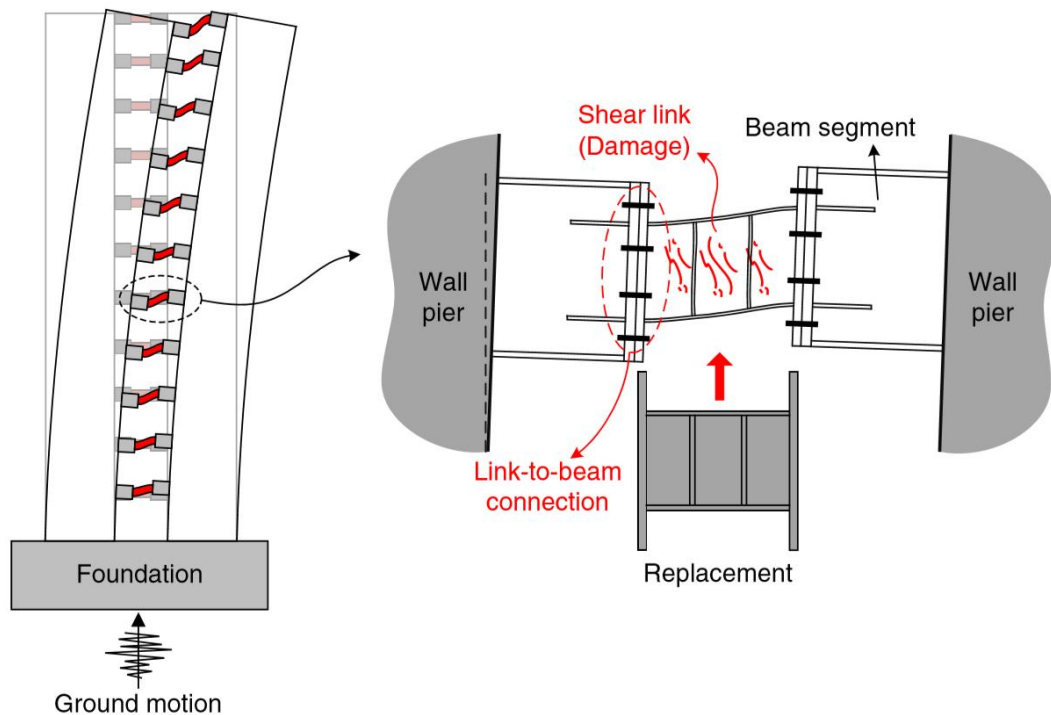


Figure 2.8: Replaceable shear links in coupled shear wall systems (Ji et al. 2017)

2.4 DESIGN PHILOSOPHY OF STRUCTURAL SYSTEMS WITH SHEAR LINKS

The desired plastic mechanism of Eccentrically Braced Frame systems with shear links is shown in Figure 2.10 where the yielded links are cross hatched. The whole system is intended to be designed in such a way that the link undergoes plastic deformation to dissipate energy and the remaining parts of the structure remain elastic. In Special Centrically Braced Frames, the braces are designed to act as structural fuses whereas, in an Eccentrically Braced Frame, the links are expected to act as energy dissipating fuses (Figure 2.9).

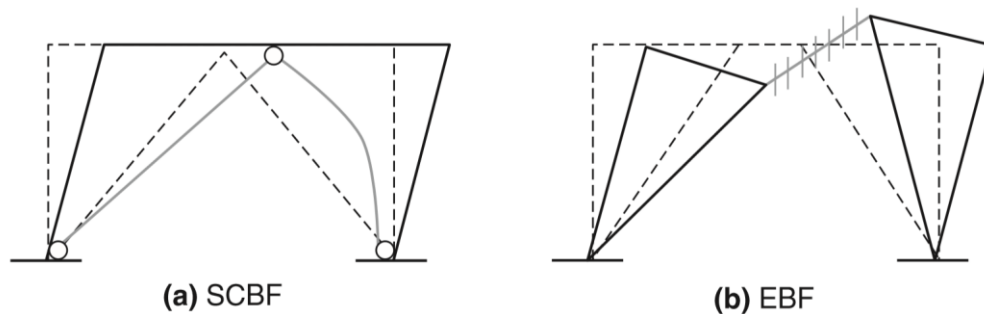


Figure 2.9: Expected deformed configurations of Special Centrically Braced Frame and Eccentrically Braced Frame (Bruneau, et al. 1998.)

Here, the effectiveness of the links as an energy dissipating device is a subject matter of concern for similar earthquake resistant structures.

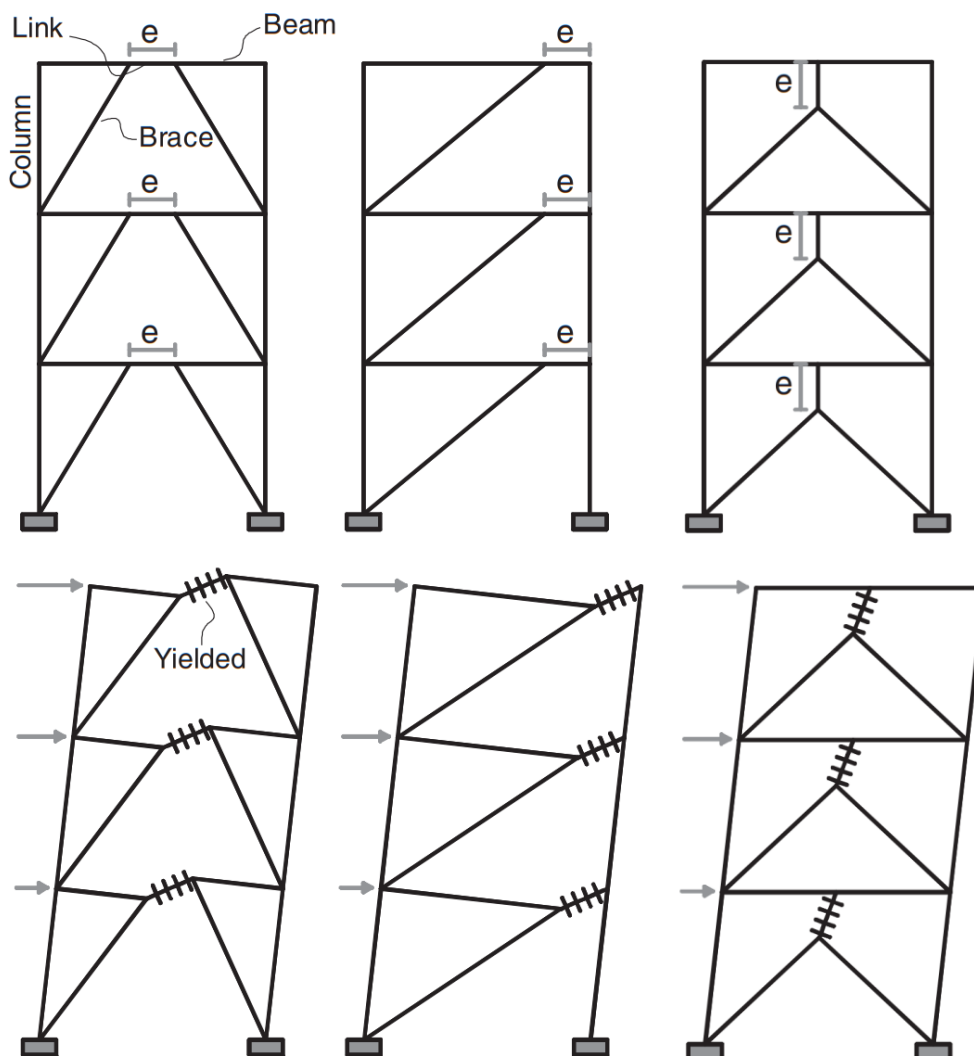


Figure 2.10: Yield Mechanism of Eccentrically Braced Frame (Azad and Topkaya, 2017)

2.5 EXISTING DESIGN GUIDELINES FOR SHEAR LINKS

According to the AISC code links in an EBF shall be I-shaped cross-sections (rolled or built-up) or built-up box sections (AISC 341-16). The schematic view of an I-shaped shear link is shown in Figure 2.11 and a sample configuration of replaceable I-link with stiffeners proposed by some of the previous researchers (Bozkurt et al. 2018) is shown in Figure 2.6 . The length of a link is usually designated as ‘ e ’. The

internal forces and geometric parameters of an I-shaped link are shown in Figure 2.11. The moment and shear force diagram of a link in an EBF subjected to lateral load is shown in Figure 2.7 (Okazaki et al. 2006).

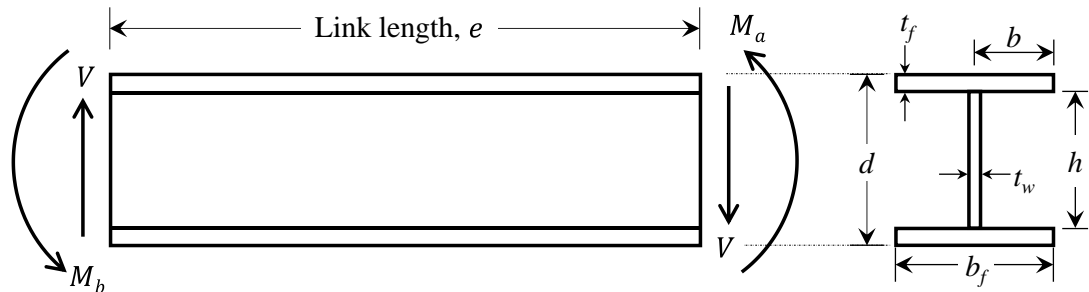


Figure 2.11: I-shaped shear link showing forces and dimensional parameters

In Figure 2.11,

d is the total depth of the I-link

h is the web height

t_w is the web thickness of the link

t_f is the flange thickness of the link

b_f is the flange width of the link and $b = b_f/2$

Links with box/tubular sections have been studied in the past by Berman and Bruneau (2007), Berman and Bruneau (2008) etc. The schematic view of a box-shaped/tubular link and the deformed shape of the box-link from the experiment of Berman and Bruneau (2007) is shown in Figure 2.12.

In Figure 2.12 (a),

d is the total depth of the box-link

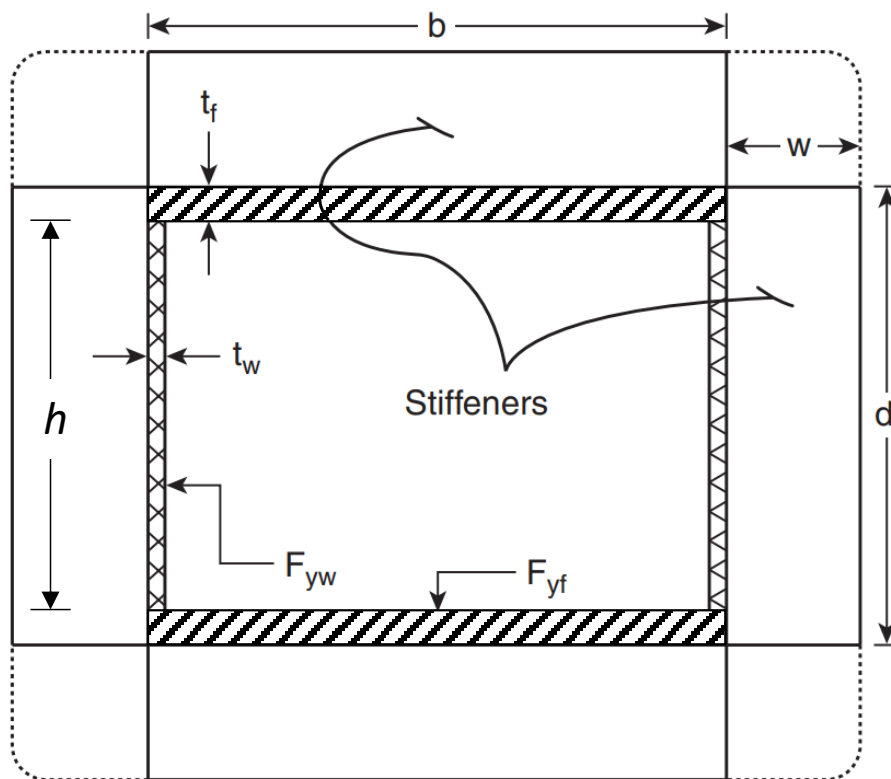
h is the web height

t_w is the thickness of the webs

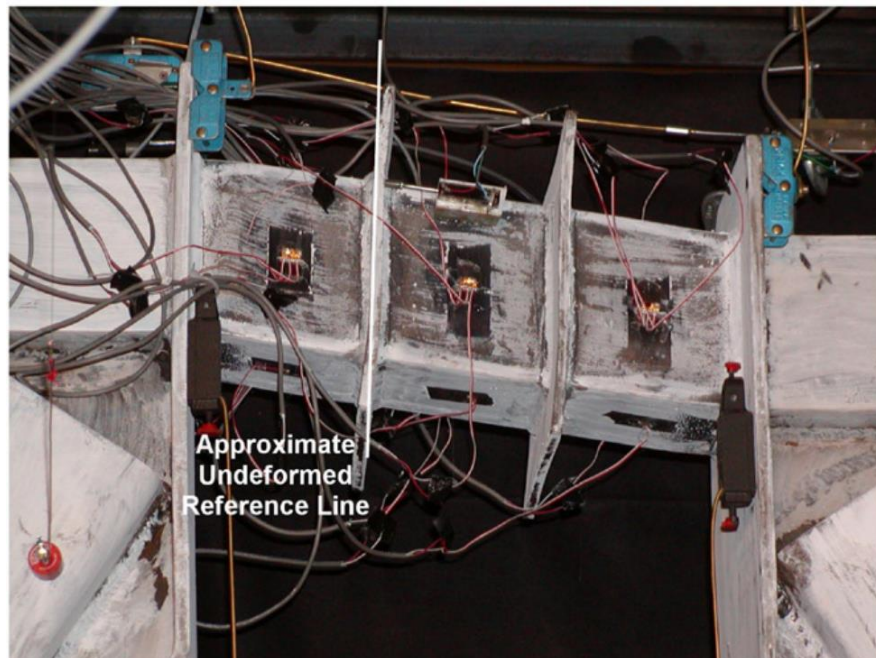
t_f is the thickness of the flanges

b is the flange width of the box link = b_f

F_{yw} and F_{yf} indicates yield stress of webs and flanges respectively



(a) Schematic view of tubular link section with stiffeners



(b) Deformed shape

Figure 2.12: Schematic view and deformed shape of a box-link (Berman and Bruneau, 2007)

2.5.1 Shear and Moment Capacity of Solid Link

According to AISC 341-16, the plastic shear capacity (V_p) and plastic moment capacity (M_p) of short shear yielding links (defined in section 2.5.2) are shown respectively in Equations 2.1 and 2.2.

$$V_p = 0.6F_y \times A_w \quad 2.1$$

$$M_p = F_y Z = M_{p(flange)} + M_{p(web)} \quad 2.2$$

where,

F_y is the yield strength of steel

$A_w = (d - 2t_f)t_w$ for I-shaped link sections

$= 2(d - 2t_f)t_w$ for box link sections

Z is the plastic section modulus about the axis of bending

2.5.2 Classification of Links

In Figure 2.11, from the equilibrium of forces, we can write $Ve = M_a + M_b$. At balanced yielding condition shear hinges and flexural hinges form simultaneously. At this condition, the link length is $e_o = 2M_p/V_p$. When $e < e_o$ (short link), a shear hinge forms and when $e > e_o$ (long link), flexural hinges form and the corresponding shear force at this point is $V = 2M_p/e$. Previous test results show that a short link with properly designed stiffeners (See section 2.5.6) can develop shear strength equal to approximately $1.5V_p$ (Hjelmstad and Popov, 1983). So, to avoid failure related to link flanges (severe flange buckling or link flange to column welds) the end moments were limited to $1.2M_p$ and the maximum length for a shear yielding link is modified as in Equation 2.3 (Kasai and Popov, 1986)

$$e = \frac{2(1.2M_p)}{1.5V_p} = \frac{1.6M_p}{V_p} \quad 2.3$$

Links are classified into three categories in terms of their length (e) or based on a term called the 'link length ratio', $\rho = e/(M_p/V_p)$. The classified links are short links, intermediate links, and long links. The classification is shown in Figure 2.13. Under severe cyclic loading short links generally have higher energy dissipation capacity and

more predictable post-yield behavior compared to long links (Engelhardt and Popov, 1989). So, short shear links which primarily yield by shear have been chosen for this study.

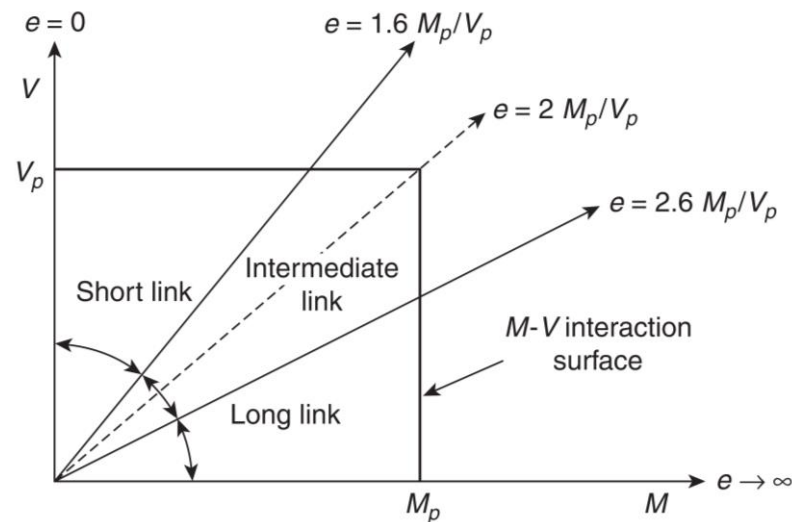


Figure 2.13: Classification of links (Bruneau, et al. 1998)

2.5.3 Dimensioning of Links

Since the links are primarily designed to dissipate seismic energies, the I-shaped link sections need to be seismically compact which means that, the aspect ratios of the web and the flange of a link needs to satisfy the limits of highly ductile members. However, the AISC code states that, the flanges of I-shaped links with link lengths $e < 1.6M_p/V_p$ are permitted to satisfy the requirements of moderately ductile members (AISC 341-16)

To achieve large plastic deformation capacity the aspect ratios of the flanges and webs of an I-shaped link and box-links should satisfy the limits shown in Equations 2.4 to 2.9 (AISC 341-16) which are for highly ductile members.

$$\text{Flanges of I-link:} \quad \frac{b}{t_f} \leq 0.32 \sqrt{E/F_{y(\text{flange})}} \quad 2.4$$

$$\text{Web of I-link:} \quad h/t_w \leq 1.57 \sqrt{E/F_{y(\text{web})}} \quad 2.5$$

$$\text{Flanges of box-link: } \frac{b}{t_f} \leq 0.65 \sqrt{E/F_{y(\text{flange})}} \quad 2.6$$

$$\text{Webs of box-link: } h/t_w \leq 0.65 \sqrt{E/F_{y(\text{web})}} \quad 2.7$$

2.5.4 Overstrength Factor

When a shear link is subjected to cyclic loading, the link can sustain/develop shear forces much greater than the plastic shear capacity of the section. The ratio of the maximum shear developed (V_{max}) to the plastic shear capacity (V_p) of the shear link is called the overstrength factor (Equation 2.8) of a shear yielding link.

$$\text{Overstrength factor, } \Omega = \frac{V_{max}}{V_p} \quad 2.8$$

2.5.5 Link Rotation Angle

The inelastic rotation (γ_p) of a link in an EBF system, is defined as the angle between the link and the beam connected with the link. In Figure 2.14, the following equation defines the inelastic rotation (Bruneau, et al. 1998) of a link in an EBF system.

$$\gamma_p = \frac{L}{e} \theta_p \quad 2.9$$

Here, θ_p is the plastic story drift angle.

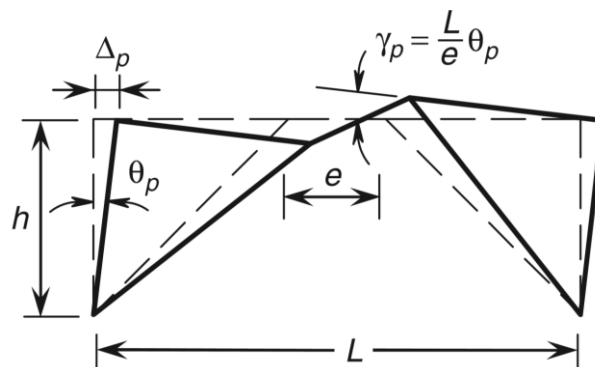


Figure 2.14: Rotation of the shear link (Bruneau, et al. 1998)

The AISC code requires that the rotation angle of the links used in Eccentrically Braced Frames (EBF) shall not exceed the following values (AISC 341-16).

- a. For $e \leq 1.6 M_p/V_p$: 0.08 radian
- b. For $e \geq 2.6 M_p/V_p$: 0.02 radian

Linear interpolation is to be done for values in between the above two ranges. So, a shear yielding link (link with $e \leq 1.6 M_p/V_p$) should be able to sustain a minimum inelastic rotation of 0.08 radian as per the AISC code (AISC 341-16).

2.5.6 Intermediate Web Stiffeners

Malley and Popov (1983) showed that local buckling of the web caused by shear can be delayed by adding transverse stiffeners in the links. It was also seen that, along with shear strength, the energy dissipation capacity of a link is also improved due to the addition of web stiffeners (Hjelmstad and Popov, 1983). The cyclic response of unstiffened and stiffened links obtained by Hjelmstad and Popov (1983) is shown in Figure 2.15. The requirements of intermediate web stiffeners for shear yielding links by the AISC code is explained in the following paragraphs.

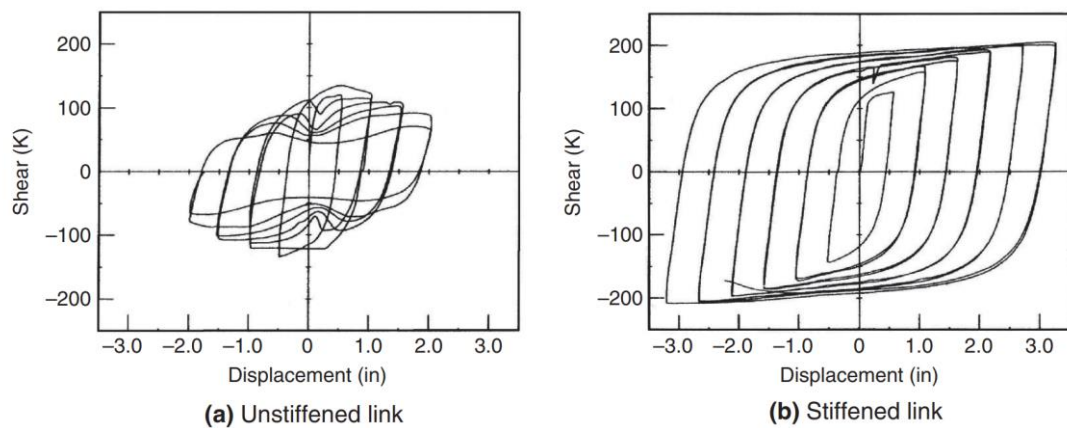


Figure 2.15: Cyclic response of unstiffened and stiffened W18×40 links, $h/t_w = 53.62$, $e = 28$ in. (Hjelmstad and Popov 1983)

For I-shaped links with $e \leq 1.6 M_p/V_p$, the AISC code requires that full depth intermediate web stiffeners shall be provided at intervals not exceeding $(30t_w - d/5)$ for link rotation of 0.08 rad (AISC 341-16). The stiffeners shall have a combined width

(of both sides of web) of at least $(b_f - 2t_w)$ and thickness of at least $0.75t_w$ or 10 mm whichever is greater.

For box-links with $e \leq 1.6 M_p/V_p$ and $h/t_w \geq 0.67\sqrt{E/F_y}$, AISC code requires that full depth web stiffeners be provided on one side of each link web, spaced at intervals not exceeding $[20t_w - (d - 2t_f)/8]$ (AISC 341-16).

2.6 REVIEW OF STATE-OF-THE-ART RESEARCH ON SHEAR LINK AND ITS DIVERSIFIED USE

Replaceable structural components as a part of the different structural systems have been studied in the recent past. These have been used in Coupled Concrete Shear Walls (CCSW) (Fortney et al. 2007), Moment Resisting Frames (MRFs) (Shen et al. 2010), EBFs (Mansour et al. 2011), and Linked Column Framed systems LCFs (Malakoutian et al. 2013). Researchers have also proposed shear links as hysteretic dissipaters for seismic protection of bridges (McDaniel et al. 2003, Sarraf et al. 2004) or buildings (Ghobarah and Abou, 2001, Mazzolani et al. 2009). Some of the recent research on shear links including the depiction of its versatility are presented in this section.

2.6.1 Loading Protocol, Overstrength And Inelastic Rotation

Four loading protocols were used by Okazaki and Engelhardt (2007) which is shown in Figure 2.16. It was found that the loading protocol has a significant effect in the inelastic rotation capacity of the links. The old-AISC loading protocol was found to be overly conservative for the cyclic tests of shear links. Later, the revised protocol was adopted by the AISC code (AISC 341-16). The loading protocol suggested by AISC 341-16 for cyclic testing of links is depicted in Table 2-1 and Figure 2.4.

Okazaki et al. (2005) investigated cyclic behavior of the links made of ASTM 992 steel. It was concluded in this study that though the mentioned overstrength factor of 1.5 appears reasonable for typical rolled W-shapes while, a higher value may be appropriate for very short links. Plastic overstrength of shear links were also studied by many other researchers. A review of the overstrength factor of the conducted experimental studies done by Azad and Topkaya (2017) is shown in Figure 2.18. Short

links with length ratio approximately equal to or less than one usually have overstrength greater than 1.5.

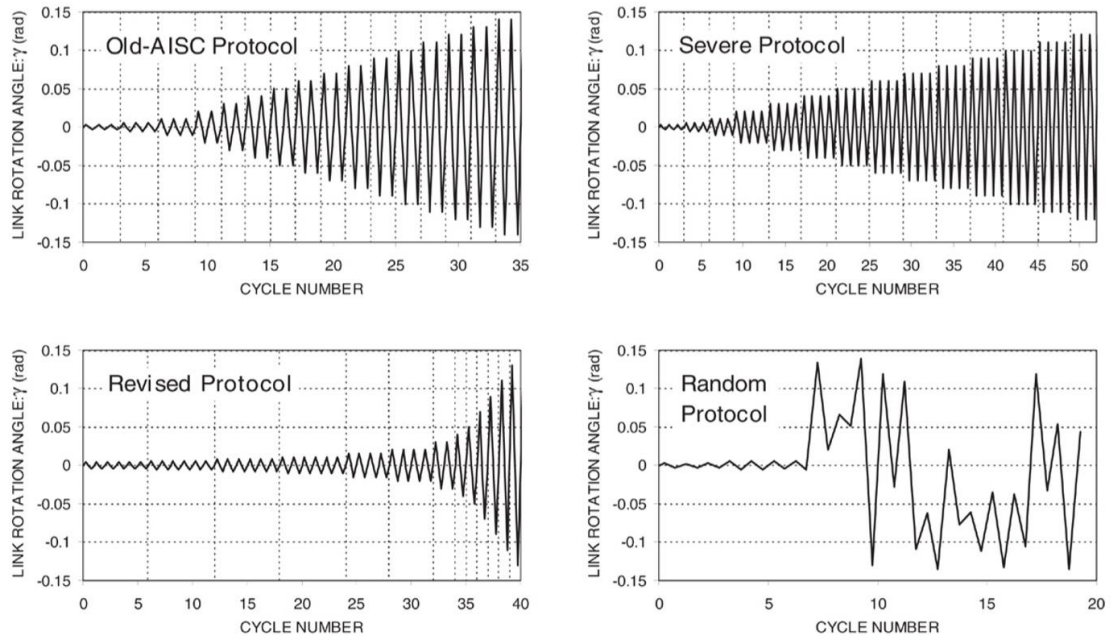


Figure 2.16: Loading protocols used by Okazaki and Engelhardt (2007)

Table 2-1: Standard loading protocol for link testing as per AISC 341-16

Cumulative cycles	No. of cycles	Total link rotation angle (radian)	
6	6	0.00375	*After 0.11 radian link rotation, loading shall be continued at increments of 0.02 radian with one cycle at each step
12	6	0.005	
18	6	0.0075	
24	6	0.01	
28	4	0.015	
32	4	0.02	
34	2	0.03	
35	1	0.04	
36	1	0.05	
37	1	0.07	
38	1	0.09	
39	1	0.11*	

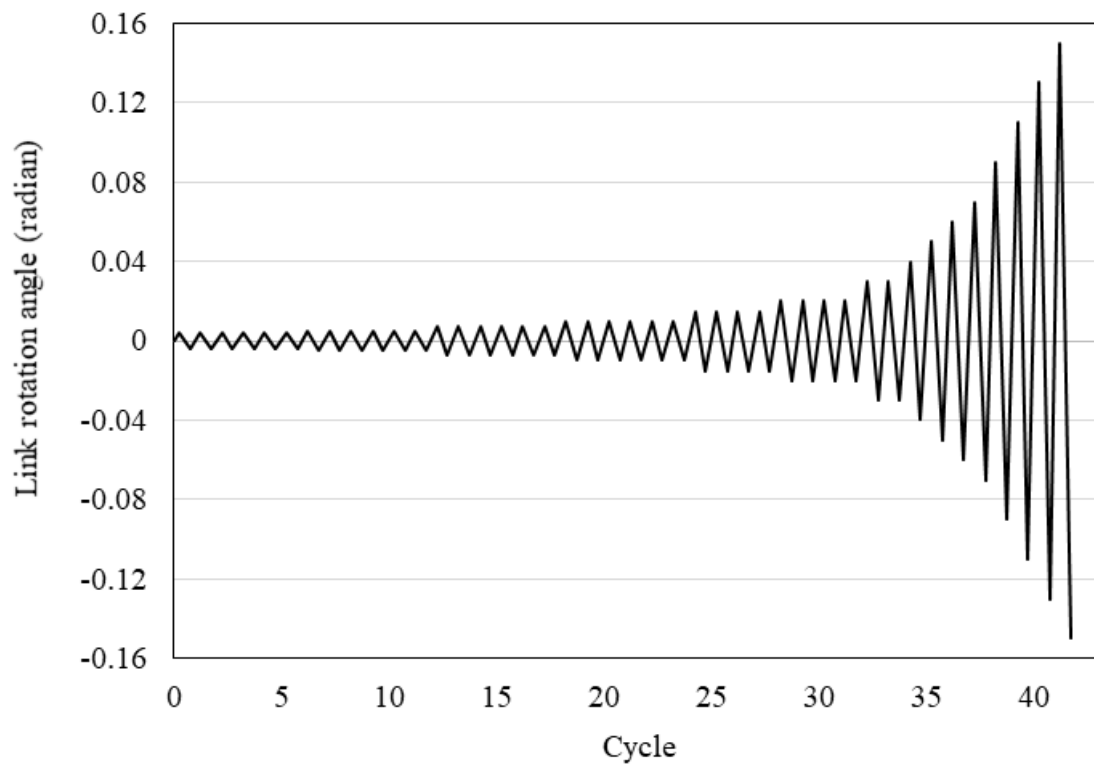


Figure 2.17: AISC loading protocol for cyclic testing of links up to 0.15 radian (AISC 341-16)

Analytical model considering axial force, ratio of flange over web area and ratio of link length to depth for predicting the overstrength of shear links with or without restraint to axial deformations has been proposed by Corte et al. (2013). It was found that larger shear forces develop in shorter links at a given link rotation, for given boundary conditions.

Figure 2.19 shows the inelastic rotation capacity achieved by links of different experimental studies. An insufficient offset between the stiffener-to-web weld and web-to-flange welds were one of the major reasons for not achieving required inelastic rotations by short links. For this reason, a gap between these two welds were recommended by AISC code later (AISC341-16). It can also be seen from the figure that, inelastic rotations of high values were achieved by properly stiffened links in some studies.

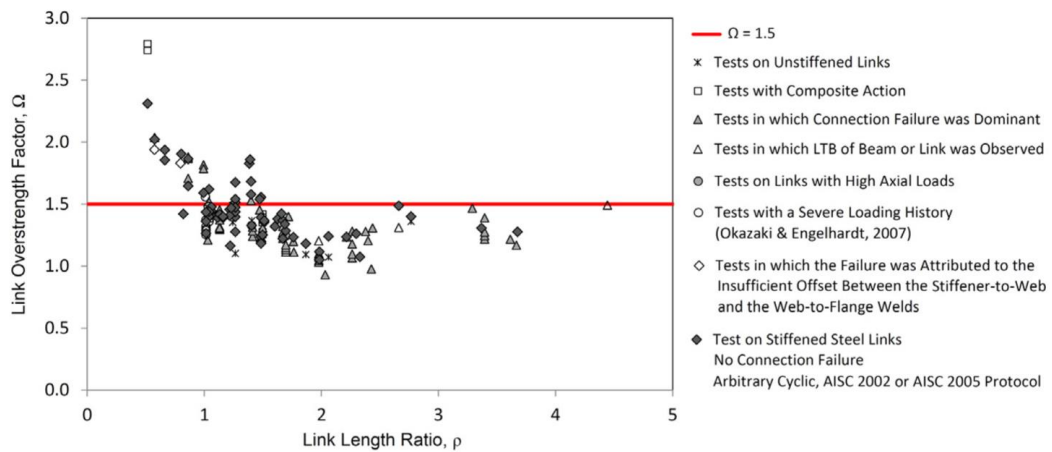


Figure 2.18: Link overstrength factors reported in different experimental studies (Azad and Topkaya, 2017)

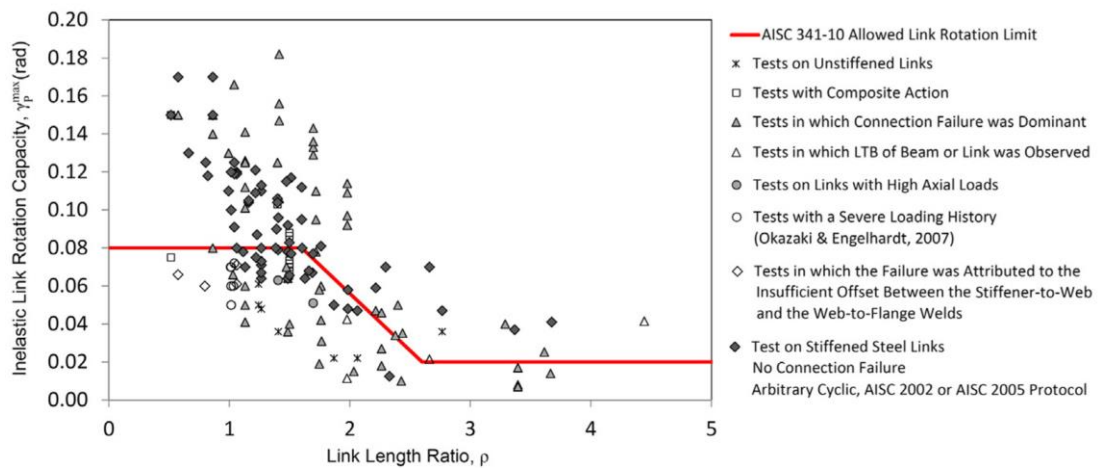


Figure 2.19: Inelastic link rotation capacities reported in different experimental studies (Azad and Topkaya, 2017)

2.6.2 Material Variation in Shear Links

Variation of material in shear link was also one of the subject matters of study by some of the researchers. Shear links made of stainless steel instead of mild steel were investigated numerically in recent times (Li et al. 2014, Chacon et al. 2019).

Li et al. (2014) studied the feasibility of using stainless steel (SS) for shear links. AISI 326L stainless steel was particularly studied by them for shear links as a seismic fuse device. The nonlinear finite element analysis of Li et al. (2014) shows that shear links made of AISI 316L stainless steel exhibit a high level of ductility. Mixed shear and

flexural failure modes were observed in SS links due to high overstrength compared to similar CS conventional links of the same length ratio. So, it was concluded that proper design requirements about the length ratio, element compactness and, stiffener spacing need to be established.

Chacon et al. (2019) compared the behavior of austenitic Stainless Steel (SS) links and Carbon Steel (CS) links through a numerical study. It was seen that, for severe levels of cyclic displacement, both strain-hardening and energy dissipation in SS links outperform identical CS elements. The energy dissipations of SS links were found to be considerably greater than the CS links for high values of displacement. However, at low levels of cyclic displacements, the behavior of both SS and CS steel was similar. In the mentioned study, it was assumed that no fracture of material would take place during cyclic loading.

2.6.3 Shear Link in Coupled Shear Wall Systems

The beam connecting two in-plane shear walls in a coupled shear-wall system is called a coupling beam. The replacement of a coupling beam becomes costly and time-consuming in a post-disaster period. As a solution to this problem, the concept of replaceable coupling beams was proposed by past researchers (Fortney et al. 2007) which comprises a central fuse shear link connected to steel segments at its two ends. As an alternative to traditional RC coupling beams, replaceable coupling beams have also been proposed in recent years (Chung et al. 2009; Christopoulos and Montgomery, 2013).

Ji et al. (2017) proposed a replaceable coupling beam which consisted of a central shear link (Figure 2.20) and investigated its cyclic behavior for four different connections of the beam to link. The link with end-plate connection had a length ratio of 0.7 and it showed overstrength of approximately 2.0 which significantly exceeds the value (1.5) specified in AISC 341-10.

Very short links were investigated by Ji et al. (2016) where the test variables were steel type, length ratio, web stiffener configuration, and loading protocol. It was found that large overstrength (approximately equal to 1.9) can be found in very short links.

The links primarily failed due to web fracture and fracture at weld connecting the link flange to the end plate.



Figure 2.20: Schematic view and test setup of replaceable coupling beam with shear link (Ji et al. 2017)

2.6.4 Shear Link in Moment Resisting Frames

In moment resisting frames, the code limits the maximum value of the span-to-depth ratio of the beams for the development of plastic hinges with sufficient length at beam ends. Since strength and stiffness design are coupled in the existing design procedure of steel moment resisting frames, it often leads to overdesigned structural elements like diaphragms and foundations. To overcome this limitation, replaceable shear links were proposed in moment resisting frames by researchers in recent times (Shen et al. 2011, Nikoukalam and Dolatshahi, 2015, Kalehbasti and Dolatshahi, 2018). Figure 2.21 shows the schematic view of a replaceable shear link in moment resisting frames.

Perforated shear links (PSL) and slit shear links (SSL) were proposed in moment resisting frames (See Figure 2.22) by Kalehbasti and Dolatshahi (2018) in a numerical

study conducted by them. The links which were weakened by perforations or slitting dissipate seismic energy through shear yielding. Perforated shear links were suggested by the author for shear strength reductions up to 40%. However, a complete guideline for such types of perforations is yet to be discovered and given for the link design.

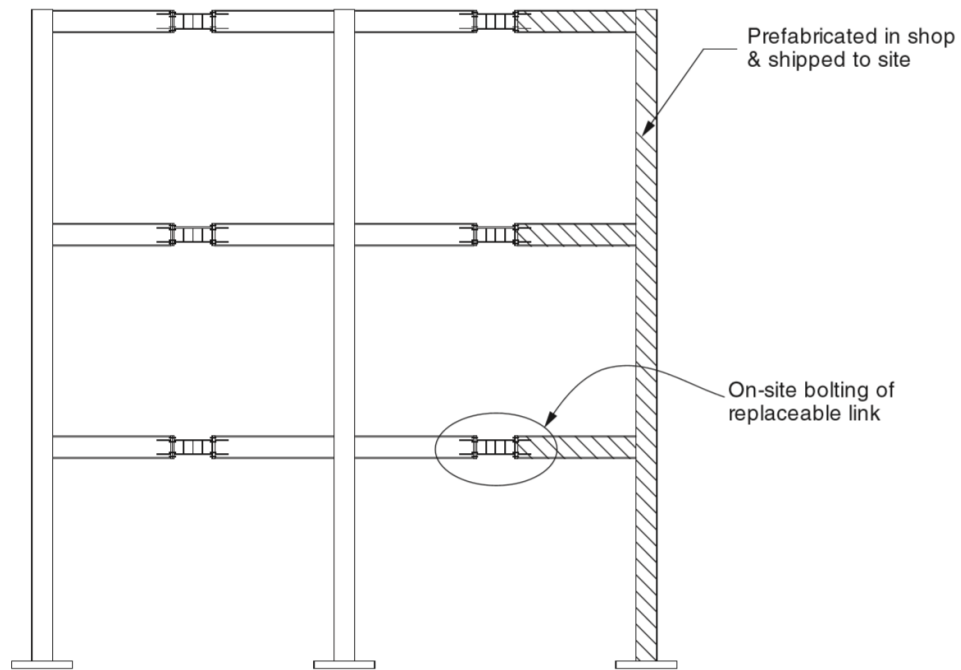


Figure 2.21: Replaceable shear links in moment resisting frames (Nikoukalam and Dolatshahi, 2015)

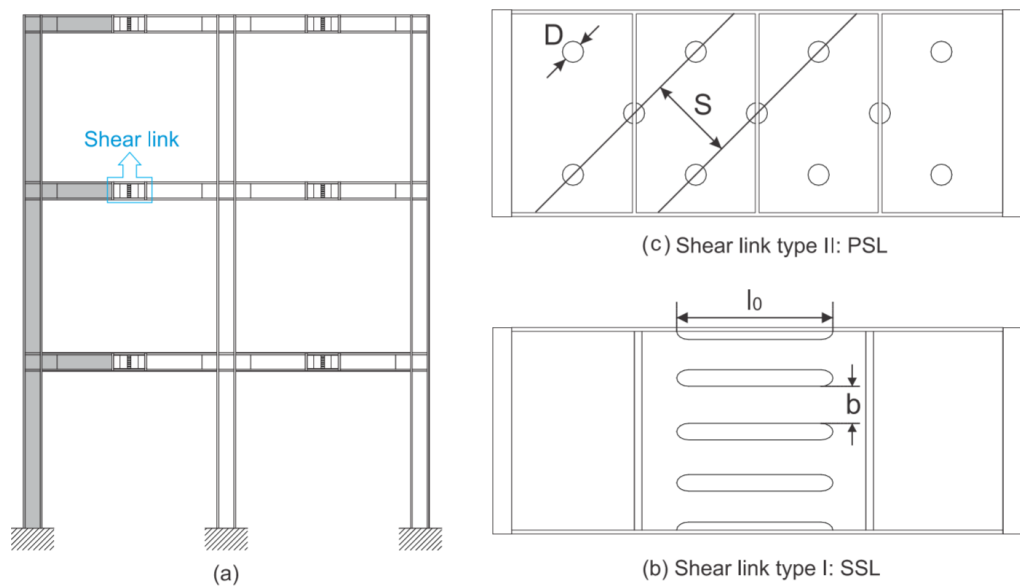


Figure 2.22: (a) Schematic view of link in moment resisting frames (b) Slit shear link (c) Perforated shear link (Kalehbasti and Dolatshahi, 2018)

2.7 EVALUATION OF STIFFENER REQUIREMENTS IN SHEAR LINKS WITH COMPACT WEBS

In the existing literature, many links were found to have undergone rotations greater than that prescribed by the AISC code for EBF links. Failure of links were seen to occur due to the initiation of fracture at the web-stiffener weld (Ji et al. 2016). One image of such failure is shown in Figure 2.23(c). Though many of those links could sustain the minimum prescribed rotation, they were seen to fail due to the initiation of fracture at the web-to-stiffener weld even before the web buckled (Dusicka et al. 2010, Okazaki et al. 2005). Hence, it was an indication of the fact that intermediate stiffeners were causing the links to fail before web buckling at their weld connections putting the requirement of prescribed stiffeners into question.

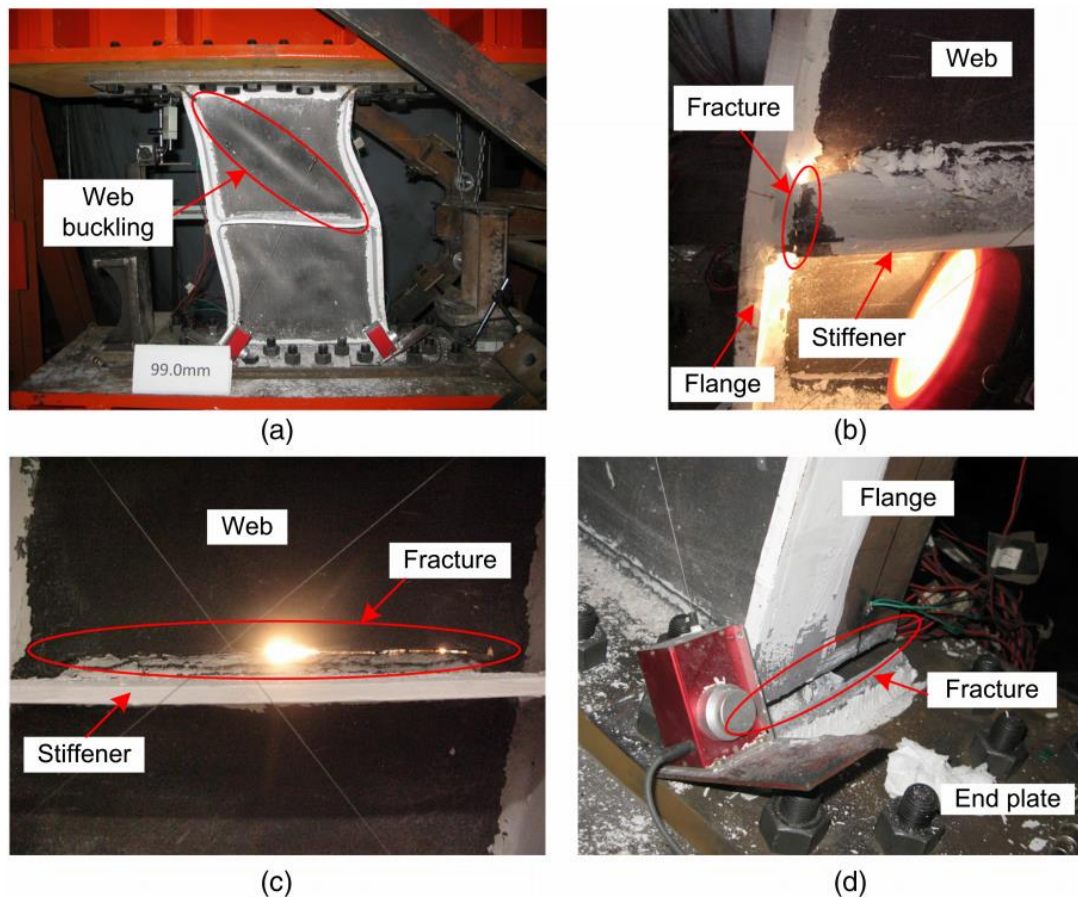


Figure 2.23: Damage of specimens: (a) web buckling (Specimen L13); (b) stiffener-to-flange weld fracture (Specimen L22); (c) web fracture (Specimen L12); (d) flange-to-end plate weld fracture (Specimen Q12) (Ji et al. 2016)

Dusicka et al. (2010) specifically concluded that the seismic provisions for stiffener spacing are overly conservative for unstiffened link webs of compactness of $h_w/t_w < 20$. To add more, Stephens and Dusicka (2014) found that the link investigated achieved required plastic rotation without having any stiffeners at all which contradicted with the stiffener spacing requirement. After review of available link data, the need to reexamine stiffener spacing was also reported by Azad and Topkaya (2017).

Stiffener requirements were specifically put into questions for stocky link webs and the theoretical transition point from slender behavior to stocky behavior of link for inelastic rotation of 0.080 rad is recommended to be at $\beta = h_w/t_w = 23$ by Volynkin et al. (2018). The results of the experimental investigation of Volynkin et al. (2018) is summarized in Table 2-2 and the hysteretic responses are shown in Figure 2.24. It was observed that attaching stiffeners to webs of stocky links were found to be redundant and often detrimental. Unstiffened stocky links not conforming to the stiffener requirements of the code achieved inelastic rotations of 0.17 and 0.19 radian compared to the code specified value of 0.08 radian and stocky links were also found to exhibit higher overstrength (around 1.80-2.0) than the expected value of 1.5 (Volynkin et al. 2018). Stiffener spacing of $s \leq 94t_w - h_w$ and web panel aspect ratio requirement of $s \leq 4.2h_w$ was proposed by the mentioned researcher.

Table 2-2: Specimen details of Volynkin et al. (2019) for evaluation of necessity of web stiffeners

Specimen	Link length, e (mm)	h/t_w	Required stiffener spacing (as per AISC code) (mm)	Provided stiffener spacing (mm)	Plastic rotation sustained (radian)
AL-BU-N1	848	21.3	285	418	0.133
AL-BU-B1 (No stiffeners provided)	848	21.3	285	-	0.170
AL-BU-N2	848	18.3	237	279	0.134
AL-BU-B2 (No stiffeners provided)	848	18.3	237	-	0.192

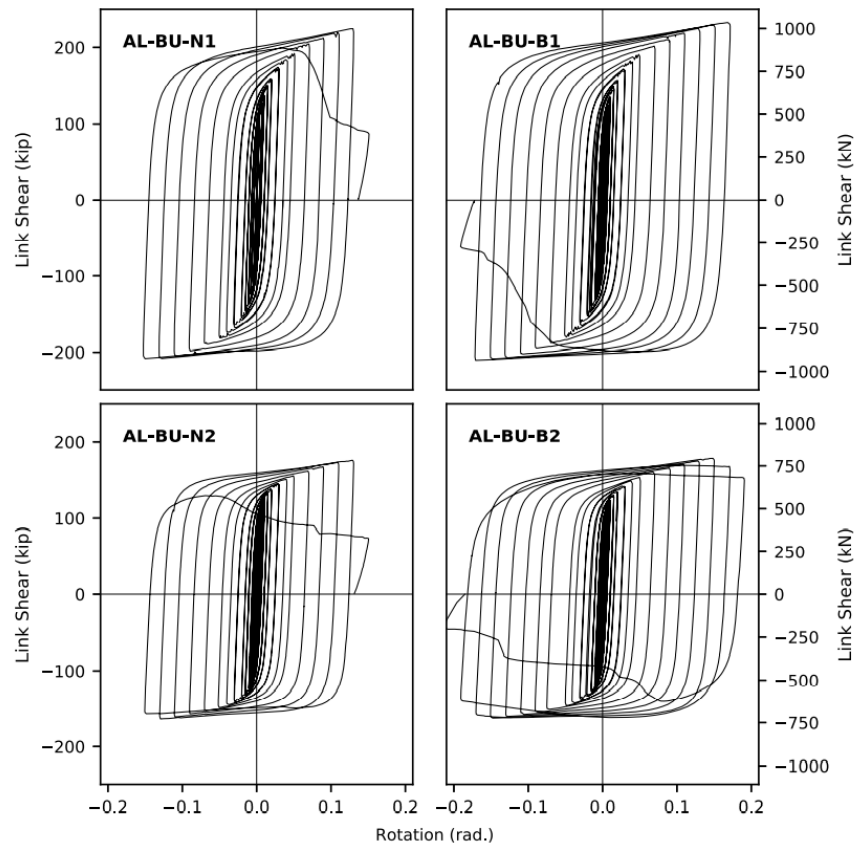


Figure 2.24: Hysteresis results of specimens of Volynkin et al. (2019) for evaluation of the necessity of web stiffeners

Hence, short stocky links can attain higher inelastic rotation but the maximum shear strength achieved by such links can be very high due to their high overstrength which will further increase the capacity demand of the structural components attached to the links. For this reason, ways of reducing the shear strength of such links are necessary. Making holes in the web can be a way to reduce the shear capacity of the links and at the same time, stocky webs can be used without stiffeners to achieve high inelastic rotations.

2.8 STRENGTH REDUCTION OF SHORT LINKS

Steel shear plates with openings as energy dissipating fuses have been investigated in the past by various researchers (Shahri and Mousavi, 2018, Ma et al. 2010, Oh et al. 2009 etc.). Some of these fuses and seismic dampers are shown in Figure 2.25, Figure

2.26 and Figure 2.27. The shear strength reduction of shear links can be done similarly by creating openings of different geometric shapes and pattern in the link web(s).

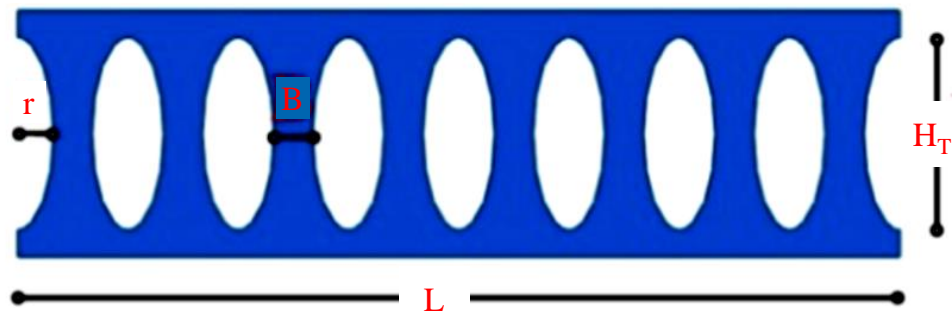


Figure 2.25: Slit dampers with elliptic holes used by Shahri and Mousavi (2018) in beam-column connection

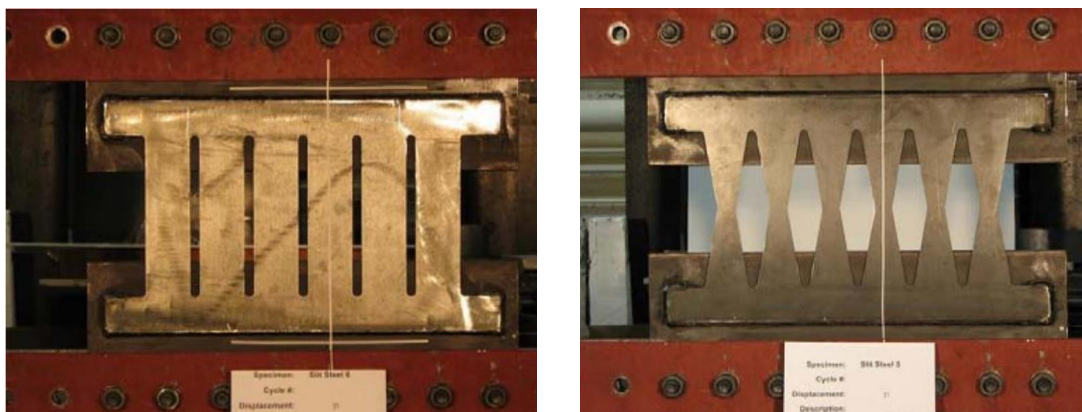


Figure 2.26: Fuses with slits and butterfly shaped openings (Ma et al. 2010)

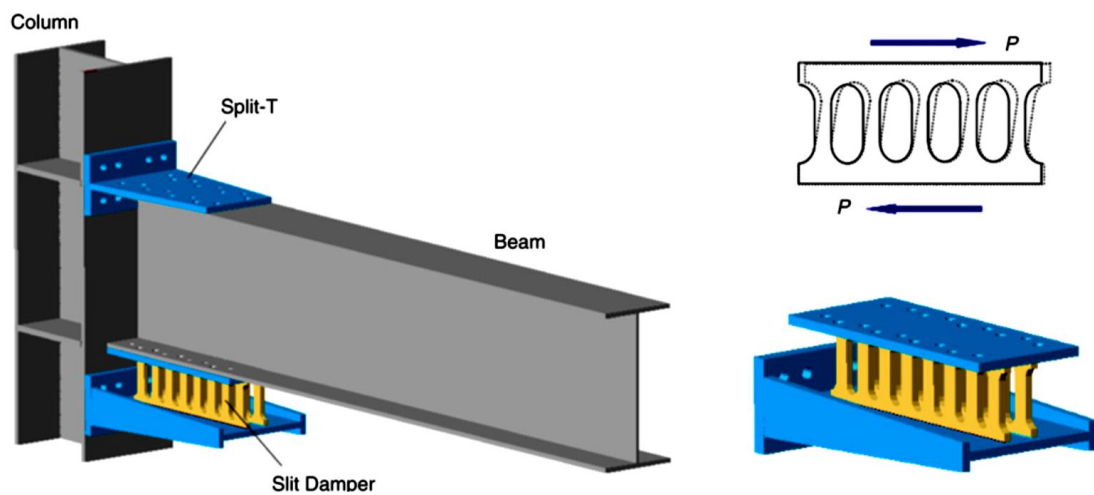


Figure 2.27: Slit damper in beam-to-column connection (Oh et al. 2009)

Circular perforations were previously used in Steel Plate Shear Wall to reduce the shear strength of steel walls which results in what is called Special Perforated Steel Plate Shear Walls (Figure 2.28, Vian and Bruneau, 2005).

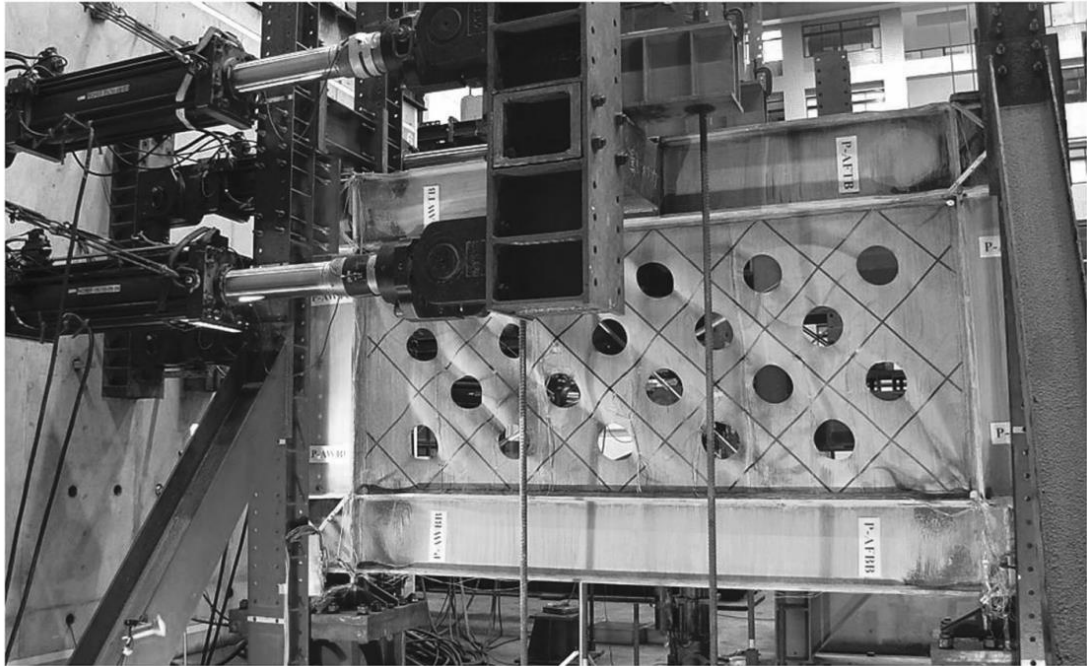


Figure 2.28: Special perforated steel plate shear walls (Vian and Bruneau, 2005, courtesy of MCEER, University at Buffalo.)

Numerical studies on perforated shear links and slit shear links were also conducted by Kalehbasti and Dolatshahi (2018) as shown in Figure 2.22. The damage indices of those links are shown in Figure 2.29. It was observed that the damage index for perforated links was less than the slit links.

Experimental studies on links with perforations on the webs were conducted by Tong et al. (2018). The deformed shapes of perforated link specimens of Tong et al. (2018) are shown in Figure 2.30. Two patterns of perforations were made in the study viz. diagonal and rectangular, and it was found that the link with the diagonal pattern of perforations sustained higher inelastic rotations.

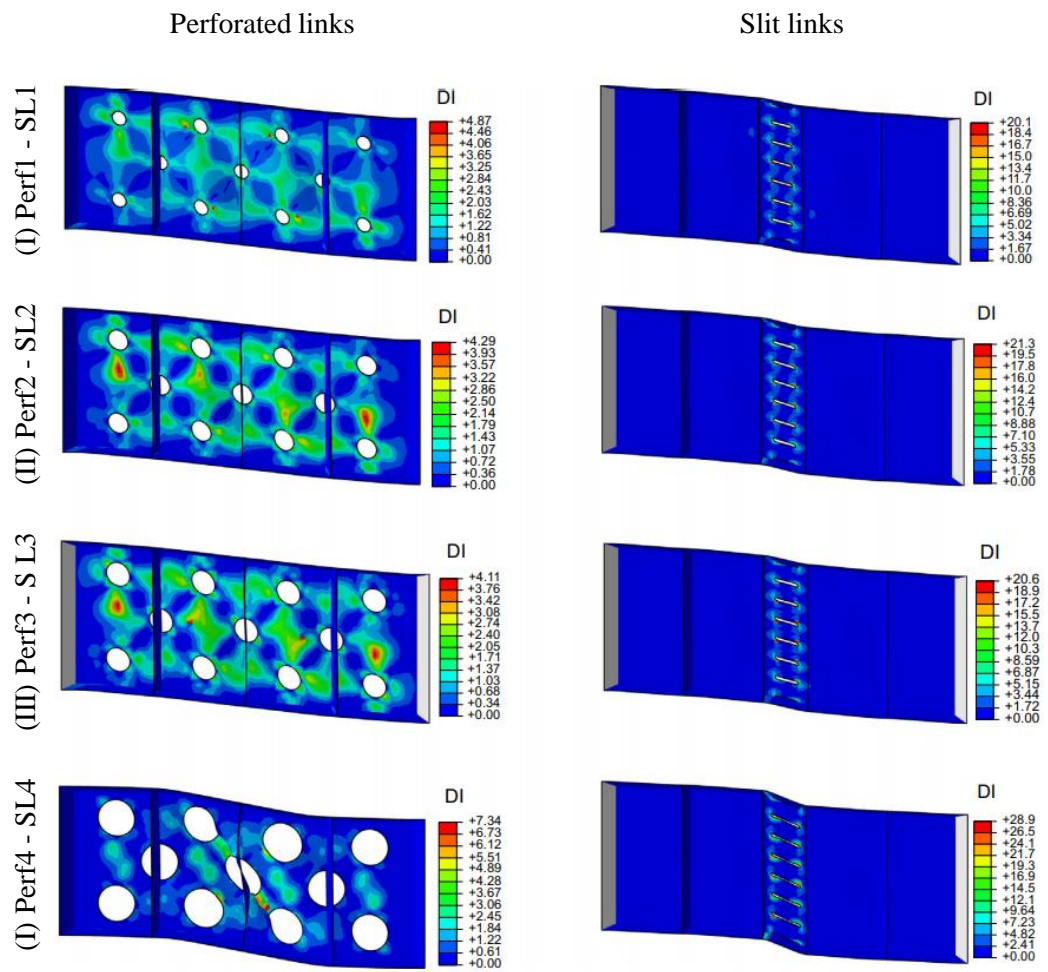
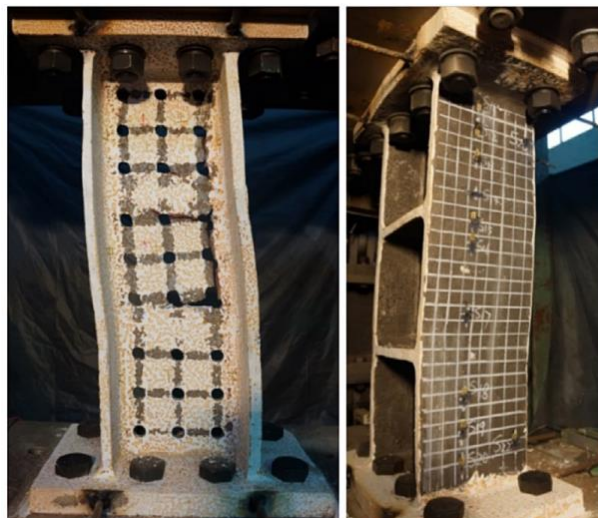
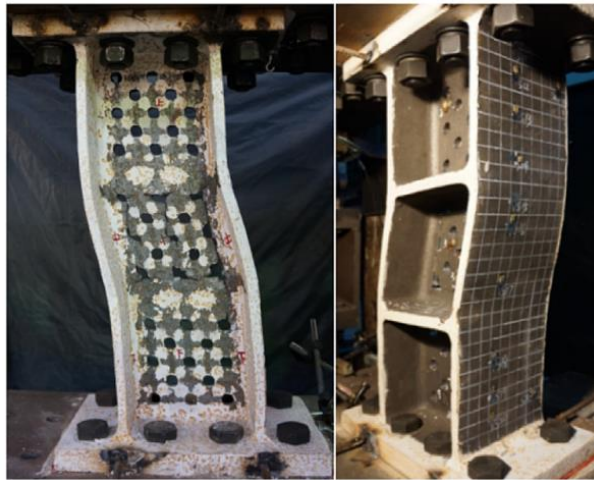


Figure 2.29: Numerical models of perforated (Perf) and slit (SL) shear links for strength reduction showing damage indices (Kalehbasti and Dolatshahi, 2018)



(a)



(b)

Figure 2.30: Perforated link specimens of Tong et al. (2018), (a) Specimen L-C-1,
(b) Specimen L-C-2

2.9 ENERGY DISSIPATION

As an energy-dissipating device, the capacity of the different links to dissipate seismic energy by stable hysteretic behavior is one of the most important parameters for study. The energy dissipation characteristic of a link can primarily be investigated by two terms viz. total energy dissipated and the hysteresis efficiency.

2.9.1 Total Energy

The total energy is calculated by adding the areas of the hysteretic loops that are generated by cyclic loading. The area of the hysteresis loops of shear vs rotation response of the link is to be multiplied with the link length to get the total energy dissipated.

2.9.2 Hysteresis Efficiency

The effectiveness of different shear links as hysteretic energy dissipating devices can be evaluated by calculating the hysteresis efficiency factor, which is defined as the ratio, E_{hyst}/E_{max} (shown in Figure 2.31). In the figure, the rectangular area ABCD

bound between the maximum and minimum values in each cycle represents the maximum theoretical energy, E_{max} , and E_{hyst} is represented by the area of the hysteretic response loop AXCYA. Hence, a hysteretic efficiency factor of 0% would represent an elastic behavior, while a factor of 100% would represent an infinitely stiff elastoplastic response.

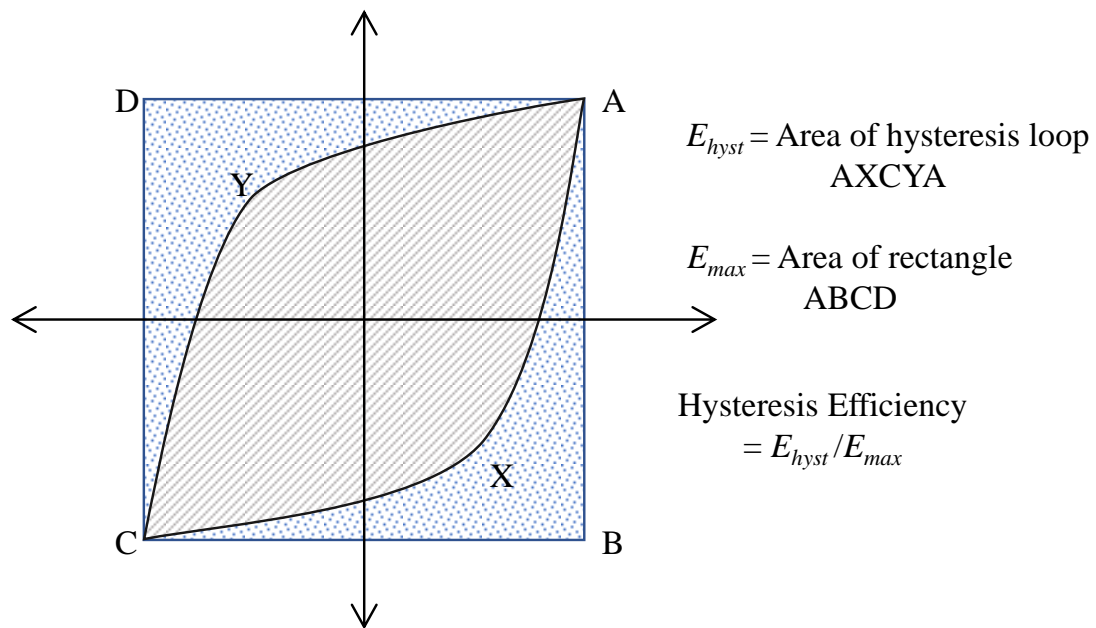


Figure 2.31: Hysteresis Efficiency

2.10 REMARKS

From the existing literature, it was found that shear links of box sections and I-sections were studied in the past and recommended by the code. However, interchangeability between these two types of shear links is yet to be established. So, the feasibility of achieving a similar cyclic response with box-links and I-links of the same shear capacity was investigated and presented in this thesis with respect to hysteretic response and energy dissipation.

Short links with compact webs were found to sustain higher inelastic rotations without web stiffeners but the shear strengths of those links are much higher due to the increased web thickness which increases demand for the other structural components attached to the shear links. The ultimate shear strength of a link can be reduced by reducing the web thickness. But using of reduced web thickness will lead to early

buckling of links. Keeping the same web thickness and same web compactness for avoiding buckling, the shear strength can be reduced by another means which is by creating openings in the link web. Thus, links with openings in the webs are needed to be studied and it is necessary to establish design equations for proper prediction of shear strengths of these types of links. Links with circular openings in webs have been studied in this research and these links are referred as perforated links. Perforated links with both box-shaped and I-shaped cross sections were studied and refined design equations are proposed in this thesis such that the cyclic responses of perforated links are equivalent to those of the solid links of the same shear capacity.

Since conducting experimental studies on a big number of steel specimens tend to be costly in Bangladesh, numerical analysis was performed by the Finite Element Method to carry the intended study. Numerical models were first developed and then validated with reference to past experimental studies. The details of the numerical modeling including the validation of the models and some conducted experimental studies are presented in the upcoming chapters.

CHAPTER 3

METHODOLOGY FOR FINITE ELEMENT MODELING

3.1 INTRODUCTION

Conducting experiments on steel structure turns out to be costly especially when a wide range of variables are included in a study. Finite Element Method was thus chosen for analysis of the shear links which is a numerical technique for solving problems. Finite Element Analysis was carried out for investigation of cyclic behavior of shear links using the software package ANSYS (Ansys Student 2020 R2 software).

3.2 ANSYS - FEM PACKAGE FOR THE PRESENT STUDY

A diverse range of engineering simulation solution sets is offered by ANSYS which provides access to virtually any field of engineering simulation that is required by a design process. ANSYS provides ways for carrying numerical analyses including static or dynamic structural analysis with both linear and nonlinear behavior. Advanced modeling of cyclic plasticity can be done by using different models available in this finite element package. Numerical study on nonlinear analysis of cyclic behavior of shear links was thus conducted by ANSYS (Ansys Student 2020 R2 software).

3.3 MODELING OF SHEAR LINKS

Finite element models of shear links of different geometry subjected to reversible cyclic loading have been developed for nonlinear analysis. The procedure of the modeling has been presented here including element description, geometric and material parameters, etc. The modeling has been done with an intention to reproduce the experimental results of some previously done research of Tong et al. (2018), Volynkin et al. (2018), Liu et al. (2017), and Okazaki and Engelhardt (2006). Both the material and geometric nonlinearities have been considered for modeling of the shear links. The steps for performing modeling processing of shear link as well as any type of structure using FEM includes defining the geometric and material parameters,

generating the model and meshing the generated model in preprocessing mode, defining boundary conditions and loading in solution mode and getting database results in post-processing mode.

3.3.1 Modeling Parameters

The geometric parameters of the model were taken from the study of the mentioned researchers to simulate their experimental studies. The main elements in the geometry include the endplates, flanges, webs, and web-stiffeners of the shear links. The Poisson's ratio of steel for all the structural steel members of all the models has been taken equal to 0.3.

3.3.2 Element Modeling

'SOLID185' element was used to model all the components of the whole structure namely: end plates, flanges, web, and stiffeners. SOLID185 is defined by eight nodes (Figure 3.1) having three degrees of freedom at each node: translations in the nodal x, y, and z directions and is used for 3-D modeling of solid structures.

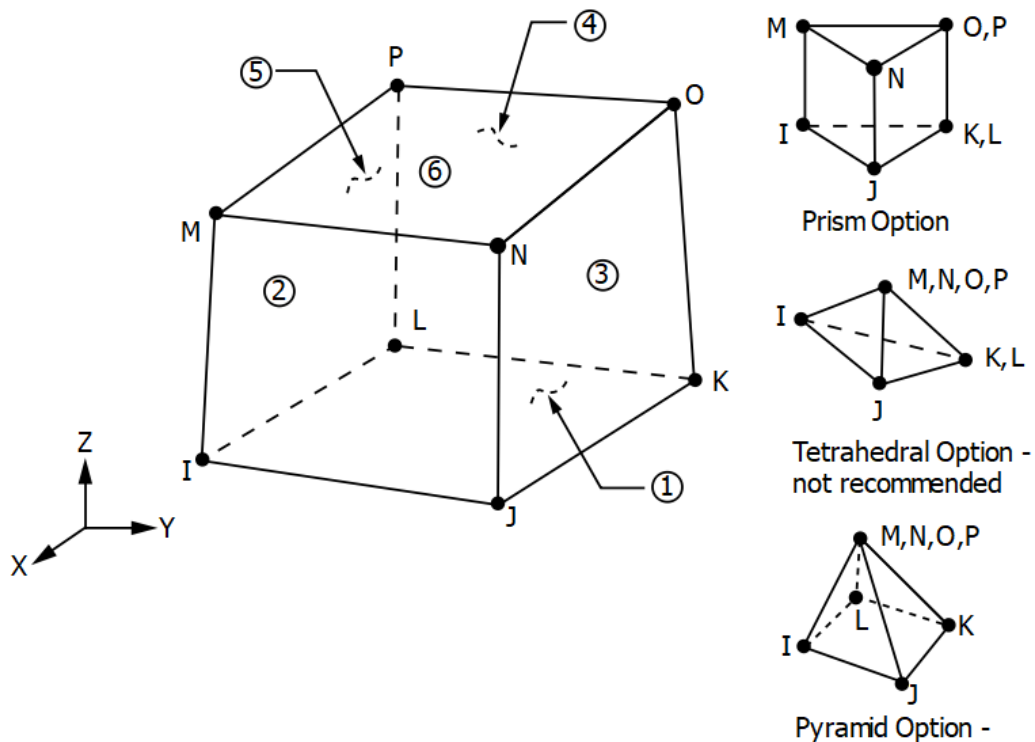


Figure 3.1: SOLID185 homogeneous structural solid geometry (ANSYS, Inc. 2019)

The element has plasticity, hyperelasticity, stress stiffening, creep, large deflection, and large strain capabilities.

SOLID185 also has mixed formulation capability for simulating deformations of nearly incompressible elastoplastic materials, and fully incompressible hyperelastic materials. (ANSYS, Inc. 2019). Figure 3.1 shows the six surfaces of the element ‘SOLID 185’ in an isometric view and different options available for this element in the finite element modeling.

3.3.3 Material Modeling

For a proper simulation of the cyclic behavior of a material, cyclic material properties like the Bauschinger effect and expansion of yield surface are needed to be considered. The Chaboche non-linear model has been used to accurately model the cyclic behavior of shear links in this study.

3.3.3.1 Nonlinear kinematic hardening

The nonlinear kinematic hardening model is a rate-independent version of the kinematic hardening model proposed by Chaboche (Chaboche, 2008, Chaboche, 1991, Chaboche, 1989). The model allows the superposition of several independent back-stress tensors and can be combined with any of the available isotropic hardening models. It can be useful in modeling cyclic plastic behavior such as cyclic hardening or softening and ratcheting or shakedown. The Chaboche kinematic hardening material model can be defined with respect to temperature and allows up to five kinematic models for each temperature. It is required that all kinematic models be defined for each temperature. (ANSYS, Inc. 2019). The yield function of the nonlinear kinematic hardening model TB, CHABOCHE is shown below in Equation 3-1 (Lemaitre and Chaboche, 1990).

$$F = \sqrt{\frac{3}{2} (\{s\} - \{\alpha\})^T [M] (\{s\} - \{\alpha\})} - R = 0 \quad 3-1$$

In Equation 3-1, $\{s\}$ is the deviatoric stress, $\{\alpha\}$ refers to the back stress and R represents the yield stress. The back stress is related to the yield surface and can be calculated as shown in Equation 3-2 (Lemaitre and Chaboche, 1990).

$$\{\alpha\} = \sum_{i=1}^n \{\alpha_i\} \quad 3-2$$

$$\{\Delta\alpha\}_i = \frac{2}{3} C_i \{\Delta\varepsilon^{pl}\} - \gamma_i \{\alpha_i\} \Delta\varepsilon^{pl} + \frac{1}{C_i} \frac{dC_i}{d\theta} \Delta\theta \{\alpha\} \quad 3-3$$

Here, ε^{pl} is the accumulated plastic strain, θ is temperature, and C_i and γ_i are the Chaboche material parameters for n number of models. C_i is the constant that is proportional to the hardening modulus and γ_i is the decreasing rate of hardening modulus with the increase of plastic strain. In Equation 3-3, the first term is the hardening modulus. On the other hand, the second term of the evolution of the back stress is a ‘recall term’ that produces a nonlinear effect.

3.3.3.2 Nonlinear isotropic hardening

The isotropic hardening rule prescribes that the yielding surface only changes in its size with plastic deformation but the change in yielding surface does not occur. The nonlinear isotropic hardening can be modeled using the ‘Voce hardening law’. The Voce hardening law contains an exponential saturation hardening term added to the linear term, as shown in Figure 3.2. The evolution of the yield stress for this model is specified by Equation 3-4 (ANSYS, Inc. 2019).

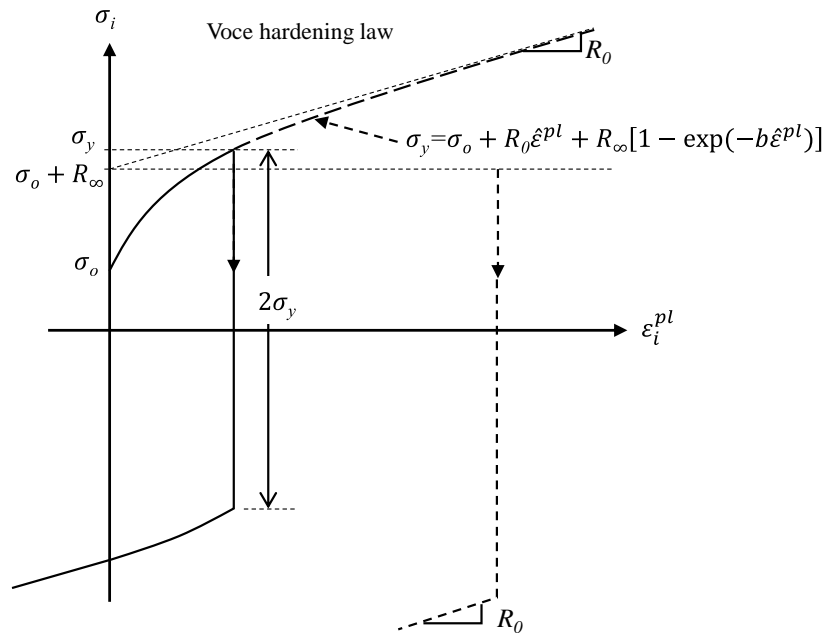


Figure 3.2: Stress vs. plastic strain for Voce hardening (ANSYS, Inc. 2019)

$$\sigma_y = \sigma_o + R_o \hat{\epsilon}^{pl} + R_\infty [1 - \exp(-b \hat{\epsilon}^{pl})] \quad 3-4$$

Here, σ_y is the yield stress, σ_o is the initial yield stress and the user-defined parameters include the difference between the saturation stress and the initial yield stress (R_∞), the slope of the saturation stress (R_o) and, the hardening parameter (b) that governs the rate of saturation of the exponential term.

3.3.3.3 Combined hardening

While the kinematic hardening rule prescribes that the yielding surface only changes in its position with plastic deformation, the isotropic hardening rule prescribes that the yielding surface changes only in its size with plastic deformation (Figure 3.3). Plastic behaviors of most metallic materials do not exactly follow either of these two basic strain hardening rules. Instead, their plastic behaviors fall in between the behaviors predicted by the two basic strain hardening rules. For modeling shear links, many previous researchers have also used the combined hardening by Chaboche nonlinear kinematic and isotropic hardening models (Kalehbasti and Dolatshahi, 2018, Chacon et al. 2019 etc.). Hence, the combined strain hardening rule (Figure 3.3c) is used for the material modeling of shear links in this study.

3.3.3.4 Defining material properties in finite element modeling

While the elastic modulus and Poissons's ratio describes the elastic behavior, the constitutive modeling using Chaboche nonlinear kinematic hardening model and the nonlinear isotropic hardening model defines the plastic behavior. Appropriate use of these models facilitates the correct simulation of cyclic behavior of a material. The elastic properties and the constants of the nonlinear hardening models of Table 3-1 and Table 3-2 are taken from the experimental data and calibrated for the validation of the numerical models developed in this thesis.

The constants of the nonlinear hardening models of Table 3-1 and Table 3-2 are defined using the command 'TBDATA'. The first constant of Table 3-1 is σ_o , or the yield stress of the material – this value may be overridden if an isotropic hardening model is added. The second and third material constants are C_1 and γ_1 – these may be

followed by additional pairs of C_i and γ_i , depending on the number n of kinematic models requested. (Lemaitre and Chaboche, 1990). Similarly, the constants of Table 3-2 are entered sequentially.

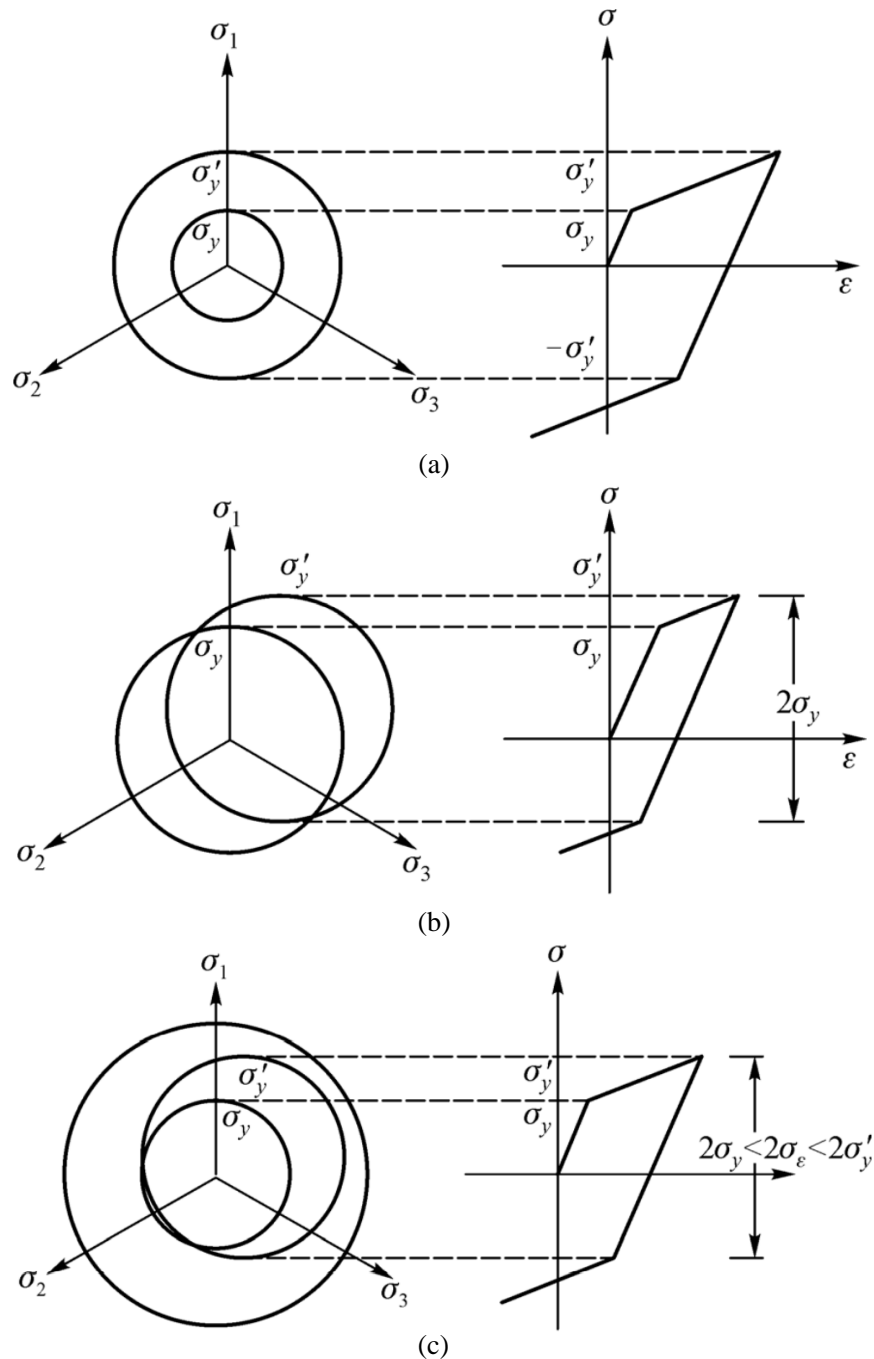


Figure 3.3: Illustration of the combined strain hardening model (a) Isotropic strain hardening model; (b) Kinematic strain hardening model; (c) Combined hardening model (LI et al. 2014)

Table 3-1: Material data table for Chaboche nonlinear kinematic hardening model (ANSYS, Inc. 2019)

Constant	Meaning	Property
C1	σ_o	Initial yield stress
C2	C_1	Material constant for first kinematic model
C3	γ_1	Material constant for first kinematic model
C4	C_2	Material constant for second kinematic model
C5	γ_2	Material constant for second kinematic model
...
C(2n)	C_n	Material constant for last kinematic model
C(1+2n)	γ_n	Material constant for last kinematic model

Table 3-2: Material data table for nonlinear isotropic hardening model using Voce law (ANSYS, Inc. 2019)

Constant	Meaning	Property
C1	σ_o	Initial yield stress
C2	R_o	Linear coefficient
C3	R_∞	Exponential coefficient
C4	b	Exponential saturation parameter

An example of the command lines for defining nonlinear hardening parameters which are given as input in FEM is shown in Table 3-3. In this example, four Chaboche models (C_1, γ_1 to C_4, γ_4) were used for nonlinear kinematic hardening.

Table 3-3: Command lines in ANSYS for providing nonlinear hardening parameters

Command lines	Comments
TB, CHABOCHE, 2, 1, 4 TBTEMP, 0.0 TBDATA, 1, σ_o	Chaboche nonlinear kinematic hardening Initial yield stress
TBDATA, 2, $C_1, \gamma_1, C_2, \gamma_2$ TBDATA, 6, $C_3, \gamma_3, C_4, \gamma_4$	Chaboche constants for 1 st and 2 nd model Chaboche constants for 3 rd and 4 th model
TB, NLISO, 2, 1, 4 TBTEMP, 0.0 TBDATA, , $\sigma_o, R_o, R_\infty, b$	Non-linear isotropic hardening Isotropic hardening parameters of Voce law

3.3.4 Generation of The Model Geometry

The element ‘Solid 185’ was used for the generation of all the volumes needed in the study. The model generation illustrated in this section is based on the specimens of Liu et al. (2017). The model mainly consists of the following volumes:

- Endplates
- Link flanges
- Link web
- Intermediate web stiffeners

All the volumes were produced either by dragging areas along straight lines or drawing full volumes directly. First, the endplates were generated where holes were kept for bolts. The arrangements of the bolt holes were primarily based on the experimental model to be verified and where adequate information was unavailable, bolt holes were arranged as per the specifications of the extended end-plate moment connections. The generated volume of an endplate in FEM is shown in Figure 3.4. The web and flanges of the link are generated such as to form an I-link connecting the two endplates. The volume formation of the whole link is shown in Figure 3.5 and the full assembly of a link without web stiffeners is shown in Figure 3.6. However, intermediate web stiffeners were also present in some of the studied links. The volume generation of

such web stiffeners within a link is shown in Figure 3.7 and the whole assembly is shown in Figure 3.8.

While creating the volumes, divisions within a volume are kept in places where the volume is attached to one or more other volumes to ensure the connectivity between the different volumes.

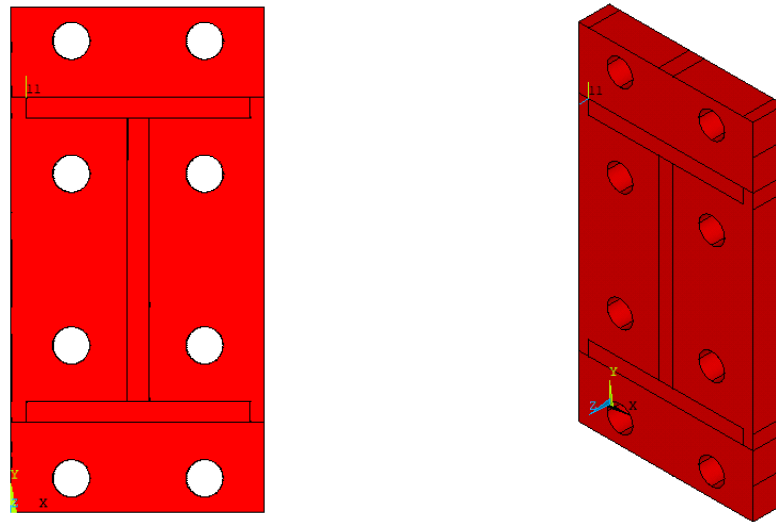


Figure 3.4: Volume formation of the endplate

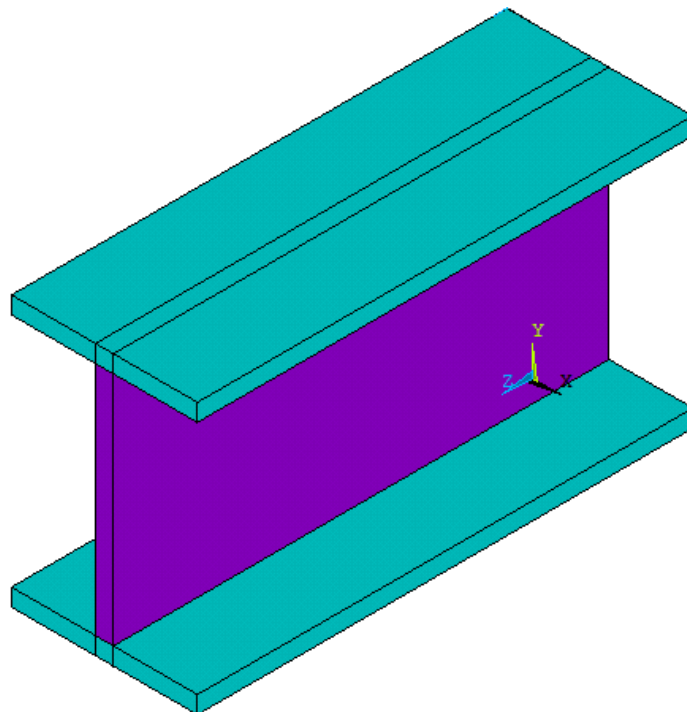


Figure 3.5: Volume formation of the flanges and web of I-shaped link (without stiffeners)

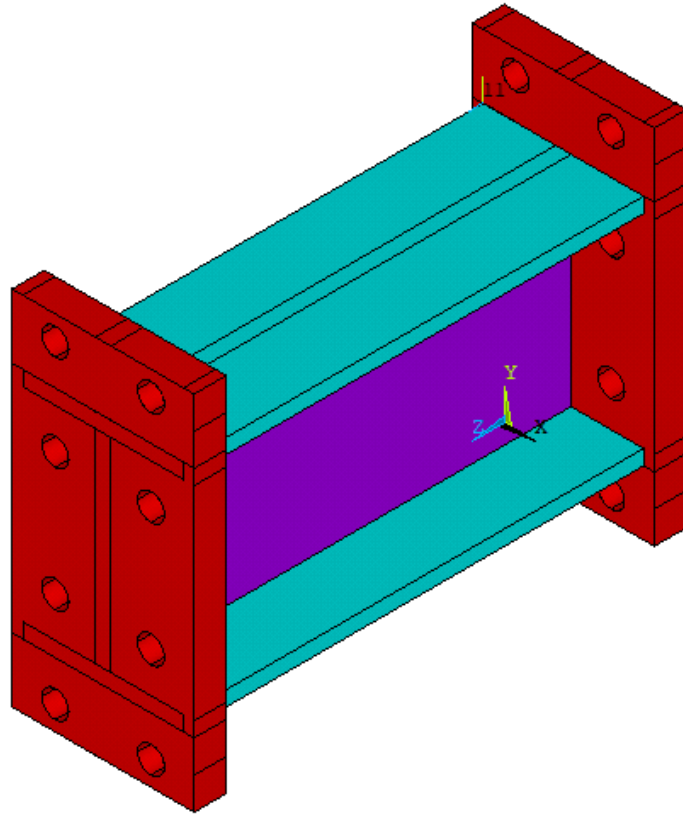


Figure 3.6: Volume of the whole assembly of I-link without stiffeners

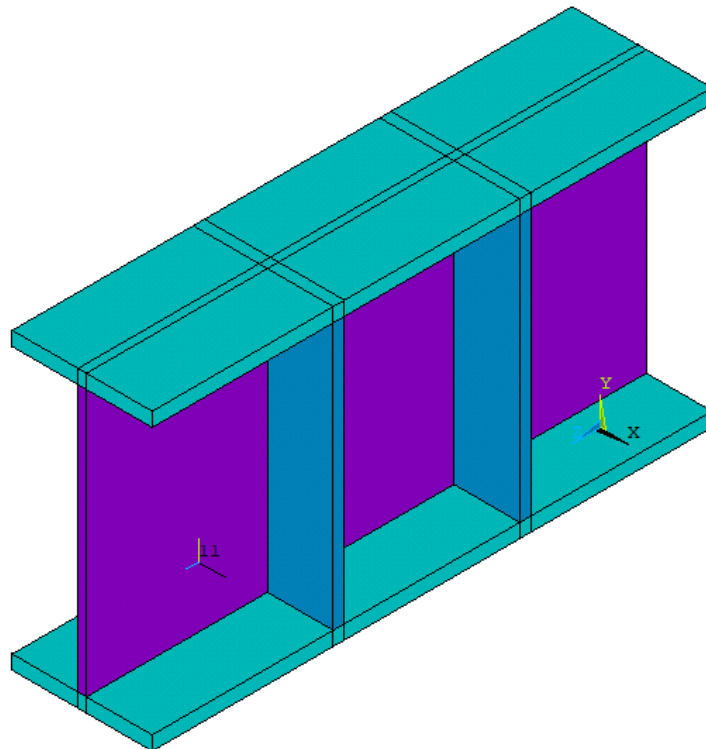


Figure 3.7: Volume formation of intermediate web stiffeners within the I-link

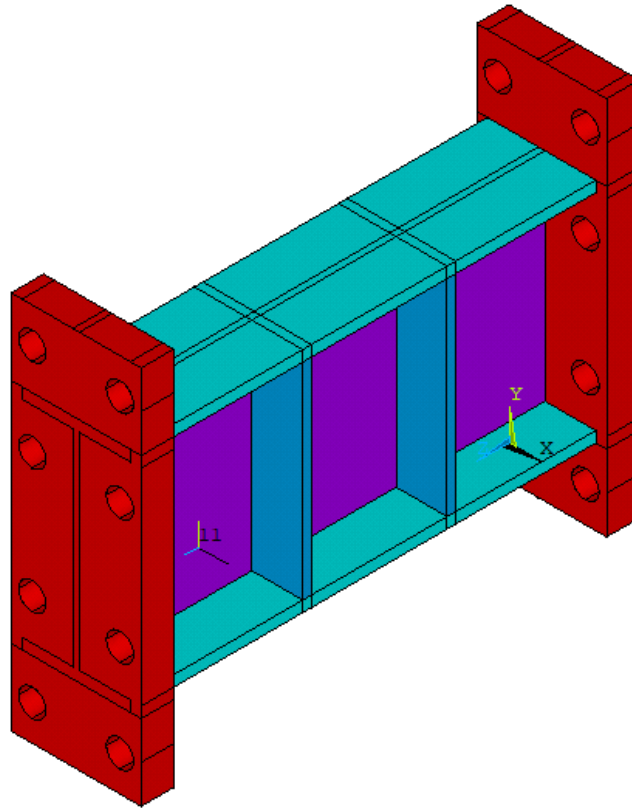


Figure 3.8: Volume of the whole assembly of I-link with stiffeners

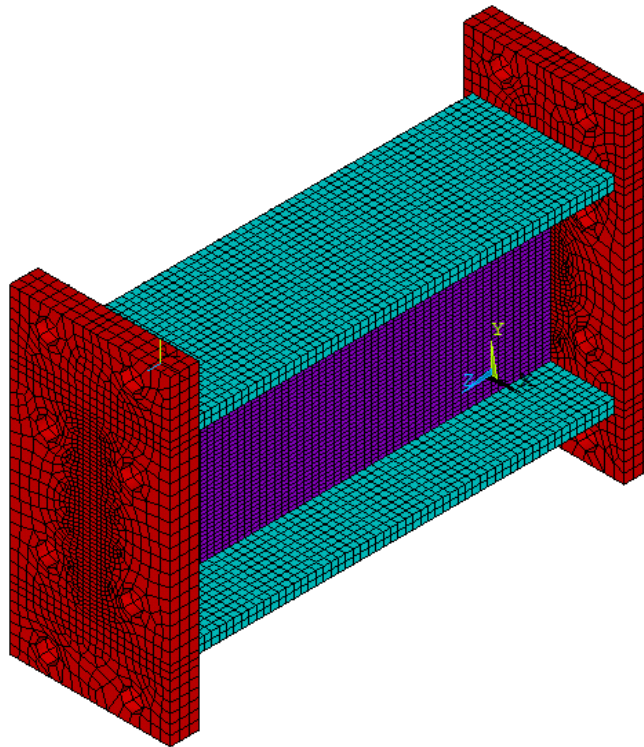


Figure 3.9: Isometric view of the link model after meshing (without stiffeners)

3.3.5 Meshing

Sensitivity analysis was performed in the developed numerical models and optimum mesh sizes were chosen for accurate simulation of cyclic behavior of the shear links. All the elements of the models were meshed using the VSWEEP command. Meshing was done in such a way that a minimum of two divisions was created across the thickness of each plate of the entire assembly. The meshing of endplates, flanges, webs and the stiffeners are done in such a way that the dividing lines of the mesh of each of these parts match with other one or more parts where connected. In this way, thorough connectivity is ensured throughout the whole system. The meshes of the endplates was coarser than that of the other parts of the structure. A meshed model of an I-shaped shear link without stiffeners is shown in Figure 3.9 and that with web stiffeners is shown in Figure 3.10.

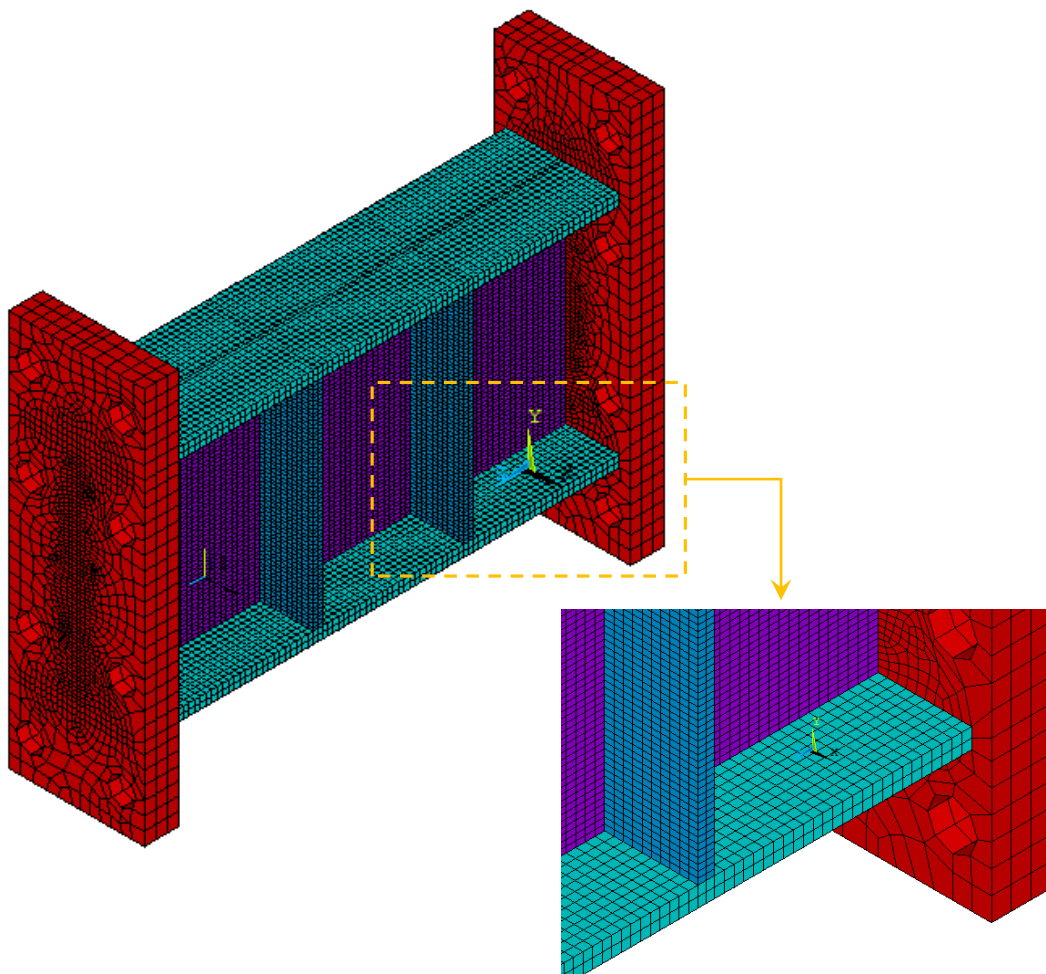


Figure 3.10: Isometric view of the link model after meshing (with stiffeners)

3.3.6 Boundary Conditions

The boundary conditions primarily consist of restraints at one of the two end and plates and coupling and application of loading at the other, both at the bolt locations of the end plates.

3.3.6.1 Restraints

Restraints are applied at the boltholes of the endplates such as to numerically simulate the boundary conditions of the link. At one end, the translations in the nodal x, y, and z directions of all the nodes of the boltholes are restricted. The restraints given in the finite element model is shown in Figure 3.11 and it has also been shown in a schematic view in Figure 3.12.

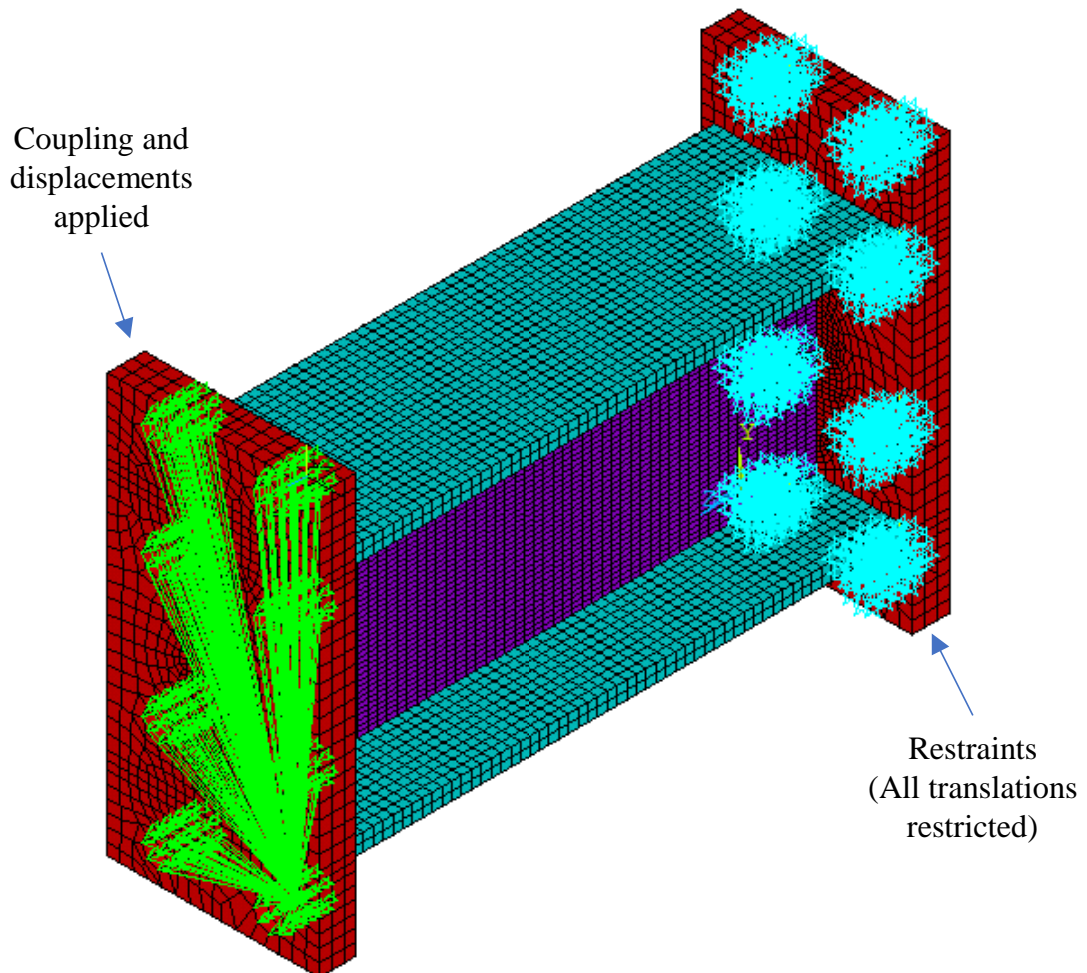


Figure 3.11: Boundary conditions of the link showing restraints at one end and coupling at the other end (where the load is to be applied)

3.3.6.2 Coupling

Coupling can be used to model various joint and hinge effects. For structural analyses, a list of nodes is defined along with the nodal directions in which these nodes are to be coupled. As a result of this coupling, these nodes are forced to take the same displacement in the specified nodal coordinate direction. A set of coupled nodes which are not coincident, or which are not along the line of the coupled displacement direction, may produce an applied moment which will not appear in the reaction forces. (ANSYS, Inc. 2019).

Hence to maintain equal displacement of all the displacement nodes along the axial direction of the link, those nodes were coupled as shown in Figure 3.11. The ‘CP’ command of ANSYS was used to apply coupling between the elements and the boltholes.

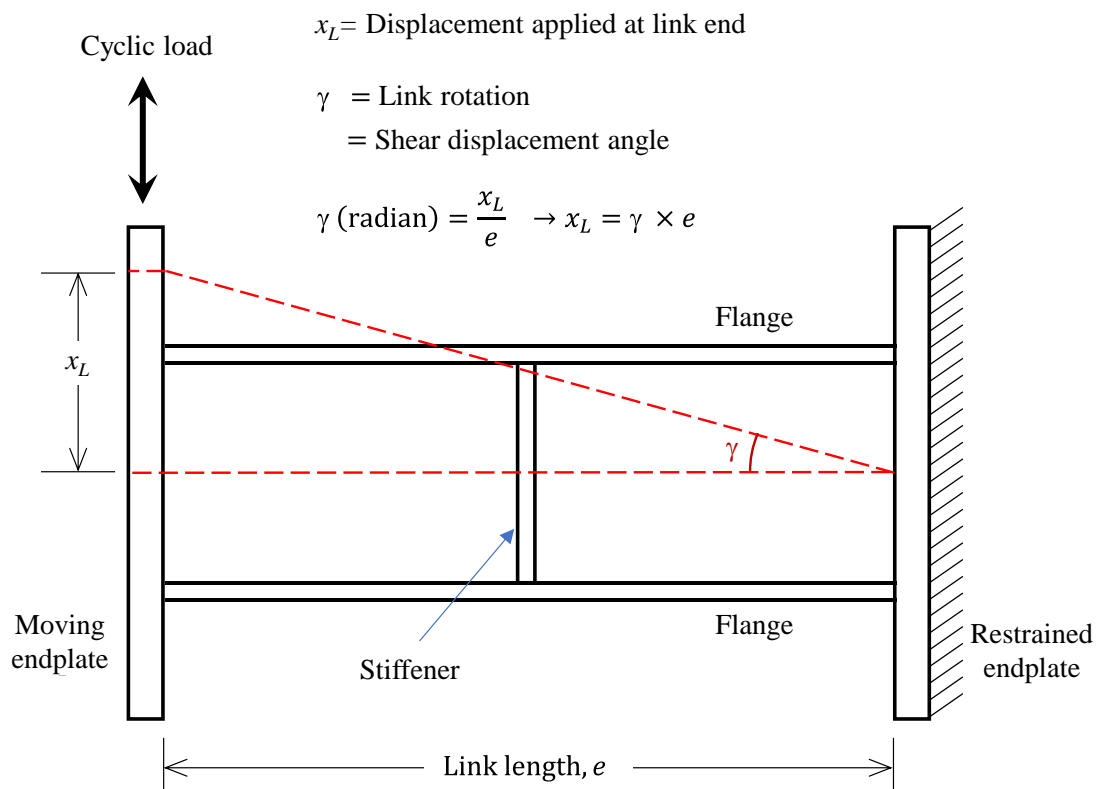


Figure 3.12: Link rotation and applied displacement at link end

3.3.7 Loading

The cyclic loading was applied at the nodes of the bolt locations of the left endplate (Figure 3.11). The same nodes were coupled as stated previously. The nonlinear analysis can be performed either by applying load or deflection. As per the AISC code and the previous studies, the cyclic loading for shear links was based on the rotations of the link which can be controlled by applying deflections. Hence, in this study, the applied cyclic loadings had to be displacement-based. The displacements to be applied to one end of a link are obtained by multiplying the link length with the corresponding link rotation (Figure 3.12)

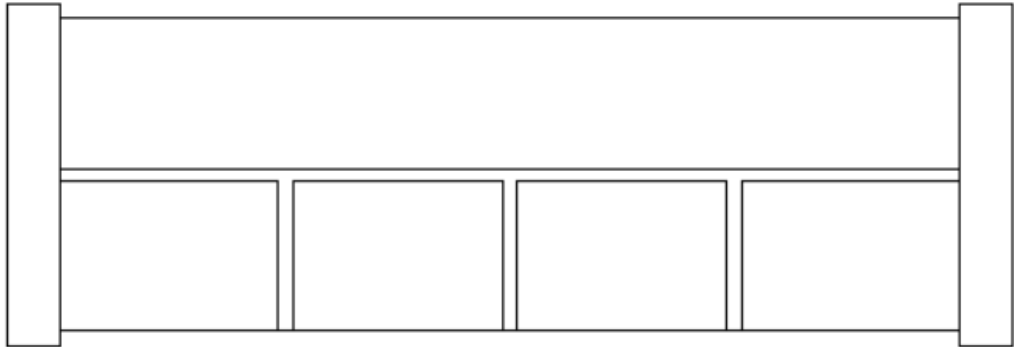
So, to simulate cyclic loading, the displacements were applied at the bolt locations of the left endplate (Figure 3.11) along both the positive and negative directions.

3.4 TYPICAL FE MODELS DEVELOPED

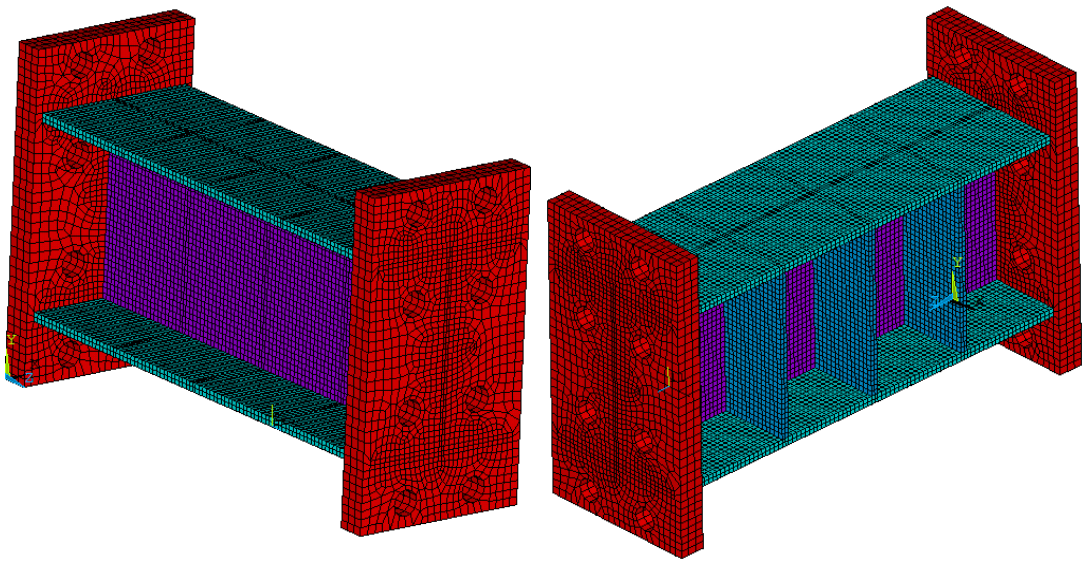
Some typical finite element models of shear links which are developed in this study are depicted are listed as follows.

1. Link with web stiffeners on one side only (specimen 4A-RLP of Okazaki and Engelhardt, 2006)
2. Link with web stiffeners on both sides (specimen AL-BU-BN2 of Volnkin et al. 2018)
3. Link with perforation in web for shear strength reduction (specimen L-C-2 of Tong et al. 2018)

Isometric views of those models are shown in Figure 3.14 to Figure 3.13. For clear understanding, other views of the developed models are presented for different link specimens. After adequate verification of the models, the different parameters in the typical models can be varied and parametric studies can be conducted. The finite element model of shear link with box type cross section is presented in Chapter 5 and is not shown in this section.



(a) Plan view



(b) Isometric views

Figure 3.13: Link with web stiffeners on one side only (specimen 4A-RLP of Okazaki and Engelhardt, 2006)

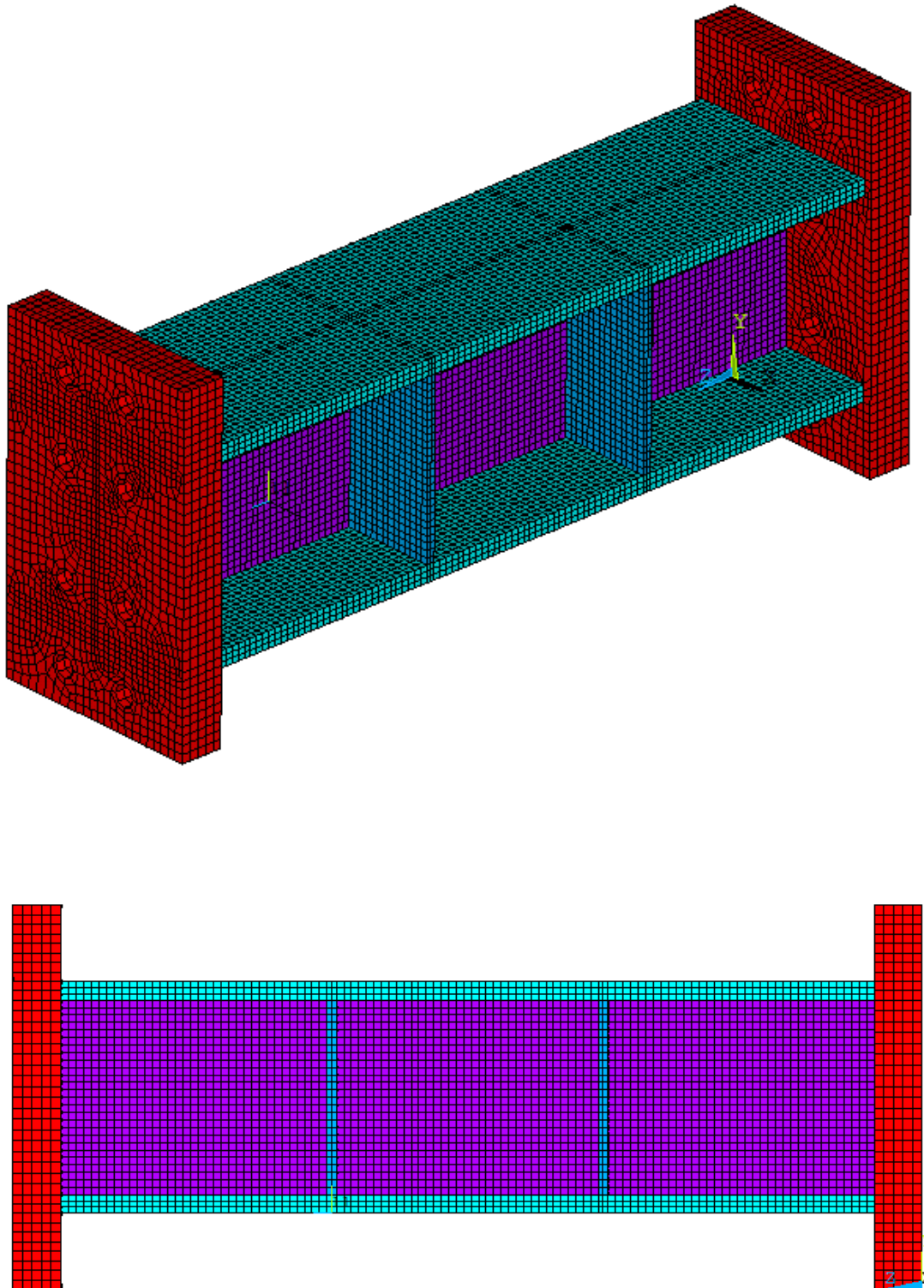


Figure 3.14: Link with web stiffeners (specimen AL-BU-N2 of Volynkin et al. 2018)

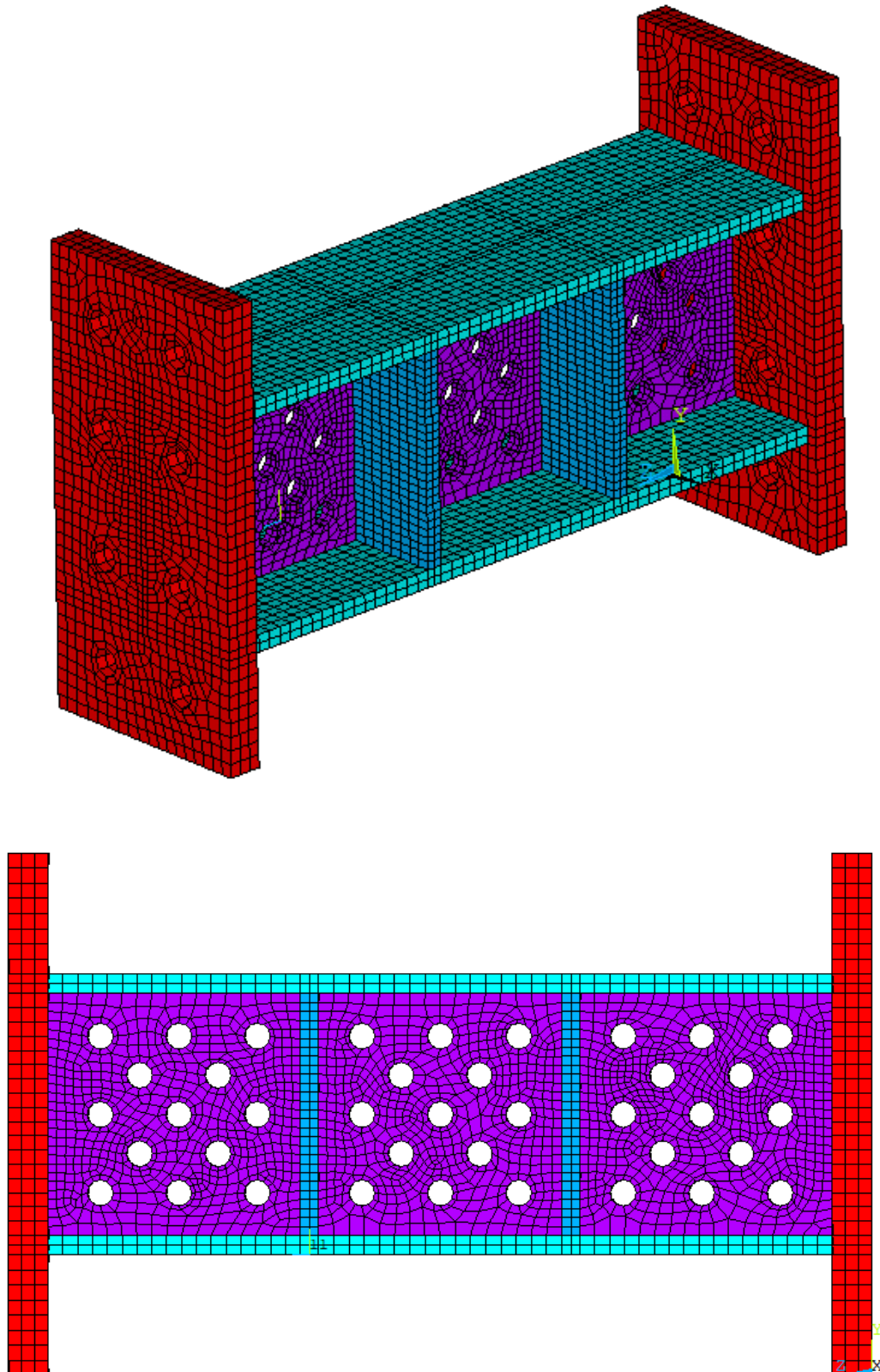


Figure 3.15: Link with perforation in web for reduction of shear strength (Specimen L-C-2 of Tong et al. 2018)

3.5 REMARKS

The developed finite element models need to be verified to establish the validation of the models. If adequate validation of the models can be established against past experimental studies, the models can be further used for simulation of the practical results. Hence, the validation of the finite element models was conducted which is presented in the upcoming chapter.

CHAPTER 4

NUMERICAL MODEL VALIDATION

4.1 INTRODUCTION

The numerical models developed and presented in the previous chapter need validation before being used for further study and simulation of results depicting practical conditions. For this reason, different experiments conducted on shear links were used as references to verify the numerical models. Validation of the numerical models were conducted with reference to the experimental studies conducted by Tong et al. (2018), Volynkin et al. (2018), Liu et al. (2017), and Okazaki and Engelhardt (2006). The verification of each experimental study with corresponding details has been presented in this chapter.

4.2 SIMULATION OF EXPERIMENTAL RESEARCH ON REPLACEABLE Q345GJ SHEAR LINKS

Shear links made of Q345GJ steel were designed and tested in the experimental study of Liu et al. (2017) where, the parameters explored were web aspect ratio, flange width-thickness ratio, the link length ratio eV_p/M_p , stiffener spacing and thickness, hysteretic loadcase, and welding details. The hysteretic behavior, overstrength, energy dissipation and related parameters were discussed. The experimental setup of Liu et al. (2017) is shown in Figure 4.1 and the typical geometric details of the links is shown in Figure 4.2. Five specimens of the experimental study were modeled by FEM. The parametric details of those specimens are shown in Table 4-1.

4.2.1 FE Modeling Parameters and Loading History

The elastic properties of the material are directly taken from the study. The plastic properties of the material which are found by calibrating the material constants consists of the Chaboche nonlinear kinematic hardening parameters and nonlinear isotropic hardening parameters (Voce law). All these parameters are listed in Table 4-2.

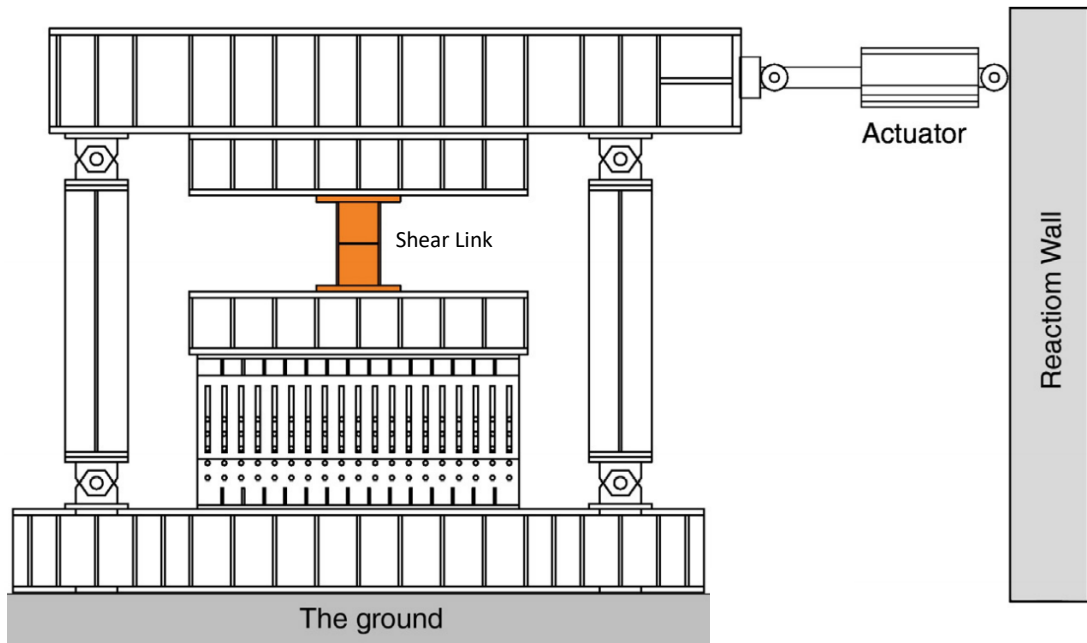


Figure 4.1: Experimental setup of Liu et al. (2017)

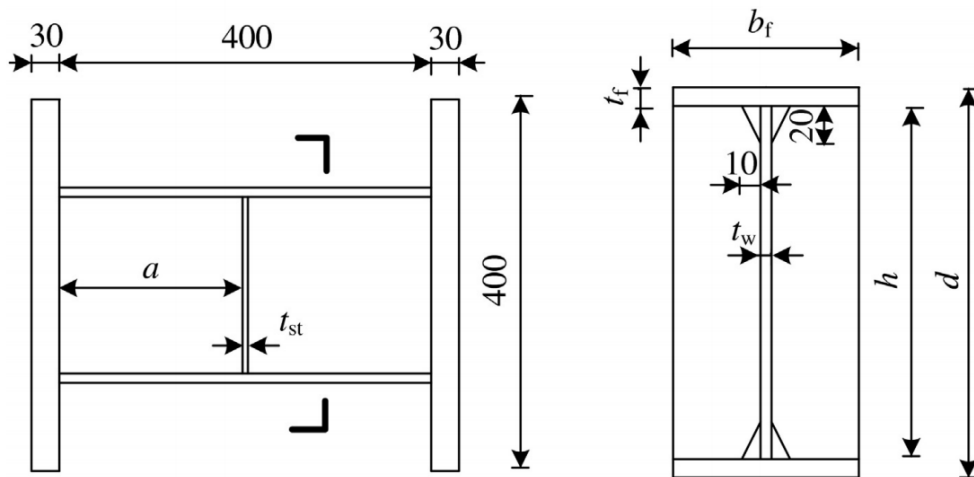


Figure 4.2: Geometric details of shear link (Liu et al. 2017)

Table 4-1: Details of the modeled link specimens of Liu et al. (2017)

Specimen	b_f (mm)	t_w (mm)	a (mm)	t_{st} (mm)	Length ratio (eV_p/M_p)	Other common parameters
RSL-3	160	10	200	6	1.53	$e=400\text{mm}$ $d=210\text{mm}$ $t_f=10\text{mm}$ $f_y=360\text{MPa}$
RSL-4	130	8	200	3	1.50	
RSL-7	130	10	133	6	1.50	
RSL-9	105	10	200	6	1.84	
RSL-10	130	10	200	4	1.50	

Table 4-2: Material parameters for verification of study of Liu et al. (2017)

Elastic Parameters: $E = 200000 \text{ MPa}$, $\nu=0.3$, $\sigma_o = 360 \text{ MPa}$										
Plastic Parameters										
Kinematic hardening parameters								Isotropic hardening parameters		
C_1 (MPa)	γ_1	C_2 (MPa)	γ_2	C_3 (MPa)	γ_3	C_4 (MPa)	γ_4	R_o (MPa)	R_∞ (MPa)	b
20000	1000	10000	100	600	20	350	0	4	70	0.2

The command lines for the input of plastic hardening parameters in finite element modeling are shown in the previous chapter (Table 3-3).

The loading protocol used in the experimental study for specimens RSL-3, RSL-4, RSL-7, RSL-9 and RSL-10 is shown in Figure 4.3. The loading protocol is more severe than the AISC loading protocol.

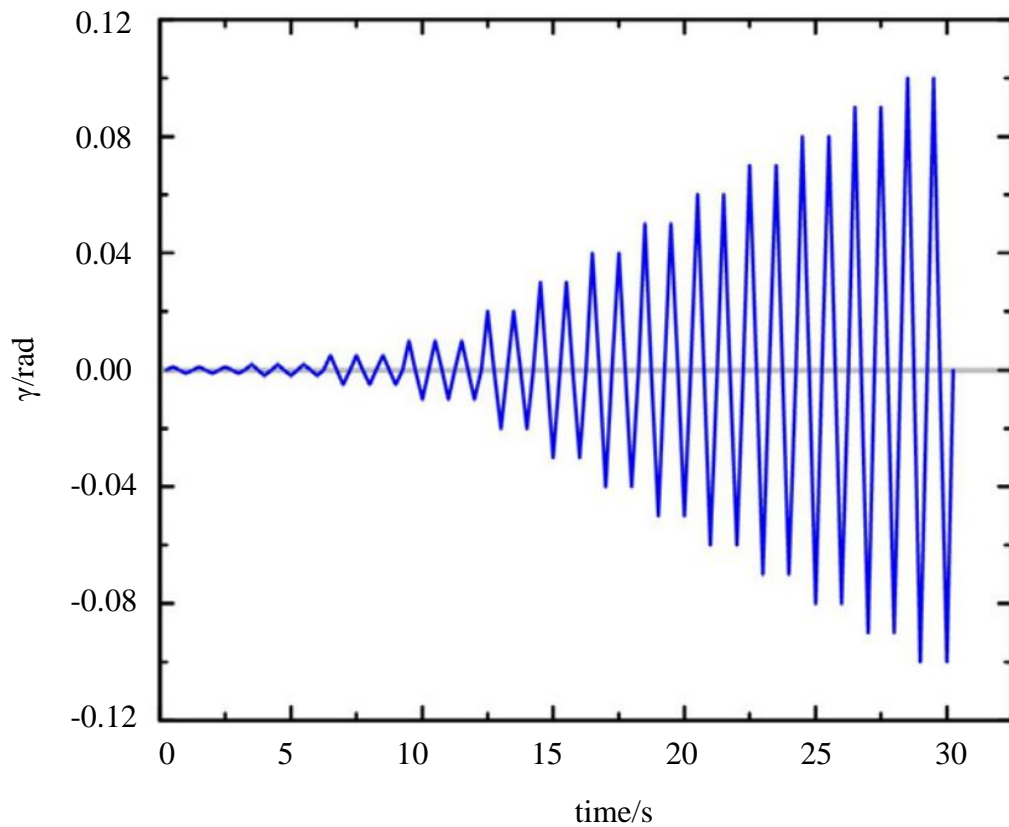
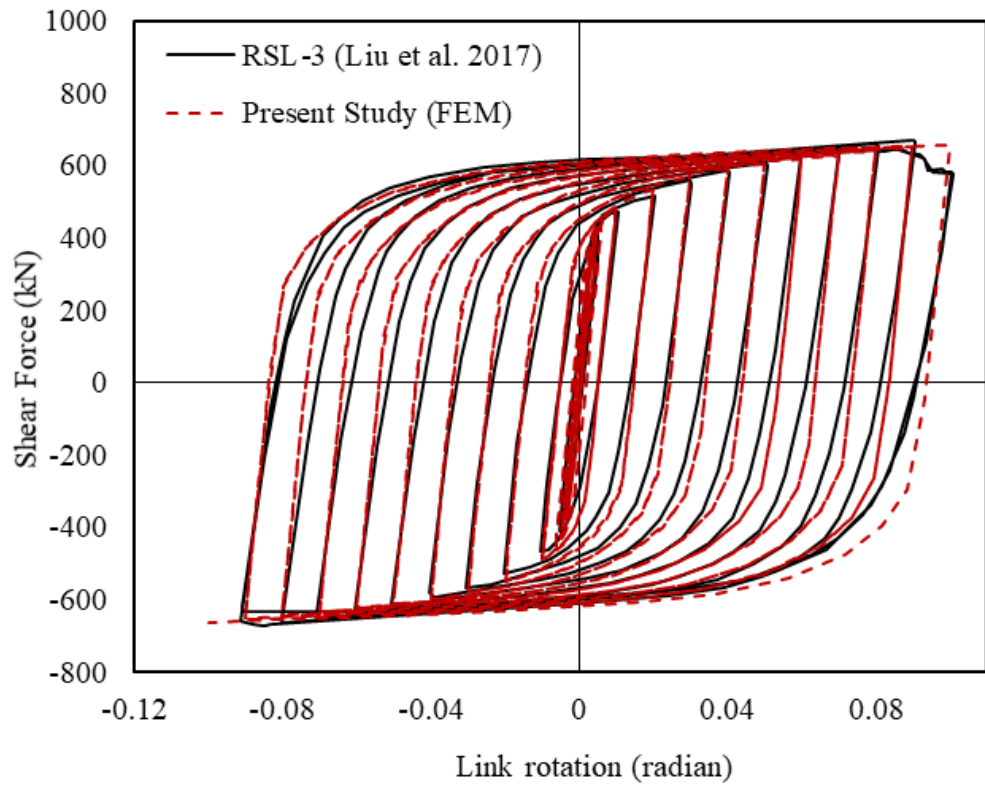


Figure 4.3: Loading history for specimens RSL-3, RSL-4, RSL-7, RSL-9 and RSL-10 of Liu et al. (2017) (time/s indicates the cycle number)

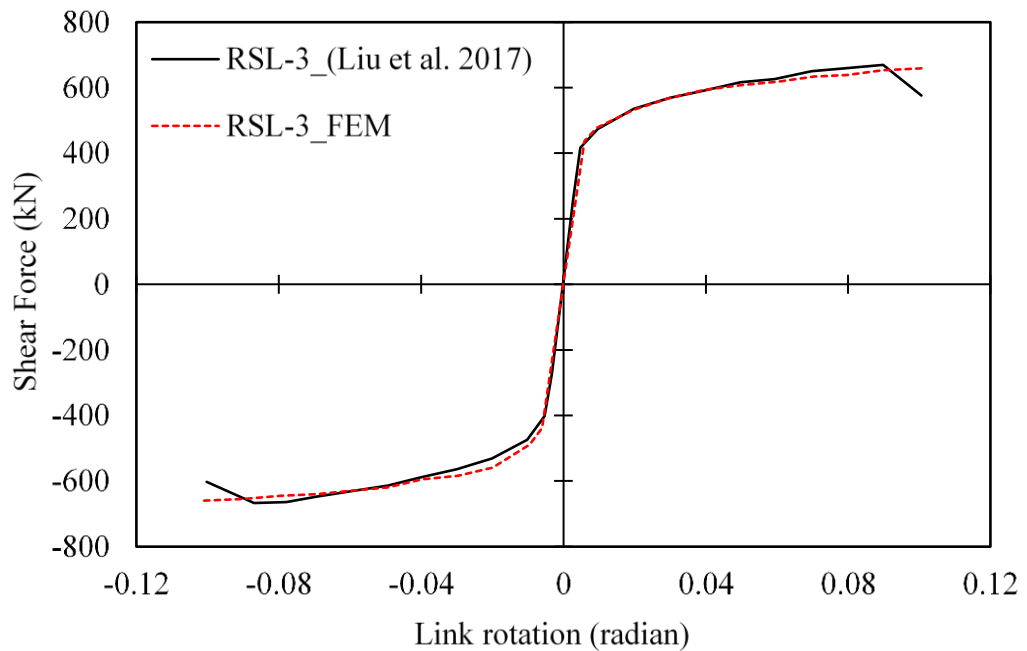
4.2.2 Verification Results

The comparison between the experimental results and the numerical simulation of the present study for specimens listed in Table 4-1 is shown in Figure 4.4 to Figure 4.8. The hysteretic responses and the skeleton curves obtained by the experimental and the numerical study are superimposed and shown in the figures. The skeleton curve is the envelope of hysteretic curve under cyclic loading, obtained by connecting the peak points at each load cycle. From the plots, adequate agreement is found to exist between the experimental and the numerical results.

The deformed shapes and von Mises stress contour of the experimental and numerical study are shown in Figure 4.9 and Figure 4.10. Similarity between deformed shapes of experimental study and the numerical simulation can be noticed from the figures. From all the comparisons and results, the models can be said to be verified against the experimental study of Liu et al. 2017.

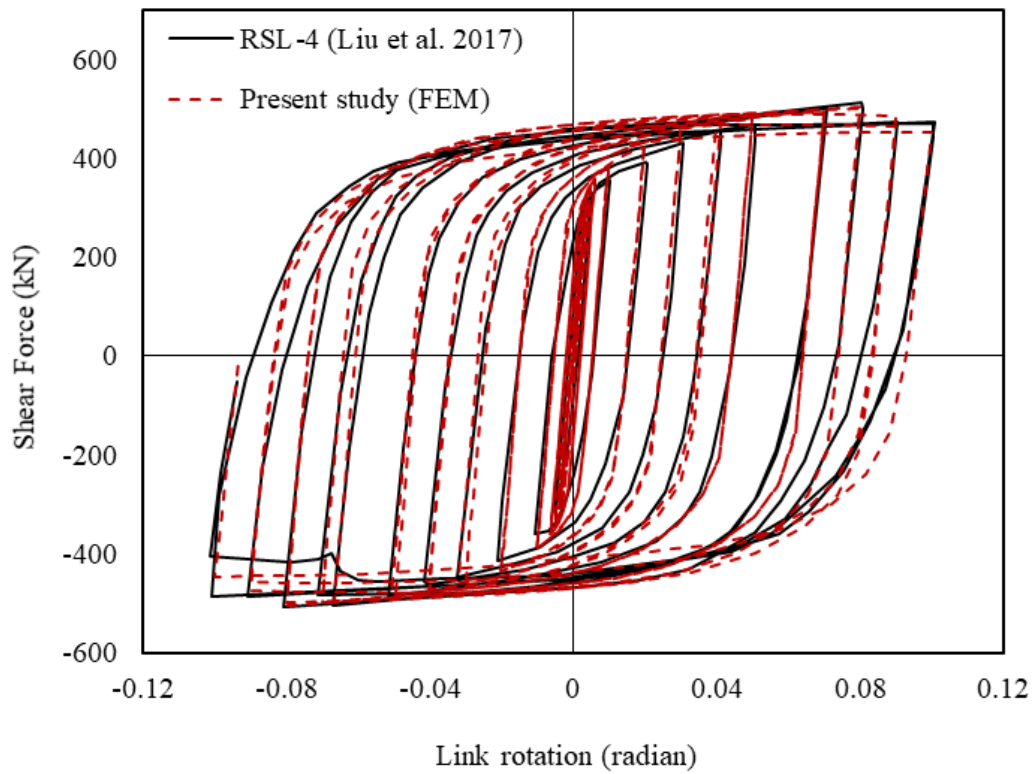


(a) Hysteretic response

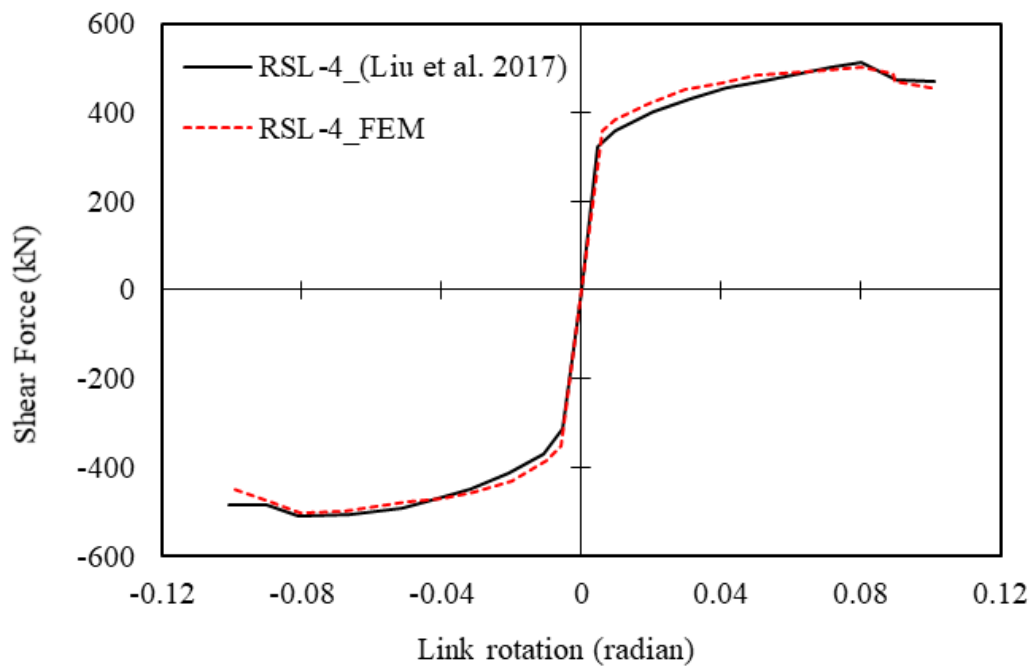


(b) Skeleton curve

Figure 4.4: Comparison between FEM and experimental results of the specimen RSL-3

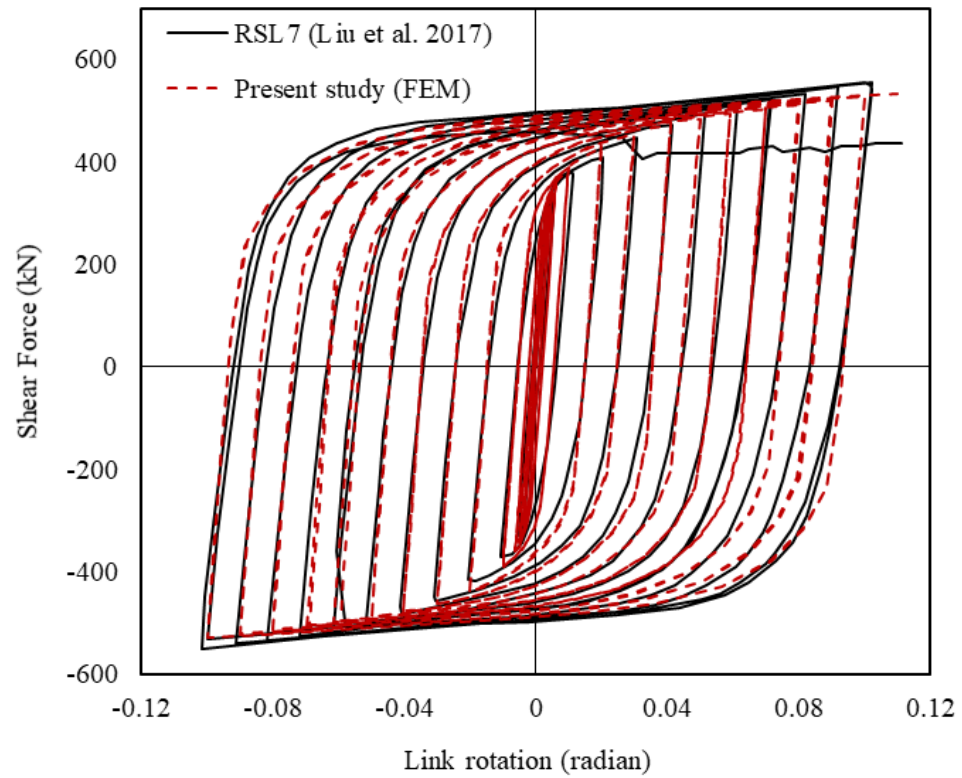


(a) Hysteretic response

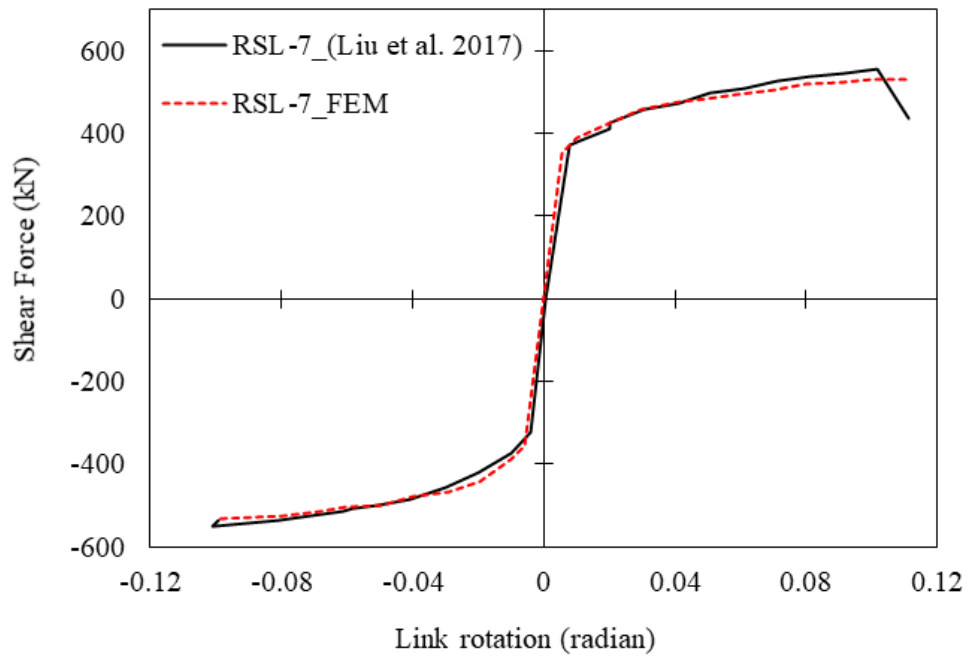


(b) Skeleton curve

Figure 4.5: Comparison between FEM and experimental results of the specimen RSL-4

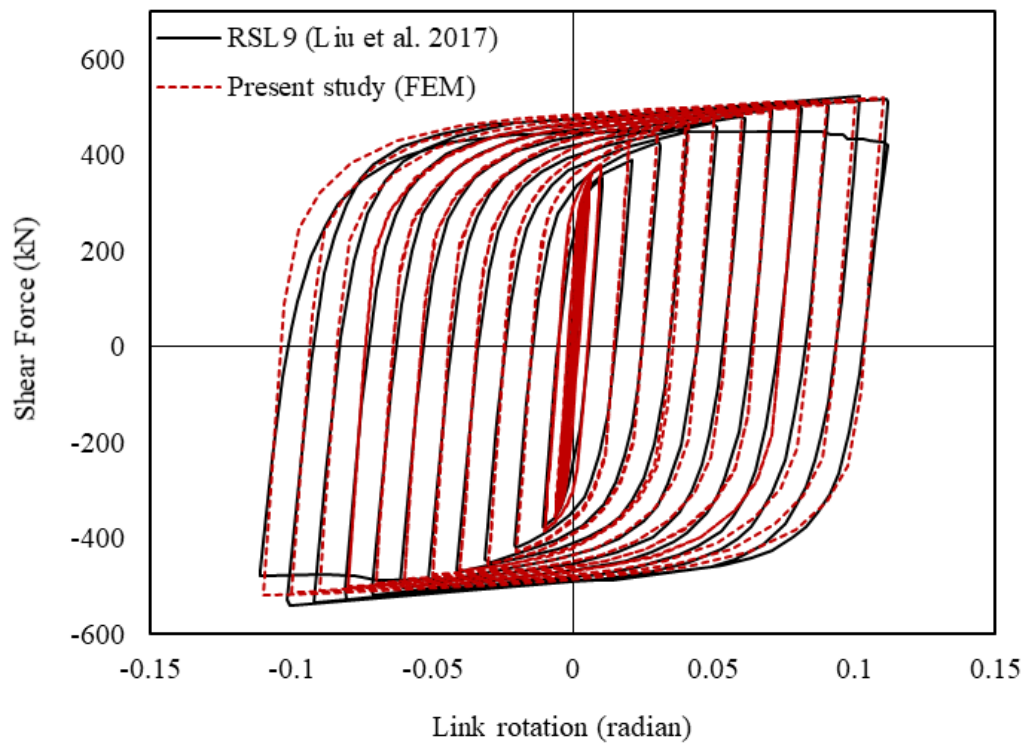


(a) Hysteretic response

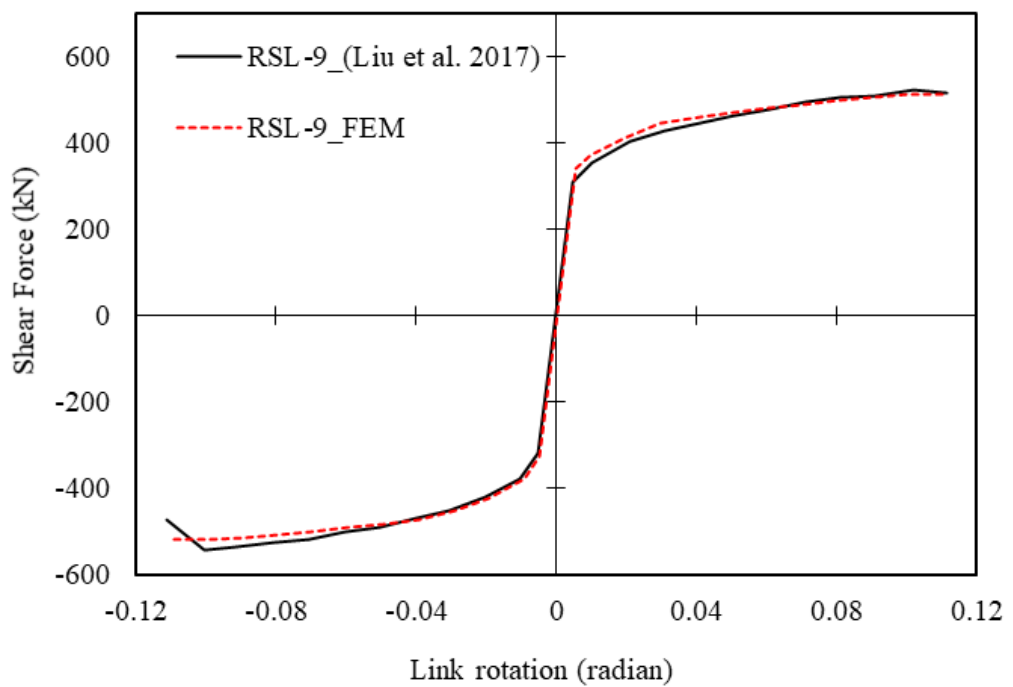


(b) Skeleton curve

Figure 4.6: Comparison between FEM and experimental results of the specimen RSL-7

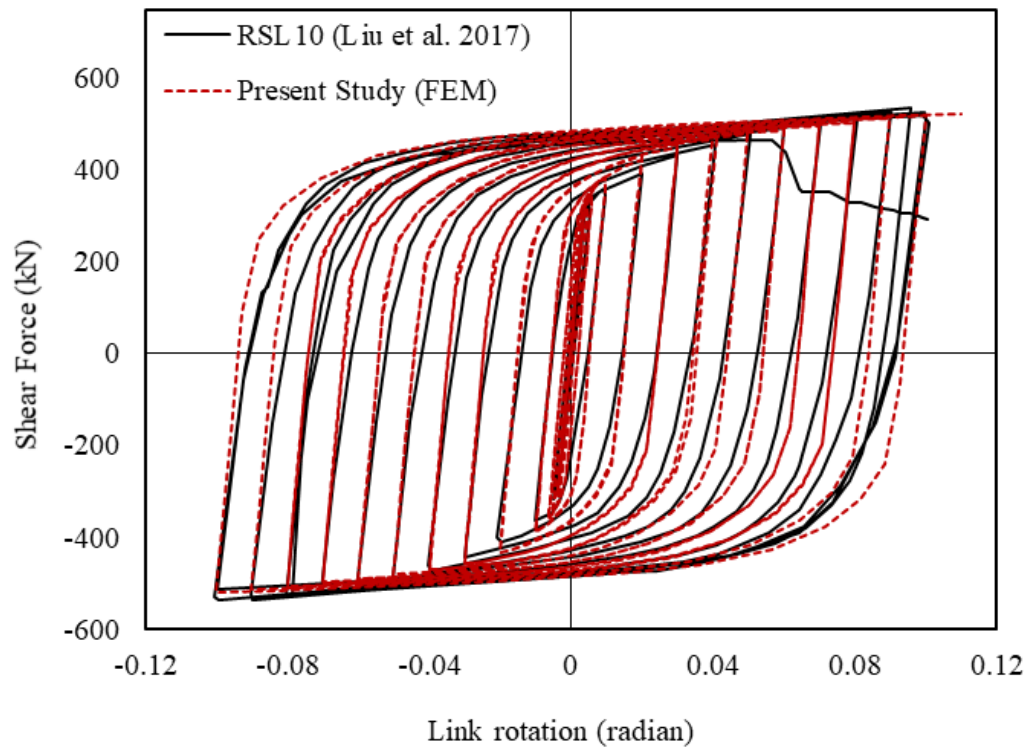


(a) Hysteretic response

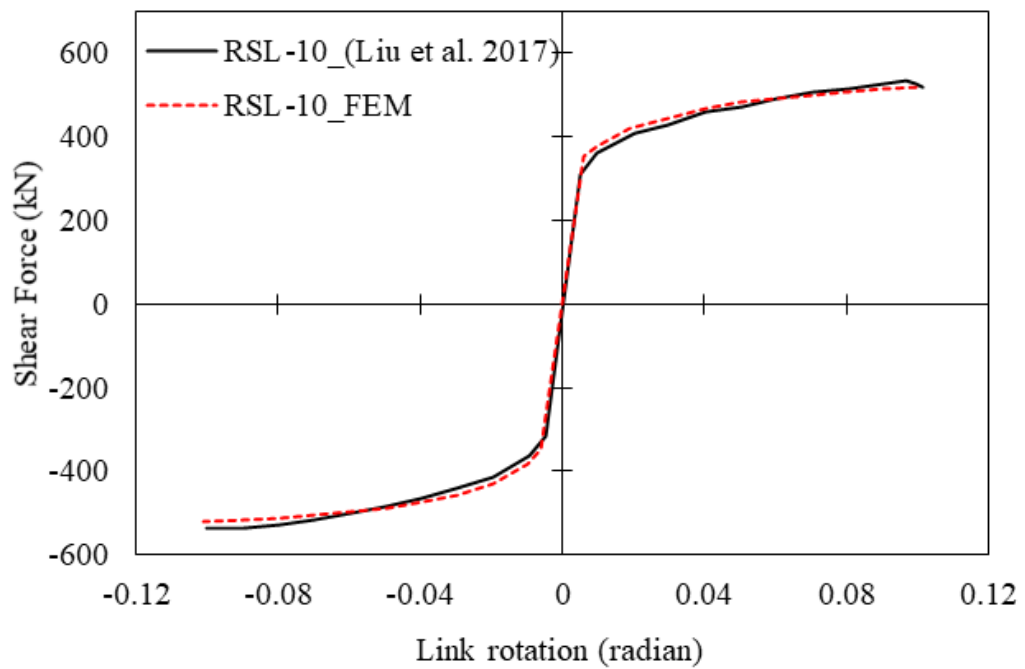


(b) Skeleton curve

Figure 4.7: Comparison between FEM and experimental results of the specimen RSL-9



(a) Hysteretic response



(b) Skeleton curve

Figure 4.8: Comparison between FEM and experimental results of the specimen RSL-10

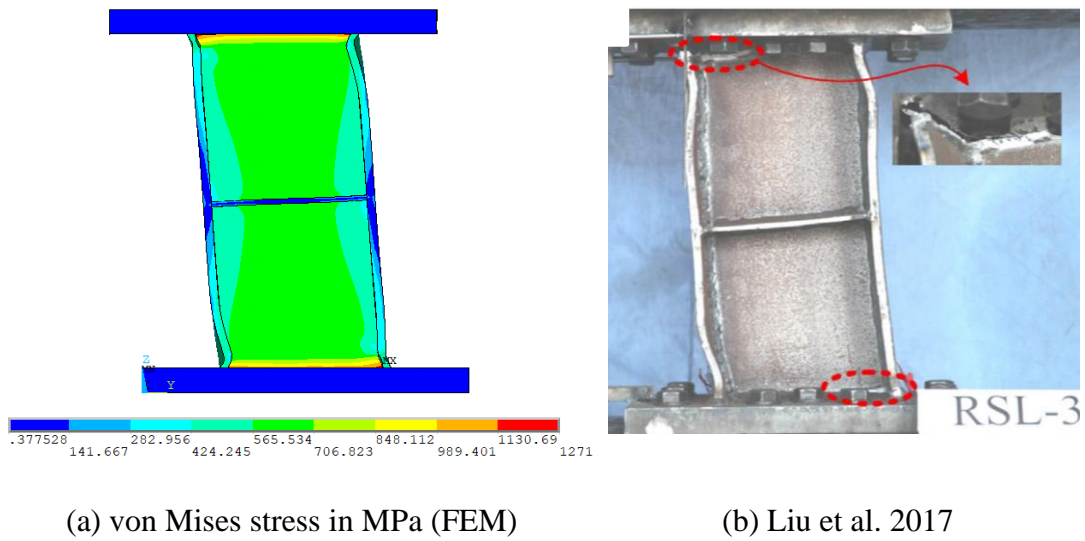


Figure 4.9: Deformed shape and von Mises stress of RSL-3 at 40mm shear displacement

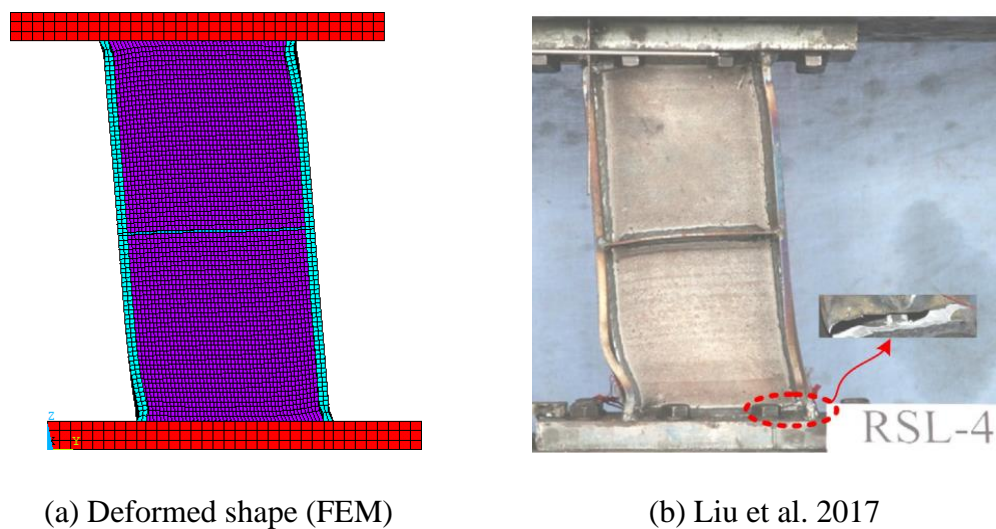


Figure 4.10: Deformed shape of RSL-4

4.3 SIMULATION OF EXPERIMENTAL STUDY ON INTERMEDIATE WEB STIFFENER SPACING OF SHEAR LINKS

The spacing requirement of intermediate web stiffeners in shear links as prescribed by AISC code was evaluated by Volynkin et al. (2018). Links were tested with both with and without stiffeners. Unstiffened links with stocky web sections (defined as web with $h/t_w < 24$ by Volynkin et al. 2018) performed to exceptional levels, achieving inelastic rotations of 0.17 and 0.19 radian compared to 0.08 radian value required by

the seismic standards. On the other hand, stiffened links with stocky webs failed to achieve such high rotations. Two of the tested specimens were numerically simulated in this study, one with web stiffeners (AL-BU-N2) and the other without web stiffeners (AL-BU-B2).

The test setup of Volynkin et al. (2018) is shown in Figure 4.11 and the link cross sectional dimensions of specimen AL-BU-N2 are shown in Figure 4.12. The specimen AL-BU-B2 has the same dimensions (Table 4-3) as that of AL-BU-N2 but does not stiffeners. The developed finite element models of the specimens are shown in Figure 4.13 and Figure 4.14.

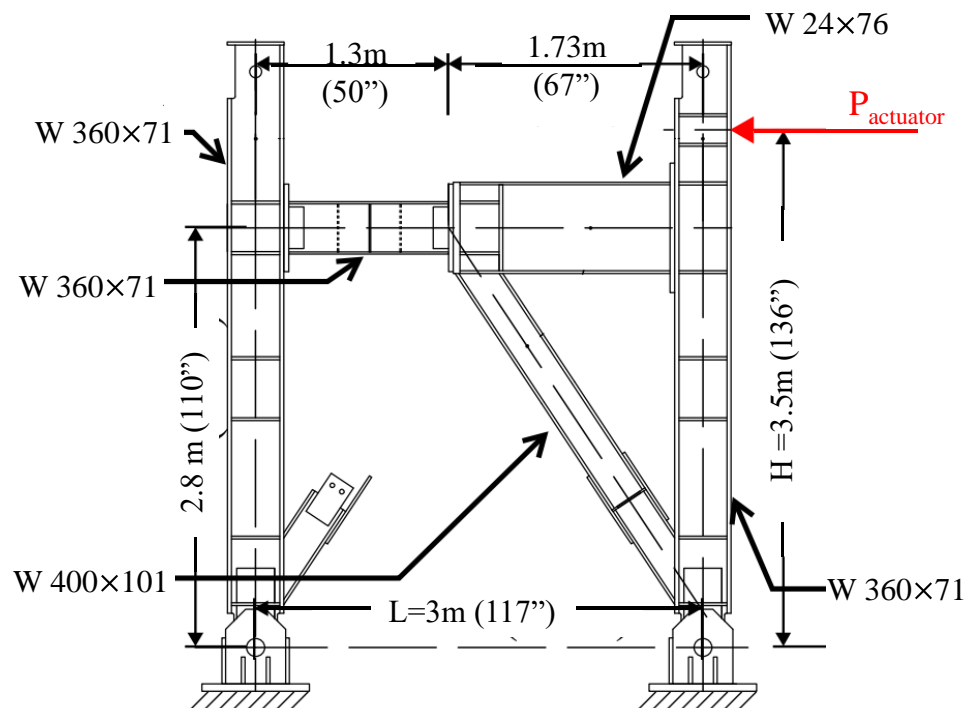


Figure 4.11: Test setup of eccentrically braced frame of Volynkin et al. (2018)

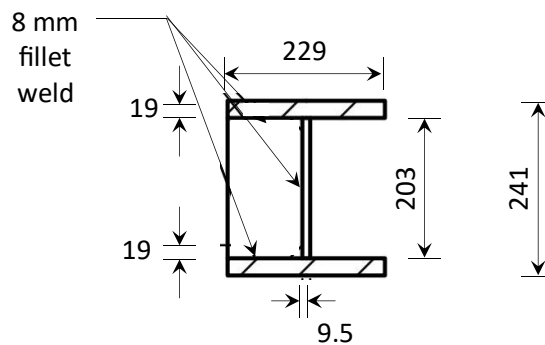


Figure 4.12: X-sectional dimensions of link specimen AL-BU-N2 of Volynkin et al. (2018)

Table 4-3: Parameters of modeled specimens of Volynkin et al. (2018)

Specimen	e (mm)	d (mm)	b_f (mm)	t_f (mm)	t_w (mm)	h/t_w	Stiffener spacing (mm)	Length ratio (eV_p/M_p)
AL-BU- N2	848	241	229	19	9.5	19.33	279	0.92
AL-BU- B2	848	241	229	19	9.5	19.33	No stiffener	0.92

4.3.1 FE Modeling Parameters and Loading History

The yield strength of flanges and webs of the specimens AL-BU-N2 and AL-BU-B2 are 455 MPa and 374 MPa, respectively. The elastic and hardening parameters for material modeling in FEM modeling are shown in Table 4-4. The elastic parameters are taken from the experimental data and calibrated plastic hardening properties (constants of Chaboche model and Voce law) shown in the table were used for simulation of cyclic behavior of the shear links.

The loading protocol used for link testing in the experiment and the numerical simulation is the one adopted by the AISC code (AISC 341-05, AISC, 341-16). This loading protocol is the same as the revised protocol of Okazaki and Engelhardt (2006) which is shown in Figure 2.16.

Table 4-4: Material parameters for verification of study of Volynkin et al. (2018)

Elastic Parameters		Kinematic hardening parameters						Isotropic hardening parameters		
E (MPa)	ν	C_1 (MPa)	γ_1	C_2 (MPa)	γ_2	C_3 (MPa)	γ_3	R_o (MPa)	R_∞ (MPa)	b
206000	0.3	30000	2000	15000	200	500	10	10	60	2

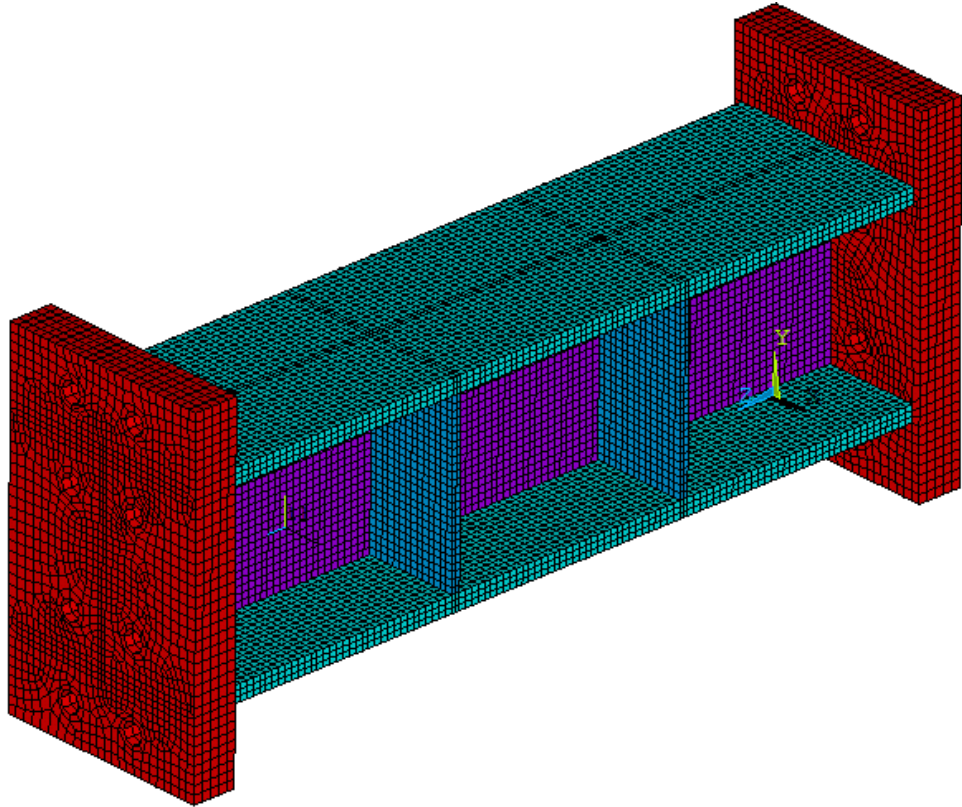


Figure 4.13: FE model of specimen AL-BU-N2

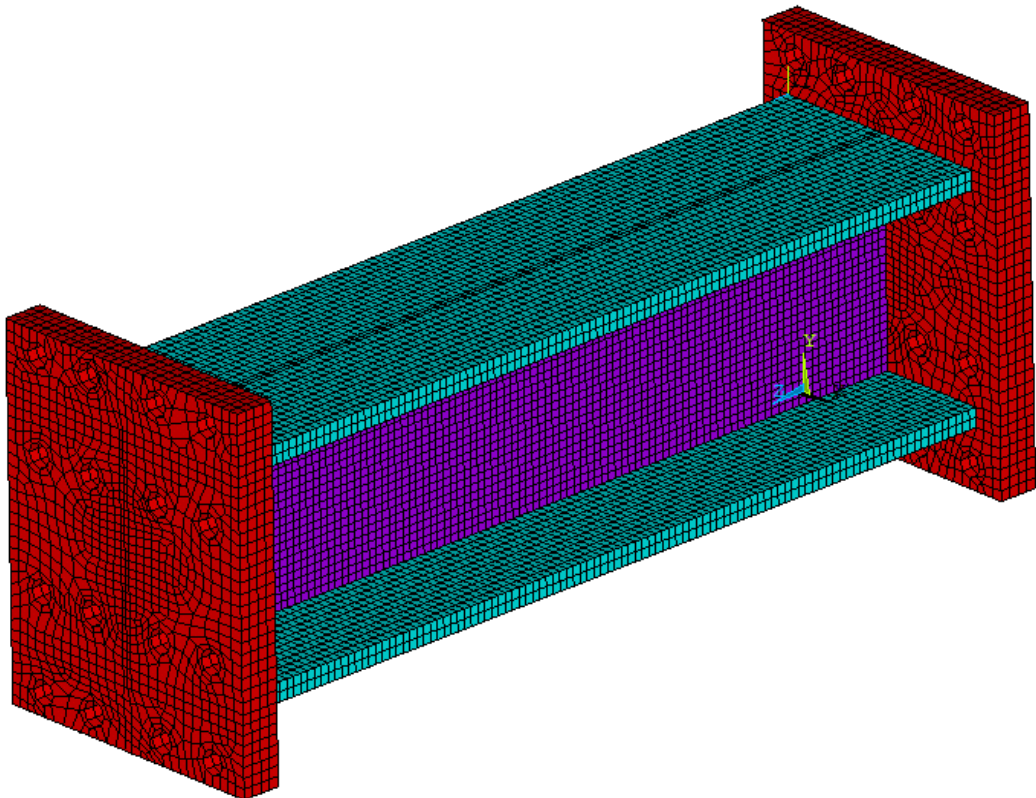


Figure 4.14: FE model of specimen AL-BU-B2

4.3.2 Verification Results

The results of the finite element analysis are compared with the results of the experimental investigation. The hysteretic plots of shear force versus link rotation of the FEM results and the results of Volynkin et al. (2018) are superimposed and shown in Figure 4.15 and Figure 4.16.

It can be observed that adequate agreement exists between the FEM results and the experimental results in terms of shear-rotation cyclic behavior of links. Also, from the deformed shapes of specimen AL-BU-B2 (Figure 4.17 and Figure 4.18), the agreement between the experimental and the numerical simulation is evident.

So, from all the comparisons and results, the models can be said to be verified against the experimental study of Volynkin et al. (2019).

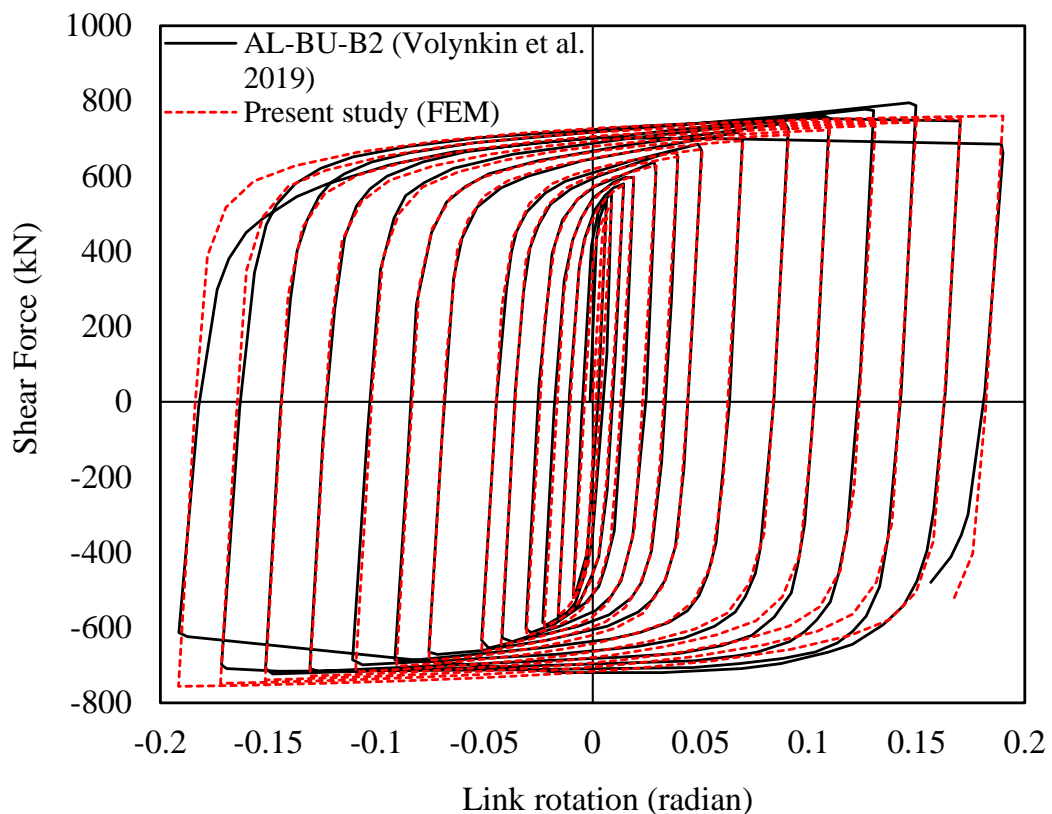


Figure 4.15: Comparison between FEM and experimental results of link AL-BU-B2

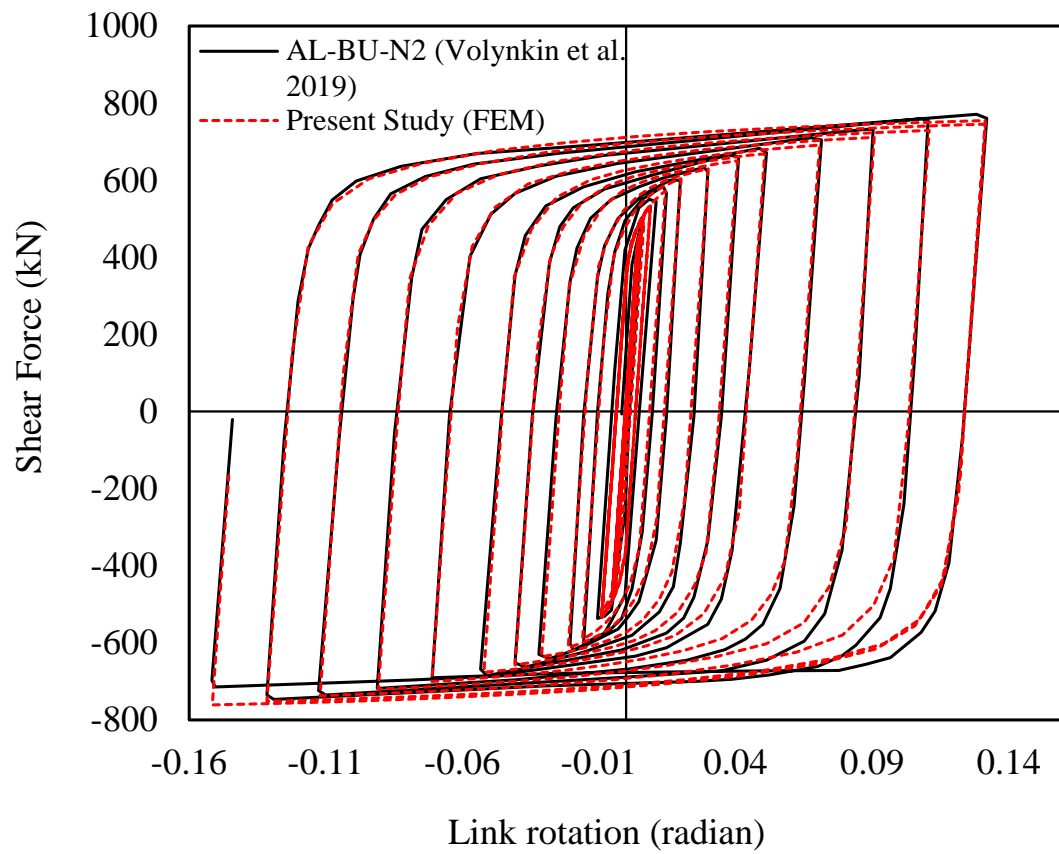


Figure 4.16: Comparison between FEM and experimental results of link AL-BU-N2



Figure 4.17: Deformed shape of specimen AL-BU-B2 (Volynkin et al. 2018)

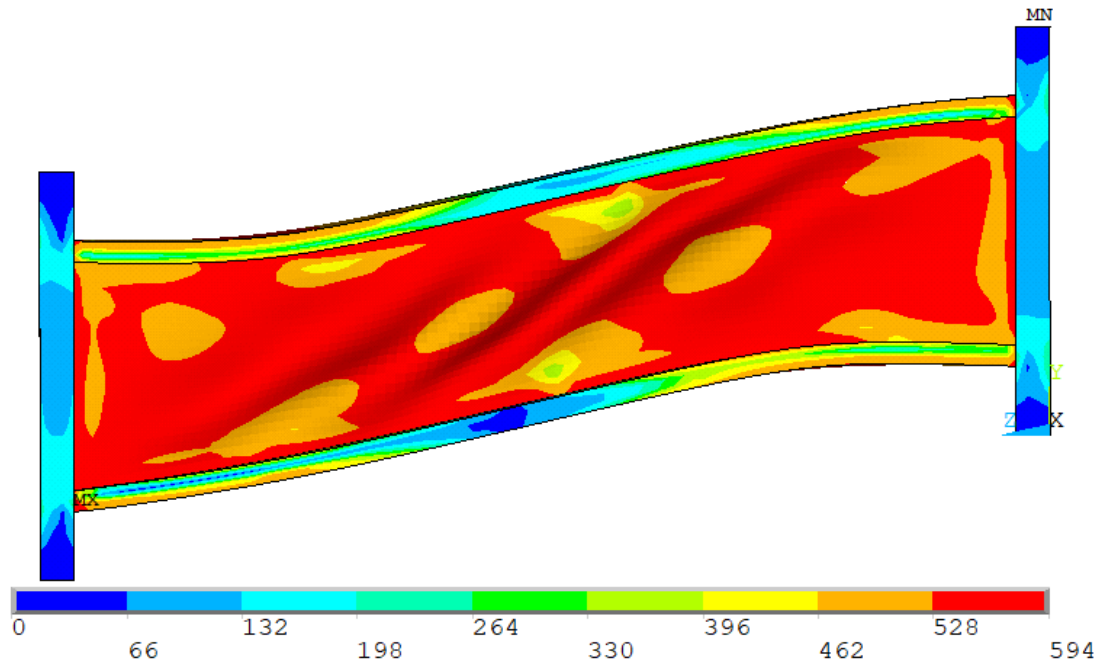


Figure 4.18: von Mises stress (MPa) and deformed shape of specimen AL-BU-B2 (FEM)

4.4 SIMULATION OF DUCTILITY AND ENERGY DISSIPATION BEHAVIOR OF PERFORATED SHEAR LINK

The study of Tong et al. (2018) presents the results of an experimental and numerical simulation study of replaceable cast steel link beams under cyclic loading, including the ductility, strength, stiffness, and energy dissipation of shear link specimens with and without circular perforations. Perforation in the links serves as a tool for the reduction of shear strength. The failure mode, ultimate load carrying capacity, ductility, stiffness, and energy dissipation were investigated of the link.

The experimental setup of Tong et al. (2018) is shown in Figure 4.19. The general dimensions of the cast steel link specimens used are shown in Figure 4.20 and the perforation patterns of the perforated link specimens of Tong et al. (2018) is depicted in Figure 4.21. The corresponding finite element models which are developed in the present study are shown in Figure 4.22, Figure 4.23, and Figure 4.24.

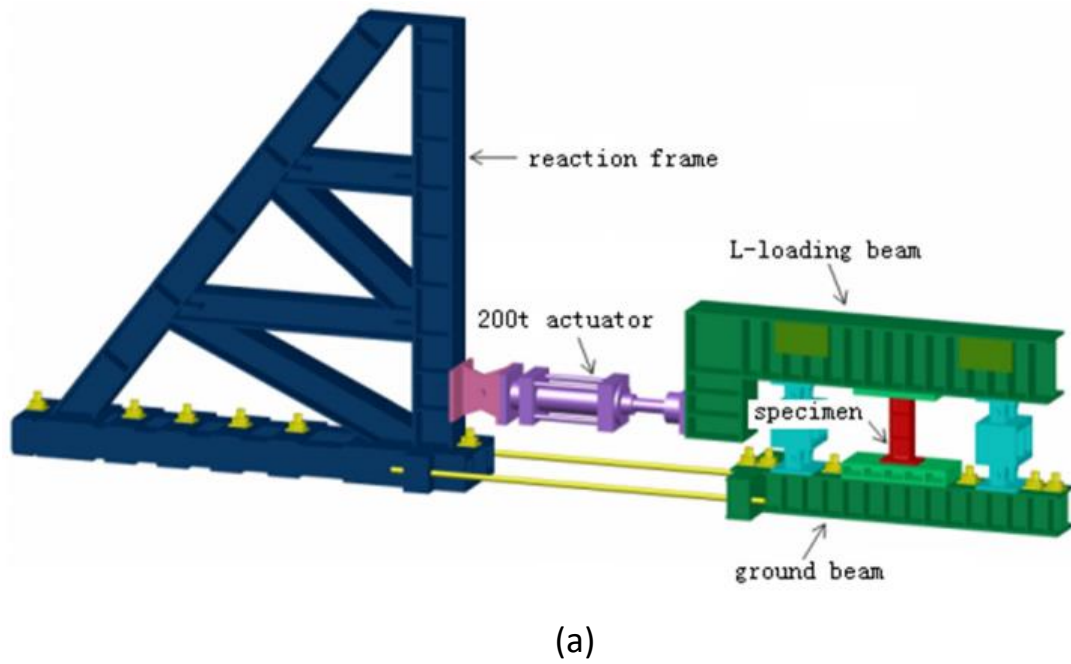


Figure 4.19: Experimental setup of Tong et al. (2018) (a) Schematic illustration (b) Photo

Table 4-5: Specimen details of perforated links of Tong et al. (2018)

Specimen	e (mm)	d (mm)	t_f (mm)	b_f (mm)	t_w (mm)	h/t_w	Perforation pattern	Perforation diameter (mm)
L-C-1	600	215	15	180	12	15.42	Rectangular	20
L-C-2	600	215	15	180	12	15.42	Diagonal	20

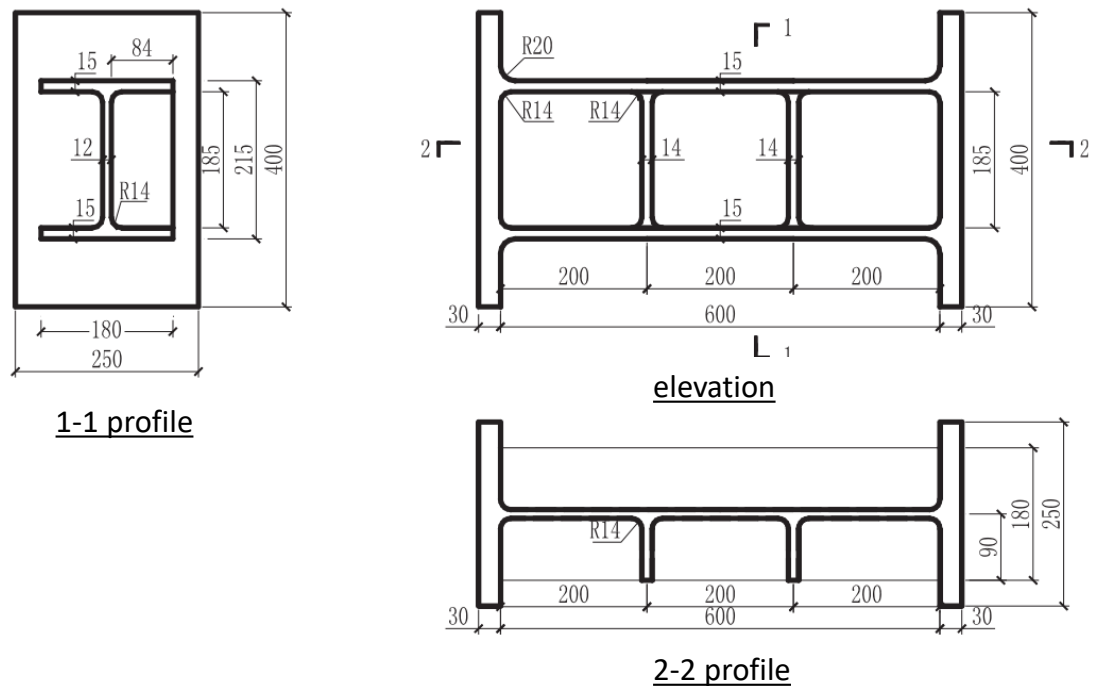


Figure 4.20: Dimensions of the cast steel link specimens tested by Tong et al. 2018
(perforations are not shown in this figure)

Hole diameter is 20 mm for all web holes. Spacing between holes in L-C-1 is 60 mm and additional holes are added to L-C-2 to grid diagonals.

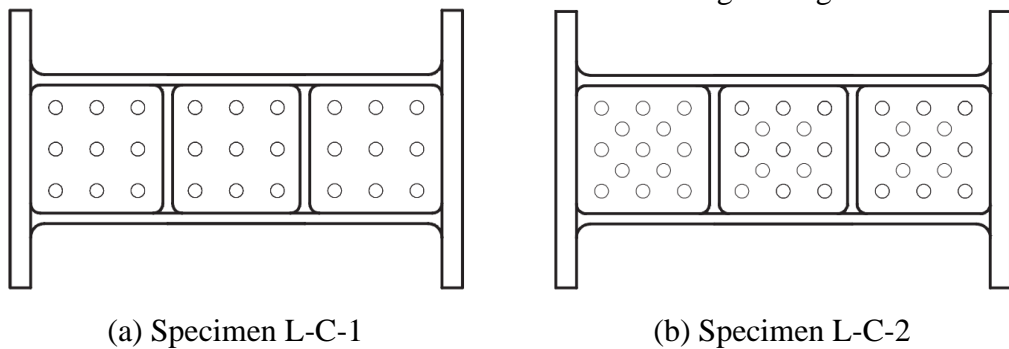


Figure 4.21: Web perforation pattern of perforated link specimens of Tong et al. (2018)

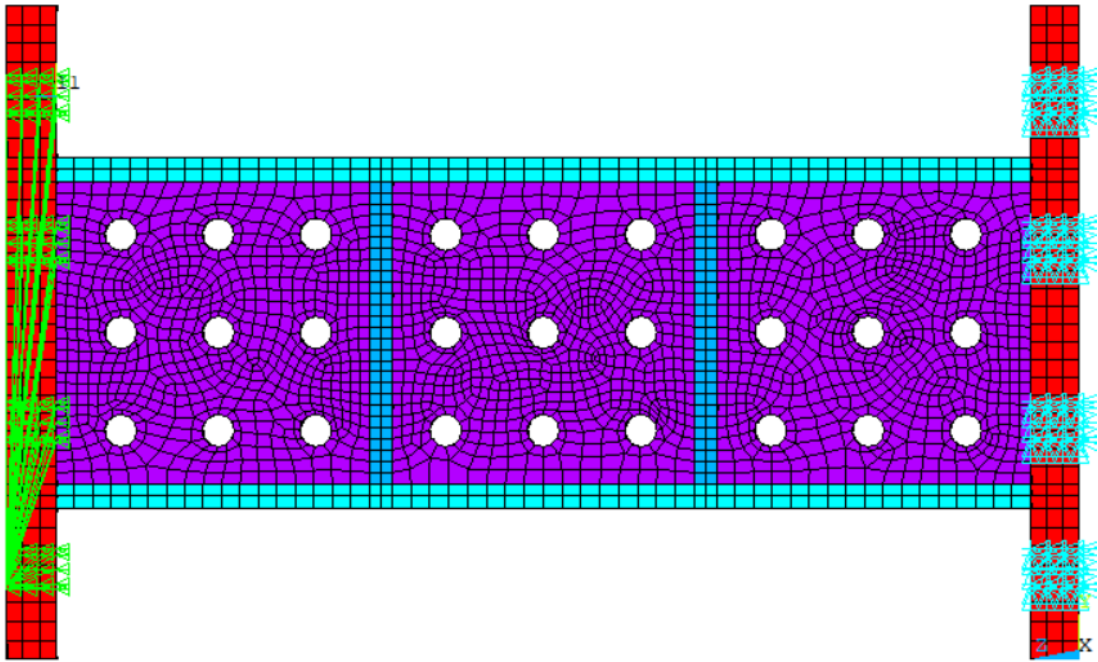


Figure 4.22: FE model of specimen L-C-1

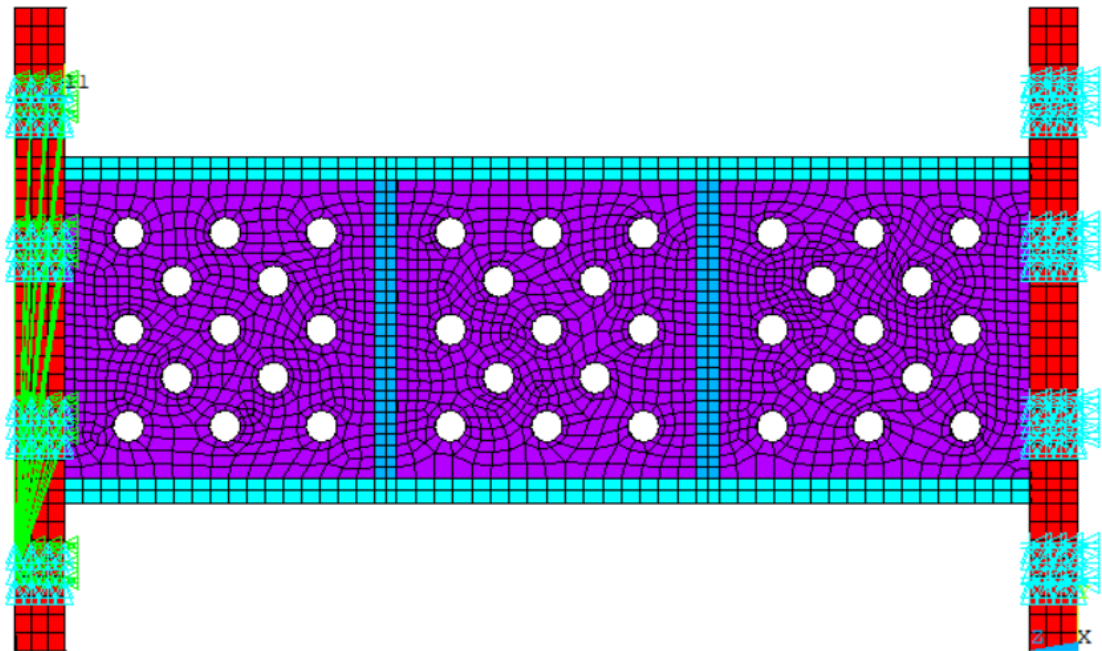


Figure 4.23: FE model of specimen L-C-2

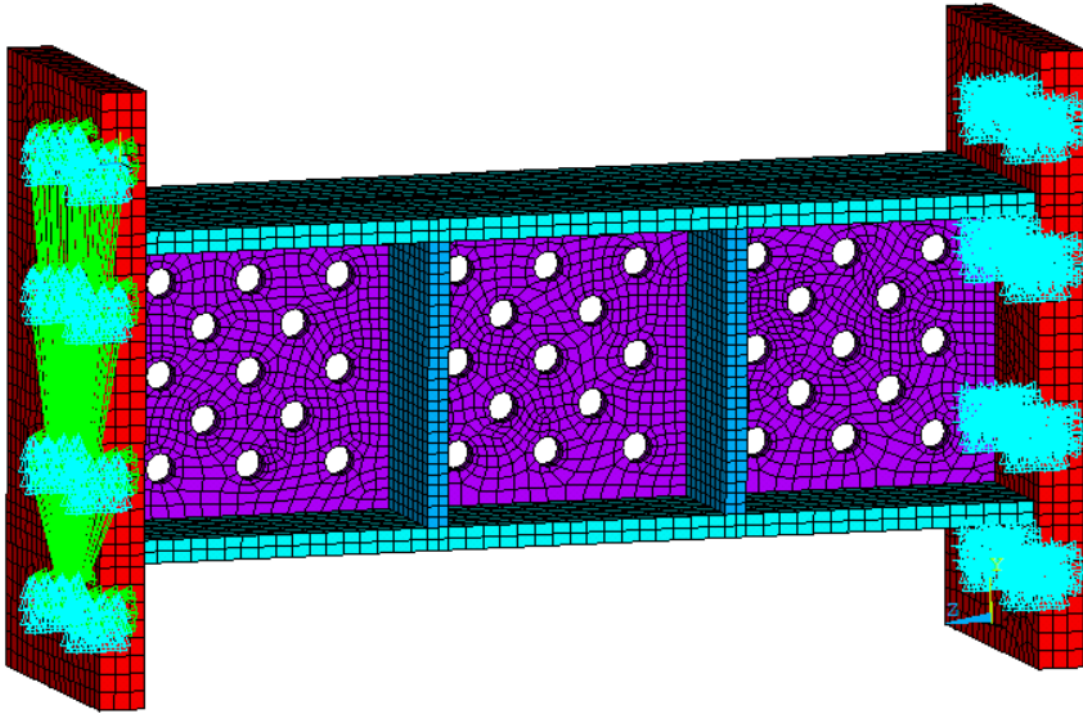


Figure 4.24: Isometric view of the FE model of specimen L-C-2

4.4.1 FE Modeling Parameters and Loading History

The material parameters for modeling were taken directly from the study of Tong et al. (2018). The elastic parameters and plastic strain hardening constants (Chaboche model and Voce law) used for FE modeling are shown in Table 4-6.

The loading history used in the experiment (Figure 4.25) is the same as that prescribed by the AISC code (AISC 341-16). The same loading was applied for the FE simulation.

Table 4-6: Material parameters for verification of study of Tong et al. (2018)

Elastic Parameters			Kinematic hardening parameters		Isotropic hardening parameters		
E	ν	σ_o	C_1	γ_1	R_o	R_∞	b
(MPa)		(MPa)	(MPa)		(MPa)	(MPa)	
200000	0.3	483	5872.7	31.51	0	21	1.2

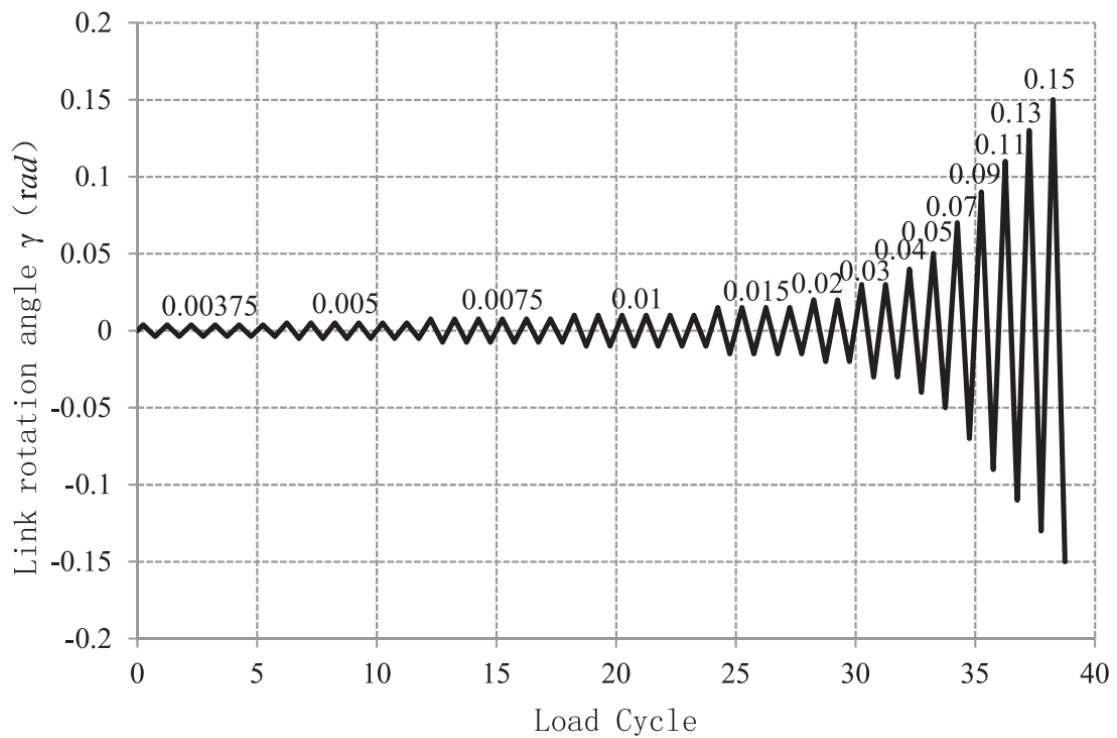


Figure 4.25: Loading history for specimens L-C-1 and L-C-2 (Tong et al. 2018)

4.4.2 Verification Results

Like the previous model verifications, superimposed hysteretic plots of the present FE analysis and the experiment of Tong et al. (2018) are shown in Figure 4.26 and Figure 4.27 where good agreement is found to exist between the experimental and FE results.

Hot spot areas with large accumulated plastic strain values occur in stripes connecting the holes, which can be clearly seen both in the deformed shapes of the experimental specimens (Figure 4.28 and Figure 4.30) and the plastic strain intensity contours of the present numerical models (Figure 4.29 and Figure 4.31). The experimental samples experienced fracture for which the shape of the flanges became more distorted after the fracture induced failure. This additional distortion of the flanges is not noticed in deformed shape of the numerical model as fracture modeling was not done in this study.

From the verified results of shear-rotation hysteretic plots and deformed shapes, the developed finite element models can be said to be validated. So, further studies on perforated shear links can be done with the developed finite element models.

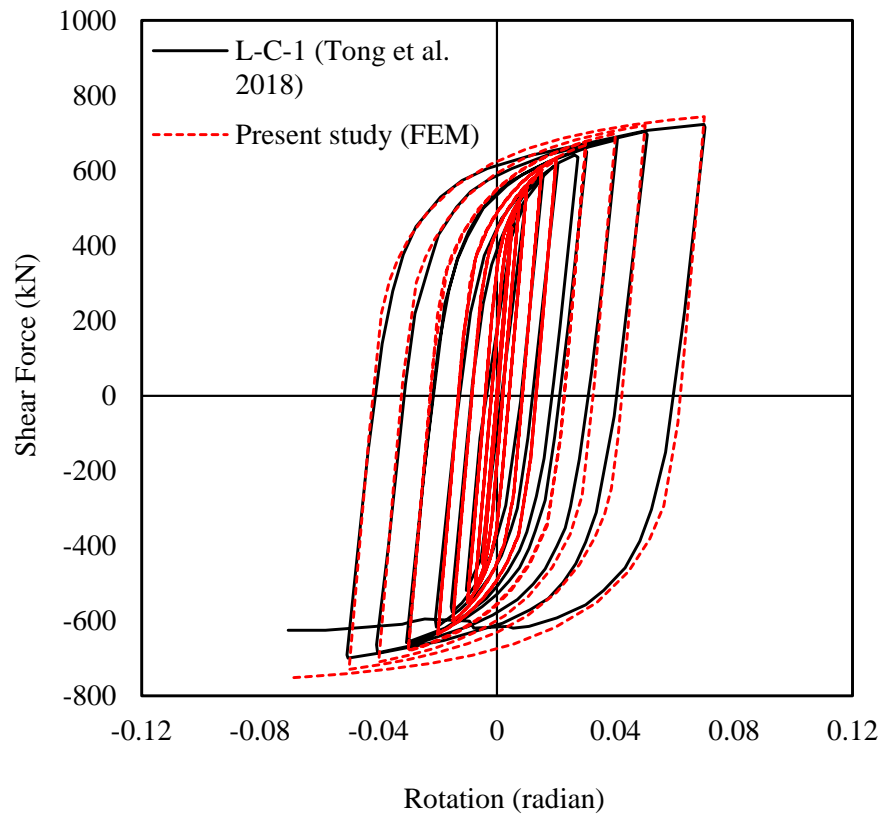


Figure 4.26: Comparison between FEM and experimental results of specimen L-C-1

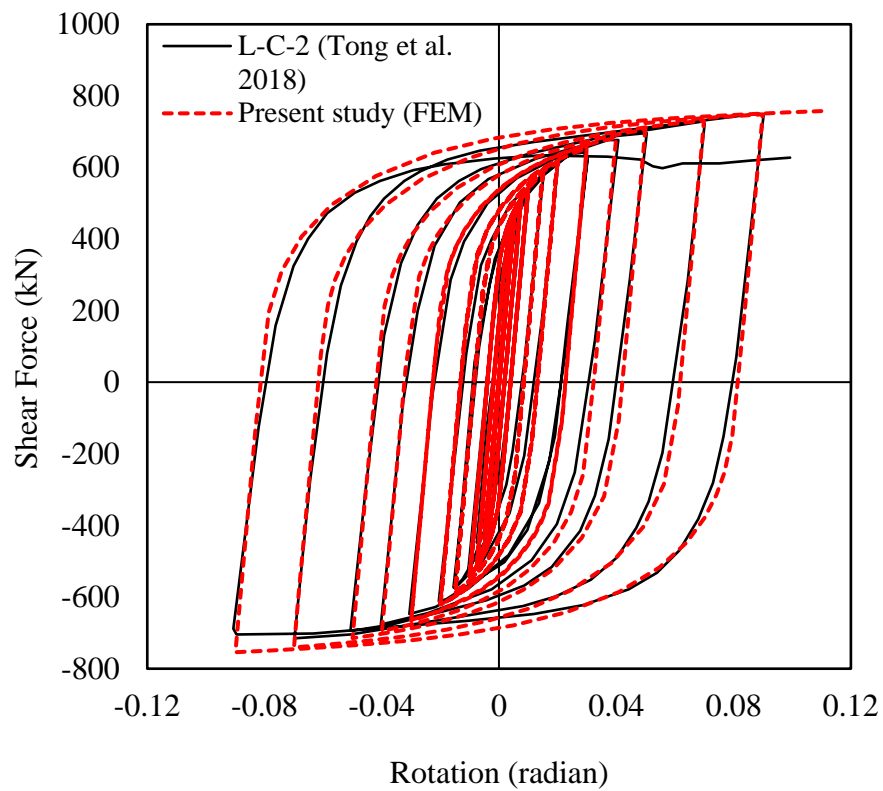


Figure 4.27: Comparison between FEM and experimental results of specimen L-C-2



Figure 4.28: Deformed shape after failure of L-C-1 (at -0.07 radian rotation) (Tong et al. 2018)

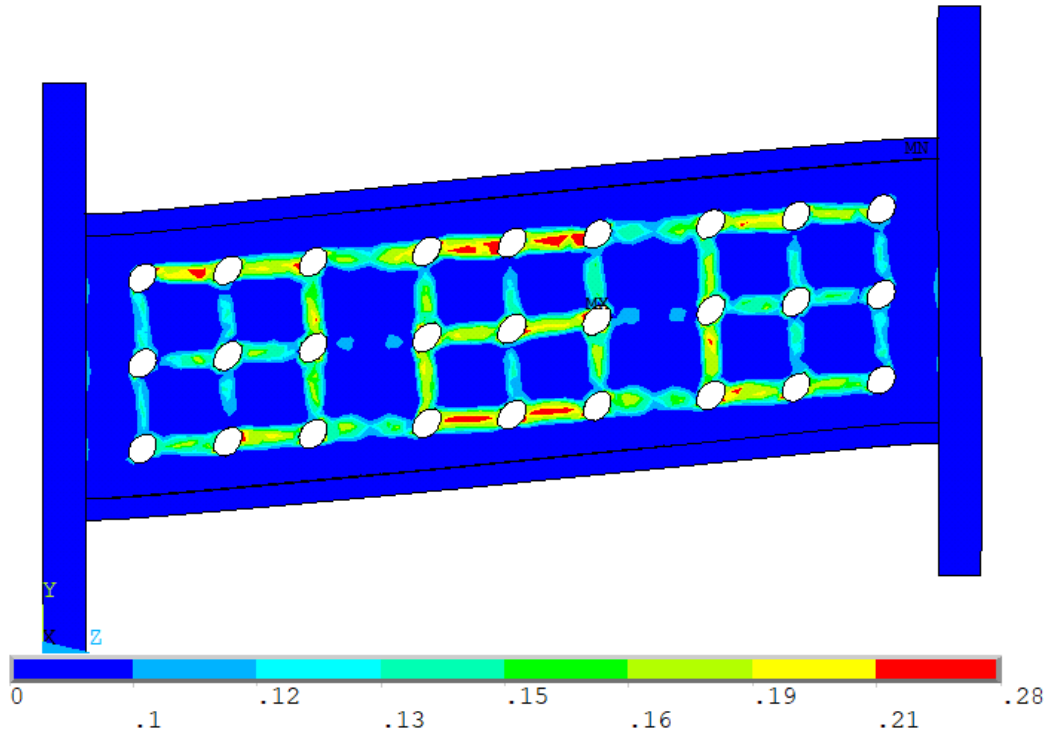


Figure 4.29: Plastic strain intensity and deformed shape of L-C-1 (Present study by FEM)



Figure 4.30: Deformed shape after failure of L-C-2 (at 0.11 radian rotation) (Tong et al. 2018)

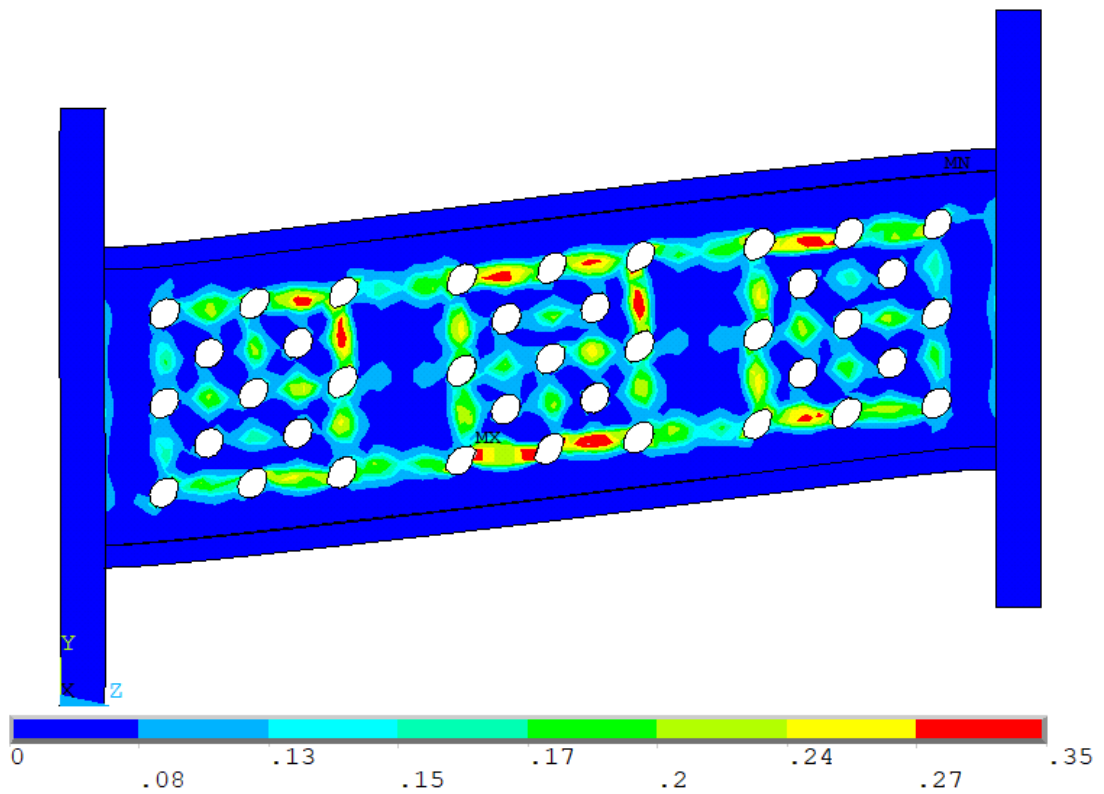


Figure 4.31: Plastic strain intensity and deformed shape of L-C-2 (Present study by FEM)

4.5 SIMULATION OF CYCLIC LOADING BEHAVIOR OF SHEAR LINKS CONSTRUCTED OF ASTM A992 STEEL

Okazaki and Engelhardt (2006) investigated links made of ASTM A992 steel with link length varying from short shear yielding link to long flexural links. A modified flange slenderness limit was proposed based on the test results. Different loading protocols were used for cyclic testing of links and it was found that the loading protocol has a significant effect on the performance of links.

The test setup of Okazaki and Engelhardt (2006) is shown in Figure 4.32. A total of thirty-seven different link specimens were tested in this setup of which the specimens 4A and 4A-RLP were numerically modeled in the present study. The isometric and elevation view of the numerical model is shown in Figure 4.34.

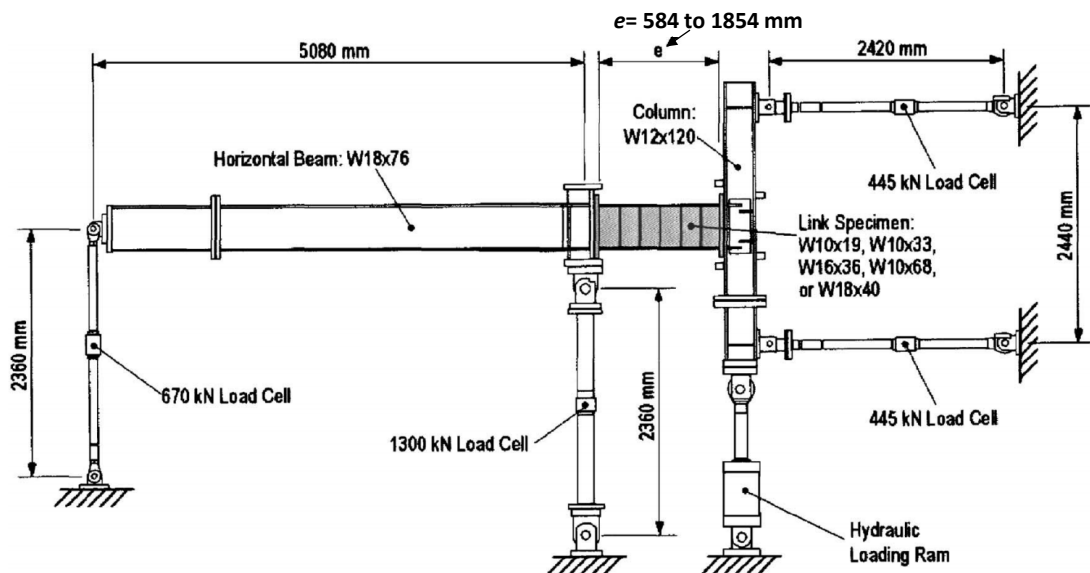


Figure 4.32: Test setup of Okazaki and Engelhardt (2006)

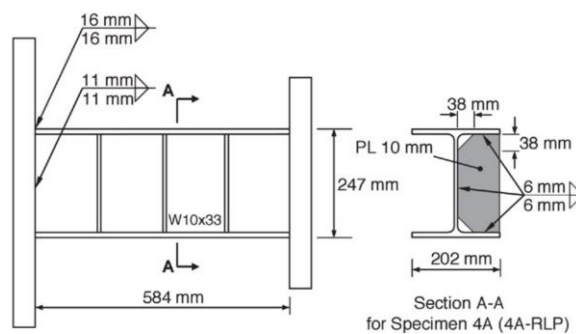
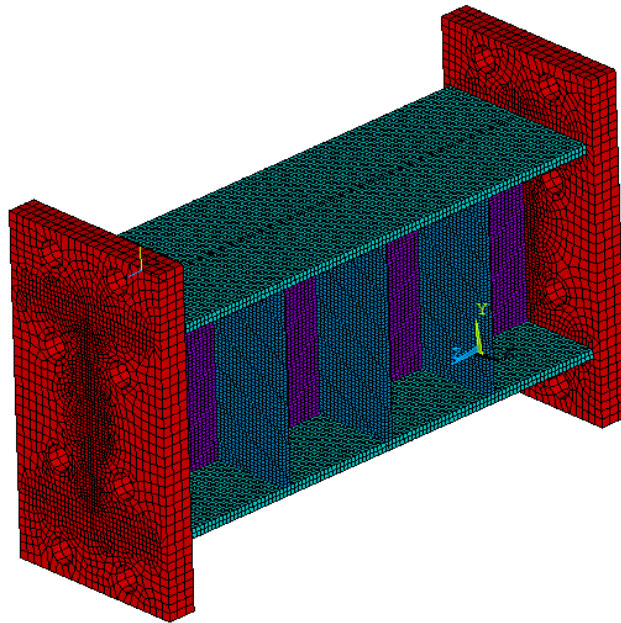


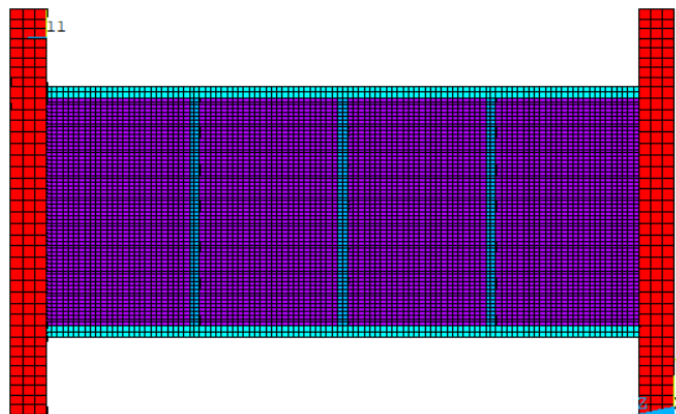
Figure 4.33: Details of the link specimens (Okazaki and Engelhardt, 2006)

Table 4-7: Parametric details of specimen 4A and 4A-RLP (Okazaki and Engelhardt, 2006)

Specimen	d (mm)	b_f (mm)	t_f (mm)	t_w (mm)	Stiffener spacing (mm)	Stiffener thickness t_{st} (mm)	Length ratio (eV_p/M_p)	Loading Protocol
4A	247	202	11	7.37	146	10	1.04	Old
4A-RLP	247	202	11	7.37	146	10	1.04	Revised



(a) Isometric view



(a) Elevation view

Figure 4.34: Numerical model of specimen 4A and 4A-RLP

4.5.1 FE Modeling Parameters and Loading History

The yield strength of flanges and webs of the specimens 4A and 4A-RLP are 356 MPa and 382 MPa, respectively. The other material parameters used for FE modeling of these specimens are shown in Table 4-8 where the elastic parameters are taken from the experimental data and calibrated plastic hardening properties were used for simulation of cyclic behavior of the shear links.

The four loading histories used by Okazaki and Engelhardt (2006) were shown in Figure 2.16 of which the old protocol was used for the specimen 4A and the revised one for the specimen 4A-RLP. The revised protocol was later adopted by the AISC code for cyclic testing of shear links (AISC 341-16).

Table 4-8: Material parameters for verification of study of Okazaki and Engelhardt (2006)

Elastic Parameters		Kinematic hardening parameters				Isotropic hardening parameters		
E (MPa)	ν	C_1 (MPa)	γ_1	C_2 (MPa)	γ_2	R_o (MPa)	R_∞ (MPa)	b
206000	0.3	13000	175	1000	20	60	50	1.2

4.5.2 Verification Results

The results of the finite element analysis are compared with the results of the experimental investigation. The hysteretic plots of shear force versus link rotation of the FEM results and the results of Okazaki and Engelhardt (2006) are superimposed and shown in Figure 4.35 and Figure 4.36.

It can be observed that the numerical results by FE modeling matches with the experimental results to a great extent. So, from the viewpoint of hysteretic response adequate agreement between the numerical and experimental results validates the numerical models developed in finite element software.

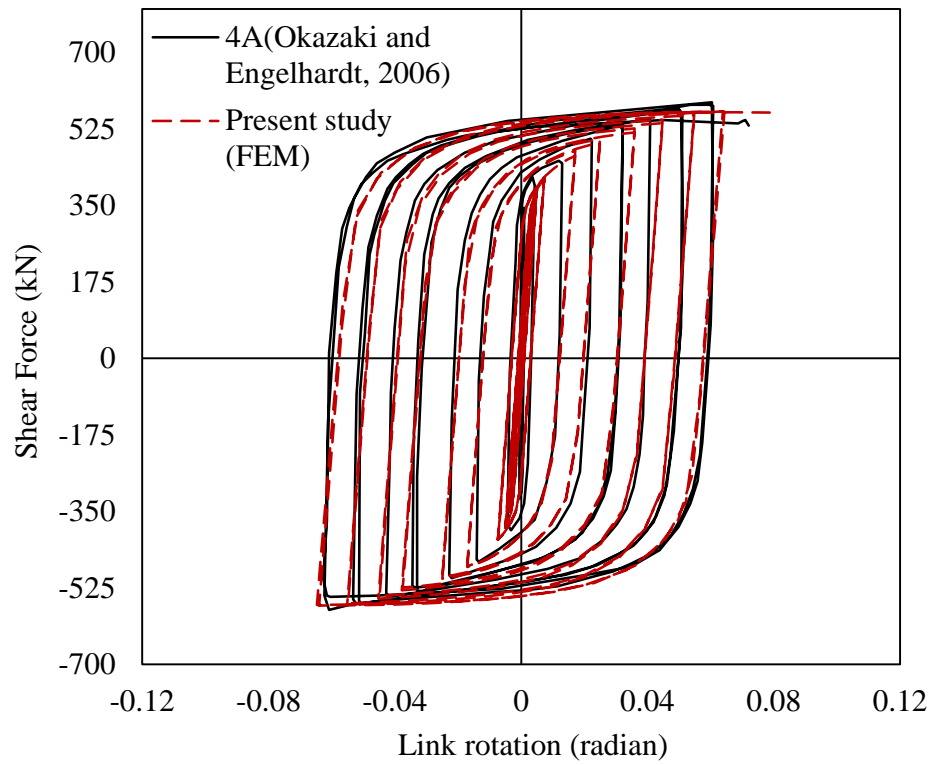


Figure 4.35: Comparison between FEM and experimental results of specimen 4A

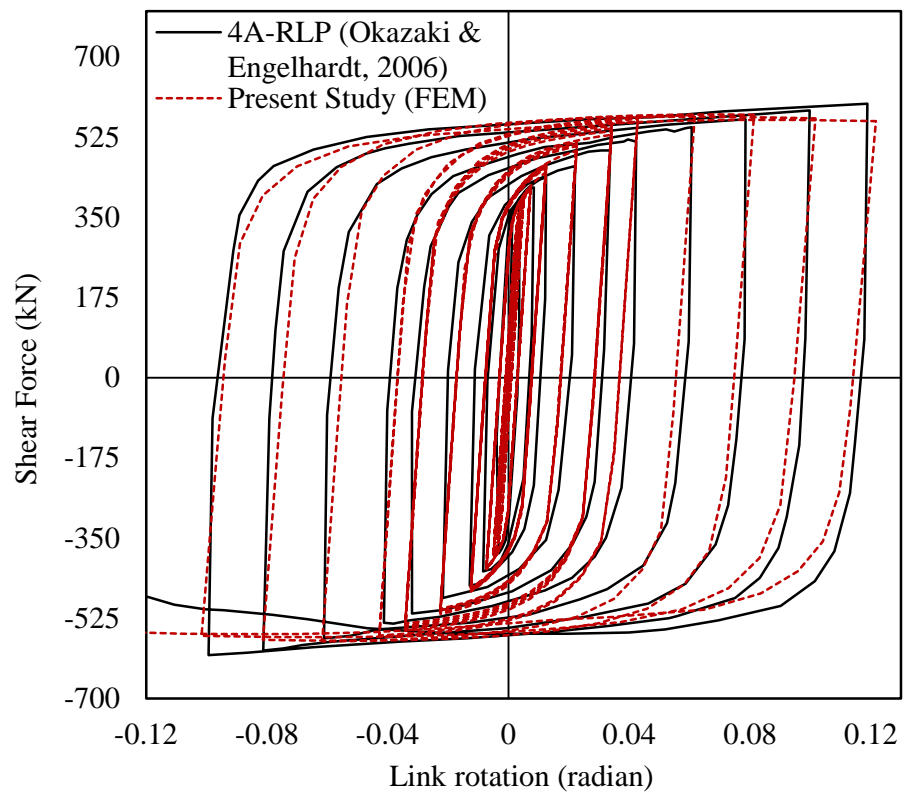


Figure 4.36: Comparison between FEM and experimental results of specimen 4A-RLP

The deformed shapes with von Mises contour and equivalent plastic strain plot (specimen 4A-RLP) of the experimental and the numerical studies are shown in Figure 4.37 to Figure 4.39. Numerical simulation of these specimens has also been conducted by other researchers of which one has been shown here for comparison. From the numerical study of Kalehbasti and Dolatshahi (2018), the damage index plot of specimen 4A-RLP (Figure 4.40) shows a plot similar to the equivalent plastic strain contour plot of the present study (Figure 4.39). All these results indicate that the finite element analysis of the specimens of Okazaki and Engelhardt (2006) yield reliable outcomes bolstering the validation of the developed models.

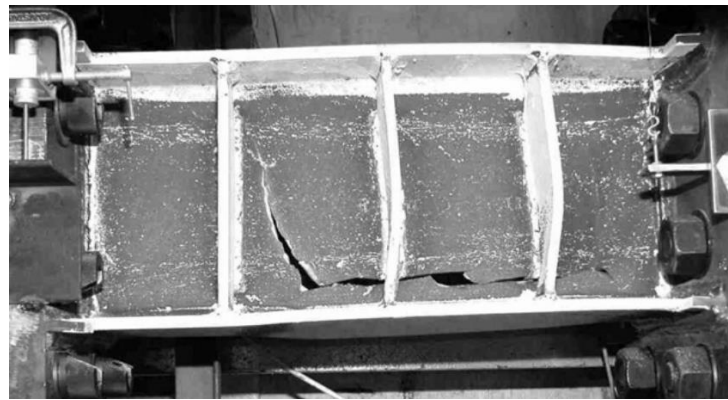


Figure 4.37: Deformed shape showing web fracture of specimen 4A-RLP (Okazaki and Engelhardt, 2006)

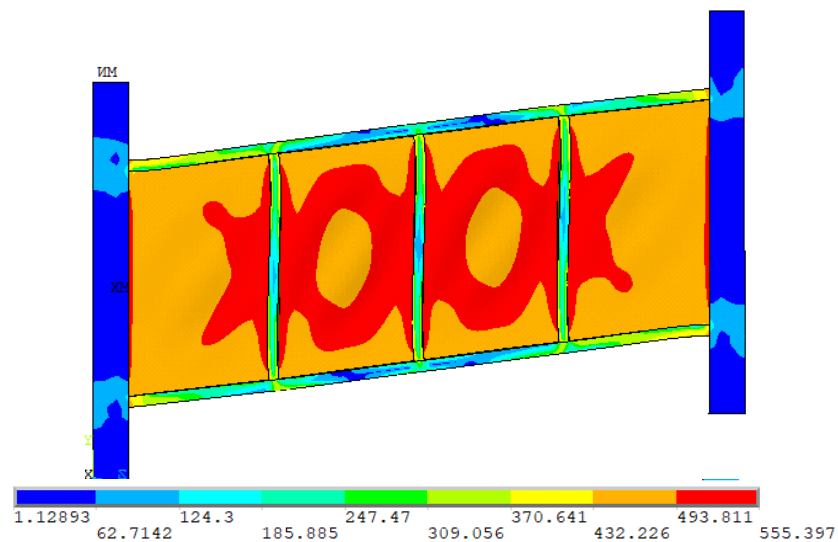


Figure 4.38: von Mises stress (MPa) and deformed shape of specimen 4A-RLP at 0.1-radian rotation (present study by FEM)

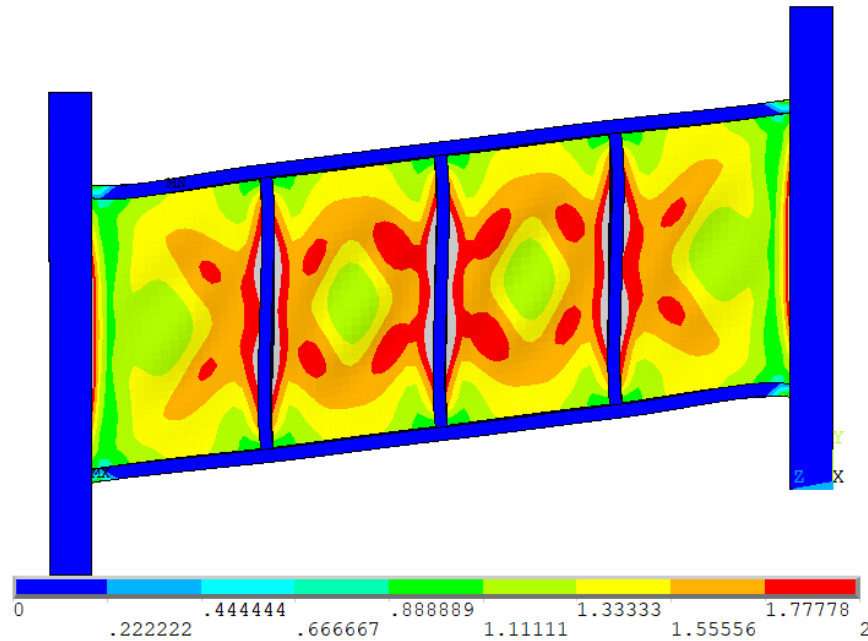


Figure 4.39: Equivalent plastic strain and deformed shape of specimen 4A-RLP (present study by FEM)

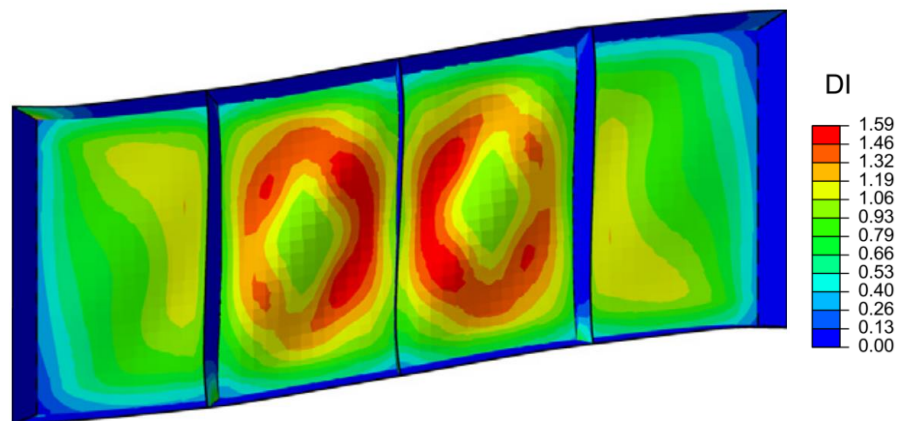


Figure 4.40: Damage index of specimen 4A-RLP from the numerical study of Kalehbasti and Dolatshahi (2018)

4.6 REMARKS

The results of the numerical models developed in this study have been checked against past experimental studies. The summary has been presented in this chapter which shows that good agreement exists between the numerical results and the experimental results. This indicates that these models have been validated and these can be used further for simulation of practical test results.

CHAPTER 5

NUMERICAL STUDY AND DISCUSSIONS

5.1 INTRODUCTION

The finite element models which were developed using finite element software have been verified with reference to the experimental studies performed by Tong et al., (2018), Volynkin et al. (2018), Liu et al., (2017), and Okazaki and Engelhardt (2006) in previous chapters. Satisfactory results have been achieved from the verification and thus it can be concluded that the models are adequate for the numerical simulation of practical test results. The verified numerical models are used for additional parametric studies. For comparative studies, the material parameters were kept same for all the links studied which are shown in Table 5-1. The following topics were studied and presented in this chapter.

- Effect of length ratio on cyclic behavior of links
- Solid I-shaped and box-shaped link
- Perforated links
- Solid I-shaped and Perforated I-shaped link
- Solid I-shaped and Perforated Box-shaped link
- Energy dissipation of various types of links
- Effect of perforation size and density
- Findings and Remarks

Table 5-1: Material parameters for parametric studies

Elastic Parameters: $E = 200000$ MPa, $\nu = 0.3$, $\sigma_o = 360$ MPa										
Plastic Parameters										
Kinematic hardening parameters								Isotropic hardening parameters		
C_1 (MPa)	γ_1	C_2 (MPa)	γ_2	C_3 (MPa)	γ_3	C_4 (MPa)	γ_4	R_o (MPa)	R_∞ (MPa)	b
20000	1000	10000	100	600	20	350	0	4	70	0.2

The schematic view of an I-shaped link showing the geometric details is shown in Figure 2.11 and that of a box-shaped/tubular link is shown in Figure 2.12. The boundary conditions of the links are same as shown in Figure 3.11 and cyclic loading applied was applied at one end plate as shown in Figure 3.12.

5.2 EFFECT OF LENGTH RATIO ON CYCLIC BEHAVIOR OF LINKS

Links having the same shear yield strength may display a different cyclic behavior due to the difference in their length ratios. As an illustration of this phenomenon, simple monotonic behavior of links with the same yield capacity but different length ratios are shown in this section (Figure 5.3). The geometric parameters and the overstrength results of the links studied are shown in Table 5-2. Figure 5.1 shows a one of the four specimens of Table 5-2 and the corresponding deformed shape and von Mises stress contour of that link is shown in Figure 5.2.

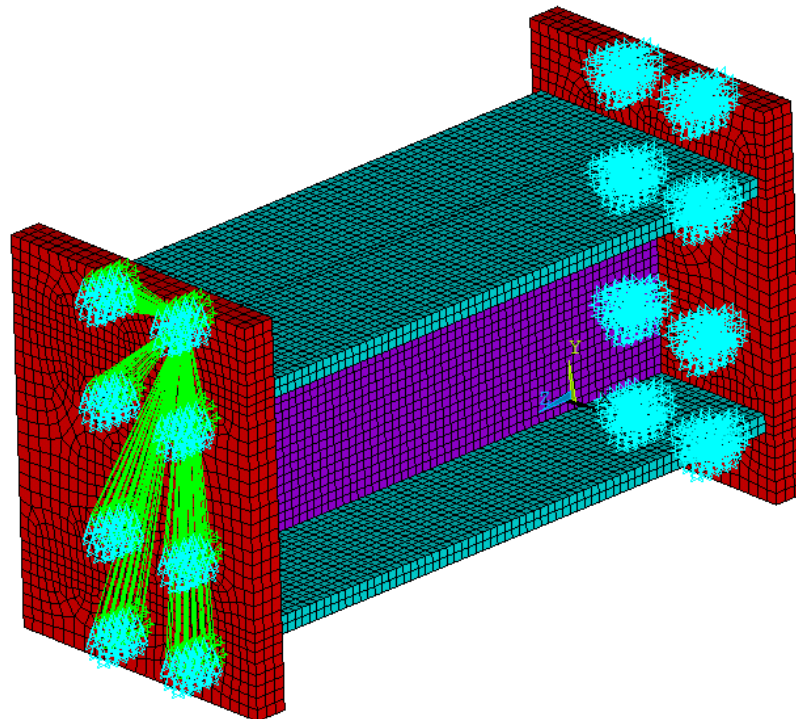


Figure 5.1: Numerical model of link specimen ILR4

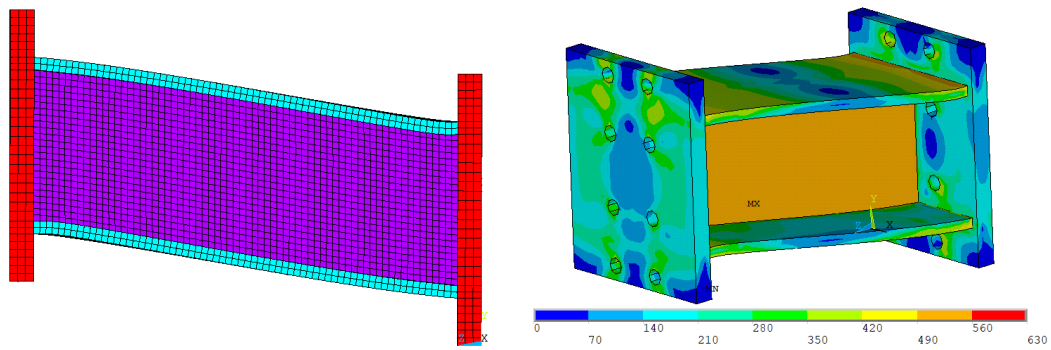


Figure 5.2: Deformed shape and von Mises stress (MPa) of link specimen ILR4

Table 5-2 shows the parameters of the studied links where only by varying the length, the length ratio is changed, and all other parameters are kept same. However, the maximum shear and consequently the overstrength factor (up to 0.15 radian rotation in cyclic loading) is found to differ among different links. Despite having same shear capacities, the overstrength of the link ILR1 with length ratio of 0.55 is 7.5% greater than the overstrength of link ILR4 with length ratio of 1.478. The difference is evident from the shear-rotation hysteretic response shown in Figure 5.4.

As the length of a link decreases it tend to incline more towards a shear dominated behavior and thus ultimate shear induced is greater and when the link length increases it tends to act more like a flexural member and thus the induced shear is a reduced value. Since the overstrength factor is directly proportional to the maximum shear strength it also increases with the decrease in length ratio.

Table 5-2: Parameters of link of same capacity but different length ratio

Link Specimen	e (mm)	Length ratio, (eV_p/M_p)	Common parameters	Overstrength, (V_{max}/V_p)
ILR1	350	0.55	$h=190$ mm	1.589
ILR2	414	0.65	$t_w = 11$ mm	1.541
ILR3	478	0.75	$b_f = 250$ mm	1.506
ILR4	541	0.85	$t_f = 16$ mm	1.478

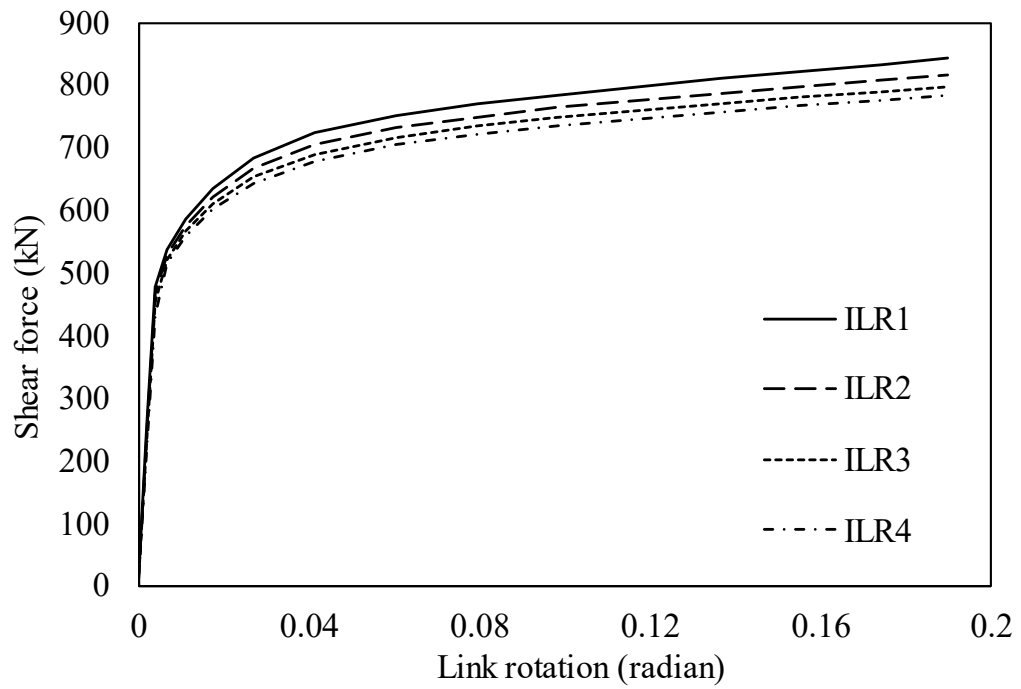


Figure 5.3: Monotonic behavior of links with same shear capacity but different length ratios

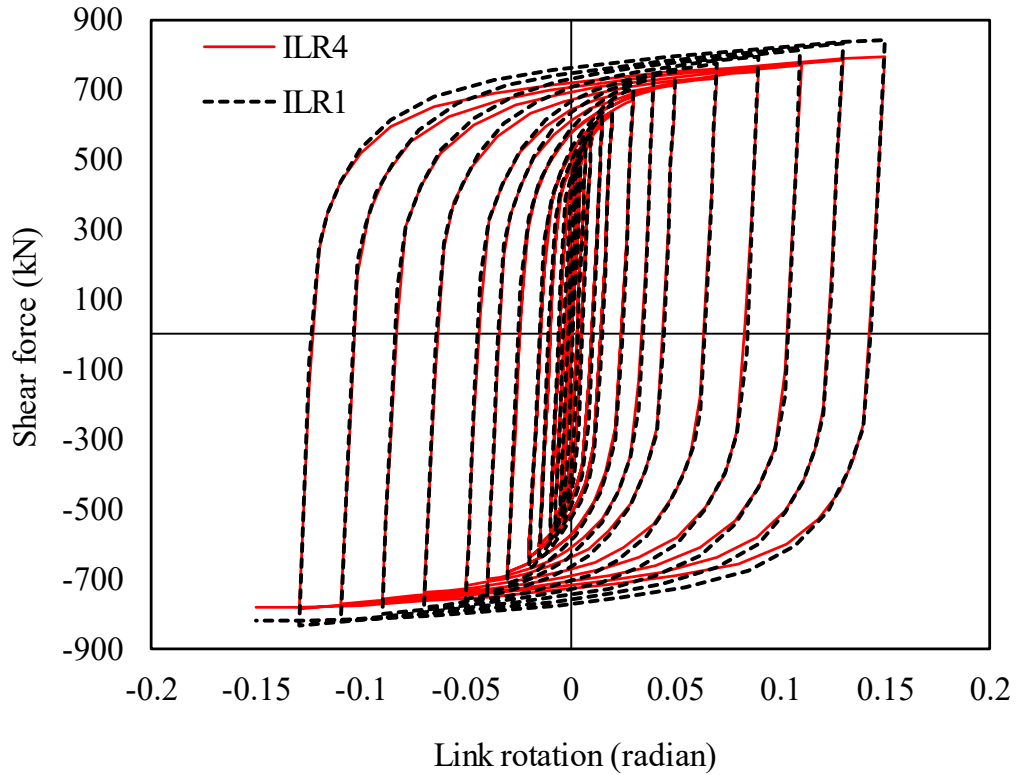


Figure 5.4: Shear-rotation hysteresis of link ILR1 and ILR4

5.3 SOLID I-SHAPED AND SOLID BOX-SHAPED/TUBULAR LINKS

For the parametric studies, a box-shaped link is shown in a schematic view with geometric details and boundary conditions in Figure 5.5

Several equations exist for predicting the shear capacities of box-shaped and I-shaped shear links. The shear capacity provided by the AISC code is represented here by V_{p2} (AISC 341-16). However, one more equation (Liu et al. 2018, Corte et al. 2013) commonly prevalent to predict the shear capacities (termed as V_{p1}) of shear links is used to compare with the AISC equation in this section.

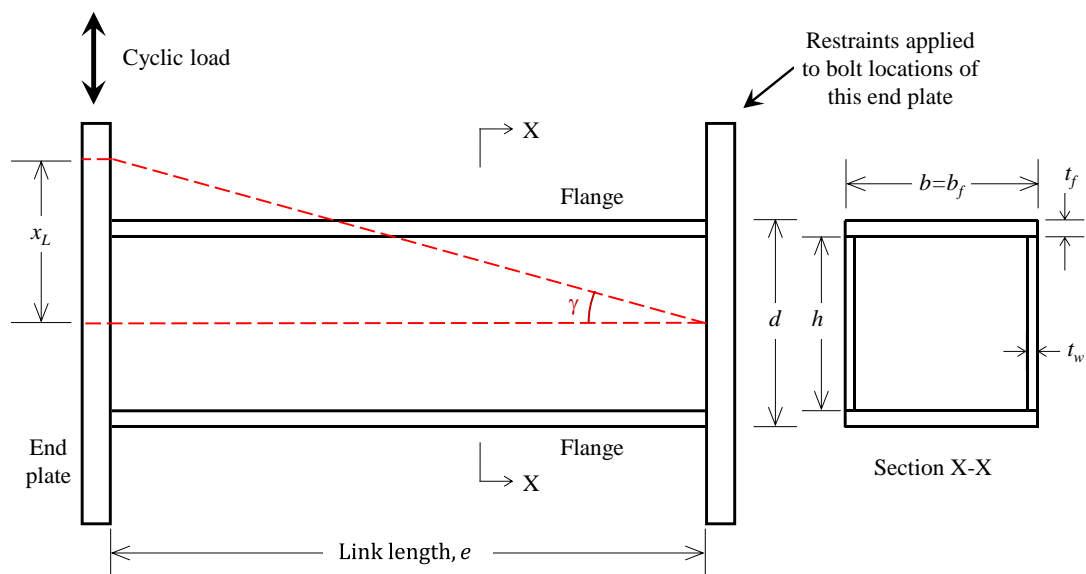


Figure 5.5: Schematic view of box-shaped link with loading and geometric details

Table 5-3: Equations of shear capacities of I-links and box-links

I-link	Box-link	Equation reference
$V_{p1} = 0.6F_y(dt_w)$	$V_{p1} = 0.6F_y \times 2(dt_w)$	(Liu et al. 2018, Corte et al. 2013)
$V_{p2} = 0.6F_y(d - 2t_f)t_w$	$V_{p2} = 0.6F_y \times 2(d - 2t_f)t_w$	(AISC 341-16)

Three pairs of links, each consisting of a box-link and an I-link are chosen in such a way that the two links of the first pair had the same shear capacity based on V_{p2} , and the two of the second and third pair had the same shear capacity based on V_{p1} (Table 5-4). Dimensioning of the links has been done satisfying the compact limits of AISC code. Developed numerical models of a box-link and an I-link are shown in Figure 5.6

and Figure 5.7 respectively. The length ratios of the links of the same pair are kept close to each other to avoid difference in shear overstrength.

The cyclic response of the two links of the first pair is shown in Figure 5.8. The response for the I-link differs from that of the box-link. However, for the second pair, the shear capacities of links of which were based on V_{pl} , identical responses were achieved for both the I-link and the box-link (Figure 5.11). The monotonic responses and cyclic responses of the links are shown in Figure 5.9 to Figure 5.12.

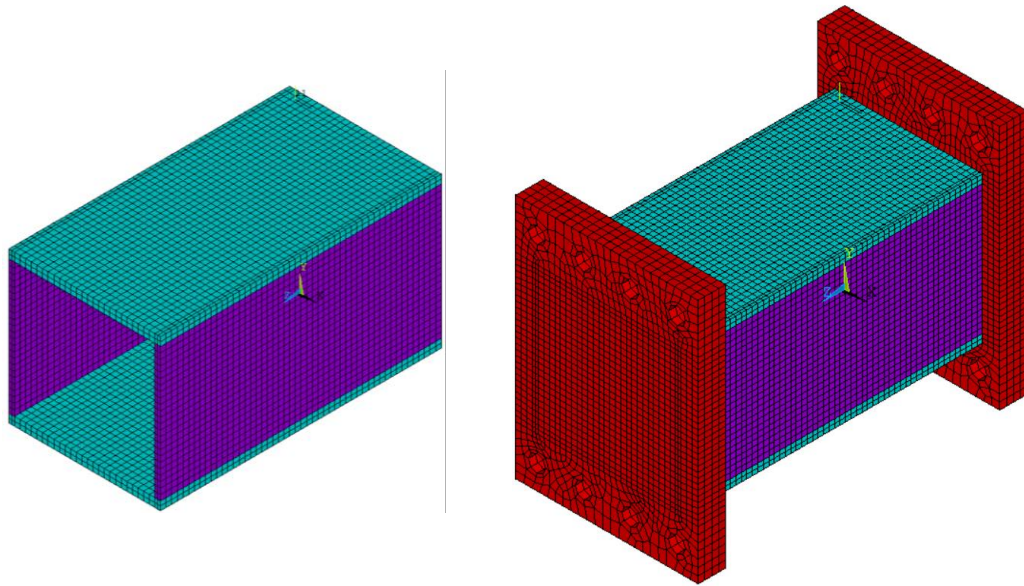


Figure 5.6: Numerical model of solid box-shaped/tubular link: B3

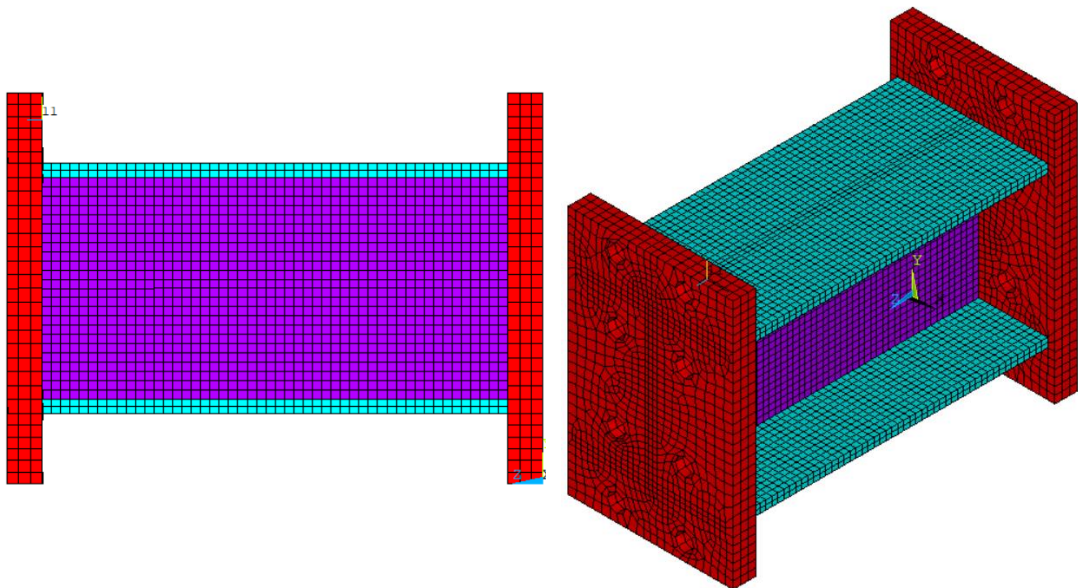


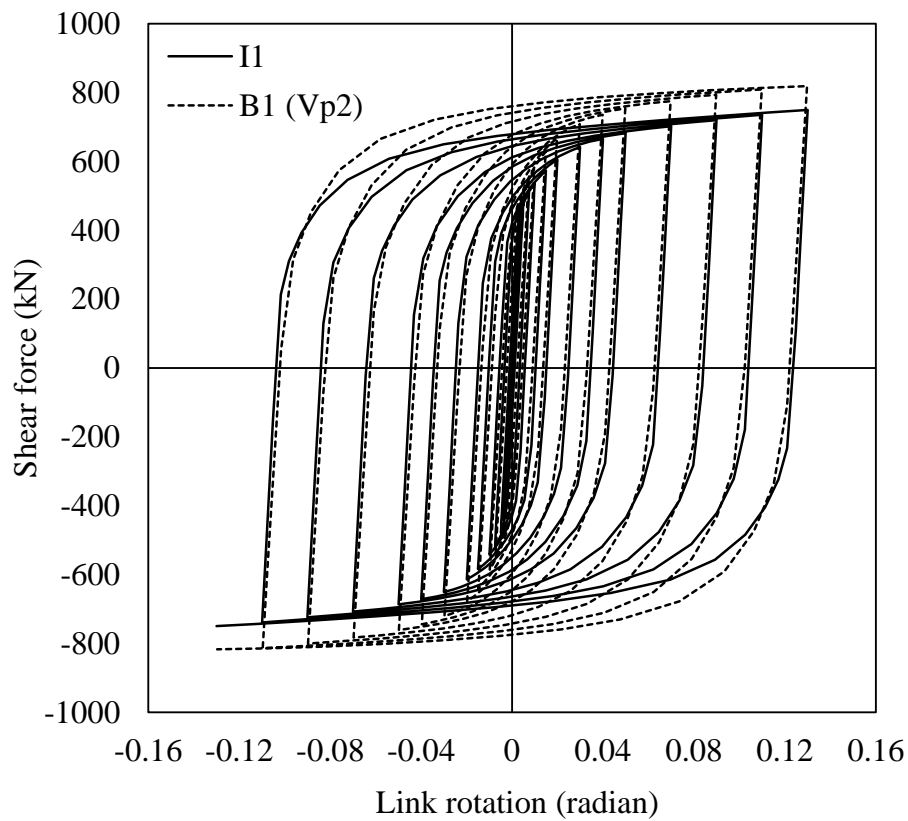
Figure 5.7: Numerical model of solid I-shaped link: I3

Table 5-4: Shear capacities of I-links and box-shaped links

Sample*	e (mm)	Length ratio	h (mm)	t_w (mm)	b_f	t_f (mm)	V_{p2} (kN)	V_{p1} (kN)
I1	400	0.7352	190	10.39	200	16	428.8	501.1
B1 (V_{p2})	300	0.6427	116	8.5	200	16	428.3	546.5
B1	300	0.7402	116	8.05	272	13.6	-	501.1
I2	400	0.9512	190	10.78	200	12	-	501.1
B2	300	0.96	96.1	9	200	16	-	501.1
I3	400	1.3	190	16.2	200	12	-	753
B3	400	1.25	190	8.1	200	12	-	753

*‘I’ indicates I-shaped link and ‘B’ indicates box-shaped link

$F_y = 362$ MPa (for both web and flanges)

Figure 5.8: Responses of links based on V_{p2}

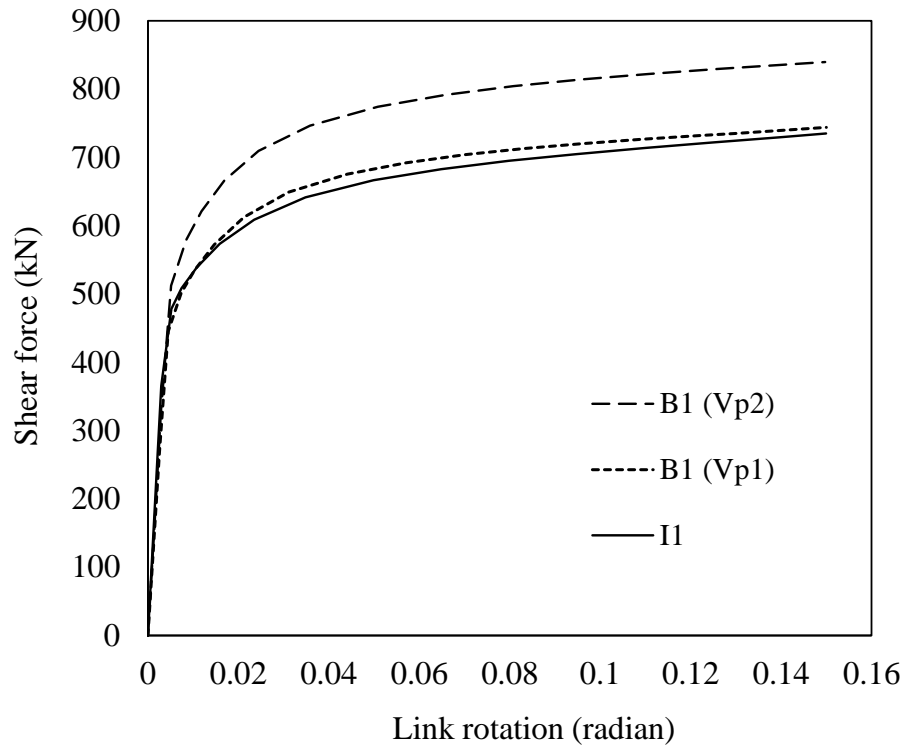


Figure 5.9: Monotonic response of I-link and box-link based on different shear capacity equations

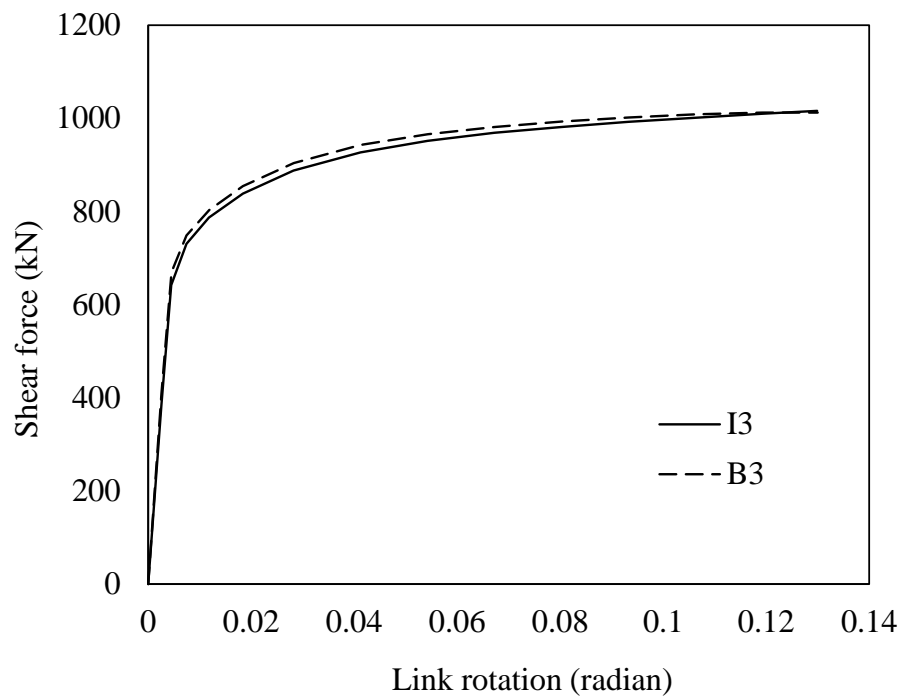


Figure 5.10: Monotonic response of I-link and box-link based on different shear capacity equations

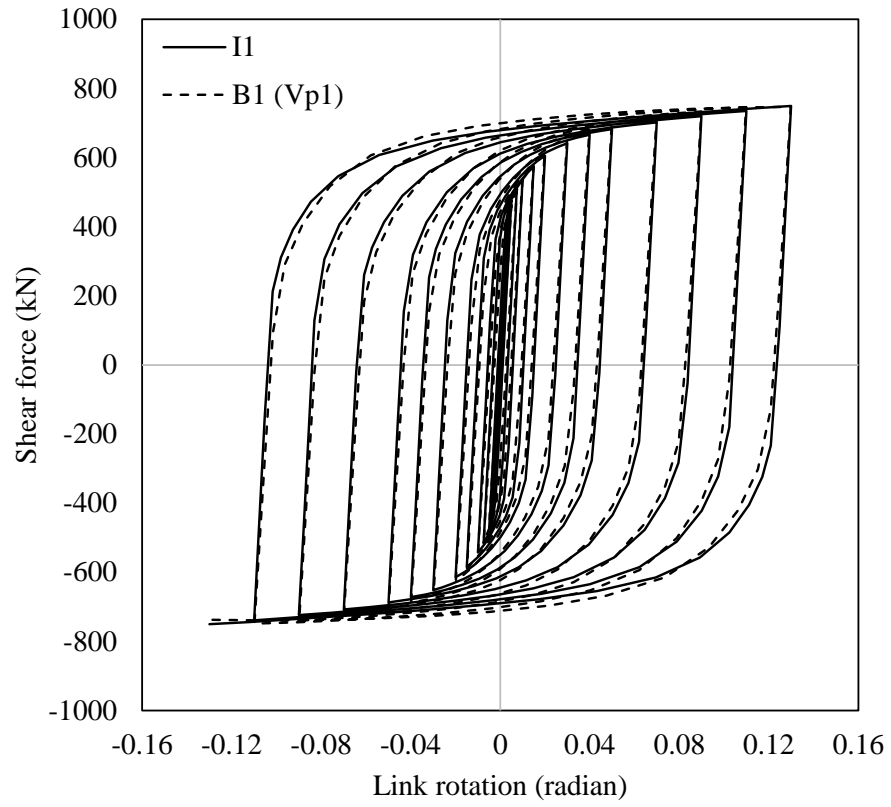


Figure 5.11: Responses of links I1 and B1 based on V_{p1}

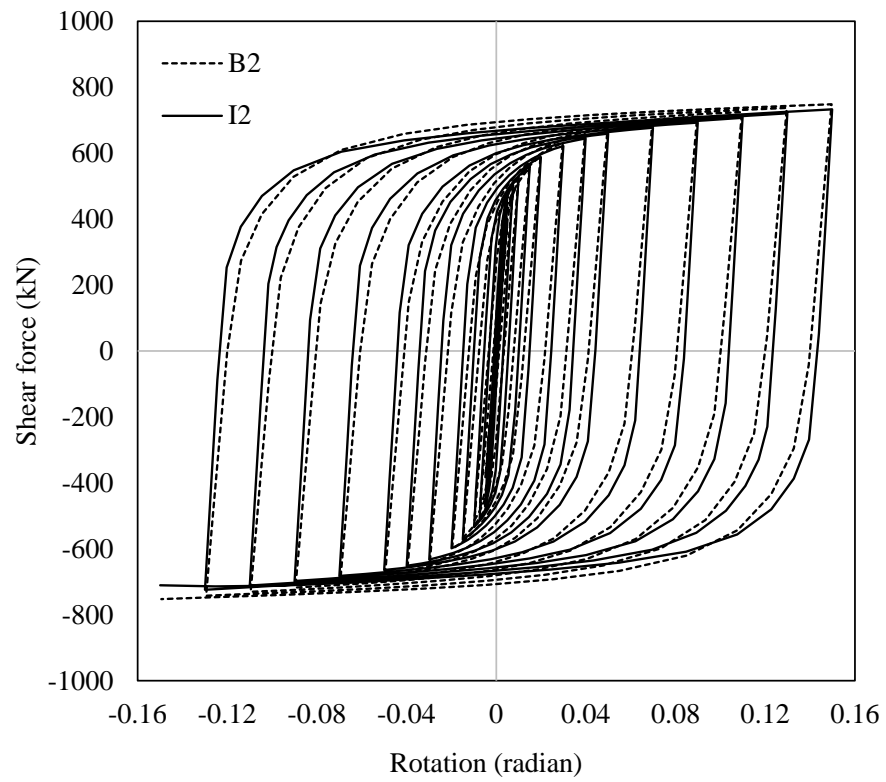


Figure 5.12: Responses of links I2 and B2 based on V_{p1}

The formula of V_{p2} , which is the equation suggested by the AISC code does not take the thickness of the flange into account (AISC 341-16, Equations F3-1, F3-4 and F3-5). Therefore, when this equation is used, the shear capacity is estimated based only on the contribution of the webs. However, flanges also resist shear force both in the elastic and the plastic strain regions (Ji et al. 2016). Hence, neglecting the thickness of the flanges results in an erroneous prediction of shear yield capacity of shear links and the magnitude of this error increases as the flange thickness increases. It may be also be noted that, the equation for shear capacity prediction of an I-shaped beam suggested by the AISC code includes the effect of the full beam depth i.e., depth including both the web and the flanges (AISC 360-16, Equation G2-1). However, as discussed in this section, for shear links, the flanges are excluded in the equation of shear capacity prediction suggested by AISC code. Therefore, an inconsistency is prevailing over prediction of shear yield capacity for the same type of cross section in the AISC code. Since the flanges are also present in the link and contributes a portion of the total shear force induced in the link, the use of equation of V_{p1} is more pragmatic.

5.4 PERFORATED LINKS

Links without stiffeners are less prone to premature failure due to fracture initiated at the stiffener welds (Okazaki and Engelhardt, 2006). So, stiffener-less short links with compact webs can sustain higher rotations. However, due to large web thickness for compactness the ultimate shear assumes an extremely high value which increases the design demand of structural members associated with the link in the same structural system. One solution to this problem can be the reduction of web strength without reducing the web thickness and changing web depth. Making perforations in a specific pattern on the web reduces the web shear strength. Experimental and numerical investigation on perforated links were conducted in the past by Tong et al. (2018) and Kalehbasti and Dolatshahi (2018) respectively. Additional studies on perforated links (Figure 5.13) have been performed in this research to facilitate the design procedures of links with perforations in the web. The current study on perforated link is presented in the following sections.

5.4.1 Pattern of Perforation

Circular perforations on the web can primarily be made in two patterns which are

- Rectangular pattern and
- Diagonal pattern.

The schematic views of perforated links with the two patterns of perforations are shown in Figure 5.13.

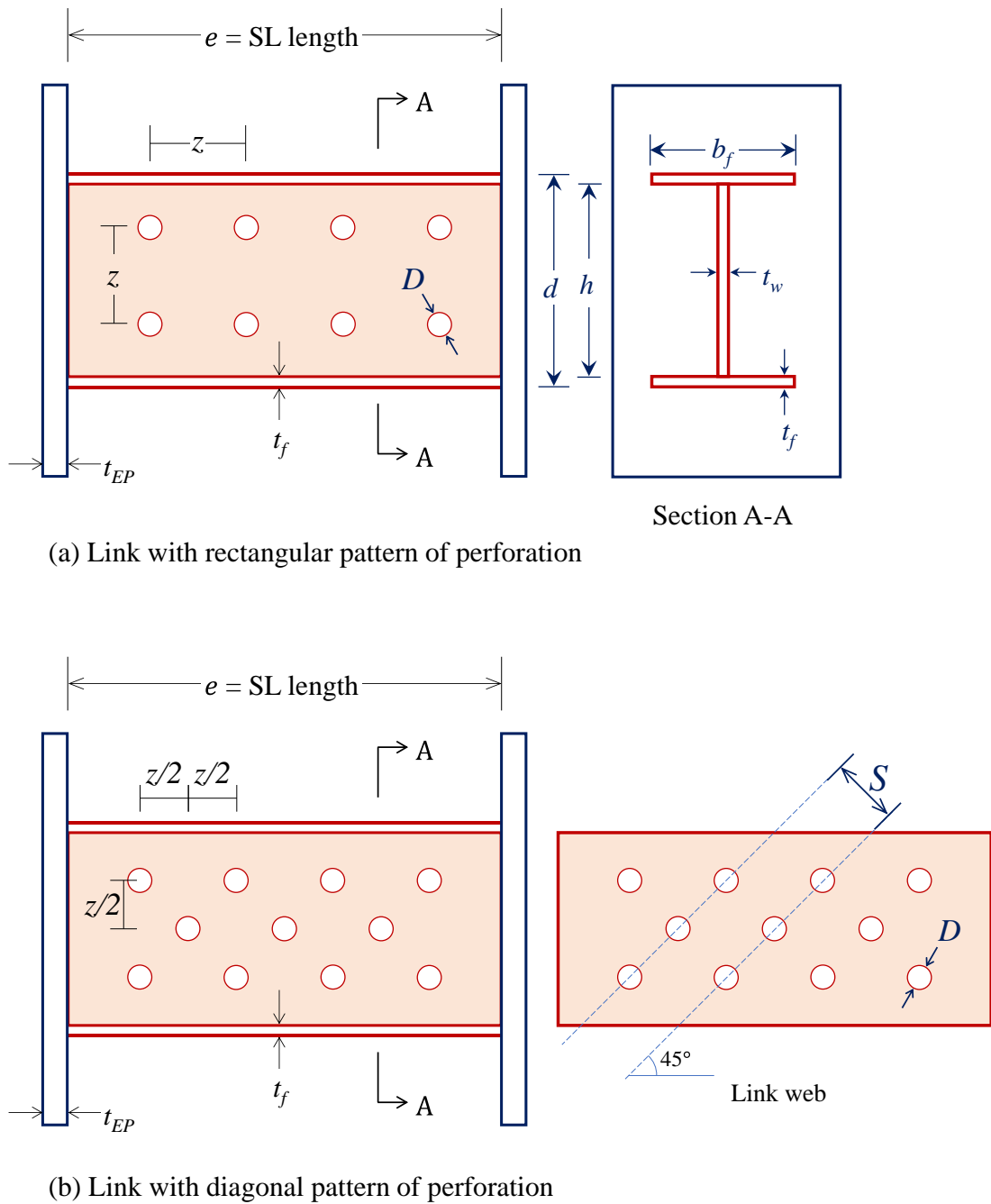


Figure 5.13: Perforated links with rectangular and diagonal pattern of perforations

In the rectangular pattern, holes are formed in rectangular grides where the horizontal and vertical spacing between the perforation holes is denoted by ‘ z ’. Introducing holes in between rectangular grids of a perforated link with rectangular pattern results in a perforated link with diagonal pattern of perforations. The inclination of the diagonal strip is 45° . The diagonal spacing between the perforation strips in shear links with diagonal perforations is termed as ‘ S ’. Since holes are introduced in between the rectangular grids the spacing between holes of subsequent rows or columns is equal to $z/2$ in a link with diagonal pattern of perforation. The value of S is equal to $z/2$ times $\sqrt{2}$.

5.4.2 Performance of Links with Different Perforations Patterns

Two links having the same material and geometric parameters but with different patterns of perforations (rectangular-‘E5rect’ and diagonal-‘E5diag’) were studied. The parametric details of the two links are shown in Table 5-5 where all the parameters are same for the two links except the perforation pattern and the value of z indicates the spacing between the holes measured horizontally or vertically. The diagonal perforations were made maintaining the angle of the perforation strips equal to 45° . The numerical models of these two links are shown in Figure 5.14 and Figure 5.15.

Table 5-5: Parameters of link specimen with diagonal and rectangular pattern of perforations

Link	e (mm)	h (mm)	t_w (mm)	b_f (mm)	t_f (mm)	D (mm)	z (mm)	Perforation pattern
E5-rect	350	190	10	130	13	23.05	64	Rectangular
E5-diag	350	190	10	130	13	23.05	64 ($S=45.25$)	Diagonal

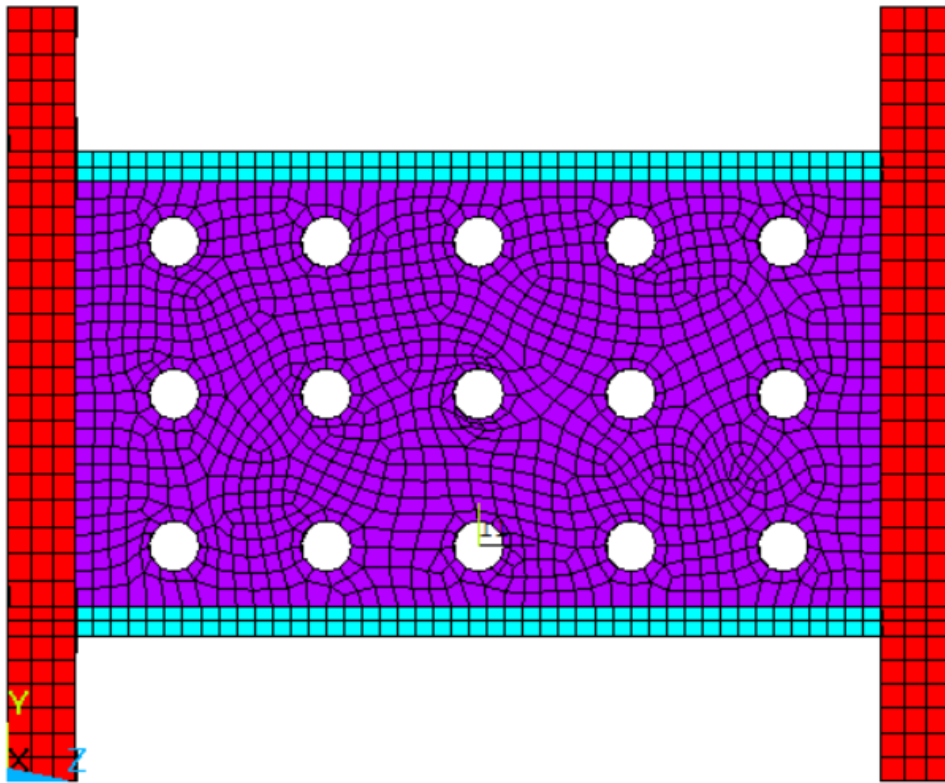


Figure 5.14: Numerical model of E5-rect

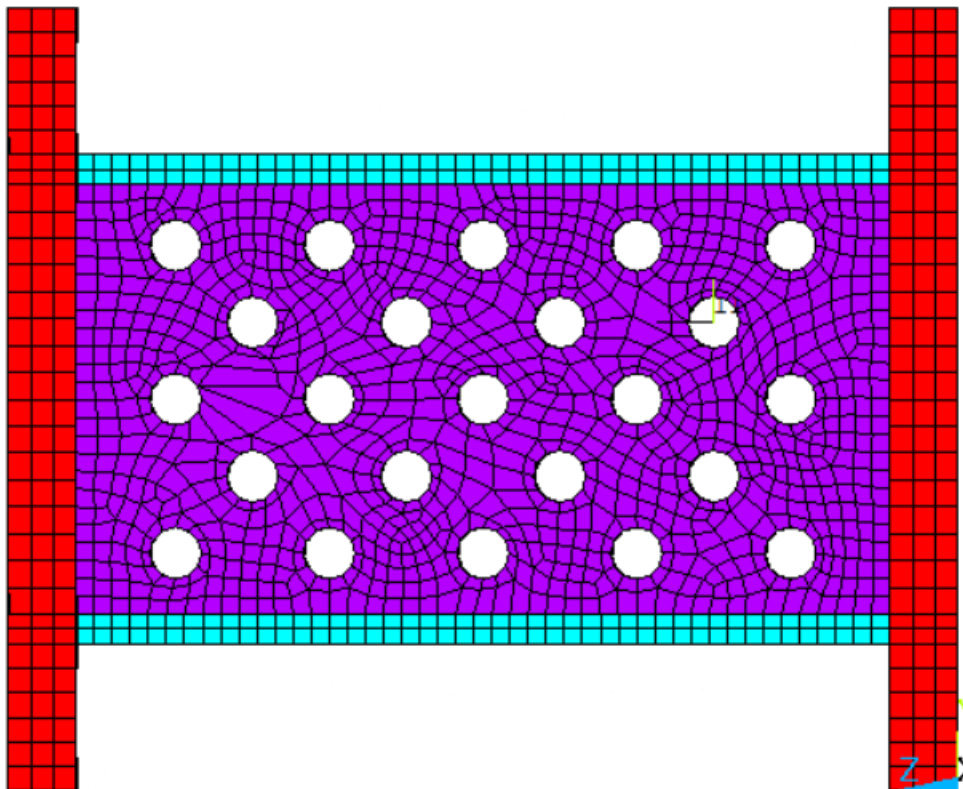


Figure 5.15: Numerical model of E5-diag

The hysteretic responses of those two links are shown in Figure 5.16 as a superimposed plot. It can be noticed that hysteretic responses are the same for both types of perforations in the link. However, contour plots of von Mises stress and plastic strain energy density (Figure 5.17 and Figure 5.18) at the same link rotation of the two links show notable variation. For the rectangular pattern of perforations, the strain energy density is more concentrated on specific locations depicting rectangular grids of concentration. On the other hand, the strain energy density on the link with the diagonal pattern of perforations seems to be more distributed over a larger area of the web. Tong et al., (2018) also found that a link with a diagonal pattern of perforation can sustain higher rotation than what can be achieved by a link with a rectangular pattern of perforation. From the numerical results and experimental evidence of Tong et al., (2018), it can be concluded that a diagonal pattern of perforation in the web is better than the rectangular for links with circular perforations. So, for further study about links with circular perforations, links with the diagonal pattern of perforations were used.

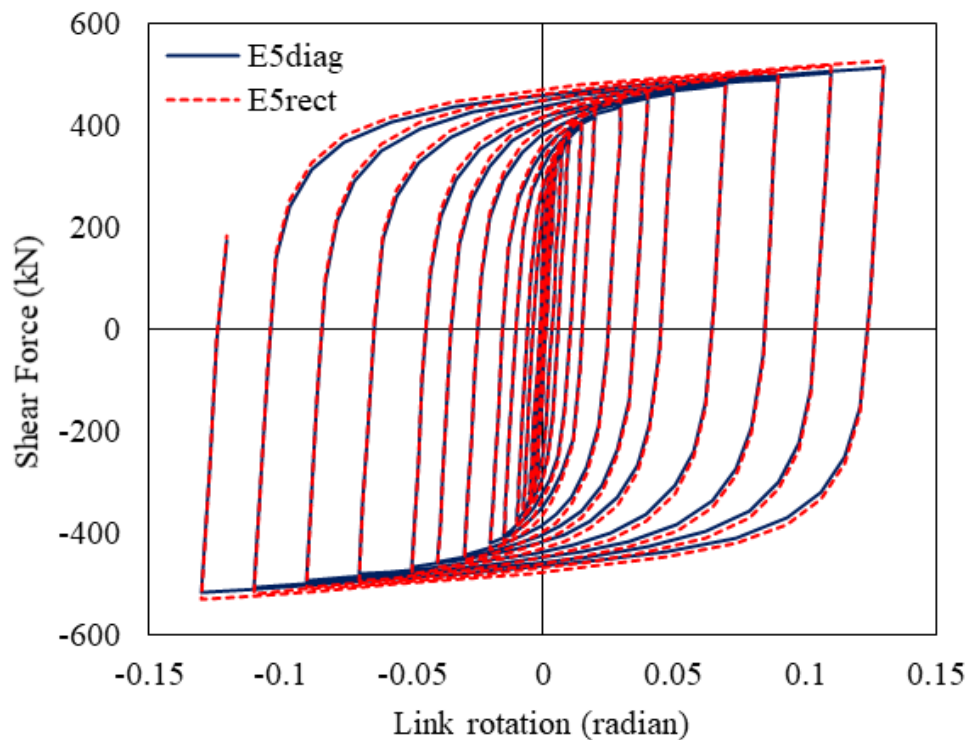


Figure 5.16: Hysteretic response of links with rectangular and diagonal perforations

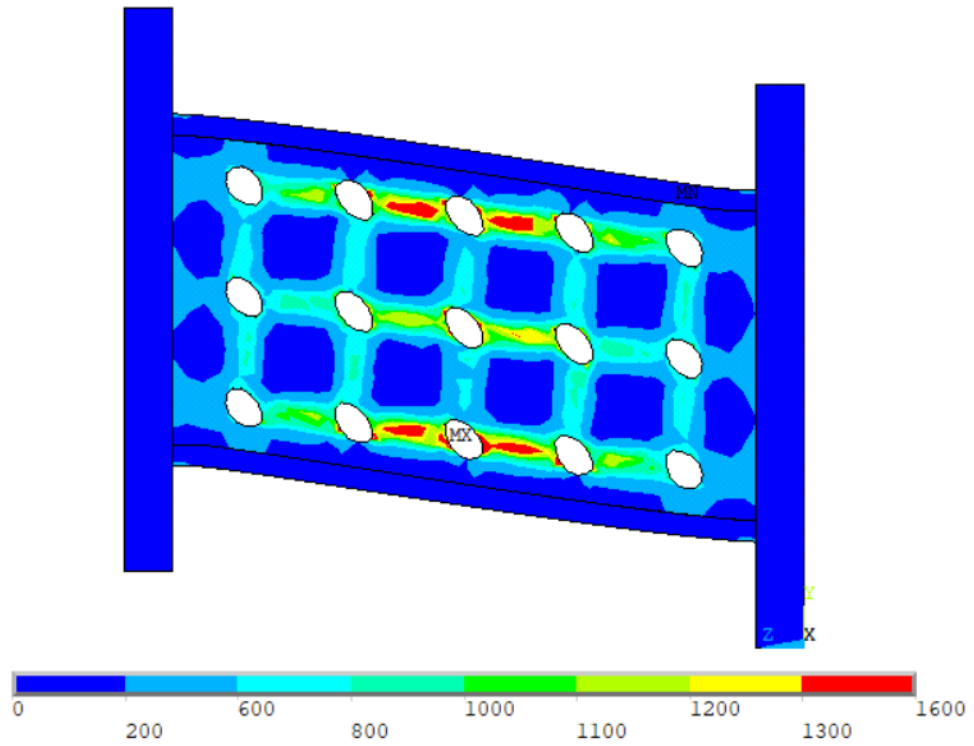


Figure 5.17: Plastic strain energy density of link with rectangular perforations

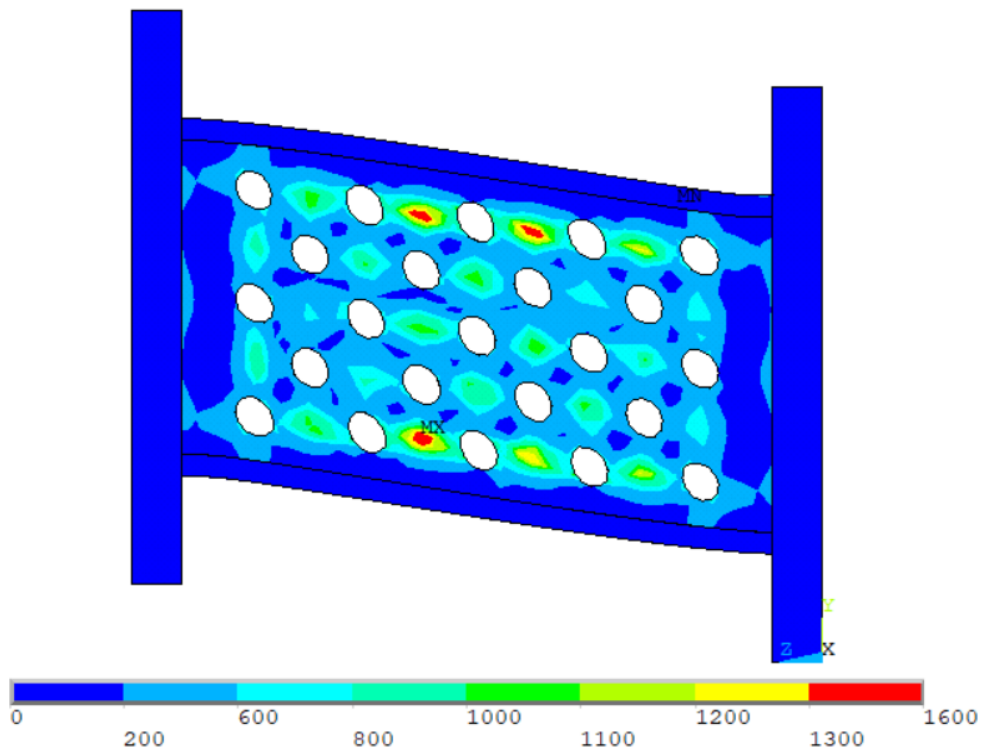
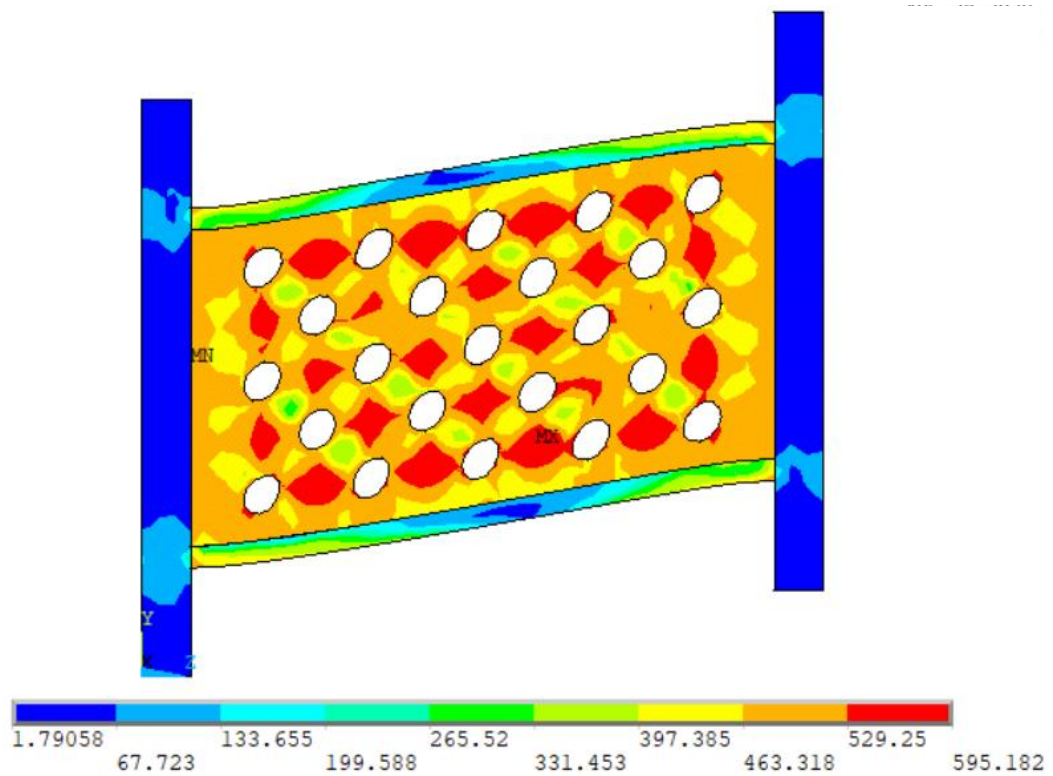
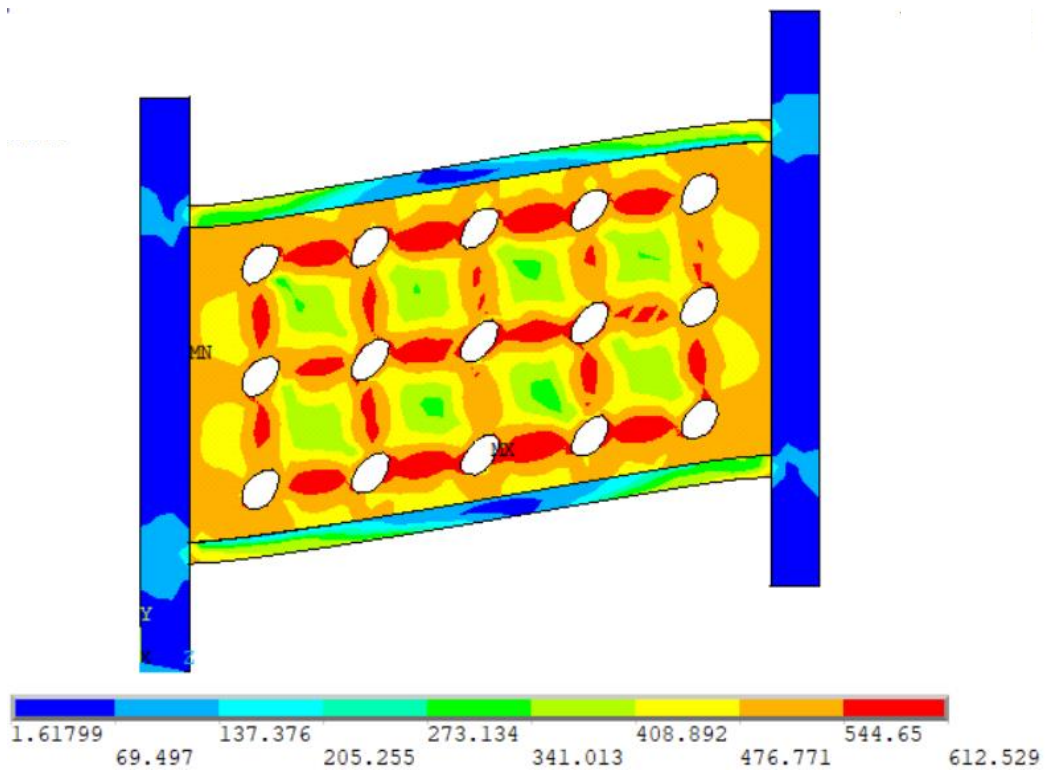


Figure 5.18: Plastic strain energy density of link with diagonal perforations



5.5 SOLID I-SHAPED AND PERFORATED I-SHAPED LINK

Solid I-shaped links are the most common shapes of links used till today. The capacity of perforated links should be able to be predicted for comprehensively using it in design. For this reason, capacity prediction of perforated links has been done comparing the cyclic response of solid I-links. Since diagonal pattern of perforation is expected to perform better, links with diagonal pattern of perforations were studied to investigate design formulas for capacity prediction and establish interchangeability with solid I-links.

The schematic view of perforated shear link with a diagonal pattern of perforations is shown in where D is the perforation diameter and S is the diagonal spacing between perforation holes measured at 45° . The distance of the first perforation holes from the web boundaries is taken to be neither less than D nor greater than $(D+0.7S)$, which is derived from the guidelines of the Specially Perforated Steel Plate Shear wall, (Bruneau, et al., 1998, AISC 341-16).

5.5.1 Equations of Shear Capacity for Interchangeability

The yield strength of Specially Perforated Steel Plate Shear Wall (SPSPSW) is given by Equation 5-1 (Bruneau, et al., 1998). The same equation was used by Kalehbasti and Dolatshahi (2018) to determine the shear yield of shear links in their study. So, in this study, the yield capacity of a perforated link (I_{perf-a}) was first calculated using Equation 5-1 and the response of the link was superimposed with that of a solid I-link of the same yield capacity to check whether the same results are achieved (Figure 5.22). The length and the flange dimensions of the two links were the same for both the link so that the length ratio does not vary between the links. So, only the web thickness which was required for the perforated link to depict equivalent behavior to that of the solid was determined. It was found that some differences between the responses of the two links existed and hence the equation needed modification.

$$\text{Existing equation (SPSPSW): } V_{y(perf)} = \left(1 - 0.70 \times \frac{D}{S}\right) \times V_{y(solid)} \quad 5-1$$

$$V_{y(solid)} = V_{p1} = 0.6F_y \times (dt_w) \quad 5-2$$

Table 5-6: Details of perforated I-link specimens

Link	e (mm)	h (mm)	t_w (mm)	b_f (mm)	t_f (mm)	D (mm)	S (mm)
Iperfa	400	190	15.55	130	13	36	70.71
Iperfb	400	190	14.4	130	13	36	70.71
Iperfc	400	190	15.3	130	13	36	70.71
Iperfd	400	190	14.84	130	13	36	70.71

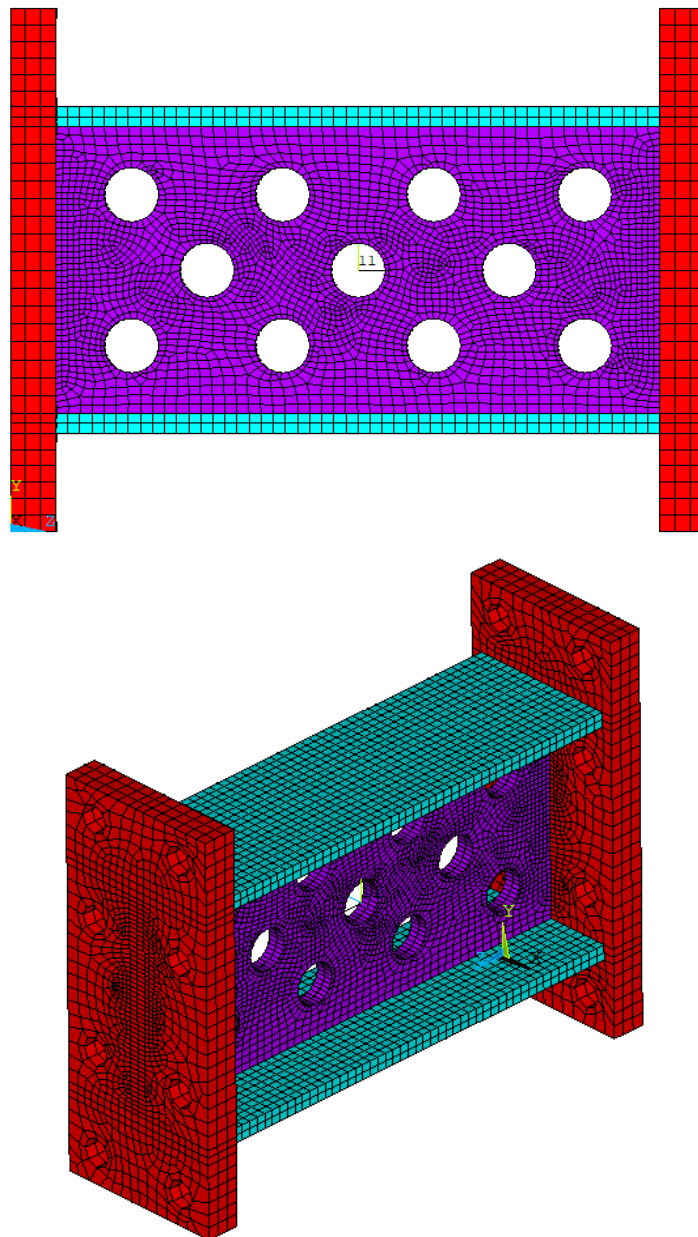


Figure 5.21: Developed model of a perforated I-shaped link: Iperfa

The factor 0.7 was modified to find the refined value of it to get results equivalent to a solid link of the same capacity. Several trials were given to find the refined equation and equivalent behavior. A few of the given trials are listed in Table 5-7. Using a reduction factor of $\left(1 - 0.60 \times \frac{D}{S}\right)$, equivalent web thickness of specimen 'Iperf-b' was calculated to check if equivalent results to that of the solid link can be obtained. The results are shown in Figure 5.23. After noticing discrepancy between the superimposed plots, another trial reduction factor of $\left(1 - 0.68 \times \frac{D}{S}\right)$ was investigated for link specimen 'Iperf-c' and results obtained are shown in Figure 5.24. After several trials in this way, a reduction factor of $\left(1 - 0.64 \times \frac{D}{S}\right)$ (specimen 'Iperf-d') was found to provide results very much similar to that of a solid I-link of the same capacity. Figure 5.25 shows the results of a perforated link with web thickness calculated using reduction factor of $\left(1 - 0.64 \times \frac{D}{S}\right)$ in the shear capacity equation of perforated links.

Table 5-7: Trial reduction factors for different perforated link specimens

Solid link	Perforated links		
Web thickness = 10 mm $V_p = 469.2$ kN	Specimen	Reduction factor in shear capacity equation	Equivalent web thickness for $V_p=469.2$ kN (mm)
	Iperf-a	$\left(1 - 0.70 \times D/S\right)$	15.55
	Iperf-b	$\left(1 - 0.60 \times D/S\right)$	14.4
	Iperf-c	$\left(1 - 0.68 \times D/S\right)$	15.3
	Iperf-d	$\left(1 - 0.64 \times D/S\right)$	14.84

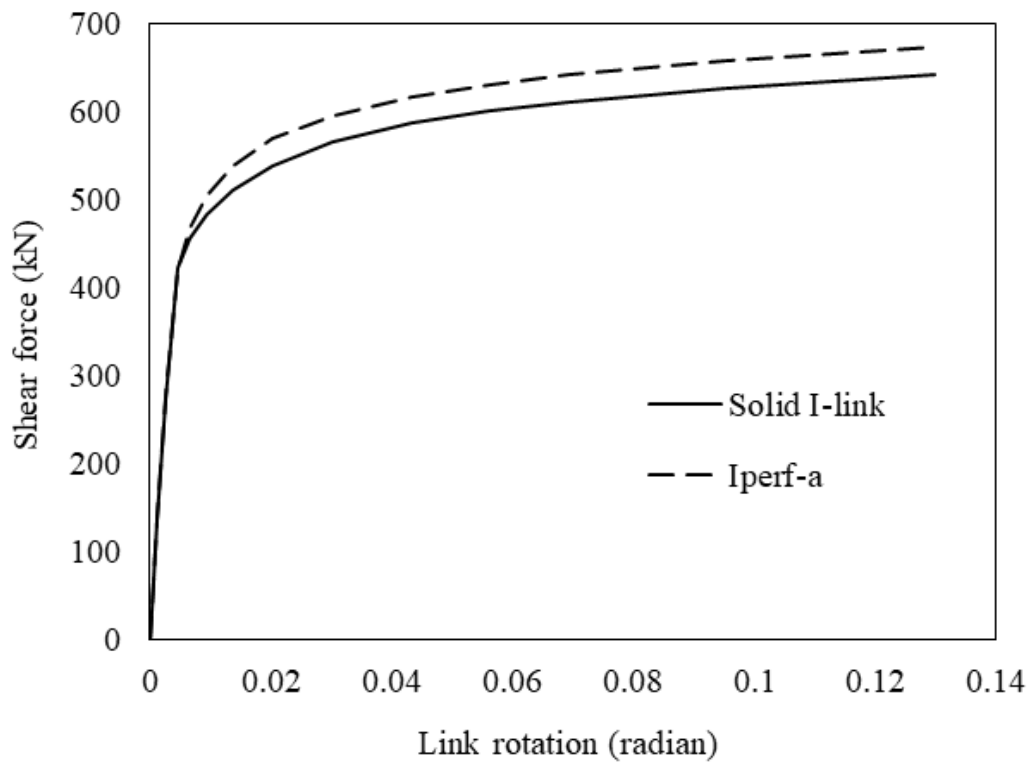


Figure 5.22: Monotonic results of solid and perforated I-link (using Equation 5-1)

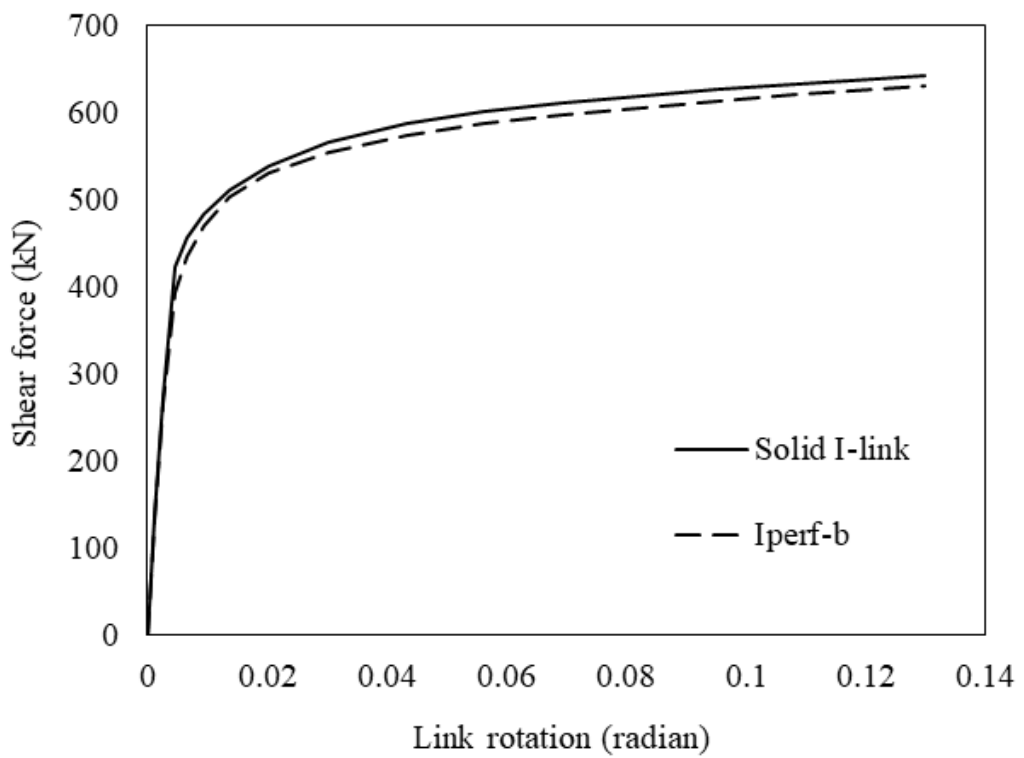


Figure 5.23: Response of perforated link using reduction factor of $\left(1 - 0.60 \times \frac{D}{S}\right)$

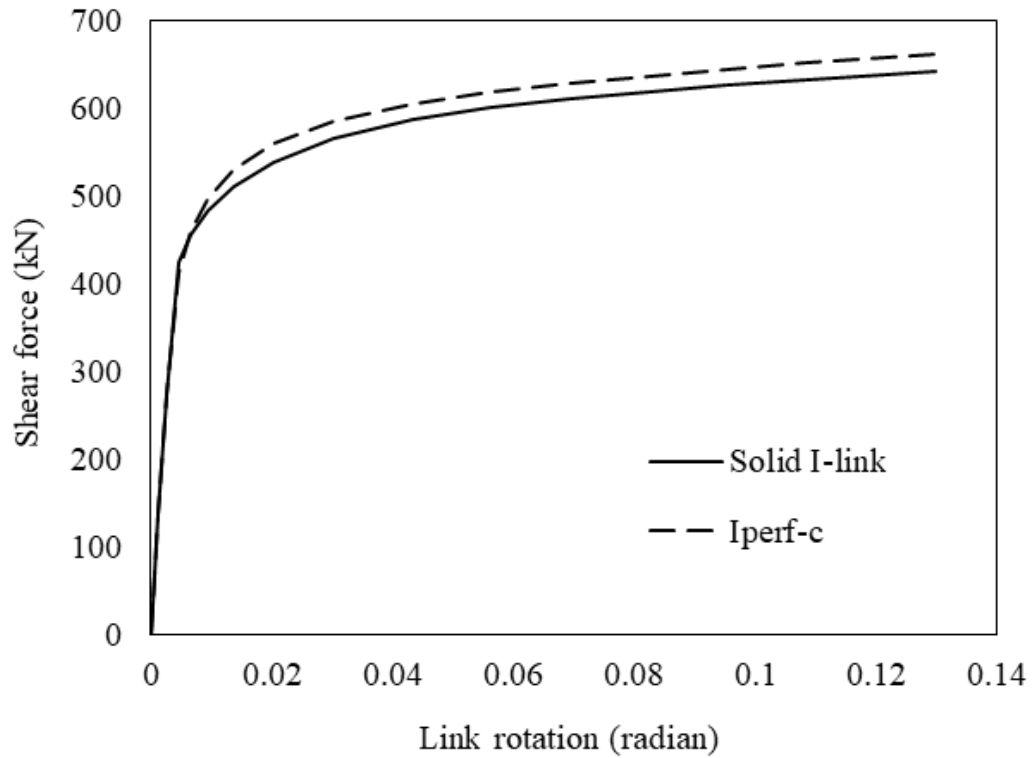


Figure 5.24: Response of perforated link using reduction factor of $\left(1 - 0.68 \times \frac{D}{S}\right)$

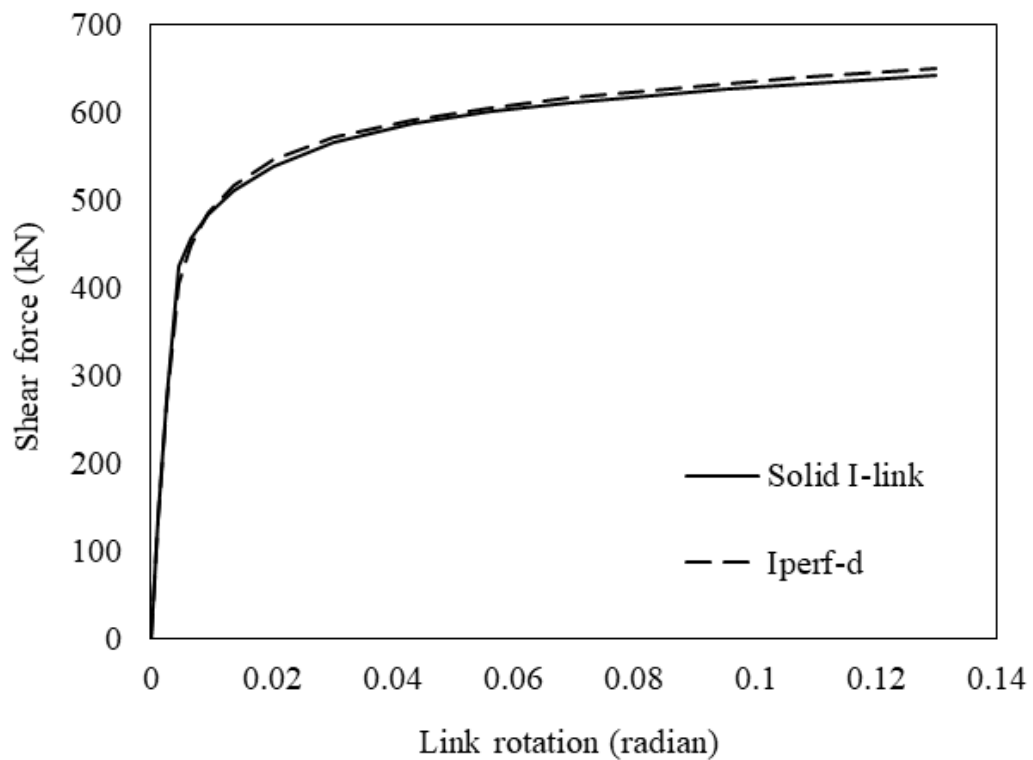


Figure 5.25: Response of perforated link using reduction factor of $\left(1 - 0.64 \times \frac{D}{S}\right)$

So, a new refined equation was proposed for prediction of plastic shear strength of shear links with circular perforations which is shown in Equation 5-3.

Proposed equation for perforated I-shear link:

$$V_{y(perf)} = 0.6F_y \times (dt_w) \left(1 - 0.64 \times \frac{D}{S}\right) \quad 5-3$$

5.5.2 Equivalent Cyclic Response of Perforated I-Link

Eight pairs each consisting of a solid I-link and a perforated I-link are investigated to check the hysteretic response with the proposed equation. The parameters are given in Table 5-8 where solid I-links are labelled as 'I' and perforated I-links are labelled as 'Iperf'.

Table 5-8: Parameters of solid I-links and perforated I-links

Pair	Sample	e (mm)	h (mm)	t_w (mm)	b_f (mm)	t_f (mm)	D (mm)	S (mm)	V_y (kN)
1	I-11	400	190	10	130	13	-	-	469.2
	Iperf-11	400	190	14.84	130	13	36	70.71	469.4
2	I-12	400	190	12.29	250	16.9	-	-	597.4
	Iperf-12	400	190	18.23	250	16.9	36	70.71	597.4
3	I-13	400	190	14.42	200	14	-	-	682.8
	Iperf-13	400	190	21.39	200	14	24.49	48.08	682.8
4	I-14	500	190	12	200	14	-	-	568.2
	Iperf-14	500	190	17.85	200	14	36	70.71	568.2
5	I-15	400	290	11	160	12	-	-	750.2
	Iperf-15	400	290	16.32	160	12	36	70.71	750.2
6	I-16	600	190	11	140	12	-	-	511.3
	Iperf-16	600	190	16.32	140	12	36	70.71	511.3
7	I-17	800	190	10	200	16	-	-	482.2
	Iperf-17	800	190	14.84	200	16	36	70.71	482.2

The superimposed hysteretic plots are shown in Figure 5.26 to Figure 5.32, which indicates that the proposed equation for perforated links can be used to achieve performance equivalent to that of a solid link.

Moreover, it can also be noticed that due to increased thickness web buckling of a perforated link does not take place at the same rotation as that of a solid I-link (at 0.13-radian rotation, Figure 5.26). Hence, web buckling can be delayed and at the same time, ultimate shear strength and overstrength factor can be reduced by using a perforated shear link.

The deformed shapes and von Mises stress contour plots of model I-14 and Iperf-14 are shown in Figure 5.33 and Figure 5.34. The values of von Mises stress at the vicinity of the holes in the perforated links are higher due to the effect of stress concentration at those locations.

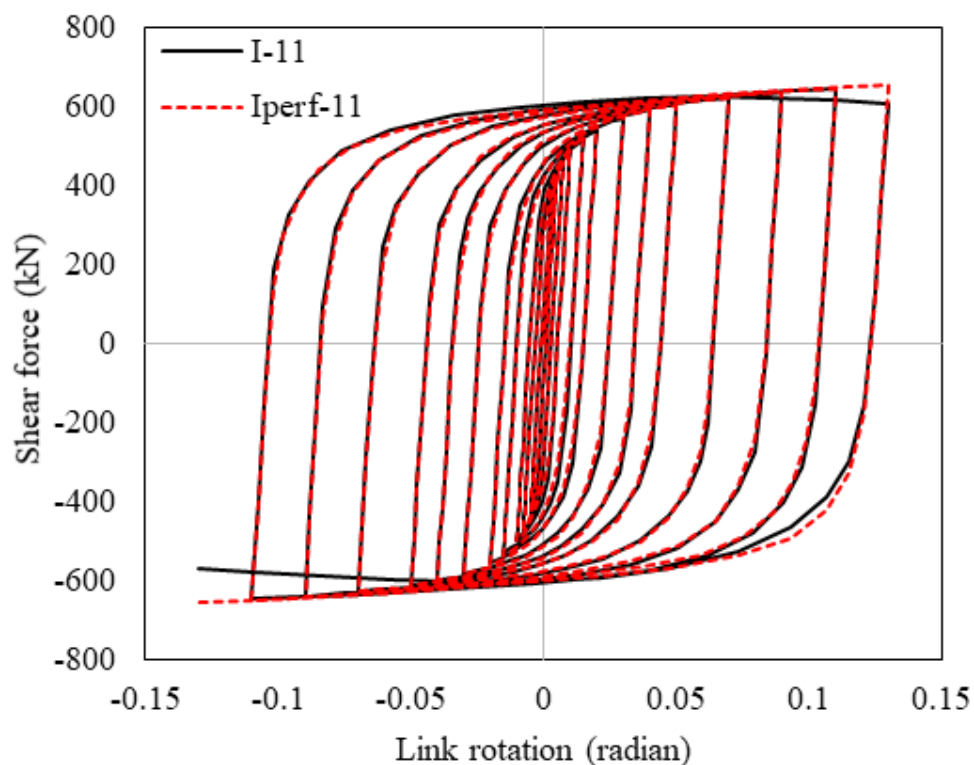


Figure 5.26: Hysteretic results of solid and perforated I-link: Pair 1

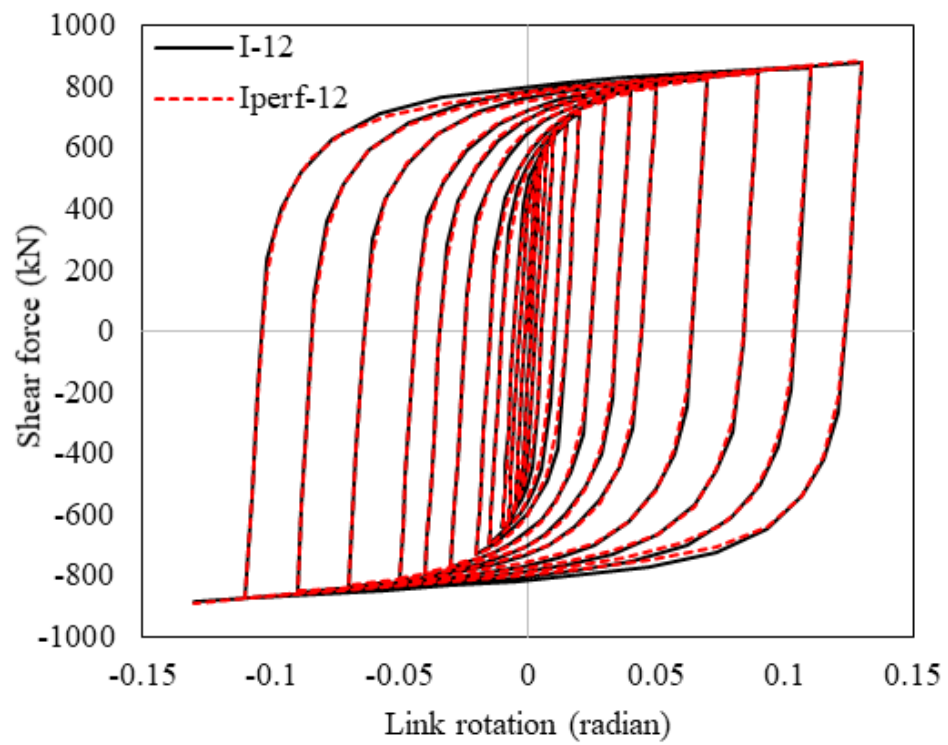


Figure 5.27: Hysteretic results of solid and perforated I-link: Pair 2

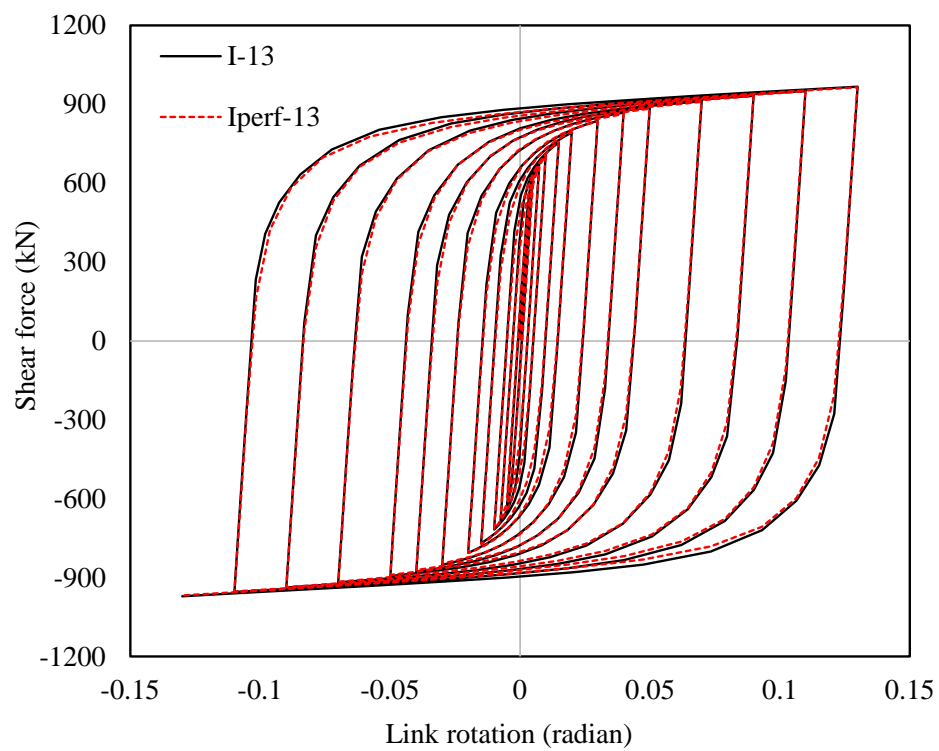


Figure 5.28: Hysteretic results of solid and perforated I-link: Pair 3

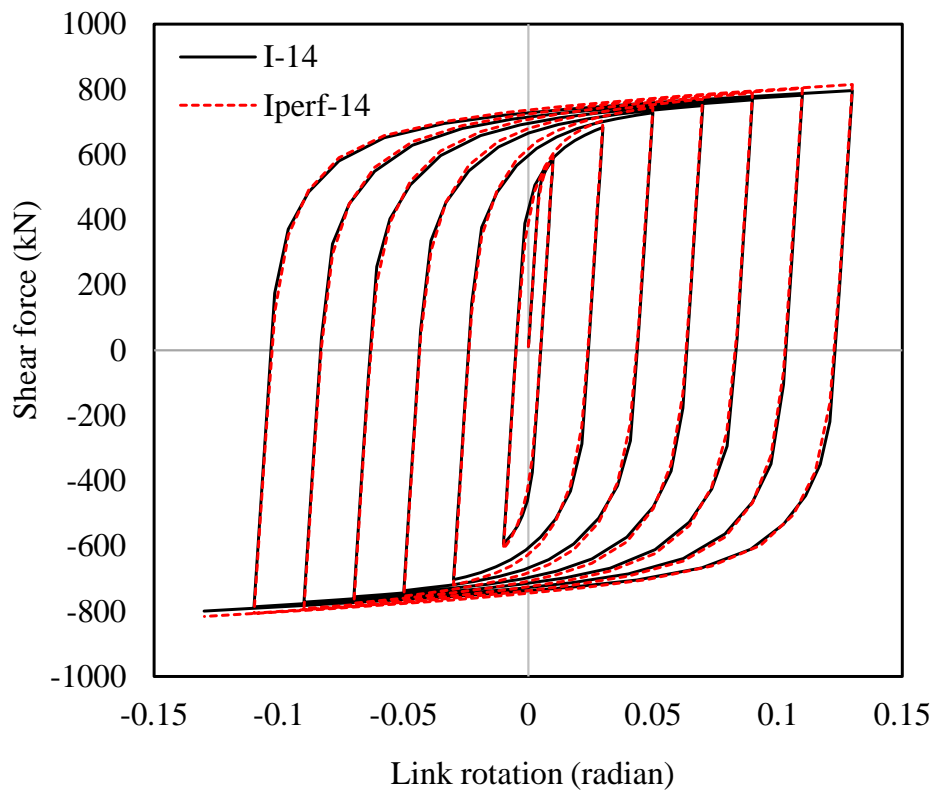


Figure 5.29: Hysteretic results of solid and perforated I-link: Pair 4

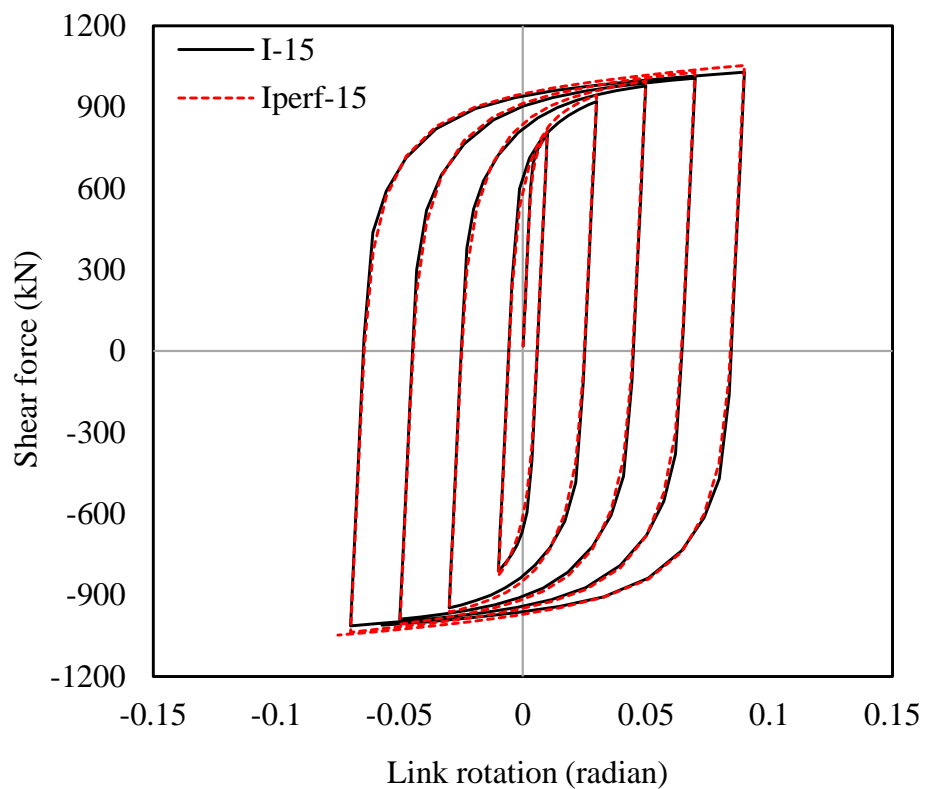


Figure 5.30: Hysteretic results of solid and perforated I-link: Pair 5

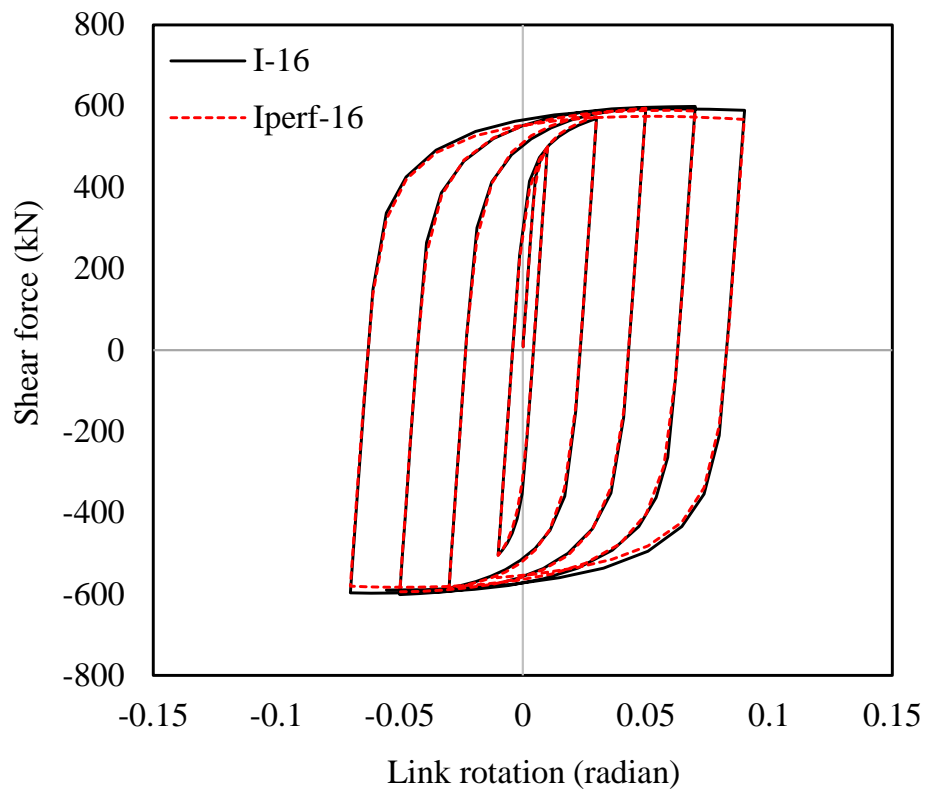


Figure 5.31: Hysteretic results of solid and perforated I-link: Pair 6

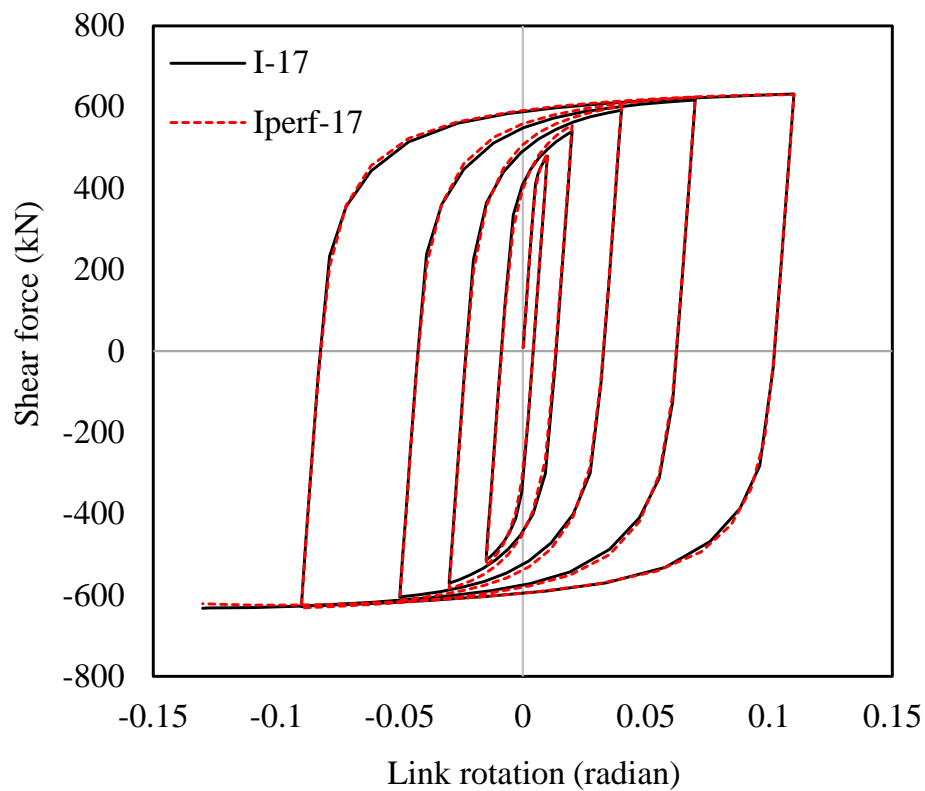


Figure 5.32: Hysteretic results of solid and perforated I-link: Pair 7

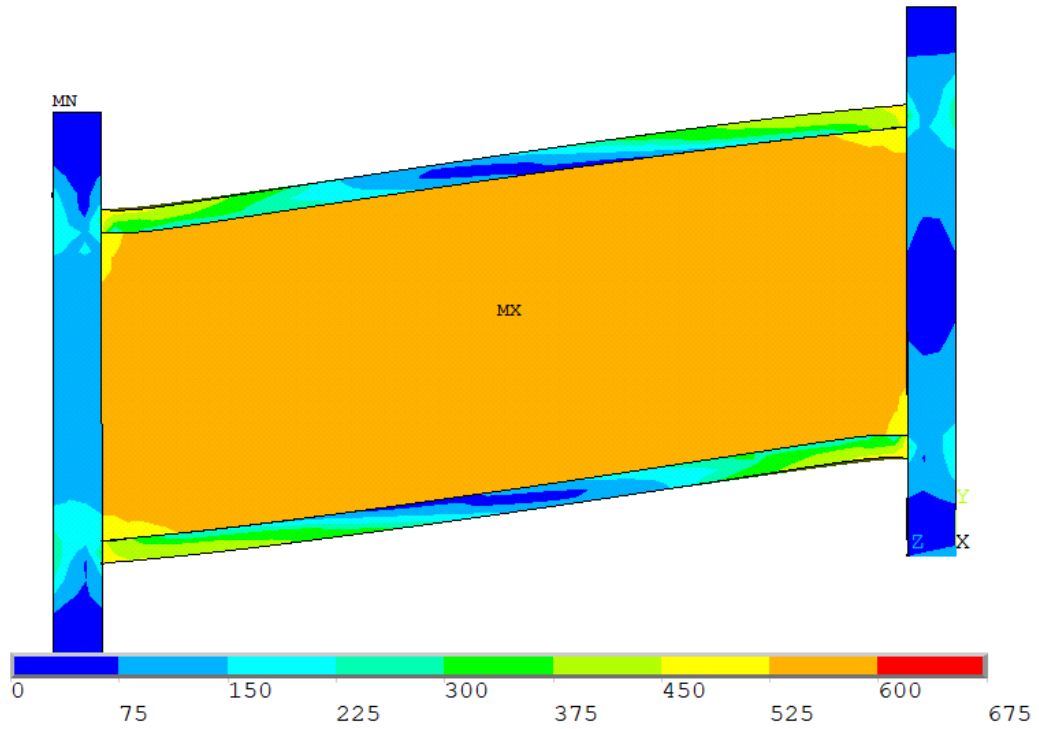


Figure 5.33: Deformed shape and von Mises stress (MPa) of link I-14 at 0.13 radian

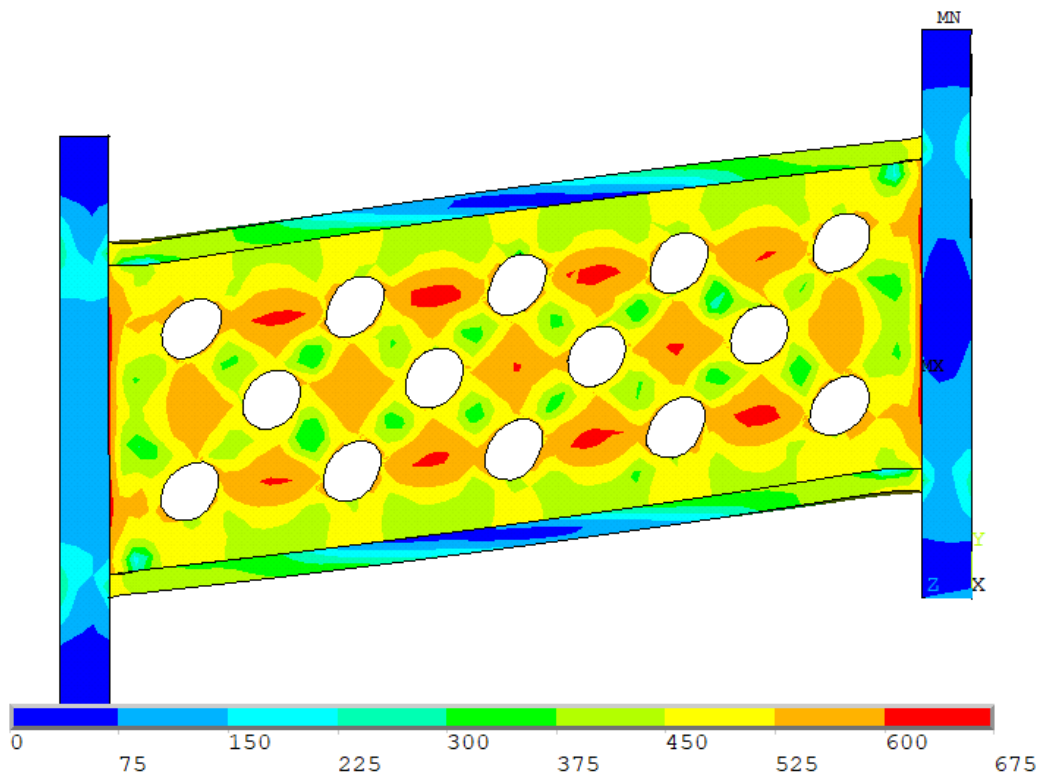


Figure 5.34: Deformed shape and von Mises stress (MPa) of link Iperf-14 at 0.13 radian

5.6 SOLID I-LINK AND PERFORATED BOX/TUBULAR LINK

A box-shaped link with the length, flange, and web dimensions same as an I-link has a shear yield capacity approximately twice that of the I-link because of the presence of two webs in the box-link. So, to establish the interchangeability between a box-link and an I-link of approximately the same length and depth, reduction of shear capacity of the box-link is necessary which can be done by making circular perforations in the webs of the box-links (Figure 5.35).

In this section, the feasibility of interchangeability between an I-shaped link and a perforated box-shaped link of approximately the same lengths is investigated. The hysteretic responses of perforated box-shaped links were investigated and compared with that of an I-link with the same shear yield and approximately similar length ratios (since the ultimate shear strength and overstrength factor depend on the length ratio) to check whether comparable and similar results can be achieved for both the links.

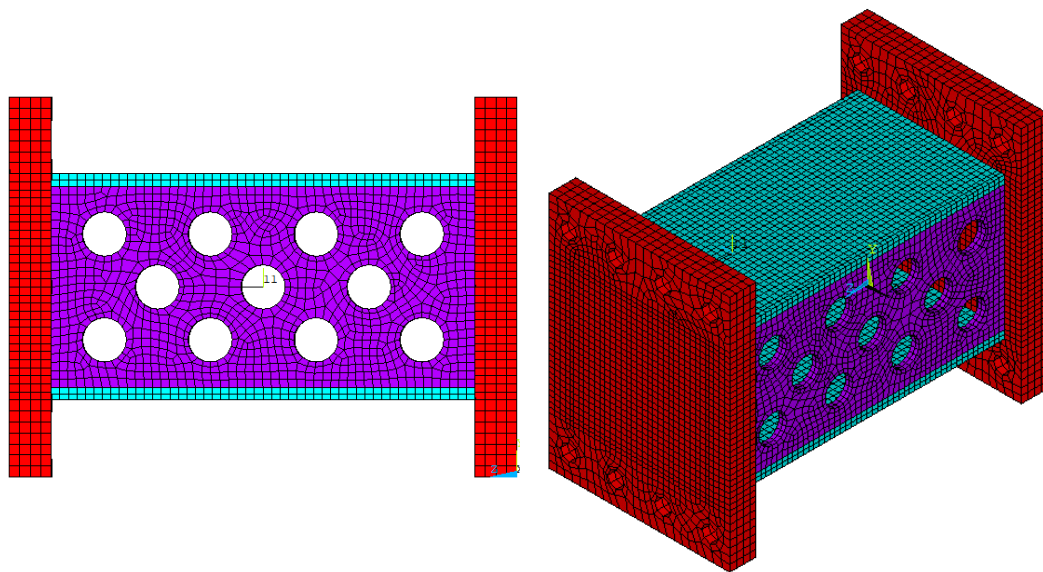


Figure 5.35: Developed model of perforated box-shaped/tubular link

5.6.1 Equations of Shear Capacity For Interchangeability

The shear capacities of box-shaped links with circular perforations on the webs were predicted using the existing equation for the shear yield capacity of a SPSW ($V_{y(perf)} = (1 - 0.7D/S) \times V_{y(solid)}$) and shear capacity of I-link was calculated using

the equation $V_y=0.6F_y(dt_w)$. The hysteretic response was superimposed with a hysteretic response of an I-shaped link with the same theoretical shear strength (Figure 5.36). In the figure, a discrepancy between the two plots was noticed which suggested that the use of the previous equation for a perforated box-shaped link does not provide accurate and comparable results.

Thus, the equation is modified, and a refined equation was found which can yield equivalent behavior in a procedure similar to that followed for perforated I-link. The following equation is proposed to estimate the shear strength of box-shaped links which have circular perforations in the webs.

Proposed equation (for perforated box shear links):

$$V_{y(perf)} = 0.6F_y \times 2(dt_w) \left(1 - 0.60 \times \frac{D}{S}\right) \quad 5-4$$

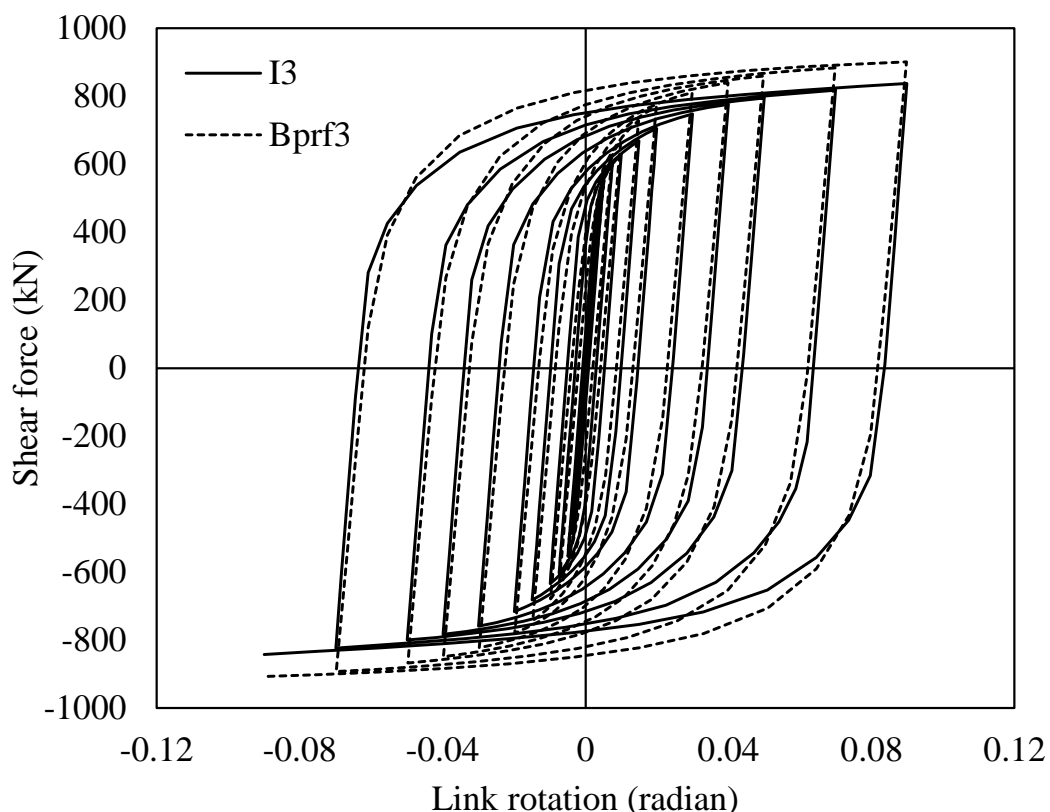


Figure 5.36: Superimposed plot of I-shaped and perforated tubular link using the equation of special perforated steel plate shear walls

5.6.2 Equivalent Cyclic Response of Perforated Box-Link

Using the proposed equation, four pairs each consisting of an I-link and a box-link were studied and results were compared by superimposing the hysteretic responses (Figure 5.37 to Figure 5.43). The parameters of the seven pairs are shown in Table 5-9. The results show that for a perforated box-link, results comparable and similar to that of a solid I-link can be obtained with the proposed equation.

Table 5-9: Parameters of I-links and perforated box-links

Pair	Sample	e (mm)	h (mm)	t_w (mm)	b_f (mm)	t_f (mm)	D (mm)	S (mm)	V_y (kN)
1	I-2	400	190	12.30	250	16.9	-	-	597.9
	Bprf-2	400	190	9.51	250	16.9	41.7	70.71	597.9
2	I-3	400	185	12.92	250	14	-	-	597.9
	Bprf-3	400	185	10	250	14	41.7	70.71	597.4
3	I-4	400	195	14.1	230	14	-	-	682.9
	Bprf-4	400	195	11	200	13	41.7	70.71	682.4
4	I-5	420	230	17.78	203	15	-	-	1004
	Bprf-5	420	230	12.07	200	13	35	84.85	1004
5	I-6	800	190	12.5	200	18	-	-	613.6
	Bprf-6	800	190	9.67	200	18	41.7	70.71	613.4
6	I-7	400	290	18.1	140	15	-	-	1250
	Bprf-7	400	290	14	140	13	41.7	70.71	1250
7	I-8	390	310	18.1	140	14	-	-	1328
	Bprf-8	390	310	13.27	140	14	30	56.57	1328

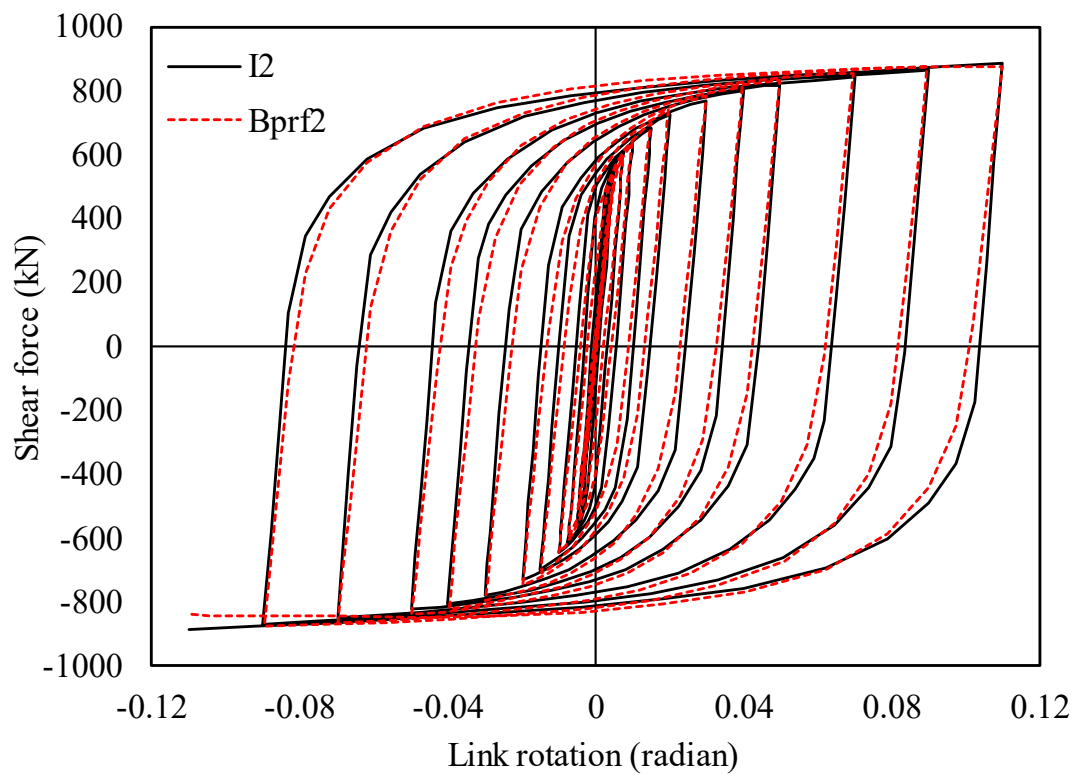


Figure 5.37: Hysteretic results of solid I-link and perforated box-link: Pair 1

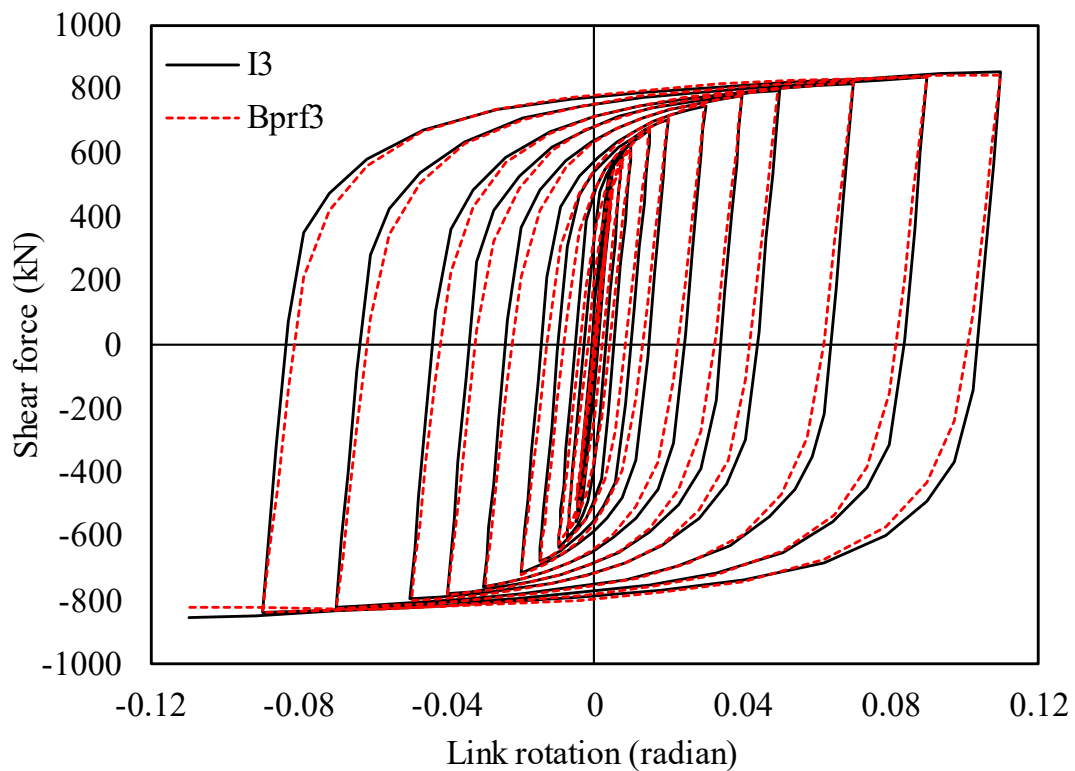


Figure 5.38: Hysteretic results of solid I-link and perforated box-link: Pair 2

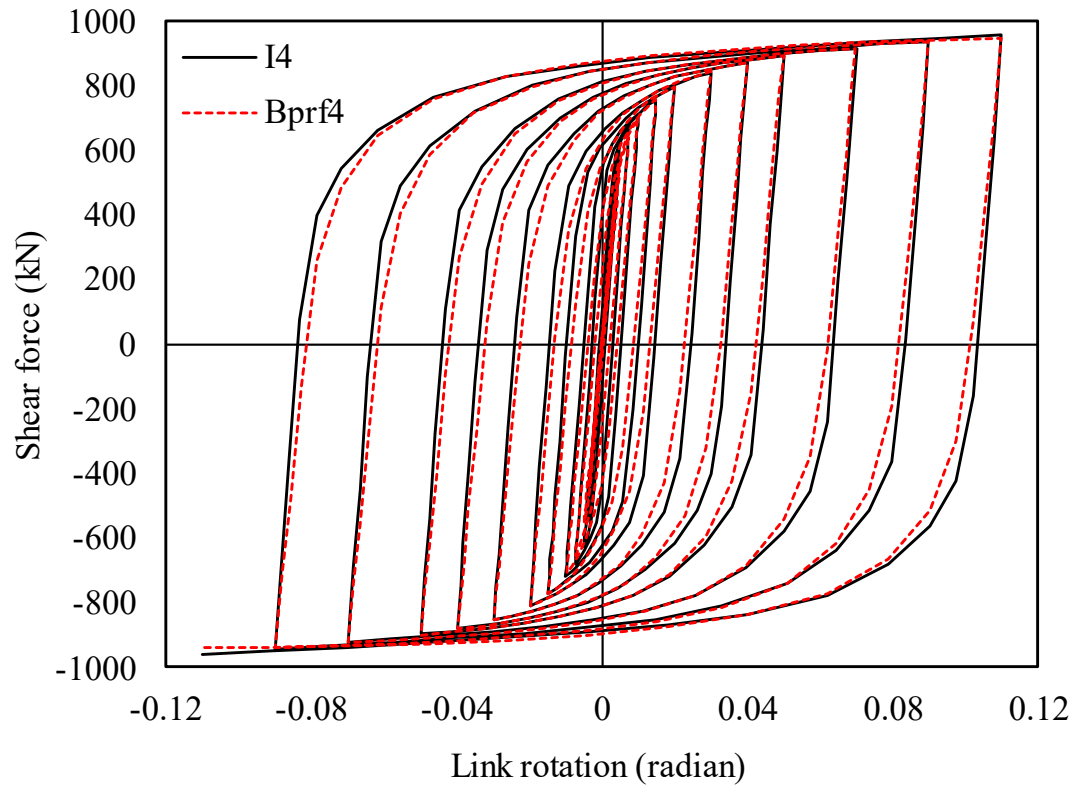


Figure 5.39: Hysteretic results of solid I-link and perforated box-link: Pair 3

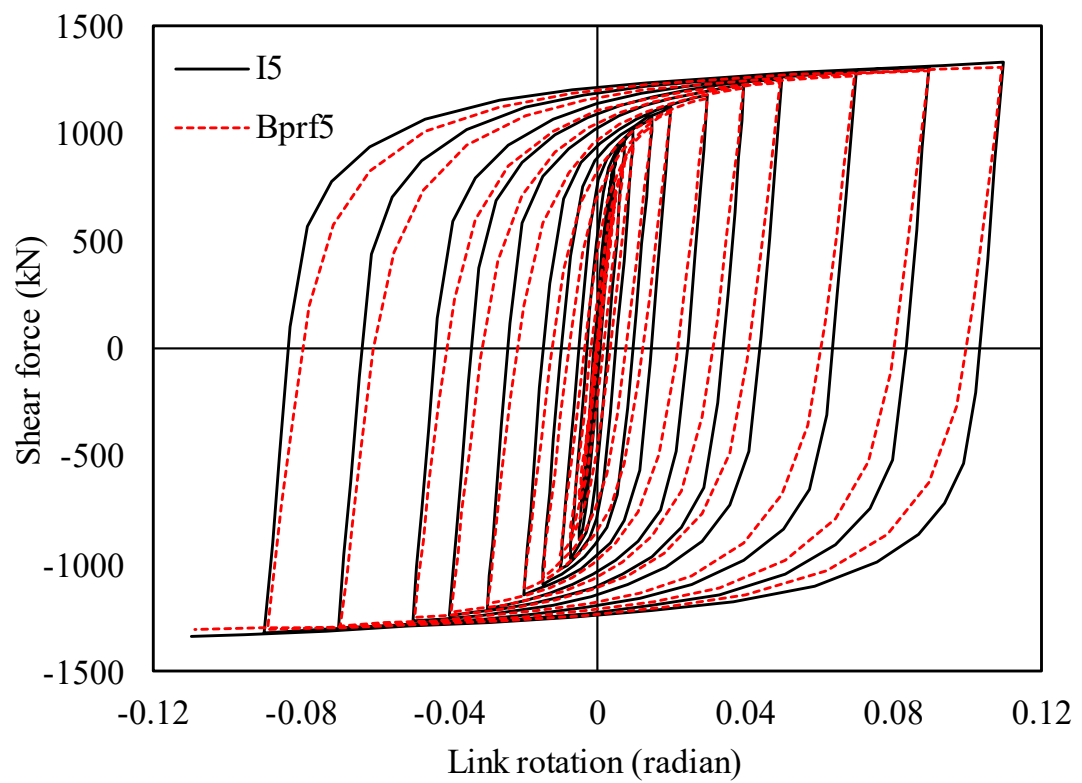


Figure 5.40: Hysteretic results of solid I-link and perforated box-link: Pair 4

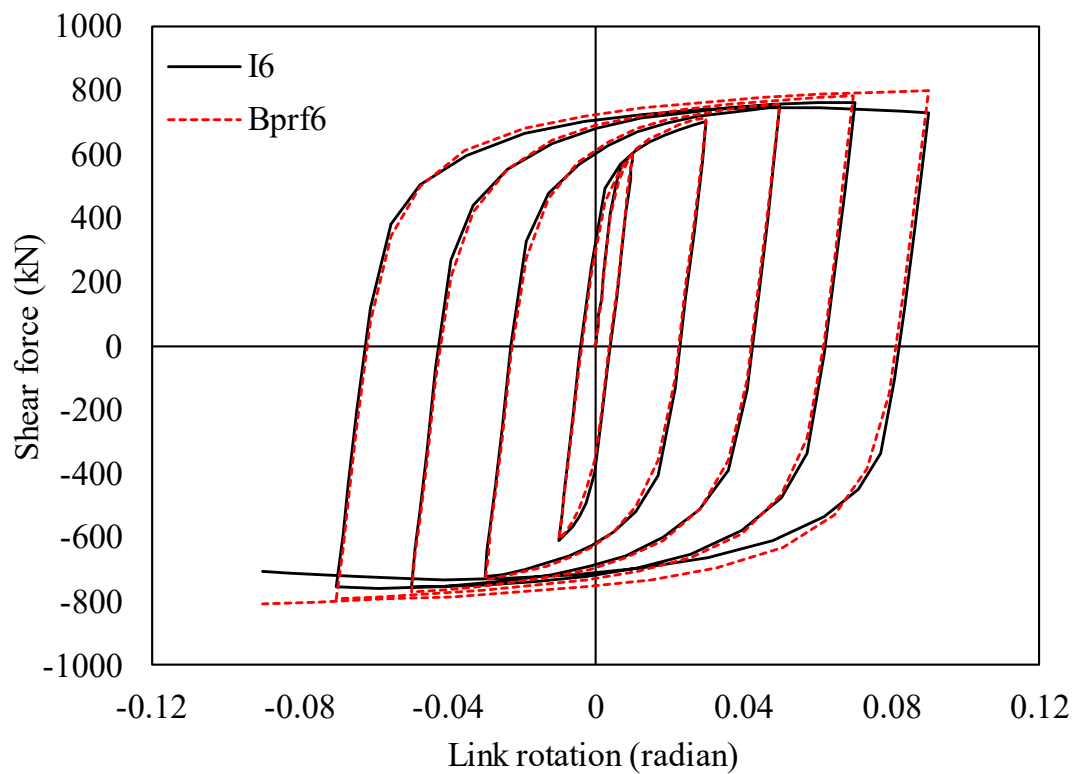


Figure 5.41: Hysteretic results of solid I-link and perforated box-link: Pair5

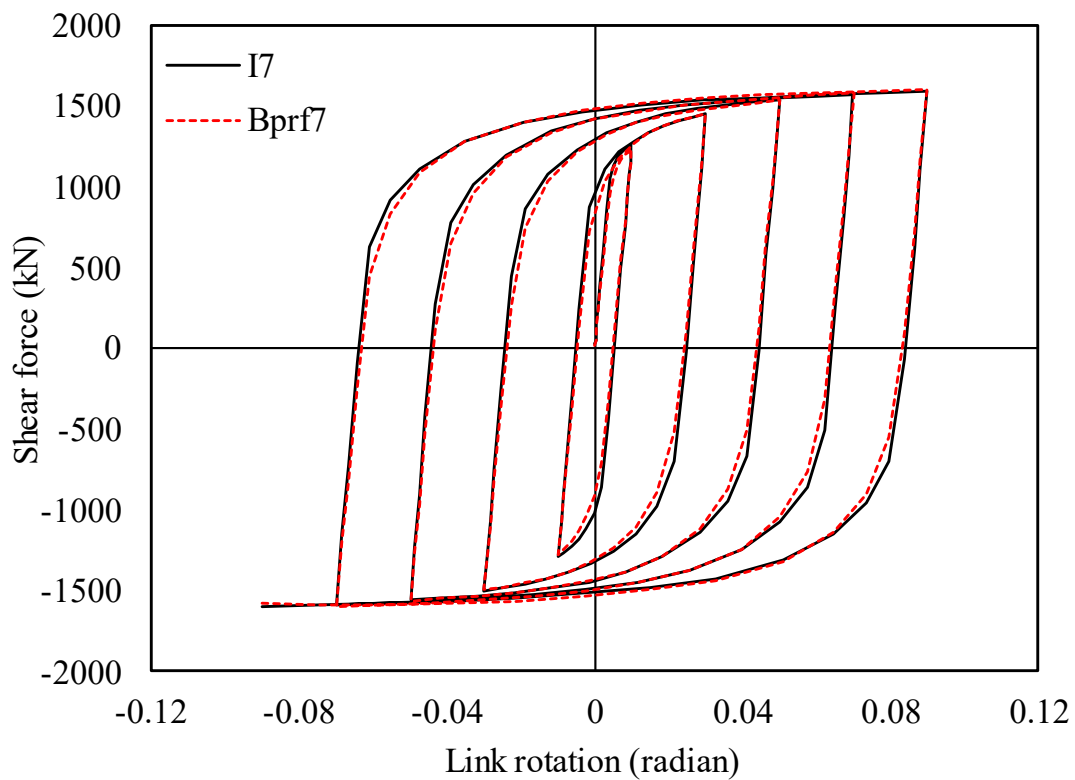


Figure 5.42: Hysteretic results of solid I-link and perforated box-link: Pair 6

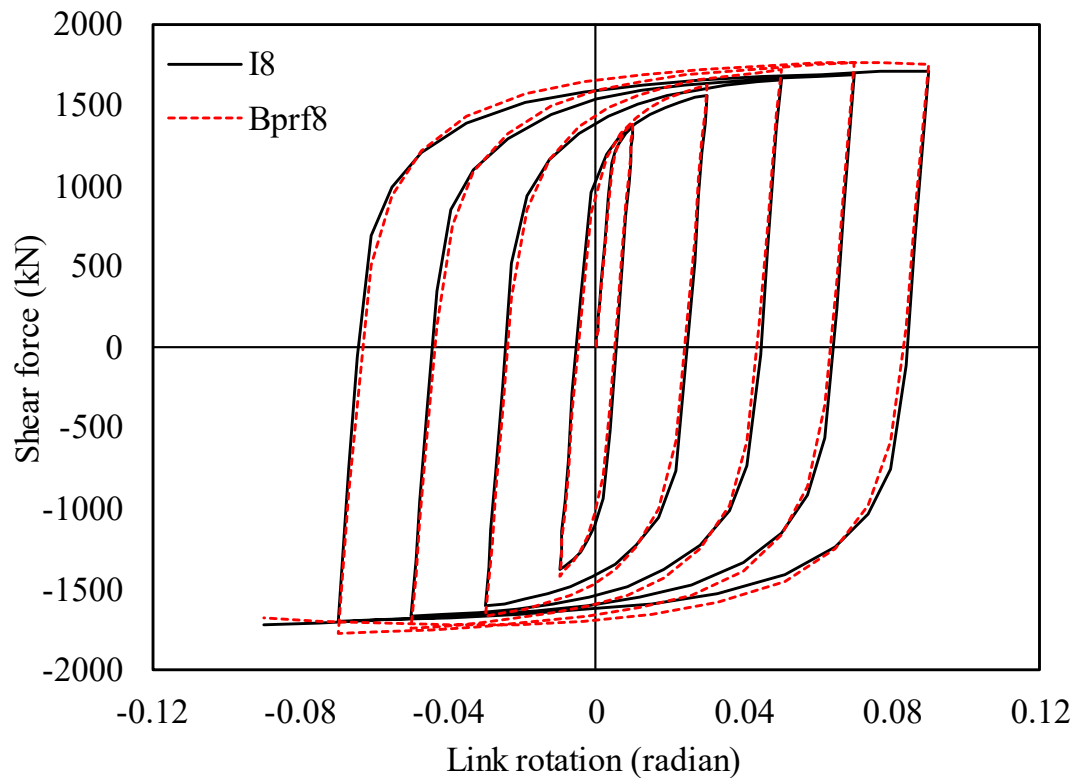


Figure 5.43: Hysteretic results of solid I-link and perforated box-link: Pair 7

5.7 ENERGY DISSIPATION

This section presents the total energy and the hysteresis efficiency of different types of links investigated in this study.

5.7.1 Total Energy

To keep the total energies of different links comparable, the total energies of different links have been calculated up to maximum rotation sustained by a link without major web buckling. The calculated total energies of the seven pairs of solid I-links and perforated I-links studied are shown in Figure 5.44. It can be seen for all pairs that, the total energies dissipated by a solid I-link is approximately equal to the total energy dissipated by a perforated I-link, if the two links have the same shear capacity.

The total energies of the samples of all the pairs of Table 5-9 were calculated from the hysteretic plots and are shown in Figure 5.45. The total energy dissipation of a solid I-link is found to be close to that of a box-link with the same shear yield capacity.

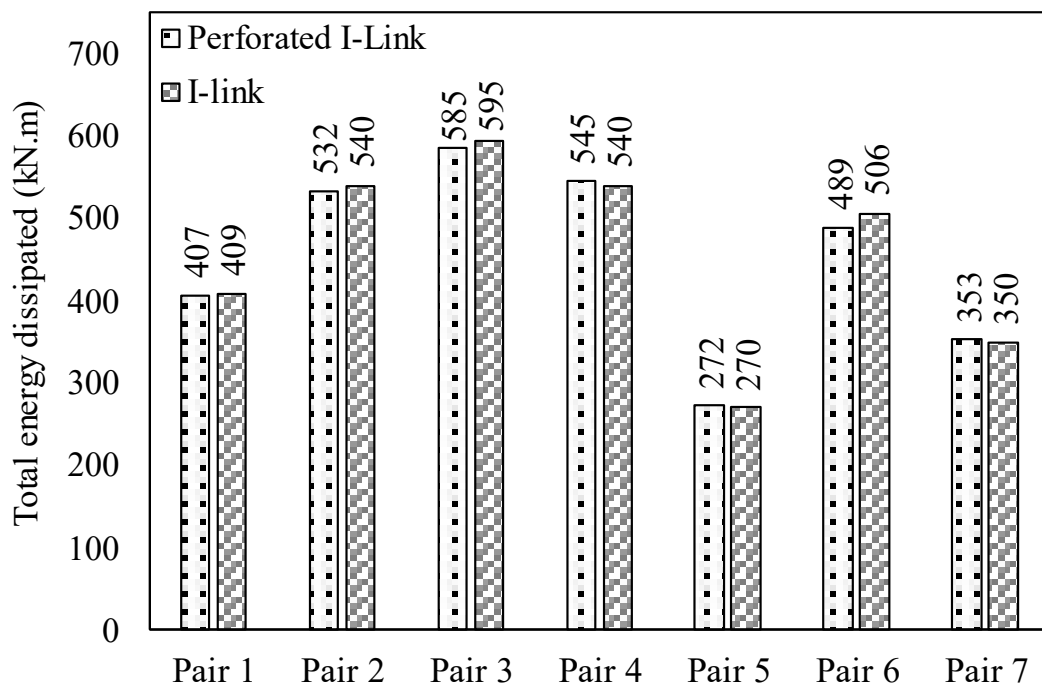


Figure 5.44: Energy dissipation of I-links and perforated I-links listed in Table 5-8

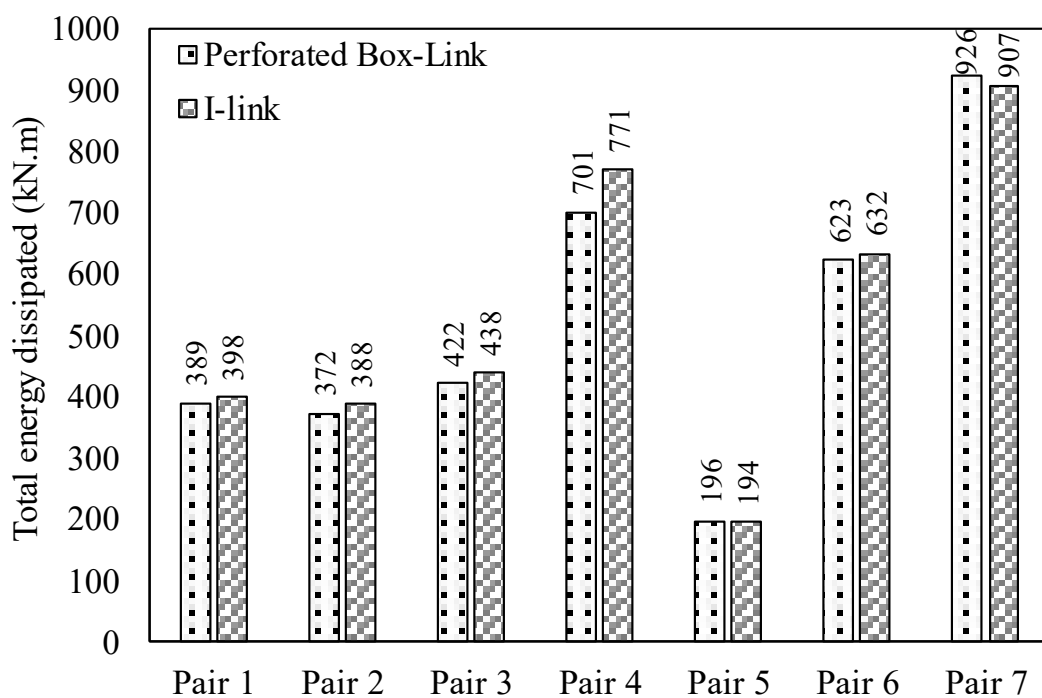


Figure 5.45: Energy dissipation of I-link and perforated box-links listed in Table 5-9

5.7.2 Hysteresis Efficiency

The cyclic responses of the compared links are similar. However, at each cycle of the cyclic loading, the effectiveness of different shear links as an energy dissipating device is evaluated by calculating the hysteresis efficiency factor.

The hysteresis efficiency comparison between a solid I-link and a solid box link is shown in Table 4 and Figure 5.46 and the same between a solid I-link and a perforated box-link is shown in Table 5-11 and Figure 5.47. It is observed that the hysteresis efficiency of a solid I-link is higher than a box-link (both solid and perforated) at lower rotations of the links. However, at and above 0.09-radian rotation, the efficiencies of box-links and I-links are approximately equal. So, the use of I-shaped links is suggested in structures where large rotations are not expected.

Table 5-10: Parameters of hysteresis efficiency of perforated box-link and I-link

Rotation (rad)	Bprf3 (Perforated Box link)			I3 (Solid I-link)		
	E_{max}	E_{hyst}	Efficiency (%)	E_{max}	E_{hyst}	Efficiency (%)
0.0048	9.623	0.430	4.420	10.92	1.610	14.74
0.01	24.66	8.160	33.08	25.20	11.48	45.57
0.02	57.29	30.79	53.75	56.96	34.96	61.38
0.03	91.17	57.07	62.60	90.41	61.53	68.06
0.04	124.9	85.86	68.74	125.0	90.25	72.20
0.05	160.6	115.5	71.92	159.75	120.1	75.21
0.07	230.0	177.8	77.30	230.3	182.2	79.11
0.09	301.7	241.9	80.17	303.12	247.0	81.49

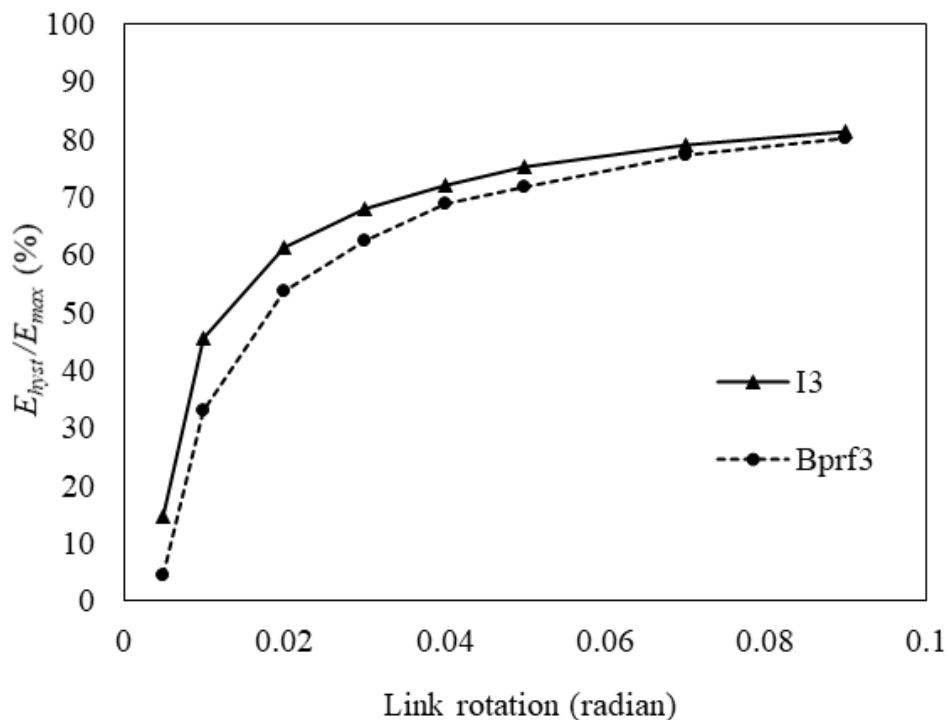


Figure 5.46: Comparison of hysteresis efficiency of I shaped and perforated box-shaped link with same yield capacity

Table 5-11: Parameters of hysteresis efficiency of solid box and I-link

Rotation (rad)	B1 (Box-shaped link)			I1 (I-Link)		
	E_{max}	E_{hyst}	Efficiency (%)	E_{max}	E_{hyst}	Efficiency (%)
0.005	9.174	0.050	0.545	52.54	1.980	3.769
0.01	21.47	8.949	41.68	21.58	10.56	48.94
0.02	49.38	28.420	57.55	48.73	30.64	62.87
0.03	79.65	51.000	64.03	77.51	53.33	68.80
0.04	109.5	76.049	69.42	107.0	77.99	72.91
0.05	148.6	108.000	72.68	136.7	103.6	75.78
0.07	202.6	156.713	77.37	194.6	156.8	80.62
0.09	267.2	214.000	80.09	260.0	213.0	81.91
0.11	328.7	271.386	82.56	324.4	268.8	82.85

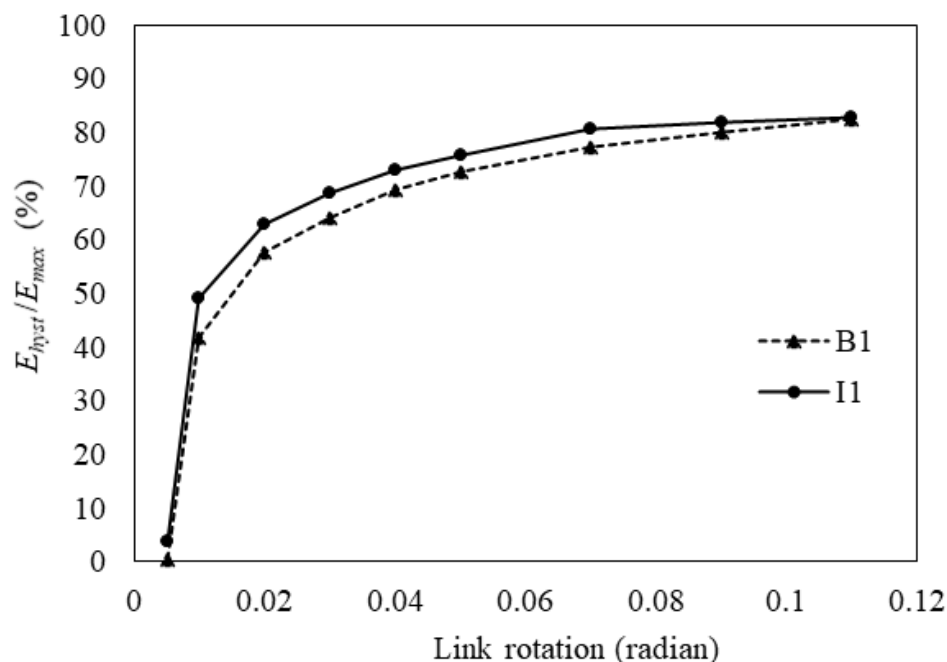


Figure 5.47: Comparison of hysteresis efficiency of I shaped and box-shaped link with same yield capacity

5.8 EFFECT OF PERFORATION SIZE AND DENSITY

To investigate the effect of the perforation density five links with identical material and geometric properties were studied. The values of the ratio: D/S for the five links were kept the same, while the perforation diameter (D) and diagonal hole spacing (S) were varied resulting in five links with five different perforation density.

5.8.1 Geometric Parameters of the Developed Models

The finite element model of the five links designated as E3, E5, E7, E9, and E11 are shown respectively in Figure 5.48, Figure 5.49, Figure 5.50, Figure 5.51, and Figure 5.52. The geometric parameters of the five links are shown in Table 5-12 and Table 5-13. From Table 5-12, it can be observed that the ratios of the net area to the gross total area (A_{net} / A_g) of the link webs are approximately the same for all five links. As per the proposed equation (Equation 5-3), the reduction in shear capacity due to perforation for all the links is 32.60 % which is equal to the term, $0.64 * D/S$.

Table 5-12: Parameters of the five perforated links with different perforation density

Sample	Total no of holes	Link length e (mm)	Web height, h (mm)	Gross area, A_g (sq. mm)	Hole diameter, D (mm)	Total area of holes / perforations A_{holes} (sq. mm)	Net area $A_{net} = A_g - A_{holes}$ (sq. mm)	A_{net} / A_g (%)
E3	11	400	190	76000	36.01	11203	64797	85.26
E5	27	400	190	76000	24.49	12717	63283	83.27
E7	59	400	190	76000	15.85	11635	64365	84.69
E9	95	400	190	76000	12.96	12541	63459	83.50
E11	137	400	190	76000	10.95	12897	63103	83.03

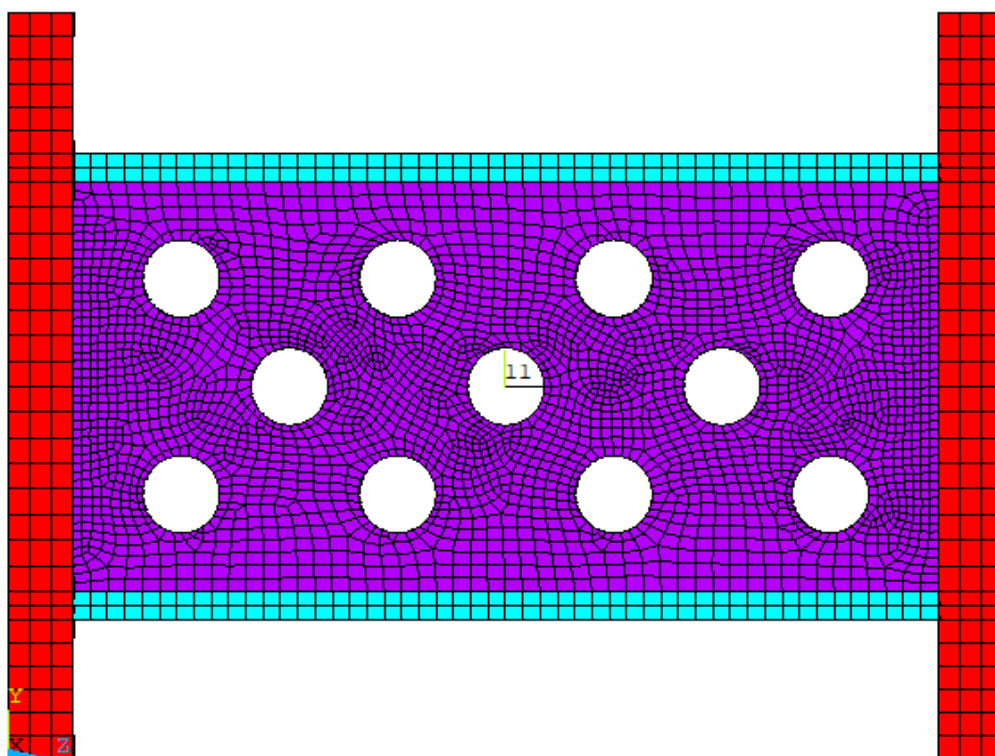


Figure 5.48: Perforated I-link sample-E3

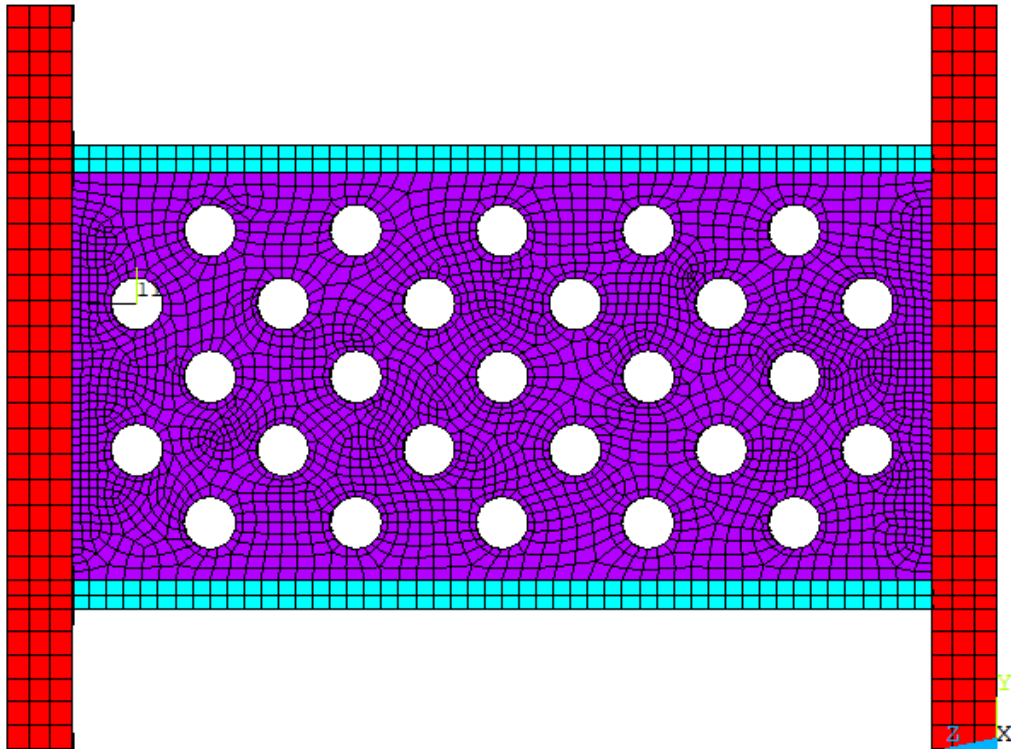


Figure 5.49: Perforated I-link sample-E5

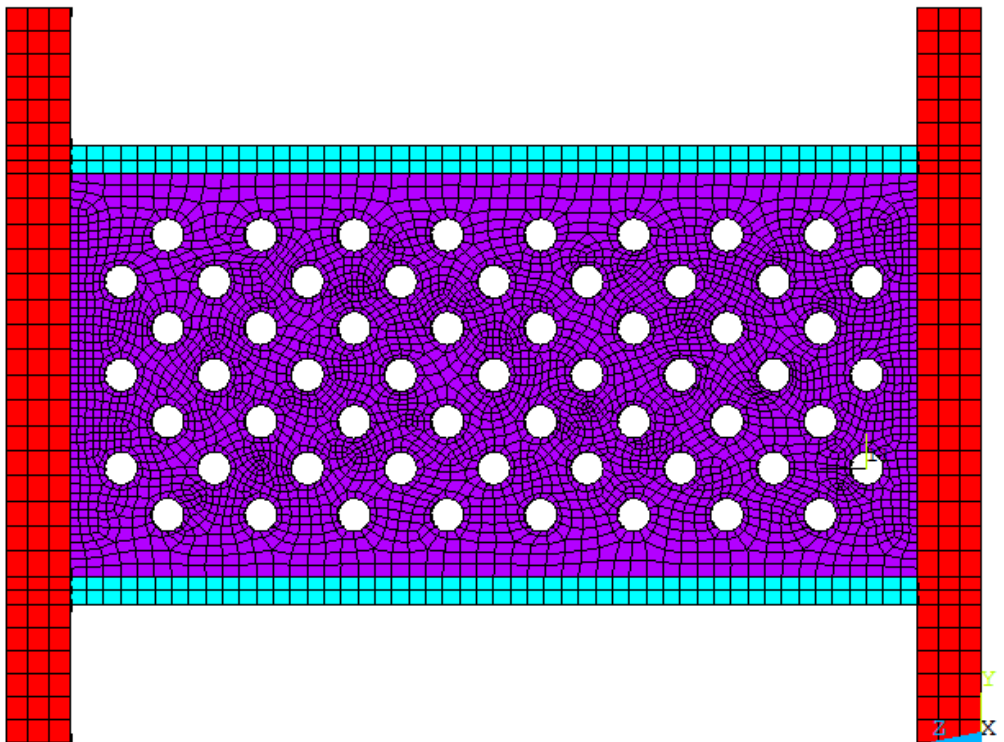


Figure 5.50: Perforated I-link sample-E7

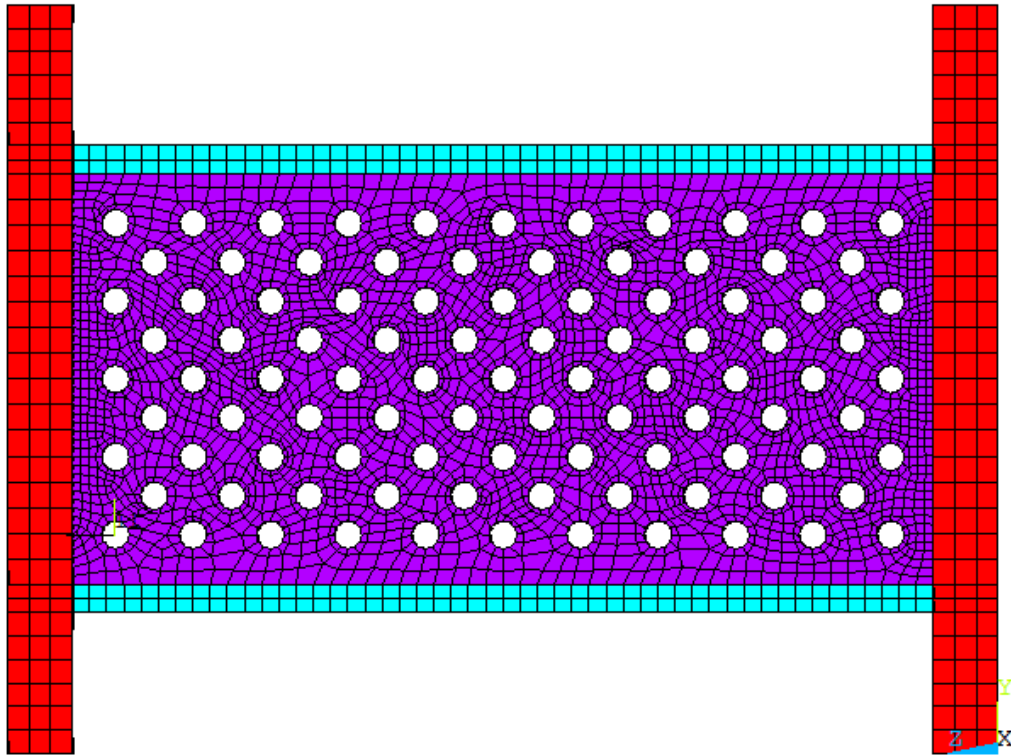


Figure 5.51: Perforated I-link sample-E9

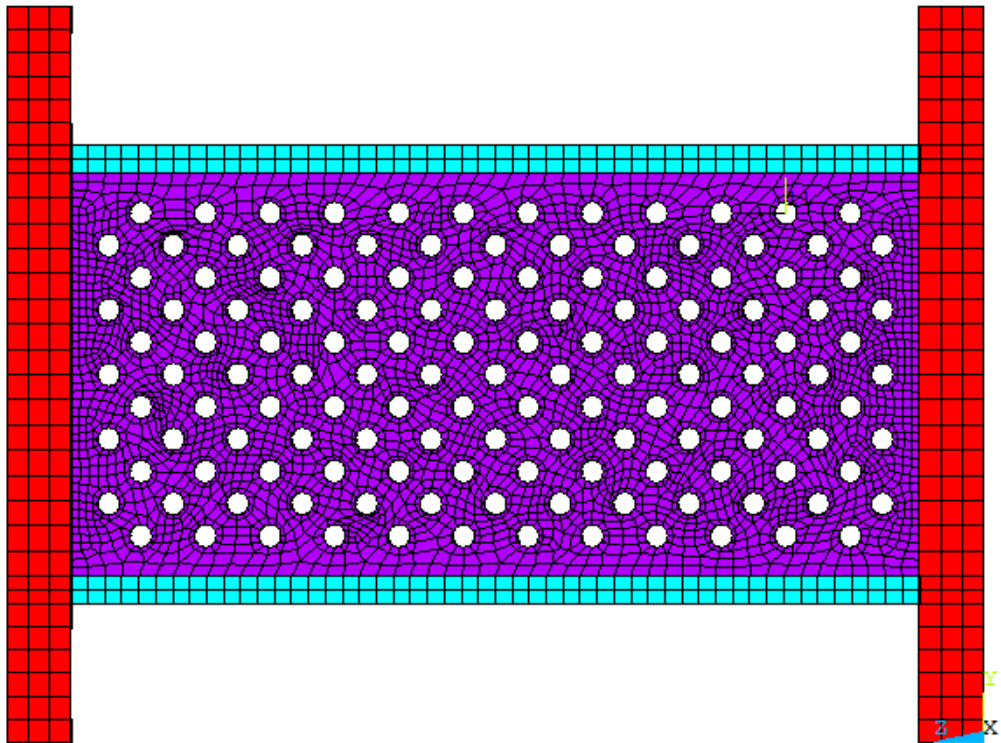


Figure 5.52: Perforated I-link sample-E11

5.8.2 Hysteretic Responses

The superimposed plot of the responses of the links with five different perforation density but the same value of D/S is shown in Figure 5.53 and individual hysteretic plots are also shown for clarity in Figure 5.54. From the figure, it can be observed that the same hysteretic response can be achieved with all the links. However, web buckling in the five links does not start at the same rotation or the same instance of the loading history (Table 5-13 and Table 5-14). Drop in peak shear force due to web buckling occurs at the earliest time in the link with the maximum density of perforation (E11). The drop of shear force is delayed as the density of perforation decreases and so, the sample E3 sustains the highest rotation without web buckling among all the five samples studied.

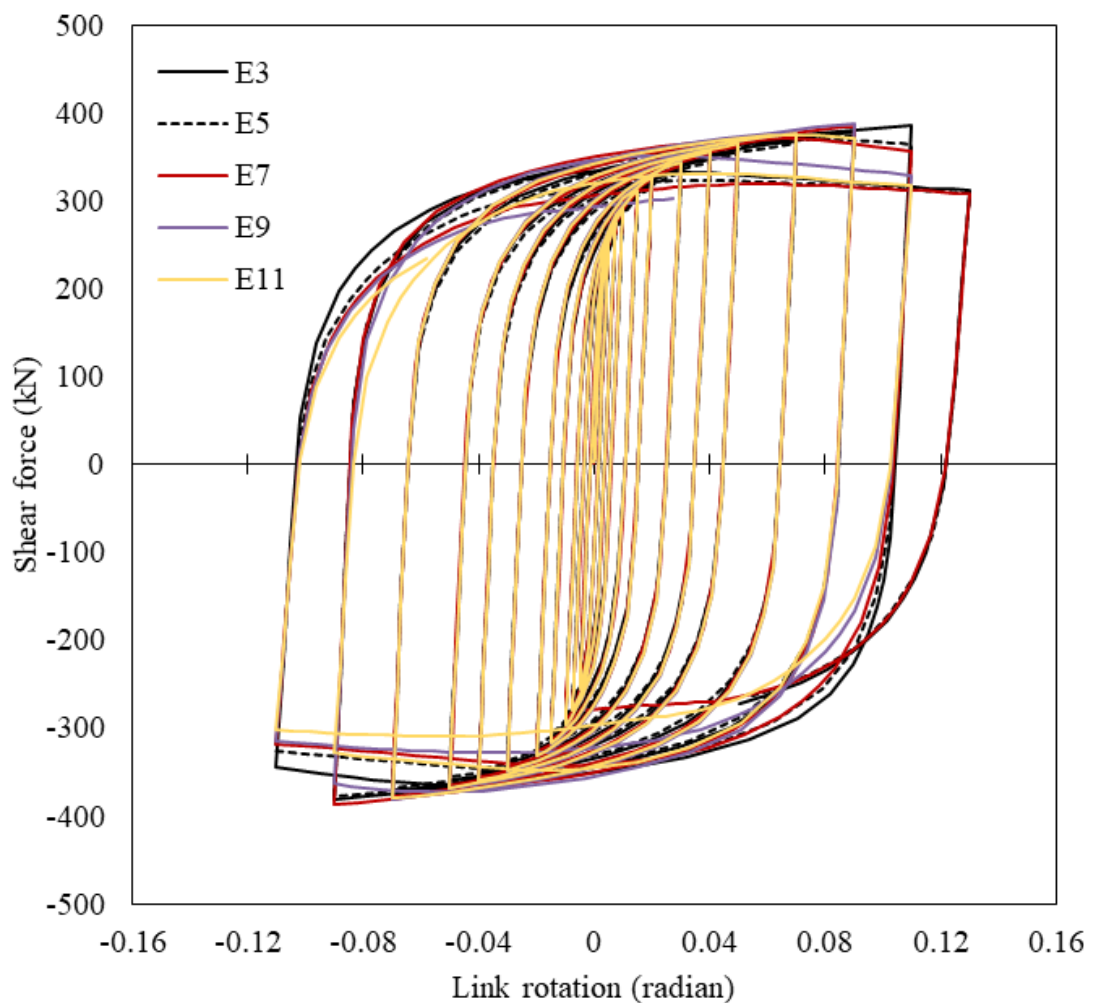


Figure 5.53: Hysteretic response of E3, E5, E7, E9 and E11 ($t_w = 8.1$ mm, $h/t_w = 23.46$)

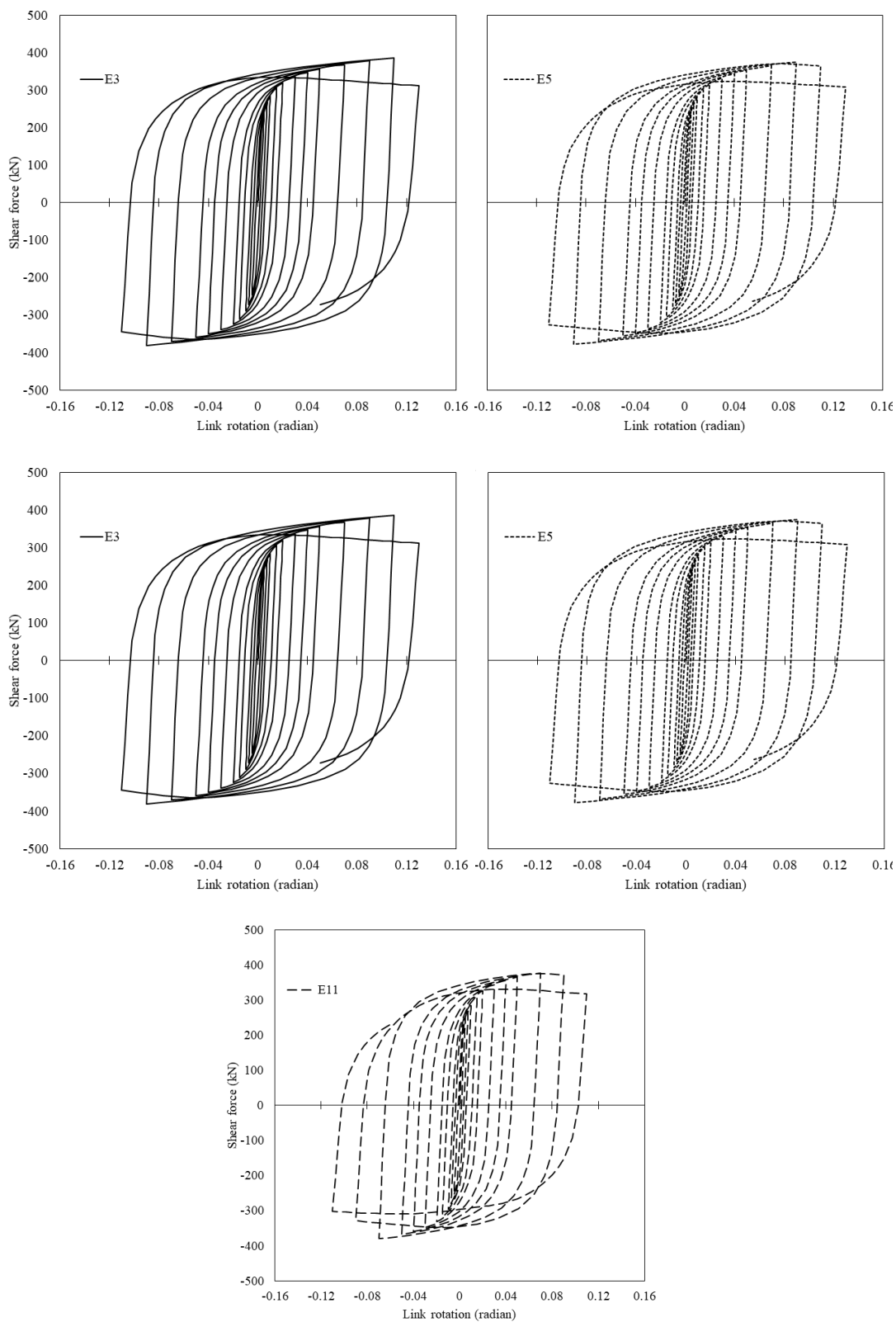


Figure 5.54: Hysteretic plots of links with five different perforation densities (E3, E5, E7, E9 and, E11) for $h/t_w = 23.46$

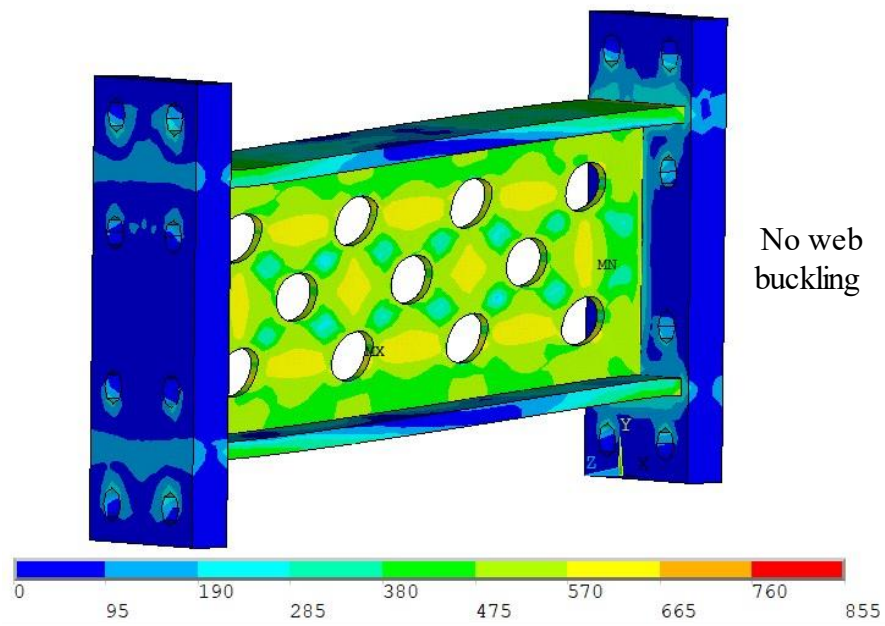
Table 5-13: Shear drop due to buckling for different densities of web perforations
($h/t_w = 23.46$)

Sample	D (mm)	S (mm)	D/S	$S_{clear} = S-D$ (mm)	h/t_w	D/t_w	Drop in shear force due to buckling starts at rotation (radian)
E3	36.01	70.71	0.5093	34.71	23.46	4.444	0.11(2nd half cycle)
E5	24.49	48.08	0.5093	23.59		3.023	0.11 (1st half cycle)
E7	15.85	31.11	0.5093	15.27		1.956	0.11 (1st half cycle)
E9	12.96	25.46	0.5093	12.49		1.601	0.09 (2nd half cycle)
E11	10.95	21.50	0.5093	10.55		1.352	0.09 (1st half cycle)

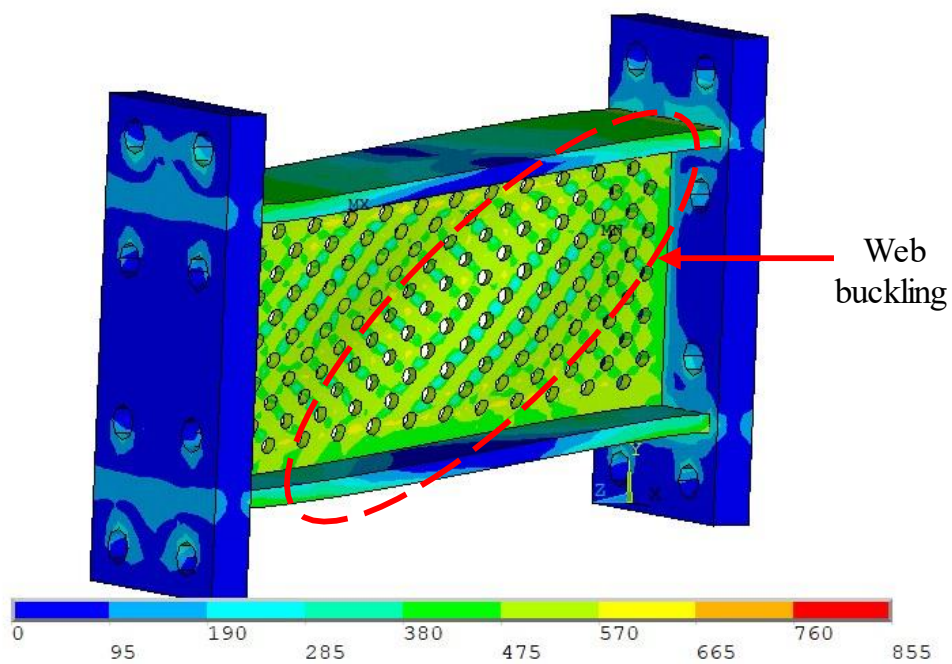
Table 5-14: Shear drop due to buckling for different densities of web perforations
($h/t_w = 19$)

Sample	D (mm)	S (mm)	D/S	$S_{clear} = S-D$ (mm)	h/t_w	D/t_w	Drop in shear force due to buckling starts at rotation (radian)
E3	36.01	70.71	0.5093	34.71	19.00	3.600	0.15 (2nd half cycle)
E5	24.49	48.08	0.5093	23.59		2.449	0.15 (1st half cycle)
E7	15.85	31.11	0.5093	15.27		1.585	0.15 (1st half cycle)
E9	12.96	25.46	0.5093	12.49		1.296	0.13 (1st half cycle)
E11	10.95	21.50	0.5093	10.55		1.095	0.11 (2nd half cycle)

For comparison and the deformed shapes and von Mises stress contour plot of link specimens with the maximum density of perforation (E11) and minimum density of perforation (E3) at three specific rotations are shown in Figure 5.55 to Figure 5.57. Figure 5.56 shows that at -0.13 radian link rotation E11 buckles but E3 does not.



(a) E3 ($h/t_w=19$) at -0.11 radian rotation



(b) E11 ($h/t_w=19$) at -0.11 radian rotation

Figure 5.55: Deformed shape and von Mises stress (MPa) of link E3 and E11 ($h/t_w=19$) at -0.11 radian rotation

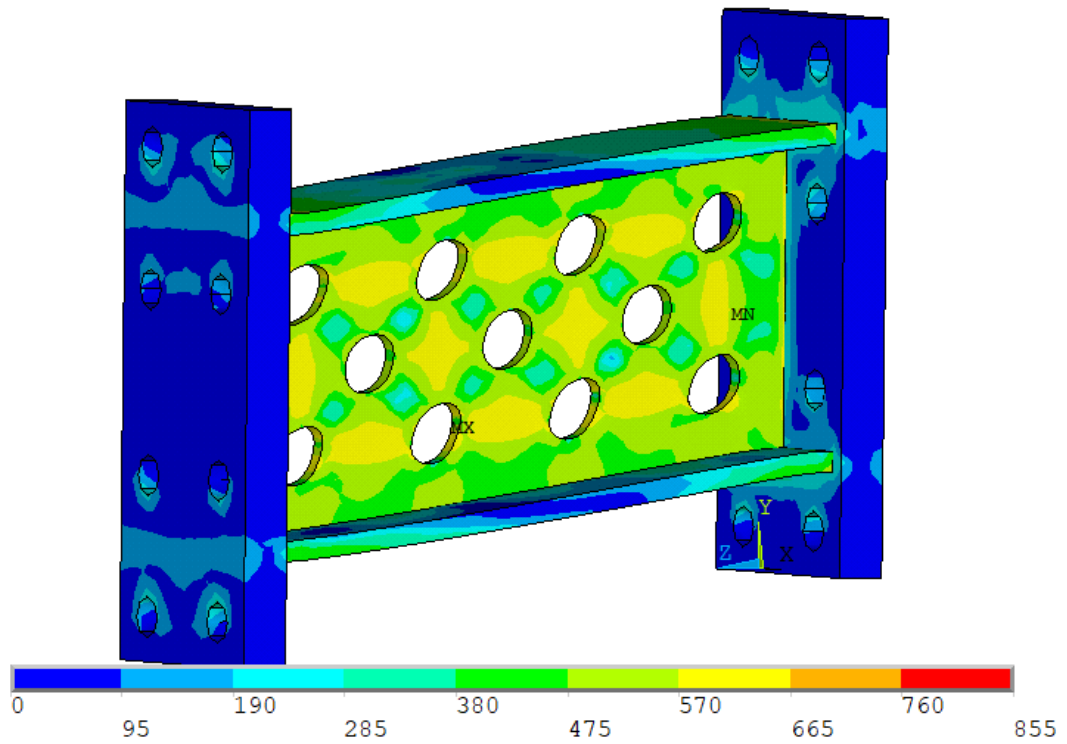
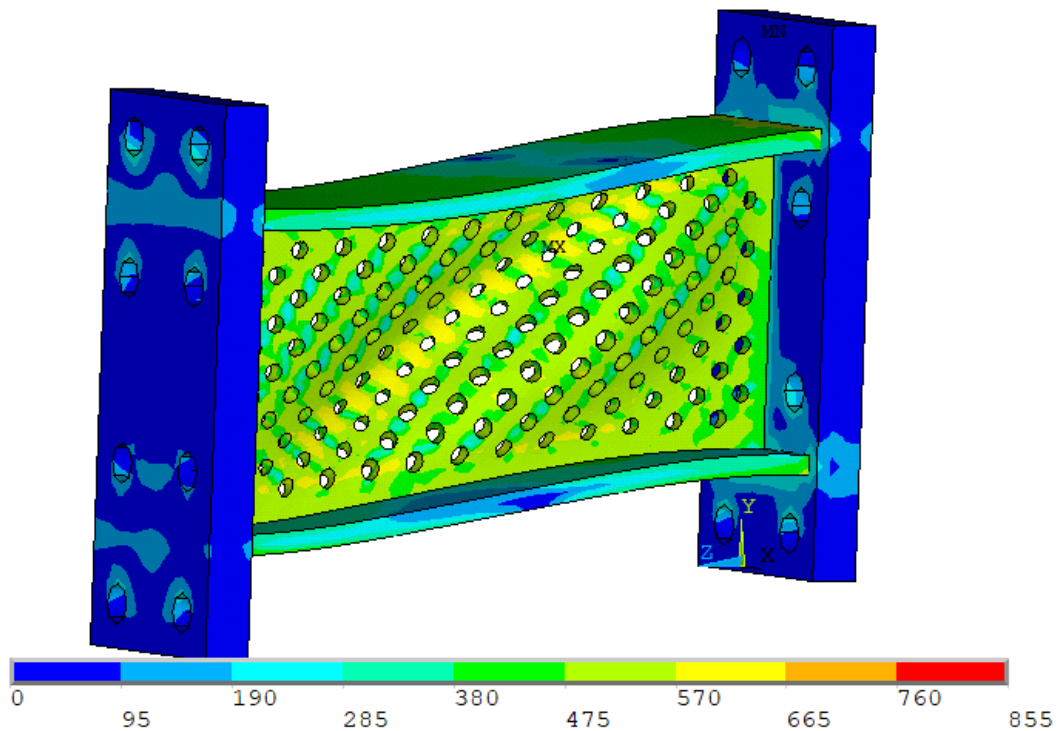
(a) E3 ($h/t_w=19$) at -0.13 radian rotation(b) E11 ($h/t_w=19$) at -0.13 radian rotation

Figure 5.56: Deformed shape and von Mises stress (MPa) of link E3 and E11 ($h/t_w=19$) at -0.13 radian rotation

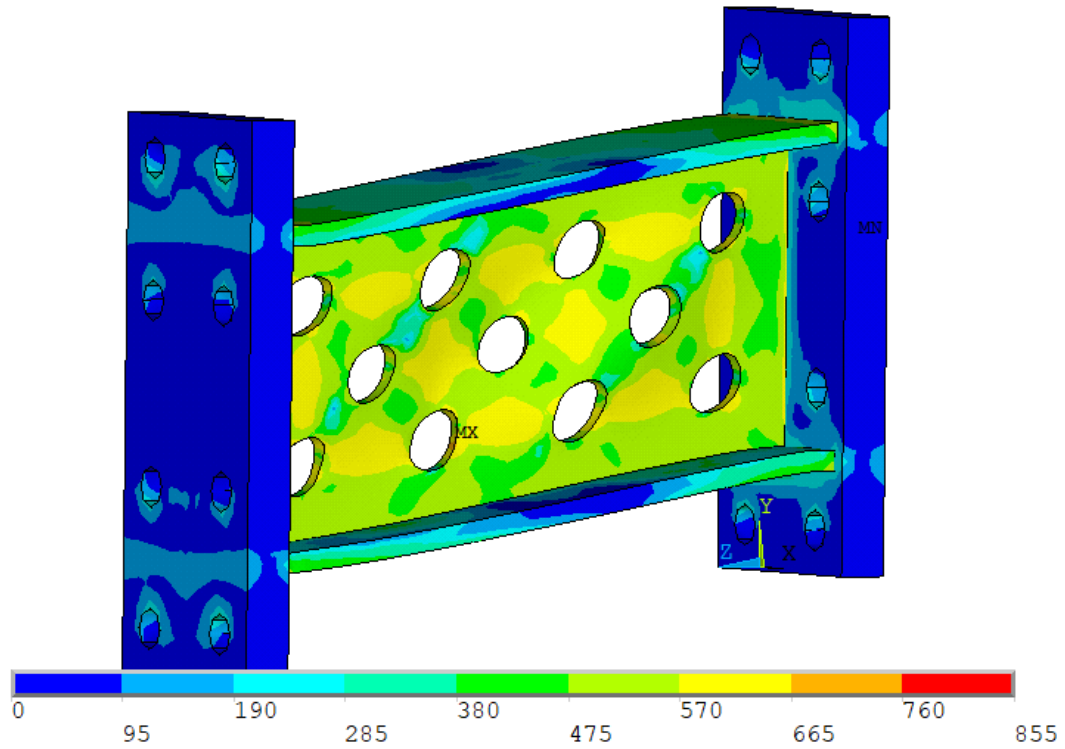
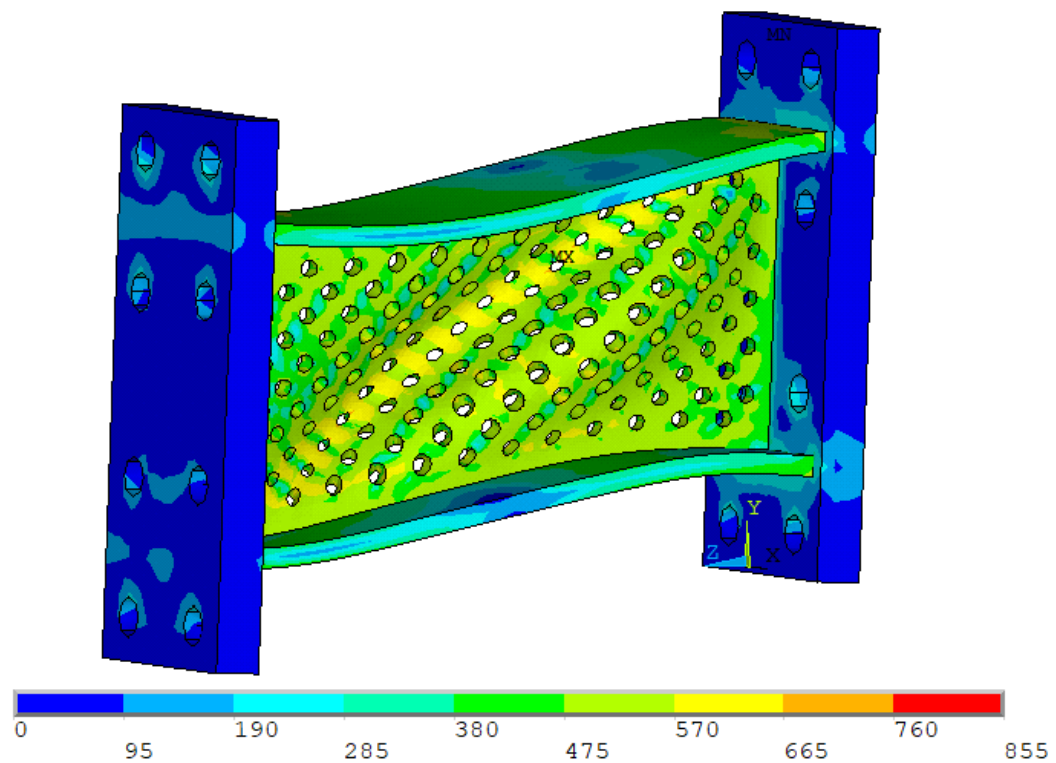
(a) E3 ($h/t_w=19$) at -0.15 radian rotation(b) E11 ($h/t_w=19$) at -0.15 radian rotation

Figure 5.57: Deformed shape and von Mises stress (MPa) of link E3 and E11 ($h/t_w=19$) at -0.15 radian rotation

5.8.3 Investigation of Web Compactness Limit to Avoid Buckling of Densely Perforated Links

From the existing literature, it was seen that the maximum rotation attained by short compact shear links reach up to 0.20 radian approximately. So, the web thickness was varied and investigated to find the web compactness (h/t_w) limit for which links with all the mentioned perforation density can sustain rotation up to 0.21 radian. Among the links presented in the previous section the perforation density was maximum for E11 link and this link experienced earlier buckling than all other links. As a representative of link with extremely dense perforations this was used for the finding the desired web compactness limit. The parametric details of the E11 links with different values of h/t_w which are used for this study are shown in Table 5-15. The links are named as E11 followed by an underscore and the value of h/t_w (e.g. E11_19 indicates a link with perforation density similar to E11 and has a web compactness (h/t_w) value of 19).

Table 5-15: E11 links with different values of web compactness (h/t_w)

Link	e (mm)	h (mm)	t_w (mm)	h/t_w	b_f (mm)	t_f (mm)	D (mm)	S (mm)
E11_36.54	400	190	5.2	36.54	130	13	10.95	21.50
E11_31.67	400	190	6	31.67	130	13	10.95	21.50
E11_27.14	400	190	7	27.14	130	13	10.95	21.50
E11_23.46	400	190	8.1	23.46	130	13	10.95	21.50
E11_19.00	400	190	10	19.00	130	13	10.95	21.50
E11_13.57	400	190	14	13.57	130	13	10.95	21.50
E11_12.67	400	190	15	12.67	130	13	10.95	21.50
E11_11.88	400	190	16	11.88	130	13	10.95	21.50

The skeleton curves for the positive cycles of loading of sample E11 for different ratios of h/t_w are depicted as a plot of ratio of shear forces to plastic shear capacities versus link rotation in Figure 5.58. These results are for a D/S ratio of 0.5093. Links with

different h/t_w ratios were investigated starting from the seismic compact limit for highly ductile members, λ_{hd} ($1.57\sqrt{E/F_y}$) of the AISC code and gradually decreasing the value toward more compact web sections. In this case, the value of $1.57\sqrt{E/F_y}$ was equal to 36.90. The drop in peak shear due to web buckling can be observed from the figure.

It is seen that buckling of webs of E11 links having compactness within the AISC compact limit for ductile members is observed even at rotations lower than the AISC prescribed minimum (0.08 radian) for shear links (AISC 341-16). E11 links with h/t_w ratio greater than 23 showed web buckling before reaching 0.08 radian rotation. But, for increasing the seismic resilience, links should be able to sustain high rotations without web buckling. For this, compactness of link web should be increased i.e. value of h/t_w should be decreased. By varying h/t_w it has been observed that, with h/t_w values of approximately less than 13, the E11 link could achieve 0.21-radian rotation without web buckling. However, a value of h/t_w less than 12 is conservatively suggested to be used for avoiding drop in shear force due to web buckling up to 0.21-radian rotation by links with perforation diameter to diagonal hole spacing ratio of 0.5093 or less.

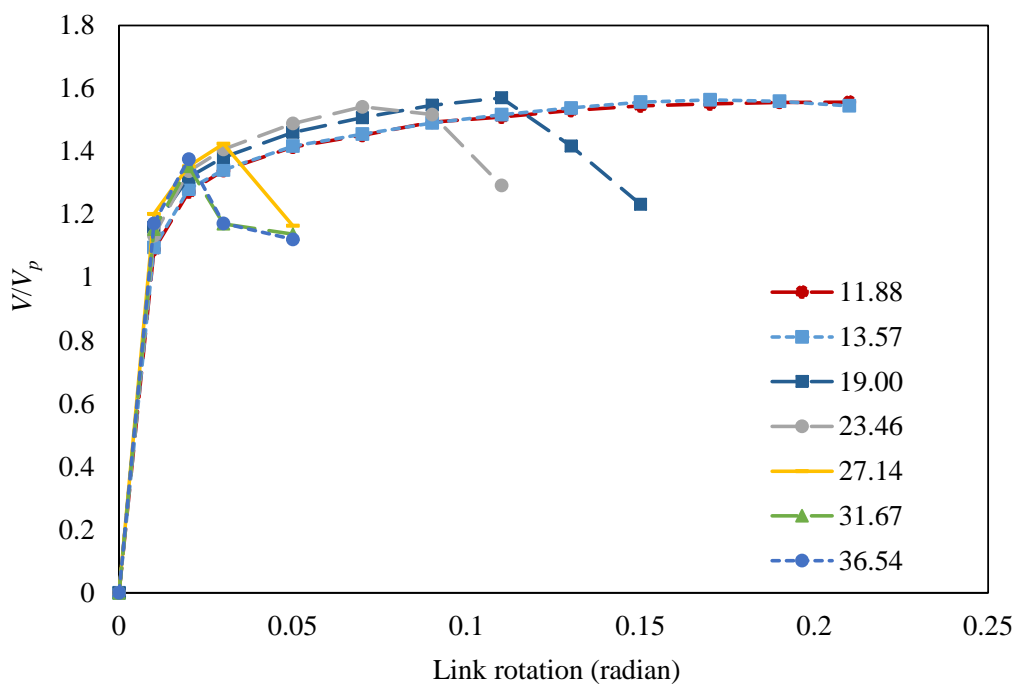


Figure 5.58: Ratio of peak shear forces to plastic shear capacities of E11 samples at different rotations showing shear force drop due to buckling

From the study of the perforation density, it can be concluded that using a lesser dense perforation i.e. using bigger holes with bigger diagonal spacing is better in terms of web buckling. As the value of h/t_w decreases, higher values of plastic shear force will be induced in a link and thus it can sustain more cycles of loading and achieve higher inelastic rotations without showing web buckling. Webs with h/t_w ratios less than 12 can allow the use of extremely dense perforations without allowing web buckling.

5.9 REMARKS

From the numerical study and results, it was found that between two links with same shear and moment capacity but different lengths, maximum shear force in link with higher length ratio is lower than the one with lower length ratio. As the length increases the link behaves more like a flexural member and the maximum shear is thus a reduced value.

The equation V_{p2} neglects the flange of links and thus the shear is calculated based in webs only. However, flange exists in the actual model. So, a box link with two webs shows higher shear force than an I-link despite both having same shear capacity as per equation of V_{p2} . Comparatively better results in terms of equivalent behavior are seen to achieve when the shear capacity equation denoted by V_{p1} is used for the links. However, to achieve equivalent cyclic behavior in both elastic and plastic region, the length ratio of the two links used for equivalence should not be significantly different. Otherwise, despite having equal shear yield the ultimate shear of the two links may vary as the ultimate shear varies with the length ratio of a link.

Making circular perforation in the link webs can reduce the shear capacity and induce early plastic deformation. Hence, thicker compact webs with perforations can be used without rise in shear strength which will aid in delaying the web buckling of the links and thus increase the inelastic deformation capacity. Refined equations are proposed for calculation of plastic shear strength of different types of shear links. The equations were validated against responses of solid I-links of the same shear capacity and it was found that equivalent cyclic response for different shear links of same capacity can be achieved.

From the study of perforation density, it was found that larger diameter of perforations performs better than smaller holes in terms of web buckling. However, the suggested web compactness limits can be followed in design of perforated links and thus web buckling can be avoided without providing stiffeners for all the perforation densities studied.

CHAPTER 6

CONCLUSIONS

6.1 GENERAL

This study focuses on the investigation of cyclic behavior of replaceable shear links for which several three-dimensional finite element models of shear links have been developed considering both geometric and material nonlinearities. Validation of the developed models has been established by comparing the FEM results to the past experimental results.

The developed models were further used for additional numerical studies on the performance of shear links of different geometry (I-shaped link and box-shaped link). Links with both solid webs and perforated webs (for shear strength reduction) were investigated. The links which were used for this study were the ones with length ratio less than 1.6 i.e., shear yielding links which yield primarily due to shear deformation. Interchangeability between the different types of links studied was investigated. For this, refined design equations for predicting the plastic shear strengths of I-shaped and box-shaped links with circular perforations were proposed based on the results of the parametric study.

To investigate the effect of perforation density in link webs, links with the same shear capacity but with different perforation density were studied. Furthermore, the values of the perforation hole diameter (D) and the diagonal spacing between holes (S) were varied but the ratio D/S was kept same for keeping shear capacities equal for all the links. Outcomes of this investigation are also presented in Section 6.2. The web compactness (h/t_w) value was varied starting from the AISC limit for highly ductile members and then decreasing towards more compact values. For this variation, the change in behaviors of perforated links with different perforation densities were also studied. The outcomes and the recommendations of these investigations are presented in the following sections of this chapter.

6.2 OUTCOMES OF THE STUDY

The outcomes of the finite element analysis on different shear links are as follows:

- i. For links with the same plastic shear and moment capacity, the maximum shear increases with the decrease in their length ratios. Thus, the overstrength factor (V_{max}/V_p) also increases as the length ratio decreases.
- ii. The AISC equation for shear links underestimates the shear capacity due to exclusion of flange thickness in calculation. Inclusion of flange thickness in shear calculation predicts better results for both I-shaped and box-shaped links.
- iii. Making circular perforation in the link webs can reduce the shear capacity and induce early plastic deformation which would be beneficial from the viewpoint of seismic energy dissipation. Hence, thicker compact webs with perforations can be used without rise in shear strength which will aid in delaying the web buckling of the links and thus increase the inelastic deformation capacity.
- iv. Diagonal pattern of perforation in link web performs better than the rectangular pattern. The plastic strain energy density is more uniformly distributed over the entire web volume for webs with diagonal pattern of perforations than with rectangular.
- v. Total energy dissipations of the different links of the same plastic shear capacity tend to be approximately the same. However, the hysteresis efficiency of I-links is greater than that of box-links, particularly at lower rotations. At rotations greater than 0.09 radian, the hysteresis efficiency of the I-shaped links and the box-shaped links become approximately equal.
- vi. The web buckling of a perforated link with larger perforation hole diameter is initiated at larger rotation than what occurs for perforated links with smaller hole diameter and denser perforations. Hence, from the viewpoint of web buckling, links with bigger holes and greater diagonal spacing i.e links with lesser density of perforations perform better.
- vii. From the study of web compactness value (h/t_w) of perforated links, it was found that for all perforation densities studied, web buckling in links can be avoided up to 0.21-radian link rotation if the value of h/t_w is less than 12.

6.3 DESIGN RECOMMENDATIONS FOR PERFORATED LINKS

Refined equations are proposed for calculation of plastic shear strength of different perforated shear links. The proposed equations were validated against response of solid I-links of the same shear capacity and it was found that equivalent cyclic response for different shear links of same capacity can be achieved. The details of the equations can be found in Chapter 5 (Equations 5-3 and 5-4).

The proposed refined equations for plastic shear capacities of perforated links (both box-link and I-link) and the suggested equations for solid I-links and box-links can be used for link design. Using these equations, the different types of links studied can be interchanged without causing significant change in the cyclic behavior.

6.4 SCOPES FOR FUTURE INVESTIGATION AND RECOMMENDATIONS

There is certainly further scope of study about the cyclic behavior of replaceable shear links. Some of these relevant to the current study are summarized and recommended as follows.

- i. In the present study, shear links with standard box sections and I sections are investigated. Links with modifications in these sections can be investigated, e.g. links with tapered flanges can be investigated as a possible tool for reducing maximum shear (V_{max}) and overstrength (V_{max}/V_p).
- ii. Shear strength reduction can be done by creating openings in the link webs. Links with only circular openings were studied here. Other types of openings like slit-shaped opening, elliptical-shaped opening, etc. can be investigated and compared to find the most efficient opening geometry for strength reduction. Detailed parametric study of links with other possible openings can also be conducted as was conducted for circular opening in the present study.
- iii. A detailed numerical study was conducted using the material parameters of mild steel. Other types of material can also be used for investigation of cyclic behavior of links and compared to identify the relative advantages of other

effective energy dissipating materials like stainless steel, low yield point steel, etc.

- iv. Comparison between using a link made of low yield point steel (LYP 225, $f_y=225$) and a link made of steel with a higher yield (e.g. ASTM A992, $f_y=350$) but with equal shear strength ensured with perforations can be made and general interchangeability between these two types can be established.
- v. Fracture analysis was not done in the current numerical study. Damage modeling can be done in a finite element package to investigate the failure points of the different types of links studied.
- vi. Effect of residual stress was not considered in this study and thus it can be considered in modeling to investigate the cyclic behavior of links.
- vii. The cyclic behavior of different shear links can be investigated for time-dependent dynamic loading.
- viii. Experimental investigation of perforated links of different perforation density can be conducted to assess how much rotation those links can sustain before failure.
- ix. Experimental investigation of the studied links can be conducted using the proposed design equations to further assess the accuracy and potential of the proposed equations to provide practical results.

REFERENCES

- ANSI, A. (2010). AISC 360-10. Specification for structural steel buildings. American Institute of Steel Construction, Chicago-Illinois.
- ANSI, A. (2010). AISC 341-10. Seismic provisions for structural steel buildings. American Institute of Steel Construction, Chicago-Illinois.
- ANSI, A. (2016). AISC 341-16. Seismic Provisions for Structural Steel Buildings. American Institute of Steel Construction, Chicago-Illinois.
- Azad, S. K., and Topkaya, C. (2017). A review of research on steel eccentrically braced frames. *Journal of Constructional Steel Research*, 128, 53-73.
- Berman, J. W., and Bruneau, M. (2007). Experimental and analytical investigation of tubular links for eccentrically braced frames. *Engineering Structures*, 29(8), 1929-1938.
- Berman, J. W., and Bruneau, M. (2008). Tubular links for eccentrically braced frames. II: Experimental verification. *Journal of structural engineering*, 134(5), 702-712.
- Berman, J. W., and Bruneau, M. (2008). Tubular links for eccentrically braced frames. I: Finite element parametric study. *Journal of structural engineering*, 134(5), 692-701.
- Bozkurt, M. B., Kazemzadeh Azad, S., and Topkaya, C. (2018). Low-cycle fatigue testing of shear links and calibration of a damage law. *Journal of Structural Engineering*, 144(10), 04018189.
- Bruneau, M. (1998). Performance of steel bridges during the 1995 Hyogoken–Nanbu (Kobe, Japan) earthquake—a North American perspective. *Engineering Structures*, 20(12), 1063-1078.
- Bruneau, M., Uang, C. M., and Whittaker, A. (1998). *Ductile design of steel structures* (Vol. 389). New York: McGraw-Hill.
- Chaboche, J. L. (1989). Constitutive equations for cyclic plasticity and cyclic viscoplasticity. *International journal of plasticity*, 5(3), 247-302.

- Chaboche, J. L. (1991). On some modifications of kinematic hardening to improve the description of ratchetting effects. *International journal of plasticity*, 7(7), 661-678.
- Chaboche, J. L. (2008). A review of some plasticity and viscoplasticity constitutive theories. *International journal of plasticity*, 24(10), 1642-1693.
- Chacón, R., Vega, A., and Mirambell, E. (2019). Numerical study on stainless steel I-shaped links on eccentrically braced frames. *Journal of Constructional Steel Research*, 159, 67-80.
- Christopoulos, C., and Montgomery, M. (2013). Viscoelastic coupling dampers (VCDs) for enhanced wind and seismic performance of high-rise buildings. *Earthquake Engineering and Structural Dynamics*, 42(15), 2217-2233.
- Chung, H. S., Moon, B. W., Lee, S. K., Park, J. H., and Min, K. W. (2009). Seismic performance of friction dampers using flexure of RC shear wall system. *The Structural Design of Tall and Special Buildings*, 18(7), 807-822.
- Della Corte, G., D'Aniello, M., and Landolfo, R. (2013). Analytical and numerical study of plastic overstrength of shear links. *Journal of Constructional Steel Research*, 82, 19-32.
- Dusicka, P., Itani, A. M., and Buckle, I. G. (2010). Cyclic behavior of shear links of various grades of plate steel. *Journal of structural engineering*, 136(4), 370-378.
- Engelhardt, M. D. (2007). *Design of Seismic-Resistant Steel Building Structures. AISC Module for Teaching the Principles of Seismic-Resistant Design of Steel Building Structures.*
- Engelhardt, M. D., and Popov, E. P. (1989). On design of eccentrically braced frames. *Earthquake spectra*, 5(3), 495-511.
- Fortney, P. J., Shahrooz, B. M., and Rassati, G. A. (2007). Large-scale testing of a replaceable “fuse” steel coupling beam. *Journal of structural engineering*, 133(12), 1801-1807.

- Fujimoto, M., Aoyagi, T., Ukai, K., Wada, A., and Saito, K. (1972). Structural characteristics of eccentric k-braced frames. *Transactions AIJ*, 195, 39-49.
- Ghobarah, A., and Elfath, H. A. (2001). Rehabilitation of a reinforced concrete frame using eccentric steel bracing. *Engineering structures*, 23(7), 745-755.
- Hjelmstad, K. D., and Popov, E. P. (1983). Cyclic behavior and design of link beams. *Journal of Structural Engineering*, 109(10), 2387-2403.
- Ji, X., Wang, Y., Ma, Q., and Okazaki, T. (2016). Cyclic behavior of very short steel shear links. *Journal of Structural Engineering*, 142(2), 04015114.
- Ji, X., Wang, Y., Ma, Q., and Okazaki, T. (2017). Cyclic behavior of replaceable steel coupling beams. *Journal of Structural Engineering*, 143(2), 04016169.
- Kalehbasti, P. R., and Dolatshahi, K. M. (2018). Two novel shear fuses in moment resisting frames. *Journal of Constructional Steel Research*, 144, 198-210.
- Kasai, K., and Popov, E. P. (1986). General behavior of WF steel shear link beams. *Journal of Structural Engineering*, 112(2), 362-382.
- Lemaitre, J., and Chaboche, J. L. (1990). *Mechanics of solid materials*. Cambridge University, Cambridge, United Kingdom, 161-241.
- Li, R., Zhang, Y., and Tong, L. W. (2014). Numerical study of the cyclic load behavior of AISI 316L stainless steel shear links for seismic fuse device. *Frontiers of Structural and Civil Engineering*, 8(4), 414-426.
- Liu, X. G., Fan, J. S., Liu, Y. F., Yue, Q. R., and Nie, J. G. (2017). Experimental research of replaceable Q345GJ steel shear links considering cyclic buckling and plastic overstrength. *Journal of Constructional Steel Research*, 134, 160-179.
- Ma, X., Borchers, E., Pena, A., Krawinkler, H., and Deierlein, G. (2010). Design and behavior of steel shear plates with openings as energy-dissipating fuses. John A. Blume Earthquake Engineering Center Technical Report, (173).

- Malakoutian, M., Berman, J. W., and Dusicka, P. (2013). Seismic response evaluation of the linked column frame system. *Earthquake engineering and structural dynamics*, 42(6), 795-814.
- Malley, J. O., and Popov, E. P. (1983). Design considerations for shear links in eccentrically braced frames. *Earthquake Engineering Research Center (UCB/EERC 83/24)*
- Mansour, N., Christopoulos, C., and Tremblay, R. (2011). Experimental validation of replaceable shear links for eccentrically braced steel frames. *Journal of Structural Engineering*, 137(10), 1141-1152. N. Mansour, C. Christopoulos, R. Tremblay, Experimental validation of replaceable shear links for eccentrically braced steel frames, *J. Struct. Eng.* 137 (10) (2011) 1141–1152.
- Mazzolani, F. M., Corte, G. D., and D'Aniello, M. (2009). Experimental analysis of steel dissipative bracing systems for seismic upgrading. *Journal of Civil Engineering and Management*, 15(1), 7-19.
- McDaniel, C. C., Uang, C. M., and Seible, F. (2003). Cyclic testing of built-up steel shear links for the new bay bridge. *Journal of Structural Engineering*, 129(6), 801-809.
- Nikoukalam, M. T., and Dolatshahi, K. M. (2015). Development of structural shear fuse in moment resisting frames. *Journal of Constructional Steel Research*, 114, 349-361.
- Oh, S. H., Kim, Y. J., and Ryu, H. S. (2009). Seismic performance of steel structures with slit dampers. *Engineering structures* Structures, 31(9), 1997-2008.
- Okazaki, T., and Engelhardt, M. D. (2007). Cyclic loading behavior of EBF links constructed of ASTM A992 steel. *Journal of constructional steel Research*, 63(6), 751-765.
- Okazaki, T., Arce, G., Ryu, H. C., and Engelhardt, M. D. (2005). Experimental study of local buckling, overstrength, and fracture of links in eccentrically braced frames. *Journal of Structural Engineering*, 131(10), 1526-1535.

- Sarraf M, and Bruneau M. (2004). Performance tests of innovative ductile steel retrofitted deck-truss bridges. In Proceedings of the 13th World Conference on Earthquake Engineering, Canada; [Paper No. 1803]
- Shahri, S. F., and Mousavi, S. R. (2018). Seismic behavior of beam-to-column connections with elliptic slit dampers. *Steel and Composite Structures*, 26(3), 289-301.
- Shen, Y., Christopoulos, C., Mansour, N., and Tremblay, R. (2011). Seismic design and performance of steel moment-resisting frames with nonlinear replaceable links. *Journal of Structural Engineering*, 137(10), 1107-1117.
- Stephens, M., and Dusicka, P. (2014). Continuously stiffened composite web shear links: tests and numerical model validation. *Journal of Structural Engineering*, 140(7), 04014040.
- Tanabashi, R., Naneta, K., and Ishida, T. (1974). On the rigidity and ductility of steel bracing assemblage. In Proceedings of the 5th World Conference on Earthquake Engineering (Vol. 1, pp. 834-840). IAEE Rome.
- Tong, L., Zhang, Y., Zhang, L., Liu, H., Zhang, Z., and Li, R. (2018). Ductility and energy dissipation behavior of G20Mn5QT cast steel shear link beams under cyclic loading. *Journal of Constructional Steel Research*, 149, 64-77.
- Tremblay, R., Filiatrault, A., Bruneau, M., Nakashima, M., Prion, H. G., and DeVall, R. (1996). Seismic design of steel buildings: lessons from the 1995 Hyogo-ken Nanbu earthquake. *Canadian Journal of Civil Engineering*, 23(3), 727-756.
- Tremblay, R., Filiatrault, A., Timler, P., and Bruneau, M. (1995). Performance of steel structures during the 1994 Northridge earthquake. *Canadian Journal of Civil Engineering*, 22(2), 338-360.
- Vian, D., and Bruneau, M. (2005). Steel Plate Walls for Seismic Design and Retrofit of Building Structures. Technical Report MCEER-05-0010. Buffalo, NY: Multidisciplinary Center for Earthquake Engineering Research, State University of New York at Buffalo.

Volynkin, D., Dusicka, P., and Clifton, G. C. (2019). Intermediate Web Stiffener Spacing Evaluation for Shear Links. *Journal of Structural Engineering*, 145(2), 04018257